UNIVERSITY OF WISCONSIN • MADISON, WISCONSIN

NEUTRINO PRODUCTION OF SAME-SIGN DIMUONS AT THE FERMILAB TEVATRON

by

PAMELA HELEN SANDLER

A thesis submitted in partial fulfillment of the
requirements for the degree of

Doctor of Philosophy
(Physics)

at the
UNIVERSITY OF WISCONSIN-MADISON
1992

Abstract

The rate of neutrino and antineutrino induced same-sign dimuon production was measured using a sample of 220 $\mu^-\mu^-$ events and 15 $\mu^+\mu^+$ events, normalized to 1.5 million neutrino-induced charged-current events and 0.3 million antineutrino-induced events with energies between 30 GeV and 600 GeV. The data was obtained with the Chicago-Columbia-Fermilab-Rochester neutrino detector at the Fermilab Tevatron during two experiments, E744 and E770. The CCFR detector is a combined steel target and calorimeter which is followed by a muon-momentum spectrometer. After background subtraction, the prompt rate of same-sign dimuon production is $(0.53\pm0.24)\times10^{-4}$ per charged-current event for neutrinos and $(0.52\pm0.33)\times10^{-4}$ per charged-current events for antineutrinos. These rates are consistent with Standard Model predictions for $c\bar{c}$ gluon bremsstrahlung and with zero. The kinematic distributions of the same-sign dimuon signal are consistent with those of the non-prompt background due to meson decays in the hadron shower of a charged-current events and $c\bar{c}$ gluon bremsstrahlung.

Acknowledgements

I give my deepest thanks to my advisor, Wesley Smith, for he taught me how to be a physicist. I could not ask for a better teacher. I admire his quick perception and insight into physics and beyond and have thoroughly enjoyed being his student. I would also like to thank Arie Bodek, who helped me work through seemingly insurmountable obstacles. I thank him for sharing his wisdom. It was Ugo Camerini's idea that I embark on this project that has led to a Ph.D. I appreciate everything he has taught me during my graduate career, physics and otherwise. I certainly would not have finished this work without him. I thank Jane Camerini, my advisor for the world outside physics, for our incredibly enlightening discussions.

This work was made much easier with the support and friendship of Christopher Watts. He has reminded me how interesting all of physics really is. I thank Tim Kinnel for listening to me think my work through, and for sharing his work with me. I thank Herbi Dreiner for conversations and company late at night in Chamberlin hall during the years we were both in graduate school. I thank Dick Gustafson for listening to my rantings and encouraging me to have fun with my work. I also thank Anna Goussiou and John Jacobsen for being great office mates.

I would like to acknowledge each member of the CCFR collaboration, for this work really represents the contributions from each

one of us. Thanks to Heidi Schellman for getting me started analyzing the data. Bob Bernstein, Frank Sciulli, Michael Shaevitz, Sanjib Mishra, Howard Budd, and Willis Sakumoto contributed invaluable insights. I thank Bruce King, Walter Lefmann, Paul Quintas, Wing Cheung Leung, Bill Seligman, Steve Rabinowitz, and Pawel de Barbaro for their contributions. I have been lucky to work with these people.

Lastly, I thank Jean Johnson and Vincent Fuh for midday conversations and for doing the bureaucratic things that must be done, and Richard Koepsel for keeping those hard disks going.

This dissertation is dedicated to my parents,

Barbara and Sheldon Sandler.

Thankyou Mom and Dad.

Table of Contents

Chapter 1

Introduction

Observation of neutrino deep inelastic scattering gives a unique view of the Standard Model of elementary particle interactions. A rare process in neutrino-nucleon interactions is the production of two muons of the same sign in the final state, called same-sign dimuon production. When the second muon is produced at the hadronic vertex of the neutrino interaction, it is called *prompt*. Since theoretical models of prompt same-sign dimuon production are based on second-order quantum chromodynamic processes, we can study the validity of the Standard Model at the limits of its predictions. When the second muon is produced by decays of pions and kaons in the hadron shower of a charged-current event, the dimuon is called *non-prompt*. Since non-prompt same-sign dimuon production cannot be distinguished from prompt same-sign dimuon production, it is a background that must be eliminated. This dissertation presents measurements of prompt same-sign dimuon production in neutrino and antineutrino scattering in a steel target for neutrino energies between 30 GeV and 600 GeV.

The rate of prompt same-sign dimuon production at energies below 200 GeV was measured by several previous neutrino experiments to be anomalously high relative to theoretical predictions as described in Chapter 11. However in 1988, the CCFR collaboration reported results

with neutrino energies up to 600 GeV that were consistent with Standard Model predictions and with zero [1]. These measurements were made by experiment E744 at the Fermilab Tevatron Quadrupole Triplet beam using the CCFR neutrino detector. The CCFR detector is a large volume and high density detector, made mostly of steel, that is designed to provide a thick target for the neutrinos and measure the topology and energy of ν-N interactions.

The results in this dissertation were made by the CCFR collaboration using data from experiment E744 combined with data from a second run called experiment E770. The members of the CCFR collaboration are listed in appendix C. These new measurements yielded a non-zero rate of same-sign dimuon production with substantially reduced errors. Not only have we decreased the statistical error with an increased sample of same-sign dimuons, but we have reduced the systematic error of the background calculation with new background measurements. In addition, the new rates are consistent with the Standard Model and with the results of E744 in 1988.

1.1 Overview of Same-Sign Dimuon Production

The primary muon in same-sign dimuon production comes from the underlying charged-current event depicted in Figure 1.1. The cross-section for charged-current events is 0.67×10^{-36} cm^2 for 100 GeV neutrinos as measured by the CCFR collaboration [2]. A second muon of opposite

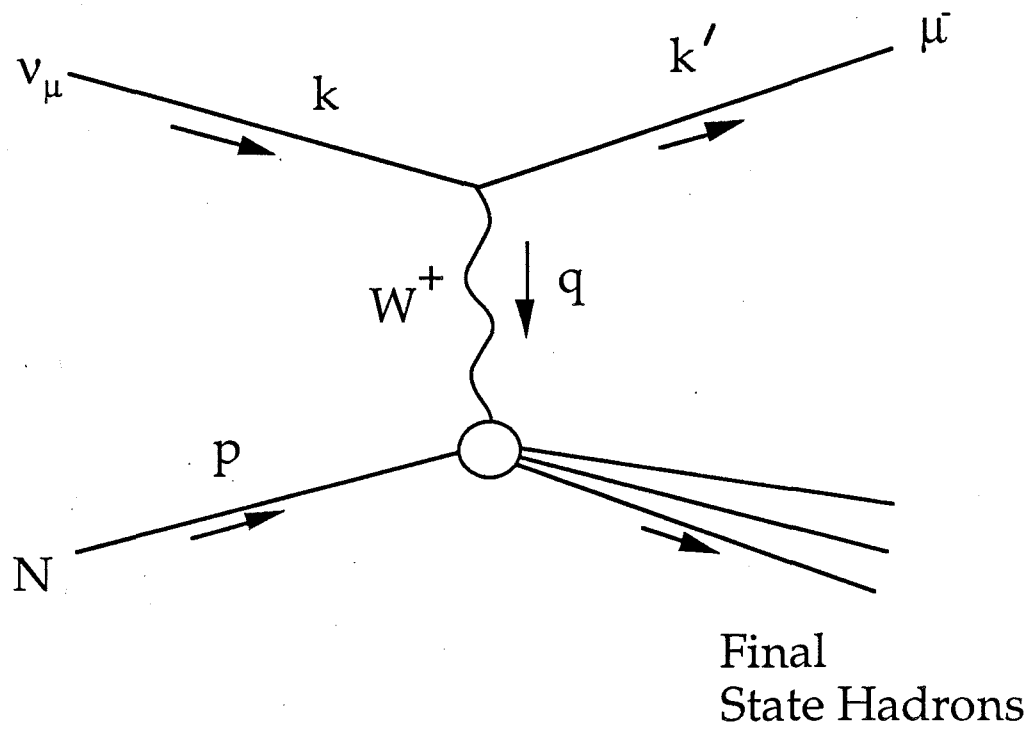

Figure 1.1 A neutrino-induced charged-current event. The charge-conjugated interaction proceeds for incident antineutrinos.

sign to the first will be produced when a charmed quark in the final state hadronizes and semi-leptonically decays, shown in Figure 1.2. This is a well understood process that occurs at a rate of $(0.91\pm0.03)\times10^{-2}$ per charged-current event for neutrino energies between 30 GeV and 600 GeV as measured by the CCFR collaboration [3]. It is called a *prompt* dimuon process because the second muon is produced at the vertex.

The majority of same-sign dimuons come from charged-current events in which pions and kaons in the hadron shower decay to a second muon. This source can be separated into two distinct components. In the

vertex component, primary hadrons decay before interacting, producing a second muon as depicted in Figure 1.3. When the primary hadrons interact before decaying, muons can be produced by decays of hadrons in the subsequent shower. This is called the *shower component*, shown in Figure 1.4. Both components are *non-prompt* because the muons are produced downstream of the vertex.

Unfortunately, non-prompt sources cannot be distinguished topologically from the more interesting prompt sources. Therefore, non-prompt sources must be statistically subtracted from the same-sign dimuon signal in order to measure prompt same-sign dimuon

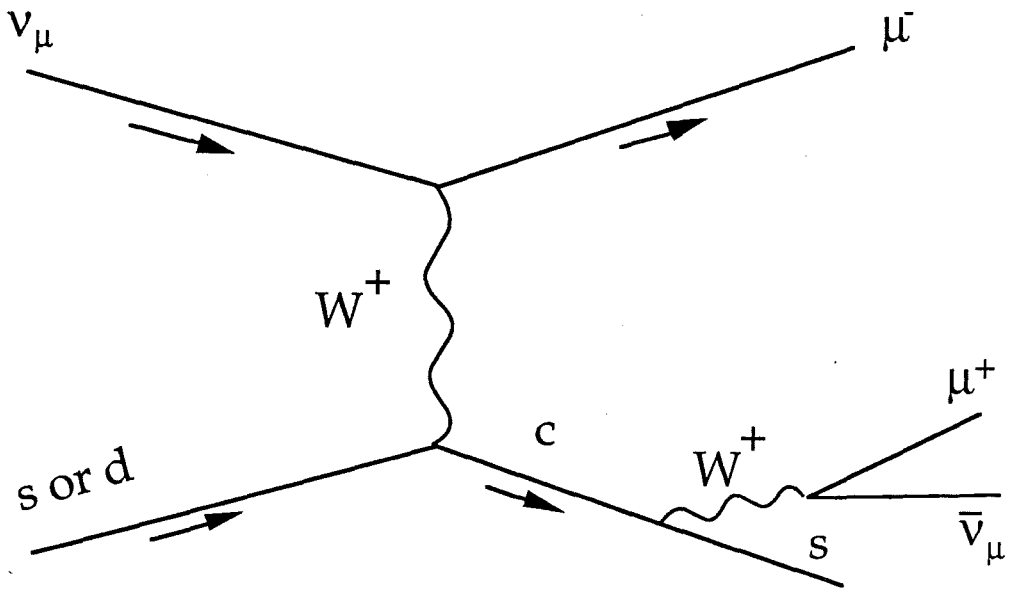

Figure 1.2 Opposite sign dimuon production. For incident antineutrinos, reverse the muon and W boson signs and change quarks to antiquarks.

production. The calculation of the vertex component uses the spectrum of primary hadrons produced at the vertex of the neutrino interaction. To calculate the shower component, we have measured the rate of muon-production by showering hadrons with a hadron beam of known energy in the CCFR detector. In addition, we measured the rate of muon-production by identified incident kaons, which was previously unknown. Together with measurements of the spectrum of primary hadrons in charged-current events from bubble chamber experiments, we calculated the expected shower background to prompt same-sign dimuon production. An important contribution of experiment E770 is in the understanding of the shower component of the non-prompt background. Overall we used experimental data to set each stage of the background calculation, so our results are independent of models for the non-prompt background.

Another source of background to prompt same-sign dimuon production is misidentified trimuon events. Trimuon production becomes a background when the opposite sign muon remains undetected. This background contributes about 5 percent of the total background and must be subtracted.

There is an additional background of about one percent from two overlapping charged-current events that appear to come from a single neutrino interaction. The CCFR detector has precise timing and spatial track resolution. Therefore, most of these are eliminated events by

looking at the relative time of arrival of the two muons and the distance of closest approach between them.

Prompt processes leading to same-sign dimuons are next to leading order in QCD and the rates are significantly smaller than the opposite-sign dimuon rates. In $c\bar{c}$ gluon bremsstrahlung shown in Figure 1.5, the final state quark radiates a gluon which produces a $c\bar{c}$ pair. A second muon comes from the semi-leptonic decay of the $\bar{c}$ quark. The rate of same-sign dimuon production by $c\bar{c}$ gluon bremsstrahlung is predicted to be less than 10^{-5} per charged-current event at the energies available in this experiment as described in Chapter 10. Another source of prompt same-sign dimuons is from vertex production of a charmed quark that fragments to a D^0 meson. Usually this results in an opposite sign dimuon when the D^0 meson decays. However, if the D^0 oscillates to a $\bar{D}^0$ and then decays, a same-sign dimuon is produced. Figure 1.6 shows this process. A third mechanism is bottom quark production, shown in Figure 1.7. A $\bar{b}$ quark, produced at the hadronic vertex of a charged-current event decays to a $\bar{c}$ quark that semileptonically decays. Neither of these processes is expected to contribute a measurable signal in our experiment. The same-sign dimuon rate due to D^0-$\bar{D}^0$ mixing is expected to be less than 2×10^{-6} at the neutrino energies in this experiment, as described in Chapter 10. The rate due to bottom production, also described in Chapter 10, is on the order of 10^{-6} at 100 GeV [4].

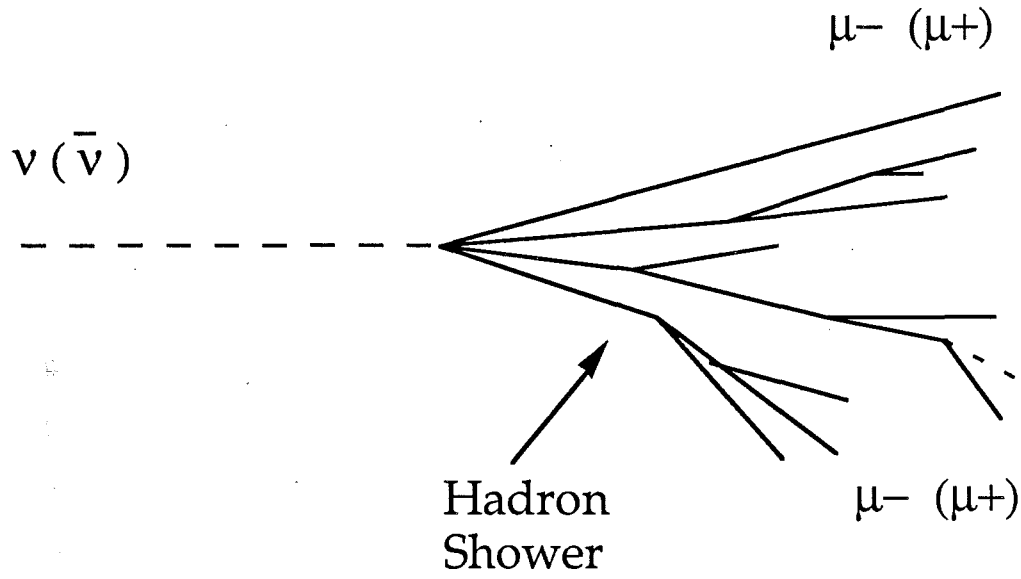

Figure 1.3 A same-sign dimuon from the shower component of the meson-decay background. A secondary muon is produced from either a pion or kaon decay in the hadron shower.

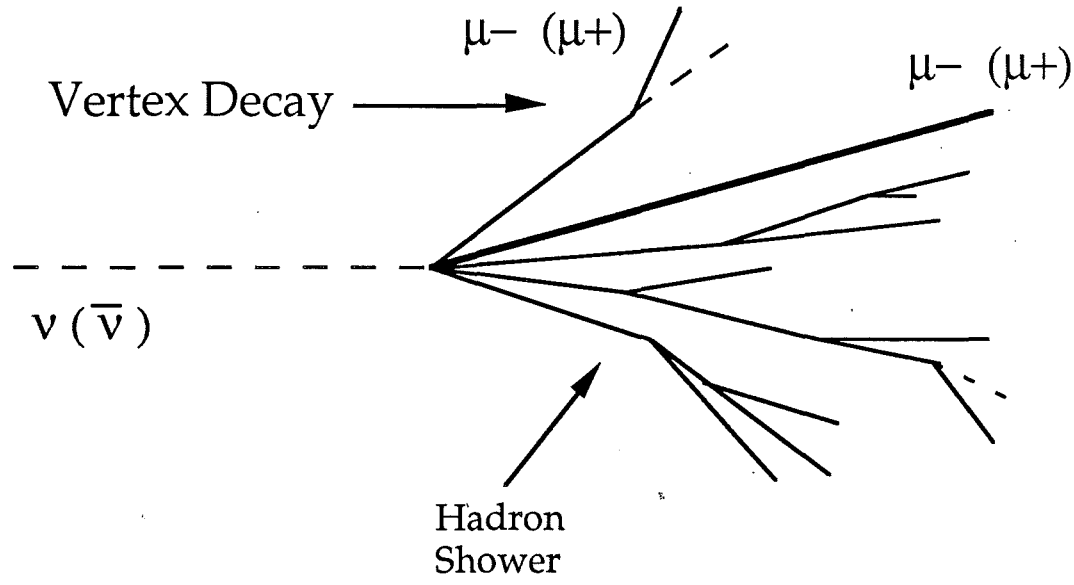

Figure 1.4 Vertex background dimuon caused by the decay of a primary hadron in the hadron shower of a charged current event.

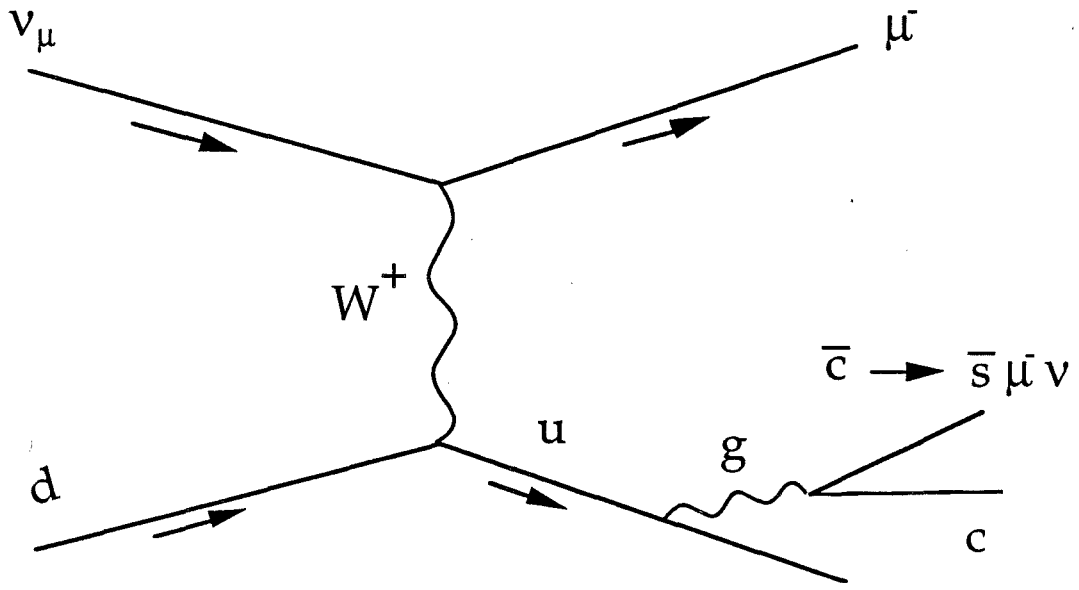

Figure 1.5 $c\bar{c}$ gluon bremsstrahlung production of same-sign dimuons.

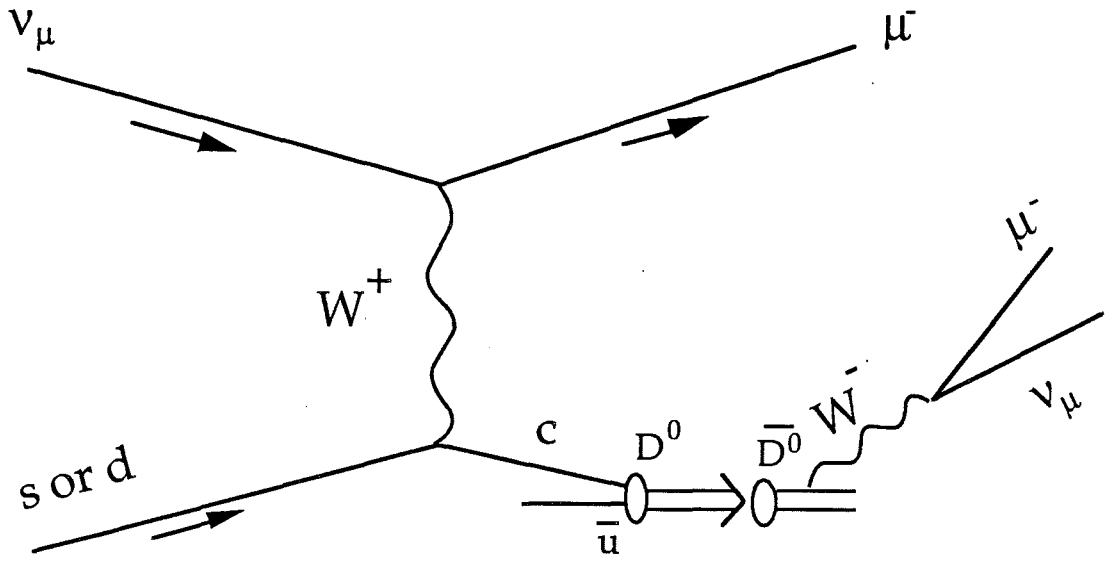

Figure 1.6 D^0-$\bar{D}^0$ mixing and production of same-sign dimuons.

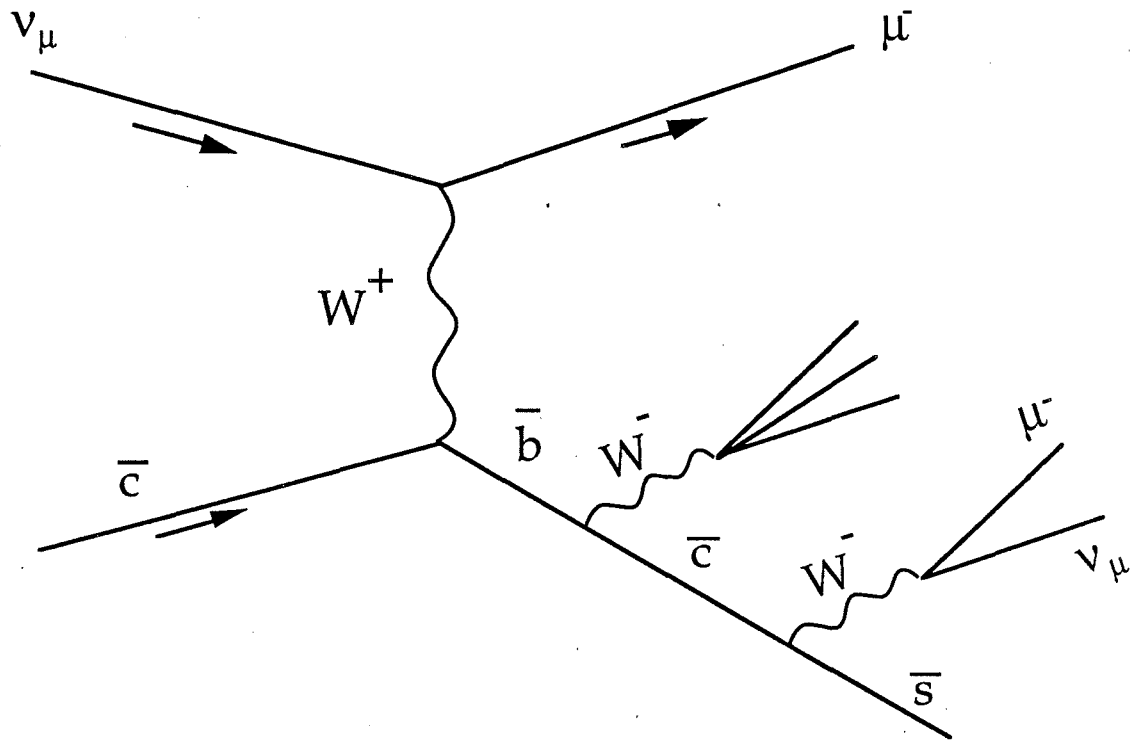

Figure 1.7 Bottom production of same-sign dimuons.

Experiments prior to E744 measured a prompt rate of same-sign dimuon production that was up to four standard deviations higher than that expected from $c\bar{c}$ gluon bremsstrahlung or zero. The reasons for this included low statistics and uncertain background estimations as described in Chapter 11. Our detailed background calculation is based on high-statistics measurements and does not rely on any particular physics model. Furthermore, the Fermilab Tevatron produced a high flux neutrino beam at higher energies than at previous accelerators. This gave us the statistical power to accurately measure same-sign dimuon production. In addition we were able to observe the energy dependence of same-sign

dimuon production with significant statistics at neutrino energies above 200 GeV, which was not possible before. For example, the CDHSW experiment, which had the largest sample prior to this experiment, observed 118 neutrino induced same-sign dimuon events with neutrino energies above 100 GeV and 20 events above 200 GeV [5]. The results in this dissertation are based on 204 events above neutrino energies of 100 GeV, 159 events above 200 GeV, and 62 events above 300 GeV.

1.2 The Kinematics of Deep Inelastic Neutrino Scattering

The kinematic variables that characterize deep inelastic neutrino scattering are presented in this section. Figure 1.1 shows the diagram for a charged-current event with the momentum vectors of each particle. In the lab frame the four-momenta of the particles are:

$k = (E_\nu, 0, 0, E_\nu)$	for the incident neutrino,
$k' = (E_\mu, 0, E_\mu \sin\theta_\mu, E_\mu \cos\theta_\mu)$	for the primary final state muon,
$p = (M, 0, 0, 0)$	for the target nucleon,
$q = (\nu, \mathbf{q})$	for the W boson

where the beam is in the z direction, and the primary muon of the final state is in the y-z plane. The following kinematic quantities are derived from these variables:

- Q^2 is the negative of the square of the momentum transfer to the nucleon squared given by,

$$Q^2 = -(k - k')^2 = 2E_\nu E_\mu(1 - \cos\theta_\mu)$$

- Bjorken y is the fractional energy transfer to the nucleon given by,

$$y = \frac{q \cdot p}{k \cdot p} = \frac{\nu}{E_\nu}$$

- Bjorken x can be interpreted in the parton model as the fraction of nucleon momentum carried by the struck parton [6] and is given by,

$$x = \frac{Q^2}{2\,p \cdot q} = \frac{Q^2}{2\,M\,\nu} = \frac{E_\nu\,E_\mu\left(1 - \cos\theta_\mu\right)}{M\,\nu}$$

- W^2 is the invariant mass of the hadronic system given by,

$$W^2 = (q + p)^2 = -Q^2 + 2p\cdot q + p^2$$

$$= -Q^2 + 2M\nu + M^2$$

$$= 2M\nu\,(1 - x) + M^2$$

Chapter 2

The Experimental Apparatus

2.1 Introduction

The Tevatron accelerates protons with superconducting magnets to 800 GeV. The neutrino beam is derived from decays of pions and kaons produced when the 800 GeV proton beam interacts with a beryllium target. The pions and kaons decay in a 340 meter long decay pipe followed by a 900 meter long earth and steel berm which stops all but the neutrinos and the highest energy muons. The CCFR detector is located in Lab E about 1500 meters downstream of the beryllium target. It is a 690 ton combined target and calorimeter, followed by a 420 ton muon-momentum spectrometer. It provided a target for the neutrinos, measured the visible energy of interacting neutrinos, and the sign and momentum of final state muons.

2.2 The Quadrupole Triplet Neutrino Beam

Protons accelerated to 800 GeV in the Tevatron are extracted each 60 second cycle in two to four spills, each about 2 ms long. Each spill contained many 2 ns long bunches of protons, called RF buckets, spaced in 18.6 ns long intervals. The time structure was determined by the radio frequency cavities in the linear accelerator used to accelerate the protons before they were injected in the Tevatron. The protons were directed on a 310 mm long beryllium target. Secondary pions and kaons from the target

passed through a collimator, then through four pairs of quadrupole magnets that focussed the beam in the transverse directions. The neutrino beam is called a *quadrupole triplet beam* (QTB) because in the past, three pairs of quadrupole magnets focussed the pions and kaons. The name remains for historical reasons and reflects the fact that all pions and kaons are used to produce the neutrino beam, as opposed to selecting ones with specific sign or momenta. The pions and kaons were allowed to decay in a 340 meter long decay pipe. A 6 meter long aluminum beam dump eliminated any pions and kaons that did not decay and a 900 meter steel and earth berm eliminated the decay muons. The neutrino beamline is depicted in Figure 2.1.

The neutrino beam retained the time structure of the proton beam. There were more than twice as many neutrinos than anti-neutrinos because the proton-beryllium collisions produce mostly positive pions and

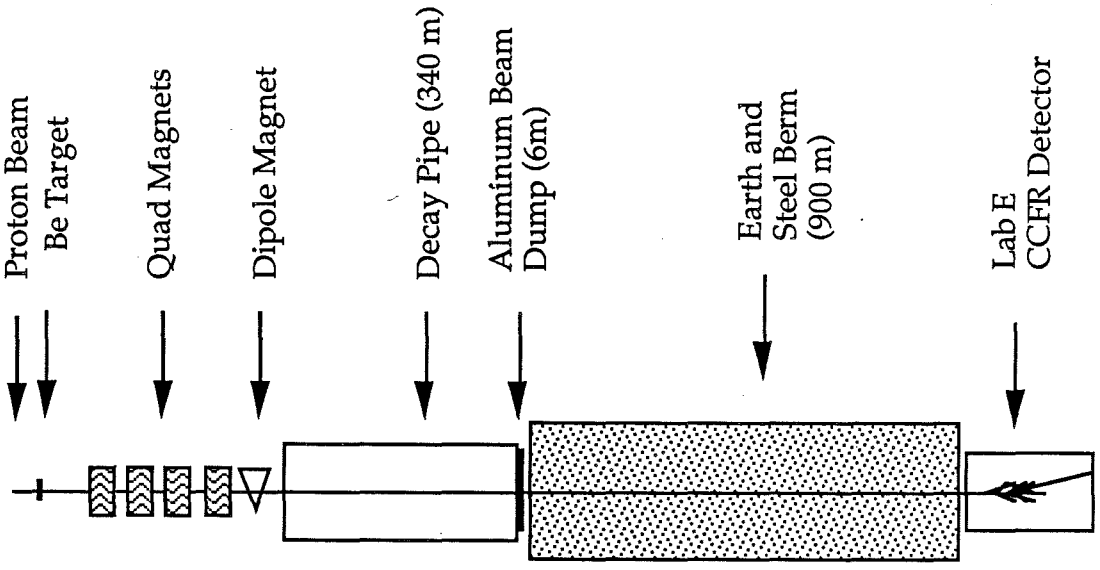

Figure 2.1 The neutrino beamline.

kaons. Negative pions and kaons, resulting in negative muons and antineutrinos, usually come from tertiary interactions in the beryllium target. Therefore, the average energy of the anti-neutrinos was lower than the neutrinos. We observed about 5.2 million neutrino interactions and 3.2 million antineutrino interactions in the CCFR detector during the two experiments E744 and E770. The spectrum of neutrinos and antineutrinos is given in Figures 4.1a and 4.1b for the two experiments. The large peak at lower energy is due to neutrinos from pion decays and the smaller bump at slightly higher energy is due to neutrinos from kaon decays. Note that the antineutrino spectrum was lower in energy and statistics than the neutrino spectrum.

2.3 The CCFR Detector

The CCFR detector, depicted in Figure 2.2, consisted of a combined iron target and calorimeter, instrumented with scintillation counters and drift chambers. It measured the hadronic energy of the event and the trajectory of emergent muons. The muon spectrometer, located just downstream of the calorimeter, consisted of three toroidal magnets with drift chambers positioned between them. By observing the bend of the muon path in the magnetic field of the toroids, we reconstructed the momentum of the muon at the front face of the spectrometer.

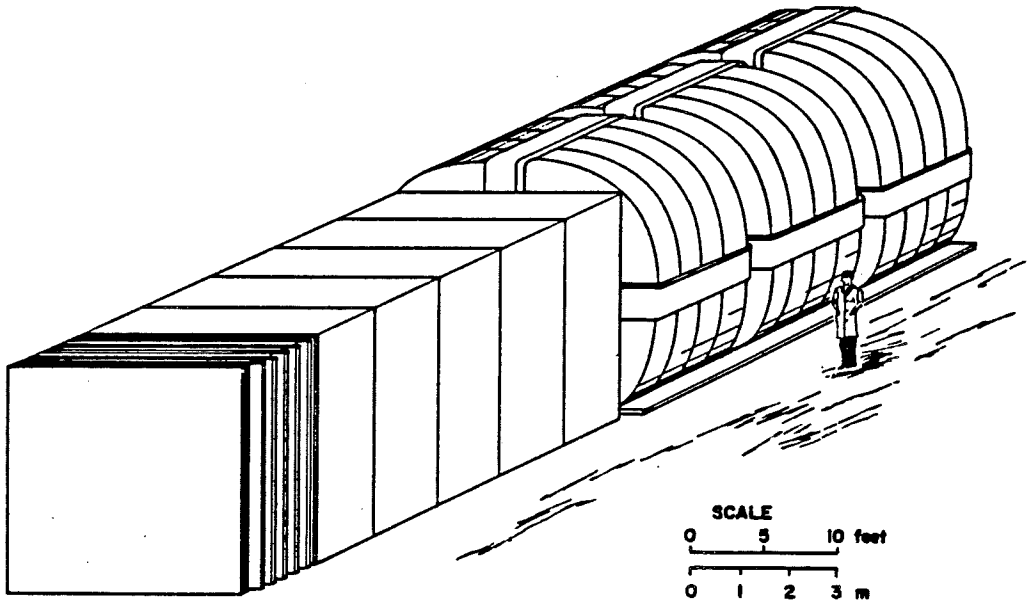

Figure 2.2 The CCFR detector.

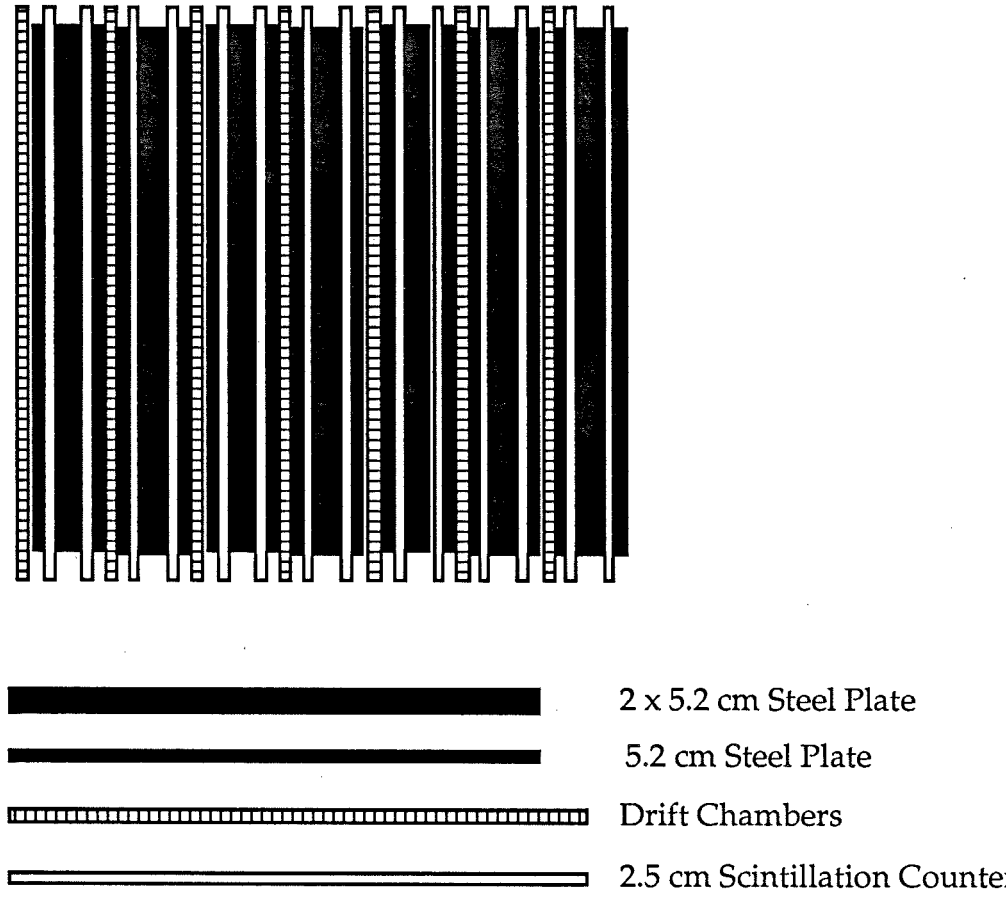

Figure 2.3 A calorimeter cart.

2.3.1 The Calorimeter

The calorimeter was divided into six movable carts. Each one contained twenty-eight 3m x 3m x 5.2 cm steel plates, fourteen 3m x 3m x 2.5 cm scintillation counters every 10 cm of steel, and seven 3m x 3m drift chambers giving x and y positions of particles every 20 cm of steel. The structure of a calorimeter cart is shown in Figure 2.3.

The 84 liquid scintillation counters in the CCFR detector were made of fluor-doped mineral oil in ribbed acrylic tanks, surrounded by polyethylene bags filled with water for structural reinforcement [7]. A charged particle passing through the scintillator excited the primary fluor which emitted UV light. The UV light was absorbed by a secondary fluor which re-emitted it as blue light. It was collected by wave-length shifter bars at the sides of the scintillator. Finally, the bars converted the light to green, and guided it to RCA 6342A bialkali-photocathode photomultiplier tubes located at each corner.

The four photomultiplier tube pulses from each counter were digitized with LeCroy 4300 FERA analog to digital converters (ADC's) in four ranges: 1) the output of each of the four phototubes was individually digitized, 2) the four phototube pulses were summed then digitized, 3) the sum of the four phototube pulses were amplified by a factor of ten, then digitized, and 4) groups of phototubes in one corner, separated by ten counters, were attenutated and summed. Digitized pulses from category 3 were used for calibrating the counter's response to muons. Digitized pulses from category 1 and 4 were used for hadron energy measurement. Category 2 was used for cross calibration of the four different ranges. For timing information, the pulse-heights were sent through a discriminator set at $1/4E_{mip}$, and digitized by time-to-digital converters (TDC's). The variable E_{mip} is the energy deposited by a minimum ionizing particle as measured with a muon test beam.

Two large banks of acrylic counters located just upstream of the CCFR detector were used to veto events induced by incident charged particles. The acrylic counters were 25 feet by 15 feet in the transverse direction so they extended about 13 feet past the edges of the CCFR detector. The large transverse dimensions of the acrylic counters were chosen so that they detected charged particles at very large angles, in addition to charged particles in the beam. The acrylic counters were shielded from low energy photons and hadrons by concrete walls surrounding them. Together with the most upstream two liquid scintillation counters of the calorimeter, they were used to identify muons in the neutrino beam and neutrino events that interacted upstream of the calorimeter. Signals from both of these sets of counters comprised VETO signals that were used in the detector triggers as described below.

The response of the target scintillation counters varied with the transverse position of charged particles in the counter due to the geometry of light collection. For example, a muon at about thirty inches from the center typically yielded about 10 percent more detected photons than a muon at the center. Using the muons present in a steerable hadron test beam, we obtained a map of the response of each counter as a function of transverse position, which was used to correct the pulse heights [8].

The drift chambers are described in detail in references [3, 9] and are summarized here. Each drift chamber contained two planes that measure x and y hit positions. In the calorimeter drift chambers, each plane contained 24 drift cells with three wires each; one field wire and the two

sense wires on either side or end. The drift chambers in the toroid spectrometer contained two planes with 24 single-wire cells. These chambers were placed in groups of five, staggered by one quarter of a cell width in both x and y to resolve hits on the left of the wire from those on the right. Electrons liberated from the gas by the passage of a charged particle drift with constant velocity to the nearest sense wire, producing a pulse. The leading and trailing edges of the pulse are digitized with multihit buffered TDC's that have 4 ns time bins. Calculation of the position of the particle path is described in Section 3.1.4. The resolution of the single-wire and three-wire drift chambers was 225 μm determined from muons in the hadron test beam. In addition to the time, the amount of charge on the sense wires was digitized with flash analog to digital converters (FADC's) in 48 nsec time bins [3]. The FADC's were used to supplement the TDC information in the hadron test beam analysis that is described in Section 5.5.4.

2.3.2 The Muon Spectrometer

The analyzing magnetic field was provided by three 3m-long toroidal magnets shown in Figure 2.4. Each toroid was made of eight 20 cm thick steel washers with 1.8 m outer radius and 12.7 cm inner radius. Current in four coils, wrapped around the outside and through the hole, magnetized the steel of the washers resulting in an 18 kGauss field confined to the volume of the toroids. All three toroids together provided a 2.4 GeV/c transverse momentum kick to the muons. The polarity of the current, and hence the sense of the magnetic field, was

reversed regularly so that negative and positive muons could be bent towards the center at different times during the run.

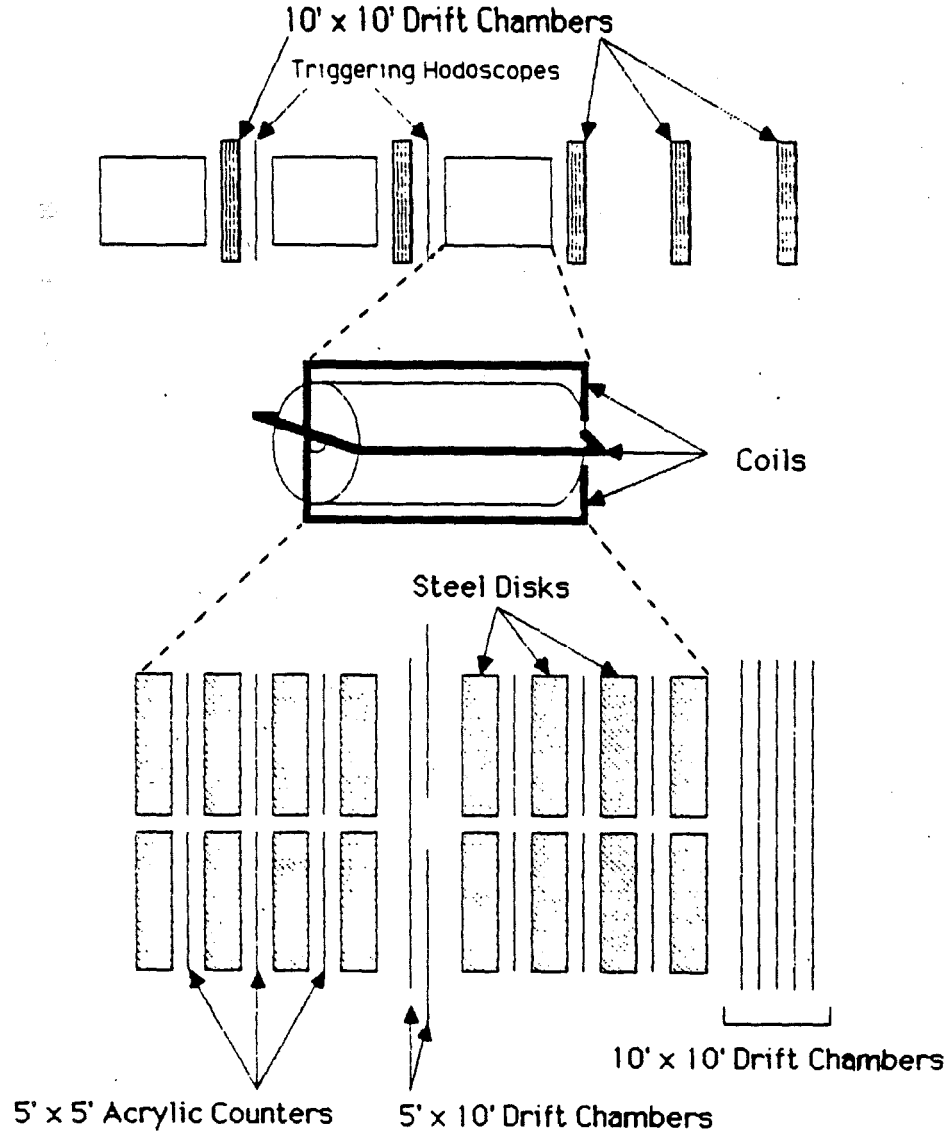

Figure 2.4 The muon spectrometer

Five groups of five single-wire drift chambers with x and y views each, were located in each gap between the toroids, immediately after the third toroid and at 3 m and 7 m downstream of the third toroid. Trigger counters made of acrylic scintillator were located downstream of the first toroid and the second toroid. In addition, four 5′x5′ acrylic quarters were placed between each washer. One of the chambers in two of these groups was tilted at 4° relative to the x-y axes to enable matching x and y views of track together. These were located just downstream of the calorimeter and three meters from the downstream end of the spectrometer. All drift chambers in the spectrometer were aligned by optical survey. During the run, we used high energy muons from charged-current events to obtain the exact positions of the sense wires [9].

2.4 The Event Triggers

Event triggers are designed to signal the electronics that data from the event should be written to tape. Two different triggers were used in this analysis; the charged-current trigger and the straight-through muon trigger. The former identified neutrino-induced events with a penetrating muon. The latter were caused by beam muons or charged-current events that were initiated upstream of the CCFR detector. These events were used for alignment and energy calibration during the run. There were several other triggers used in the CCFR experiment which are described in detail in reference 3.

The charged-current trigger: This trigger identified charged-current events in which the muon penetrated the spectrometer and events in which the muon ranged-out before reaching the spectrometer. The logic of this trigger is given in Figure 2.5. Note that the calorimeter counters are numbered 1 through 84, where counter 1 is the most downstream counter. The trigger was set if 1) there was at least one quarter minimum ionizing energy deposition ($1/4E_{mip}$), in two of the four most downstream counters (1-4), signals from the trigger counters in the first (T2 and Hodo) and second toroid gaps (T3), and no signal from the veto counters. The trigger was also satisfied if 2) there was at least $1/4E_{mip}$ in the counters numbered 1-4 and 9-12, and no signal from the veto counters. There were 2.7 million charged-current trigger events in experiments E744 and E770. The efficiency of the charged-current trigger was better than 99%, determined from the number of events that satisfied both of the charged-current trigger conditions 1) and 2) above [9].

The straight-through muon trigger: This trigger, shown in Figure 2.6, used all six target carts and the acrylic counters between the toroid washers. It required at least $1/4E_{mip}$ in one of four calorimeter counters in six groups of counters numbered 5-8, 17-20, 33-36, 45-48, 61-64, and 69-72, and a veto signal. In addition, at least one toroid acrylic counter out of four adjacent counters must detect the muon, and it had to pass through the same quadrant of the counter registering the signal (PTOR).

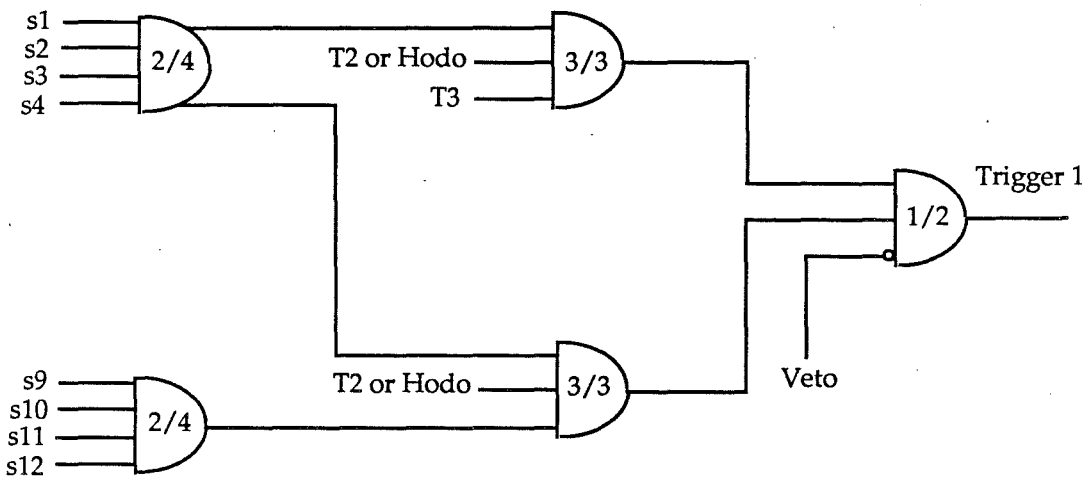

Figure 2.5 Charged-current trigger logic. The inputs s1-s4 and s9-s10 are set by $1/4E_{mip}$ in the counters 1-4 and 9-12 respectively. The calorimeter counters are numbered 1 through 84, where counter 1 is the most downstream counter. The labels T2 and T3 refer to the acrylic trigger counters located in the gaps downstream of the first toroid and second toroid, respectively. Hodo refers to hodoscopes also in the first and second toroid gaps.

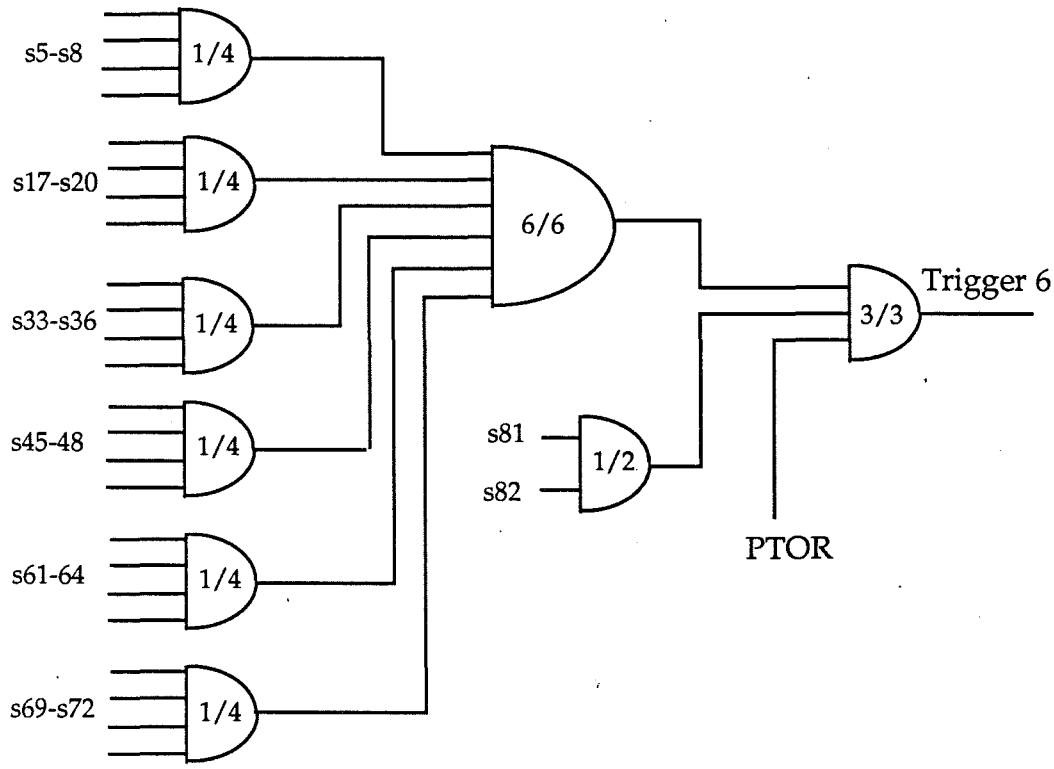

Figure 2.6 Straight through muon trigger logic. The inputs s1-s82 are set by $1/4E_{mip}$ in each counter numbered 1 through 82, where counter 1 is the most downstream counter. The label PTOR is explained in the text.

Chapter 3

Event Reconstruction and Selection

3.1 Introduction

This chapter describes extraction of the kinematic variables from the raw data that are necessary to select and analyze charged-current and multi-muon events and the selection procedure. The raw data for each event written to tape consists of pulse heights from the target calorimeter, the time associated with the trigger signal, times of the counter pulse heights, and times of drift chamber hits. The acquisition of raw data is described in Chapter 2.

The kinematic variables that describe ν-N deep inelastic scattering are derived from the total hadronic energy E_h, the muon momentum at the event vertex P_μ, and the angle of the primary muon with respect to the incident neutrino direction θ_μ. It is also necessary to reconstruct the event vertex and the event time to ensure that the observed event triggered properly and that it was not due to the overlap of two charged current events. By comparing of the time of the trigger signal with the time of the muon track in the toroid and the time of the largest hadron shower, we can confirm that an observed muon belongs with an event, otherwise it may be due to a second neutrino interacting at the same time. In addition, the event vertex is needed to ensure that the event was fully contained in the detector volume.

Good single muon, dimuon and trimuon events are selected from the sample of reconstructed charged-current trigger events. The selection process ensures that they are properly reconstructed in the detector and that the momentum of each muon is accurate. The good charged-current events provide the normalization for the rate of same-sign dimuon production. The sample of identified trimuons checks the trimuon Monte Carlo simulation that is used to calculate the background due to misidentified trimuons. The reconstruction and selection of charged-current events and dimuon events has been described in references [3, 9]. A summary is given below in Section 3.2.

3.2 Event Reconstruction

3.2.1 The Event Vertex

The position of the event vertex along the beamline, or the longitudinal event vertex, V_z, is halfway between the two most upstream target scintillation counters that detect more than E_{th} which is given by

$$E_{th} = 4\,E_{mip} + E_{mip}[\log_{10}(E_h)]$$

where E_{mip} is the energy deposited by a minimum ionizing particle and E_h is the hadron energy described in Section 3.1.2 below. The second term accounts for energy due to albedo, which is the spray of backscattered particles at the vertex. The vertex V_z is placed in the steel because the

neutrino is most likely to interact there. The resolution of V_z is limited by the fact that the actual longitudinal vertex is somewhere between two counters, not necessarily halfway. Assuming the actual longitudinal vertex is distributed according to a Gaussian between the two counters, the resolution is $\sqrt{12}$ of the spacing between the counters or 6 cm. The efficiency of the V_z algorithm was studied by obtaining the track longitudinal vertex V_t, from the intersection of the two muon tracks in dimuon events. It was found that the average difference between V_z and V_t is about 10 cm for the dimuon events and V_t was downstream of V_z on the average [10].

The transverse vertex is given by the transverse position of the track at V_z. The resolution of the transverse vertex is determined by the intrinsic drift chamber resolution which is 250 μm.

3.2.2 The Hadron Energy

The CCFR target calorimeter is a sampling calorimeter in which hadronic interactions occur in the iron plates and are observed with the scintillation counters. Charged particles in the hadron shower deposit visible energy in the form of ionization in the scintillation counters that are located every 10 cm of iron. Neutral particles remain undetected unless they decay to a pair of charged particles. Each charged particle deposits approximately the energy of a minimum ionizing particle E_{mip}, in each counter that it traverses until it ranges out, decays or interacts. *The total hadronic energy is proportional to the sum of the energy deposited in the calorimeter counters.* We determine the constant of

proportionality, called the *calibration*, by exposing the calorimeter carts to momentum analyzed hadron test beams [8]. This calibration compensates for the average energy not sampled and the energy lost in the form of neutral particles and nuclear breakup. The energy resolution of the detector is limited by shower-to-shower fluctuations in the energy that is not deposited in the form of ionization in the scintillation counters [11].

The ADC pulse heights from each phototube in a scintillation counter are summed and converted to the equivalent energy measured in GeV. We first correct the summed pulse heights for the *gain* of the ADC's and phototubes, where the gain is the number of ADC counts per minimum ionizing particle obtained by studying muon tracks in charged current events. This amounted to 60 counts on the average. The calibration (Calib) that converts the number of minimum ionizing particles to an energy is known to better than 1 percent from the hadron test beam exposures. It is 0.211 GeV/mip [8]. In summary, the energy measured in GeV in each counter E_i, is given by:

$$E_i = \frac{ADC_i}{Gain_i \times Mapcor\,(x,y)_i} \times Calib$$

where ADC_i is the number of ADC counts in the counter i and $Gain_i$ is the gain of counter i. $Mapcor(x,y)_i$ corrects for the variation in the light collection efficiency with the transverse position of the shower in the counter. It is measured by steering the momentum analyzed hadron beam

at various transverse positions within each counter. The target carts themselves are individually exposed to the steered hadron beam to determine longitudinal variations in the target response. There is also a correction for the variation with time of the response of the phototubes during the run. The ADC pulse heights at time $t=\tau$ are converted to the equivalent ADC pulse heights at a time t=0 when $Gain_i$ was measured, according to

$$ADC_i(t=0) = ADC_i(t=\tau)\frac{g_i(0)}{g_i(\tau)}$$

where $g_i(t)$ is the gain of the counter at a time t. The relative gain, $g_i(0)/g_i(\tau)$ is constantly monitored during the run with momentum analyzed muons that satisfied the straight through muon trigger. The gains of some tubes changed by up to 10 percent over a six month period, whereas others were more stable.

Finally, the total hadron energy is the sum of E_i over twenty counters starting downstream of the longitudinal vertex, less the energy deposited by the muon(s) over these twenty counters.

The energy resolution for hadron showers averaged over all incident between 25 GeV and 500 GeV was fit to the following function:

$$\frac{\sigma(E_h)}{E_h} = \frac{(0.847 \pm 0.015)}{\sqrt{P}} + \frac{(0.297 \pm 0.115)}{P} \qquad 3.1$$

where E_h is measured in GeV and P is the momentum in GeV/c of the hadron test beam used to extract the resolution function. The second term is associated with noise generated by the amplifiers in the digitizing electronics [12]. Figure 3.1 shows the measured hadron energy for the 100 GeV hadron test beam. The momentum of each test beam hadron was known to 1 percent from magnetic analysis in the spectrometer located upstream of the calorimeter, as described in Chapter 5. The curve in Figure 3.1 is the hadron energy resolution function given by equation 3.1 above. The calorimeter was linear to 1% between 25 GeV and 450 GeV, which were the lowest and highest energy hadron beams used to calibrate the detector.

For charged-current and multi-muon events, the energy deposited by the muon(s) in the counters is subtracted from the measured energy deposit to obtain the hadron energy. The hadron energy resolution in this case is the energy resolution for muons added in quadrature to the hadron energy resolution function given in equation 3.1. The energy resolution for muons was about 1.7 GeV averaged over all energies [9].

3.2.3 The Event Time

The event time is given by the digitized time of the trigger signal. The time associated with tracks in the target, relative to the time of the trigger signal, is given by the arrival times of the calorimeter counter pulse heights. Depending on the length of the track, the resolution of the track time, relative to the trigger, is between 5 and 10 ns.

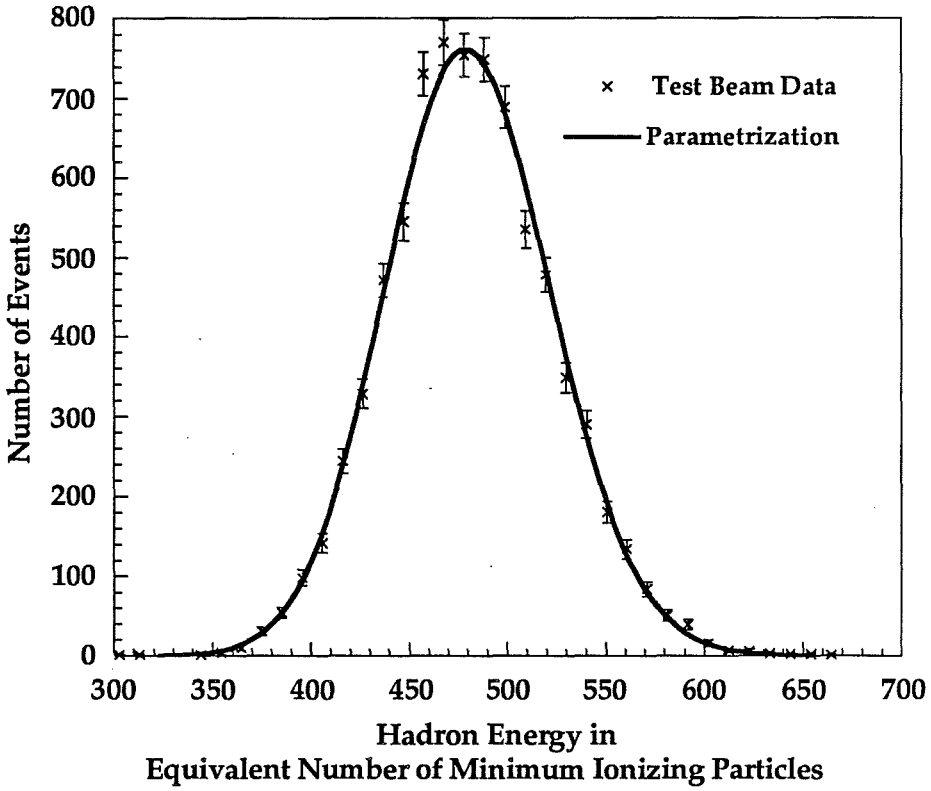

Figure 3.1 Reconstructed hadron energy of a momentum analyzed 100 GeV test beam. The curve is given by the parametrization of the hadron-energy resolution given by equation 3.1.

Once the tracks in the toroid spectrometer are found, they are used to refine the event time relative to the trigger time t_0. Given the position of a hit on a track from the fit, x_{fit}, the time of arrival of the drift electrons at the wire, t, the drift velocity, v_D, and x_0, the position of the sense wire we obtain t_0 by minimizing the following chi-square function with respect to t_0:

$$\chi^2 = \sum [x_{fit} - (t - t_0)\, v_D - x_0]^2$$

where the sum is over all hits on the track. It represents the difference between the distance to the wire given by the fit, and the distance to the wire calculated from v_D and the drift time $(t-t_0)$. The final time resolution is 2 ns [9].

3.2.4 Angle (θ_μ) and Muon Momentum (P_μ) at the Vertex

The angle of the muon at the vertex is calculated from the track in the calorimeter. The muon momentum at the front face of the spectrometer $P_{\mu f}$, is measured from the bend of the muon trajectory in the magnetic field of the toroid spectrometer. If the muon ranged out before reaching the first toroid gap where the first group of drift chambers are located, the momentum was obtained from the length of the track in the calorimeter assuming the energy was lost in the form of ionization. This section describes the track fitting in the calorimeter and the spectrometer.

Calorimeter Tracking

The x and y positions of drift chamber hits are calculated from t, the time of arrival of the drift electrons, according to

$$x = (t - t_0)\, v_D + x_0$$

$$y = (t - t_0)\, v_D + y_0$$

where t_0 is the event time extracted from the calorimeter counters, v_D is the drift velocity and (x_0,y_0) is the position of the sense wire. These last two variables were obtained with optical alignment and tracks of straight-through muons.

The tracking algorithm in the calorimeter found candidate track segments in each view, in groups of eight chambers. First it fitted straight lines to pairs of drift chamber hits; one from each end chamber of the group. In the intermediate chambers, it used hits that were between this initial line and the nearest sense wire. The algorithm then attempted to add hits to the tracks upstream and downstream of the group of eight chambers. It also attempted to combine tracks in the longitudinal direction. The χ^2 for each candidate track was obtained from a linear least squares fit to the hits on the track. Duplicate tracks and those tracks with bad χ^2 from the fit were rejected.

The track fits were complicated by multiple Coulomb scattering that depends on the momentum of the muon. The χ^2 of the calorimeter fits were first calculated including the effects of multiple Coulomb scattering, assuming the muon has a nominal energy of 50 GeV as described below. Once the actual momentum was found, from the spectrometer or the length of the track in the calorimeter, the tracks were refitted using the new momentum. New fits were made with each iteration of the momentum until the difference between the momentum of the last two iterations is less than 0.5 percent. Finally, if there was at least one track in

each view that reaches the front face of the toroid, the x and y tracks were linked together using hits from the U-V chambers that were inclined at 4 degrees with respect to the normal transverse direction.

The angle of the muon, θ_μ at the vertex is most accurately determined by the segment of the track that is closest to the vertex. Towards the end of the muon track, multiple Coulomb scattering changes the direction of the muon relative to its direction at the vertex. Therefore, the segment of the track closest to the vertex yields the best value for θ_μ. However, identifying muon hits near the vertex is difficult because there are many other hits due to hadron shower particles. For the track segment that determines θ_μ, we used six consecutive chambers near the vertex, starting at one chamber from the vertex for hadron energies (E_h) less than 50 GeV, two chambers from the vertex for E_h between 50 and 100 GeV, three chambers from the vertex for E_h between 100 and 150 GeV and four chambers for E_h greater than 150 GeV. These numbers are based on studies of how close to the vertex hits can be identified with a muon track [13]. The resulting resolution on θ_μ was 1 mr for muon momenta greater than 200 GeV increasing to 5 mr for muon momenta less than 20 GeV [14].

Muon Spectrometer Tracking

There are five chambers in each of the three gaps in the spectrometer, which each have separate x and y views. Straight lines, called segments, are fit to the hits in each view of each gap. The full spectrometer fit in each view uses the position of the muon at the front face from the calorimeter track, the error on the track from the resolution

of the drift chambers, and an estimate of the muon momentum, $P_{\mu f}^{*}$. The estimate $P_{\mu f}^{*}$ in GeV is calculated from the angular deflection in the most upstream toroid, $\Delta\theta_{bend}$ in milliradians according to

$$P_{\mu f}^{*} = \frac{0.3\, B_{av}\, d}{\Delta\theta_{bend}}$$

where B_{av} is the average magnetic field in the first toroid and d is the length of steel in centimeters traversed by the muon in the first toroid. The muon is traced through the toroids including the effects of the magnetic field [15] and ionization loss. A χ^2 is calculated based on the difference between the projected track and the actual track including multiple Coulomb scattering in the uncertainty. Since the effects of multiple Coulomb scattering are correlated from chamber to chamber, we must use a correlated error matrix that has non-zero off-diagonal elements. The χ^2 is given by

$$\chi^2 = \sum_i \sum_j (x_i - x_i P)\, M_{ij}^{-1} (x_j - x_j P)$$

where the sum is over all hits in the track x_i, and $x_i P$, is the projected hit position. The error matrix M_{ij} is given by

$$M_{ij} = \langle (x_i - x_i P)(x_i - x_i P) \rangle$$

$$= \sum_{k=1}^{3} \sigma_k^2 \left[\frac{L_k^2}{3} + \frac{L_k}{2}(z_{kj} + z_{ki}) + z_{ki} z_{kj} \right] + \sigma_0^2 \delta_{ij}$$

where L_k is the length of the projected track in the k^{th} toroid, z_{ki} is the distance between the k^{th} and the i^{th} plane and σ_0 is the intrinsic drift chamber resolution. The variable σ_k is the width of the distribution of the multiple Coulomb scattering deflection, given by

$$\sigma_k = \frac{0.015}{P_{\mu f}^*} \sqrt{\frac{L_k}{L_{rad}}}$$

where L_{rad} is the radiation length of steel and $P_{\mu f}^*$ is the trial momentum in GeV. We invert the error matrix M_{ij} using an iterative procedure based on the trial momentum. The momentum for each iteration is obtained by interpolating between the initial and final momenta of the previous iteration. This is repeated until the momenta of the last two iterations are within 0.5 percent. The final momentum at the front face $P_{\mu f}$, is extrapolated from the toroid front face back to vertex by adding on the energy lost by ionization. This gives P_μ, the momentum at the vertex.

The momentum resolution of the muon spectrometer is limited by multiple Coulomb scattering and catastrophic energy losses such as δ-ray production. This is the process in which a substantial amount of the muon energy is lost in liberating an electron from an atom. The muon

spectrometer was calibrated to 1 percent with a momentum analyzed muon test beam for which the energy was known to better than 1 percent [16]. Figure 3.2 shows the fractional error F in $1/P_\mu$ which is defined as

$$F = \frac{\frac{1}{P_{meas}} - \frac{1}{P}}{\frac{1}{P}}$$

where P_{meas} is the measured muon momentum from the toroid spectrometer and P is the actual muon momentum from the upstream beam spectrometer that is described in Chapter 5. The data is from a 120 GeV test beam and the curve is from our detector simulation, described in Chapter 4, that models ionization loss, catastrophic energy loss, pair production, and bremsstrahlung. Note the good agreement between the data and the simulation over three orders of magnitude. The tail at high F is due to catastrophic losses in which the muon loses a substantial amount of its energy. In this case, the muon track is bent out of the volume of the detector by the magnetic field so that the momentum is underestimated. The muon momentum resolution of the toroid spectrometer is a constant and equal to 10.1 percent. At low muon momentum the resolution is limited by multiple Coulomb scattering. At high momentum it is limited by the finite drift chamber resolution.

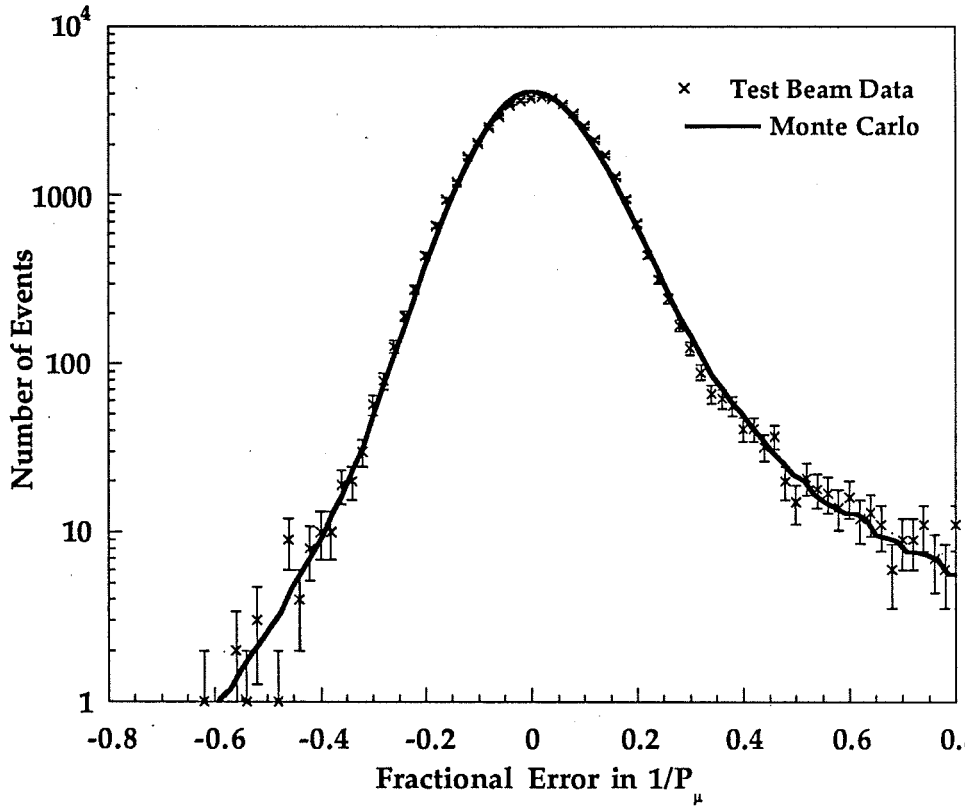

Figure 3.2 The fractional error in $1/P_\mu$ for reconstruction of a 120 GeV muon test beam. The curve is the result of a Monte Carlo calculation of muon energy loss in the CCFR detector that includes bremsstrahlung, pair production, and ionization losses, as well as catastrophic energy loss.

3.3 Event Selection

3.3.1 Introduction

The charged-current, dimuon, and trimuon events must pass selection criteria designed to ensure the events are fully contained in the detector volume. They also must pass through regions of the detector where the acceptance is understood, and have an accurately reconstructed muon momentum. When the shower leaks out the side or the end of the calorimeter, the full hadron energy cannot be reconstructed. The same is true for the muon trajectory; the reconstructed muon momentum will be underestimated if the muons escape out the side of the calorimeter or the most upstream spectrometer toroid, or if they pass through the holes in the toroids. Overlays are two charged-current events that occur at the same time or place and look like multimuon events. We eliminate overlays with cuts on the event time and position of the muons. The following sections present each cut in detail.

3.3.2 Charged-current Event Selection

- Events must cause a charged-current trigger, which is described in Section 2.3.
- Events must have a reconstructed hadron energy greater than 2 GeV, because the detector is not calibrated below this energy.

Detector Volume Cuts

- The longitudinal vertex must be between the third most upstream counter and the 20th most downstream counter, inclusive. This leaves a volume that extends sixty counters for the neutrino to interact. The most upstream two counters were used for vetoing charged particles in the beam, in addition to the veto wall. This cut allows about $10\lambda_i$ for the hadron shower to fully develop after the event vertex.
- The transverse vertex must lie within a 100" square centered on the detector, leaving 20" on the side for transverse containment of the hadron shower.
- The transverse vertex must lie within a 60" circular cut centered on the beam direction. This rejects events in the corners of the counters where the effects of the light collection efficiency are difficult to correct. In addition, simulating the neutrino beam at large radii is difficult.

Event Time Cuts

- The time of the hadron shower and muon track, measured with the calorimeter counters, must be within 36 ns of the trigger time. This corresponds to two RF buckets, and ensures the shower and track are associated with one RF bucket within a margin of error.

- The time from the drift chambers in the toroid gaps must also be within 36 ns of the trigger time. These cuts ensure the event is associated with the trigger time.

Muon Track and Fit

- The angle of the muon at the vertex, θ_μ must be less than or equal to 250 mrad with respect to the incident neutrino. This ensures the muon did not exit the side of the detector before reaching the spectrometer.
- The track in the calorimeter must extend at least eight chambers, equivalent to $5\lambda_i$, beyond the longitudinal event vertex. This eliminates punchthrough hadrons that look like muons [17].
- The calorimeter track must extend to within 5 chambers of the spectrometer. This ensures that the calorimeter track may be linked with a track in the toroid, and prevents unassociated tracks from being linked.
- The calorimeter track must be successfully associated with at least one toroid segment in both the x and y views.
- The position of the track at the most downstream chamber in the calorimeter, obtained by extrapolating the calorimeter track to that chamber, must be within 58" of the center line in both x and y views. In addition, the track from the chambers in the first toroid gap, extrapolated to the most downstream chamber in the calorimeter, must be within 58" of the center line in both views.

This ensures that the track intersects the charged-current trigger counter in the first toroid gap.

- The calorimeter track, extrapolated to the front face of the toroid, must be between 6″ and 69″ of its center line. The track from the chambers in the first toroid gap, extrapolated to the front face of the spectrometer, must also be between 6″ and 69″ of the center line. This ensures that the track avoids the center hole and the edges of the toroid where the magnetic field is distorted.
- The extrapolated calorimeter track and the extrapolated toroid track must have less than 30 percent of their length in the first toroid within 6″ of the center, where the field is unknown.
- The χ^2 of the fit in the spectrometer must be less than or equal to 10 per degree of freedom.
- The momentum of the muon at the front face of the spectrometer must be at least 3 GeV/c. The momentum of the muon at the vertex, obtained by correcting the momentum back for ionization losses must be at least 9 GeV/c. Muons with energies less than this were likely to be swept out or range out of the toroids and were not properly reconstructed in the toroid.

3.3.3 Multi-muon cuts

A sample of candidate dimuons and trimuons were selected using powerful and highly efficient criteria to identify events that may have at least two good muon tracks. Pictures of the events were scanned by

physicists to search for errors due to hits not properly placed on the tracks. The events that needed to be fixed were due to δ-rays that produced many hits in one toroid gap, or events in which the pattern recognition did not successfully separate two tracks in the spectrometer. They were fixed interactively when necessary. Approximately 15,000 events were scanned by the group in E770 and E744. About 4 percent of them required interactive refitting. This section gives the criteria for selecting the events that were scanned, then it gives the multi-muon cuts that defined the final dimuon and trimuon samples.

We used two different algorithms to select events for scanning. The first algorithm relied on the tracking, called the track criteria. The second, called the pulse-height/hit criteria, relied on pulse-heights that give the number of minimum ionizing particles passing through the counters, and the number of hits in the chamber that indicate the number of muons in the event.

- Track criteria: Two tracks must be found that extend to within two chambers of the end of the calorimeter in either view. Each track must be at least eight chambers long in either view. Finally, the transverse distance of closest approach between the two tracks must be less than 25 cm. The transverse distance of closest approach (DCA) is the minimum distance in the x-y plane between the two tracks. It is calculated from the equations of the lines corresponding to the muon tracks. If the longitudinal position of DCA is more than 60" from the vertex,

DCA is set to the transverse distance between the two tracks at a longitudinal position 60" from the vertex. This is only necessary when the opening angle between the two tracks is very small.

- Pulse-height/hit criteria: These criterion were applied to the 16 most downstream counters of the calorimeter and the eight most downstream chambers. At least 7 of the 16 counters must record greater than or equal to $1.5E_{mip}$, where E_{mip} is the energy deposited by a minimum ionizing particle. No more than one counter may record less than E_{mip}. This rejects single muons with a statistically high amount of energy deposition in some counters. Finally, after throwing out the three highest and three lowest counter pulse heights, the average pulse height must be less than $6\,E_{mip}$. In addition, after the highest and lowest number of hits in the eight most downstream drift chambers are thrown out, the average number of hits per chamber must be greater than 1.5.

The efficiency of these criteria for finding multi-muons was over 99 percent [9]. In addition, 98 percent of the final sample of same-sign dimuons in E744 were found without interactively refitting, so this was a minor effect. About 93 percent of all multi-muons were found without the interactive refitting.

Same-Sign Dimuon Selection

- These events must pass all the charged-current event cuts and the second muon must pass all the cuts applied to the first muon. The second muon is defined as the muon with the lower transverse momentum relative to the hadron-shower direction. The hadron shower direction is computed from the direction and energy of the higher energy muon and the hadron shower energy.
- The transverse distance of closest approach between the two muon tracks, calculated as described above, must be less than 15 cm.
- The most upstream chamber in one track must be within six chambers of the most upstream chamber in the other track.
- The number of chambers between the vertex and the downstream end of the track, for x and y views summed, must be at least 13 chambers.
- The time between the arrival of the first and second muons must be less than 28 ns as determined with the spectrometer tracks. The resolution of the measured time of the muon track relative to the trigger time was about 2 ns and the time between RF buckets was about 19 ns. This cut ensures the muons come from the same RF bucket within a margin of error. The time and closest approach cuts eliminate most

overlay events. The number of overlays that lie within these cuts is estimated and statistically subtracted from the sample as described in Section 8.2.

- The signs of the muons must be the same. The chance of misidentifying the sign of the muon is negligible. For example, none of the sixty thousand 120 GeV test beam muon tracks were reconstructed with the wrong sign [16].

Trimuon Selection

- Two of the three muons must pass all dimuon cuts, other than the cut on the sign of the muons.
- The third track must span at least 20 counters downstream from the vertex.
- The transverse distance of closest approach between the third muon and the first must be less than 15 cm. There is no cut on the time of the third muon because its time comes from the counter pulse heights averaged over the track length. Times obtained in this way have a coarser resolution, about 10 ns, than the timing resolution obtained from momentum analyzed tracks which is about 2 ns.
- The momentum of the third muon at the vertex must be at least 4.5 GeV. The efficiency of finding muons with lower momentum is small because they are hidden by the hadron shower.

3.4 Data Sample

The final sample of charged-current events after all cuts consists of 1.5 million neutrino-induced events and 0.3 million anti-neutrino-induced events. There are 220 $\mu^-\mu^-$ events and 25 $\mu^+\mu^+$ events in experiments E770 and E744 combined. There are a total of 86 trimuon events. Table 3.1 shows the number of events at each stage in the selection for experiments E744 and E770 separately.

Selection Criterion	E744	E770
Total triggers	3.2×10^6	5.2×10^6
Charged current trigger,	1.7×10^6	2.0×10^6
and within the detector volume,	1.6×10^6	2.0×10^6
and at least two muons,	11.7×10^3	5.9×10^3
and only one muon with $P_\mu > 9$ GeV,	8.5×10^5	10.2×10^5
μ^+	1.4×10^5	1.8×10^5
μ^-	7.1×10^5	8.4×10^5
and two muons with $P_{\mu 1} > 9$ GeV and $P_{\mu 2} > 9$ GeV,		
$\mu^+\mu^+$	15	10
$\mu^-\mu^-$	101	119
and three muons with $P_{\mu 1} > 9$ GeV/c, $P_{\mu 2} > 9$ GeV/c and $P_{\mu 3} > 4.5$ GeV/c.	54	32

Table 3.1 Numbers of events at various stages in the event selection for experiment E744 and E770.

Chapter 4

Monte Carlo Simulation of Charged-Current Events and the CCFR Detector Simulation

4.1 Introduction

The backbone of the same-sign dimuon analysis is the charged-current Monte Carlo simulation for single muon production in neutrino-nucleon interactions in the CCFR detector. Each physics background to same-sign dimuon production is simulated by adding a second muon to generated charged-current events, as described in Chapters 7 and 8. Furthermore, the charged-current Monte Carlo simulation is used to correct for the effects of the finite resolution and acceptance of the detector on the observed number of charged-current events, which normalize the rate of same-sign dimuon production.

Charged-current events are generated using calculated ν and $\bar{\nu}$ fluxes in the CCFR detector and charged-current cross-sections. In a quadrupole triplet neutrino beam, neither the momentum nor the sign of the individual pions and kaons producing the incident neutrinos are determined. Therefore, we must use reconstructed events in the detector to extract the relative neutrino flux as a function of neutrino energy. The charged-current cross-sections can be expressed as functions of the nucleon structure functions, $F_2(x,Q^2)$ and $xF_3(x,Q^2)$, which have been measured by the CCFR collaboration in experiments E744 and E770 [18].

The CCFR detector simulation propagates generated charged-current and multi-muon events through the detector. It reproduces the effects of energy loss and multiple Coulomb scattering on the muon trajectories, while placing hits in the drift-chambers corresponding to their passage. It also applies energy resolution smearing to the generated hadron energy. The simulated events are then reconstructed in the same manner as the data events. The detector simulation is extremely important because we use it to characterize the acceptance of the detector, enabling us to calculate acceptance corrected rates. It also enables us to check the dimuon, charged-current, and trimuon physics generators for consistency with their corresponding data.

4.2 Flux Measurement

This section describes the flux measurement used as input to the charged-current Monte Carlo simulation, which is extracted from observed charged-current events. For example, Figures 4.1a and 4.1b show the number of neutrino and antineutrino charged-current events as a function of total visible energy for experiments E744 and E770 respectively. The source of the neutrino beam, decays of pions and kaons, is reflected in the structure of the plots. The large peak at around 100 GeV is due to neutrinos from pion decays and the smaller peak at higher energy is due to neutrinos from kaon decays.

Because same-sign dimuon production is normalized to the charged-current cross section, the final rate is independent of the flux to

first order. The energy dependence of the measured flux effects the energy dependence of the same-sign dimuon rates through the subtracted background, which is based on the charged-current Monte Carlo simulation. However, provided the charged-current Monte Carlo events agree with the observed charged-current events, the flux measurement is correct for the purposes of same-sign dimuon production.

The measurement of the relative flux, or the ratio of the flux from neutrino energy bin to bin, is described in detail in reference 19 and is summarized here. It was calculated from the charged-current data using two independent methods outlined below – the results of which agree within 1.5% [20]. The charged-current data used in the flux analysis passed all the standard charged-current selection criteria given in Chapter 3. In addition, the momentum of the muon at the vertex was required to be greater than 15 GeV and the angle of the muon at the vertex was required to be less than 150 mrad. These last two requirements are stricter than the angle and momentum requirements on charged-current and dimuon events in the same-sign analysis described in Chapter 3. This is to ensure that the reconstruction efficiency for events used in the flux analysis was close to 100 percent.

The y-intercept method for the relative flux uses the fact that the flux $\Phi(E_i)$ in the energy bin E_i is proportional to the y-intercept of the y-distribution of the number of events, $N(E_i)$ in the energy bin, E_i. In other words, the relative flux can be expressed as follows,

$$\frac{\Phi(E_i)}{\Phi(E_j)} = \lim_{y \to 0} \frac{\frac{dN(E_i)}{E_i dy}}{\frac{dN(E_j)}{E_j dy}} \qquad 4.1$$

It uses the following relationship between the flux, the cross-section and the number of events in each energy bin given by

$$\frac{dN(E_i)}{dy} = \Phi(E_i)\frac{d\sigma}{dy}$$

Equation 4.1 is derived from the fact that as y approaches zero, the differential cross-sections $d\sigma/dy$ in a given energy bin must be equal for neutrinos and antineutrinos and therefore equal a constant. The y-intercept is obtained from fits to the y-distribution of the charged-current data in each energy bin.

The second method, called the fixed ν-cut method, uses the fact that the number of events per energy bin with $\nu < \nu_0$ is proportional to the relative flux per bin up to corrections on the order of $O(\nu_0/E_\nu)$. This is derived from the general expression for the charged-current cross-section given in equation 4.2. The parameter ν_0 was chosen to be 20 GeV yielding 426 000 neutrino- and 146 000 antineutrino-induced events used for this flux measurement.

Small corrections to the flux were calculated in nineteen 20 GeV E_ν and three twenty inch R bins from the ratio of the number of

reconstructed charged-current data events to Monte Carlo events. In addition, an overall flux normalization was calculated from the total number of charged-current data events and Monte Carlo events. After the overall normalization, the bin-by-bin corrections were less than 2%.

The neutrino flux used as input to the charged-current Monte Carlo simulation explicitly agrees with the observed flux as shown in section 4.4. The absolute normalization of the flux is not important, since it cancels out in the calculation of the rate of same-sign dimuon production. The energy dependence of the input flux, which does effect the rates, is explicitly set to the energy dependence of the observed flux.

4.3 The Charged-Current Cross Section

The differential charged-current cross section for ν-N interactions can be expressed in terms of the structure functions F_2 and xF_3 as follows,

$$\frac{d\sigma^{\nu(\bar{\nu})}}{dxdy} = \frac{G_f^2 s}{2\pi}\left[\left(1 - y - \frac{M x y}{2 E_\nu}\right)F_2(x,Q^2) + \frac{y^2}{2} 2x F_1(x,Q^2) \pm y\left(1 - \frac{y}{2}\right)xF_3(x,Q^2)\right] \quad 4.2$$

where $G_f = 1.166 \times 10^{-5}$ GeV^{-2} is the weak Fermi coupling constant, M is the nucleon mass, E_ν is the incident neutrino energy, x and y are the Bjorken scaling variables introduced in Chapter 1, and s is the ν-N center of mass energy. The structure function $2xF_1$ is expressed in terms of F_2 as follows:

$$2x F_1(x,Q^2) = \frac{1+4M^2x^2}{1 + R(x,Q^2)} F_2(x,Q^2)$$

where $R = \sigma_L/\sigma_T$, the ratio of the total absorption cross sections for longitudinal and transverse polarizations of W bosons. The function R is given by a parametrization of deep inelastic electron scattering measurements made at SLAC [21] and the structure functions were given by parametrizations of our measured structure functions [19]. These CCFR structure functions span the largest range in Q^2 of any experiment. Furthermore, they agree with previous measurements by BCDMS, the CCFR experiment E616, and SLAC [18], and with theoretical predictions for QCD [20, 22].

4.4 Results of the Charged-Current Monte Carlo

Figures 4.1-4.6 show comparisons of the charged-current Monte Carlo simulation and the charged-current data for experiments E744 and E770. The total visible energy E_ν is given in Figure 4.1a for E744 and 4.1b for E770 and the radius of the event vertex, R is given in Figures 4.2a and 4.2b. They show the good agreement resulting from the flux normalization in E_ν and R bins. Figures 4.3 and 4.4 give the x-position and y-position of the vertex which also show excellent agreement. In addition, the data from the two experiments agree, apart from slight differences in the radial distributions due to the difference in the direction of the neutrino beam. In addition, the acceptance-corrected charged-current data from E744 and E770 were combined in the structure function analysis, where they were found to be consistent [19]. The consistency

between E744 and E770 is important because the same-sign dimuon rates are normalized to the combined charged-current data from E744 and E770 after the events are corrected for detector acceptance and smearing separately, as described in Chapter 9.

An important test of the underlying physics of the charged-current Monte Carlo simulation is the agreement with the charged-current data in intrinsic kinematic variables that are not used in the flux normalization. For example, Bjorken x and y are shown in Figures 4.5 and 4.6. Again the agreement is very good, showing that the charged-current generator, based on the CCFR structure functions, is a good model of charged-current interactions in our experiment.

4.5 The CCFR Detector Monte Carlo

The CCFR detector Monte Carlo simulates the effects of hadron-energy smearing, muon-energy and angle smearing, and muon acceptance in the calorimeter and spectrometer. The result of the detector simulation is a set of measured variables identical to those obtained for the data.

The longitudinal event vertex, the x and y vertices corresponding to a previously specified radial vertex, and the azimuthal angle of the muon are generated according to flat distributions between their physical limits.

The hadron energy is smeared according to a Gaussian distribution of width corresponding to the energy resolution of the detector given by equation 3.1. This is a parametrization of data from hadron test beams of 25 GeV up to 500 GeV. For example, Figure 3.1 shows the reconstructed

hadron energy of a 100 GeV hadron test beam and the parametrization of the hadron energy resolution given in equation 3.1, which agree.

To simulate the effects of energy loss and angle smearing, the generated muon is traced through the target calorimeter and toroid spectrometer while placing hits in the drift chambers along its path, until all its energy is deposited in the detector or it exits. For muon momenta at the vertex greater than 5 GeV/c, the simulated energy loss mechanisms include ionization, bremsstrahlung, pair production and δ-ray production. The energy deposited in the scintillation counters from δ-rays is not modeled, rather it is accounted for in the data. For muon momenta less than 5 GeV, the ionization loss is calculated using tabulated values of ionization loss in steel [23]. To account for the difficulty of identifying hits on a track within the hadron shower, the track is set to begin at the first chamber after the vertex, for hadron energies (E_h) less than 50 GeV. For E_h between 50 GeV and 100 GeV the track begins two chambers downstream of the vertex, for E_h between 100 GeV and 150 GeV it begins three chambers downstream, and for E_h greater than 150 GeV it begins four chambers downstream of the vertex. This placement of the start of the track is based on a study of the longitudinal position where the muon track can first be identified within the hadron shower [13]. The track near the vertex is used to obtain the angle of the muon at the vertex, θ_μ as described in Section 3.1.2. Finally, the effects of multiple Coulomb scattering are applied to all muon trajectories and the positions of the hits are smeared by the intrinsic drift chamber resolution of 225 μm. Figure 3.2

shows the agreement in momentum over three orders of magnitude between a momentum-analyzed 120 GeV muon-test beam and the results of the detector simulation. Agreement for lower energy muons with $P_\mu > 4$ GeV is shown by comparing the reconstructed momenta of muons produced in the hadron showers of a hadron test beam to the reconstructed momenta of generated muons from the shower Monte Carlo, as described in Chapter 6.

The detector simulation was applied to generated charged-current events, which were then subject to the standard track reconstruction algorithm and selection criteria as the charged-current data, which are described in Chapter 3. Figures 4.7a and 4.7b show θ_μ for the charged-current data and the reconstructed charged-current Monte Carlo simulation for experiments E744 and E770. The data and the Monte Carlo show good agreement, which reflects the agreement between the θ_μ-resolution in the data and the resolution derived from the above method of simulating the tracks. Figures 4.8a and 4.8b show the longitudinal event vertex for the reconstructed charged-current Monte Carlo and the charged-current data for experiments E744 and E770. Again the data and Monte Carlo agree. Figures 4.9a and 4.9b make the same comparison for the reconstructed momentum of the muon, showing that the momentum resolution in the data and the detector simulation are consistent. Finally, Figures 4.10a and 4.10b show the comparison of the hadron energy distributions that agree, confirming our model of the hadron energy resolution. The agreement between the charged-current Monte Carlo and

the charged-current data in these extrinsic variables is within the statistical uncertainty of the data.

4.6 Conclusions

It is imperative that the detector simulation accurately model the effects of the detector because we use the simulation to reconstruct generated charged-current and multi-muon events. The reconstructed events are used to check the physics generators against observed events and to calculate the detector acceptance. The detector simulation reproduces the reconstructed muon momentum of a muon test beam, as shown in Figure 3.2, and low energy muons produced in hadron showers, described in Chapter 6. It also accurately reproduces the reconstructed hadron energy of hadron-induced showers, shown in Figure 3.1. Furthermore, the reconstructed values of the x, y and longitudinal vertex positions, the angle of the muon at the vertex, the hadron energy, and the muon energy in generated charged-current events all agree with the charged-current data.

We have shown that the Monte Carlo accurately models charged-current events in our experiments. More evidence of the accuracy of the detector simulation comes from the CCFR structure function analysis which relies on charged-current Monte Carlo events. The measured CCFR structure functions are consistent with other experiments and with theoretical predictions. Since the reliability of the detector simulation is

established, we conclude that the charged-current generator is a good model of charged-current events observed in our detector.

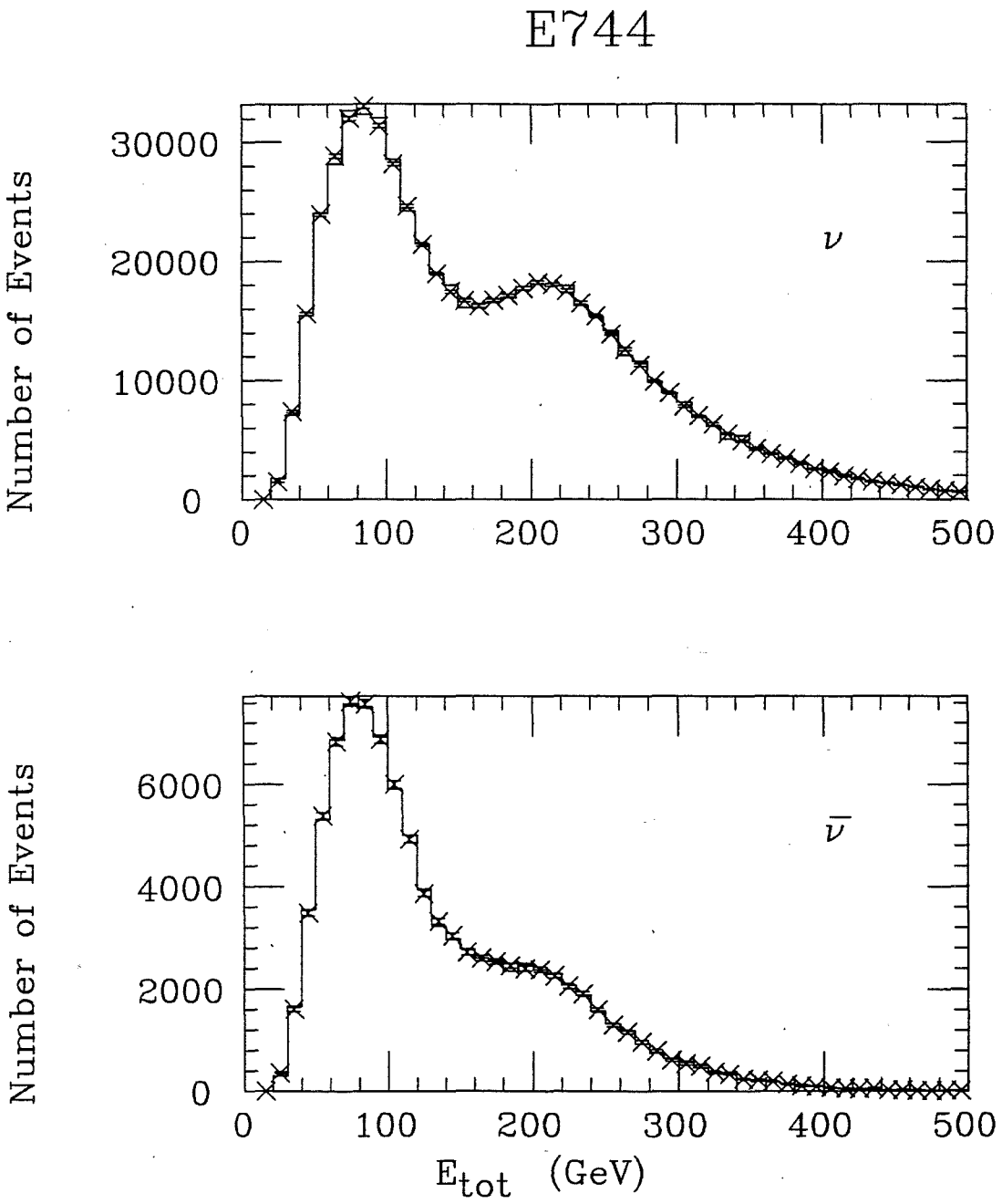

4.1a Total visible energy for the charged-current Monte Carlo (histogram) and the charged-current data (crosses) for incident neutrinos (top) and antineutrinos (bottom) in experiment E744.

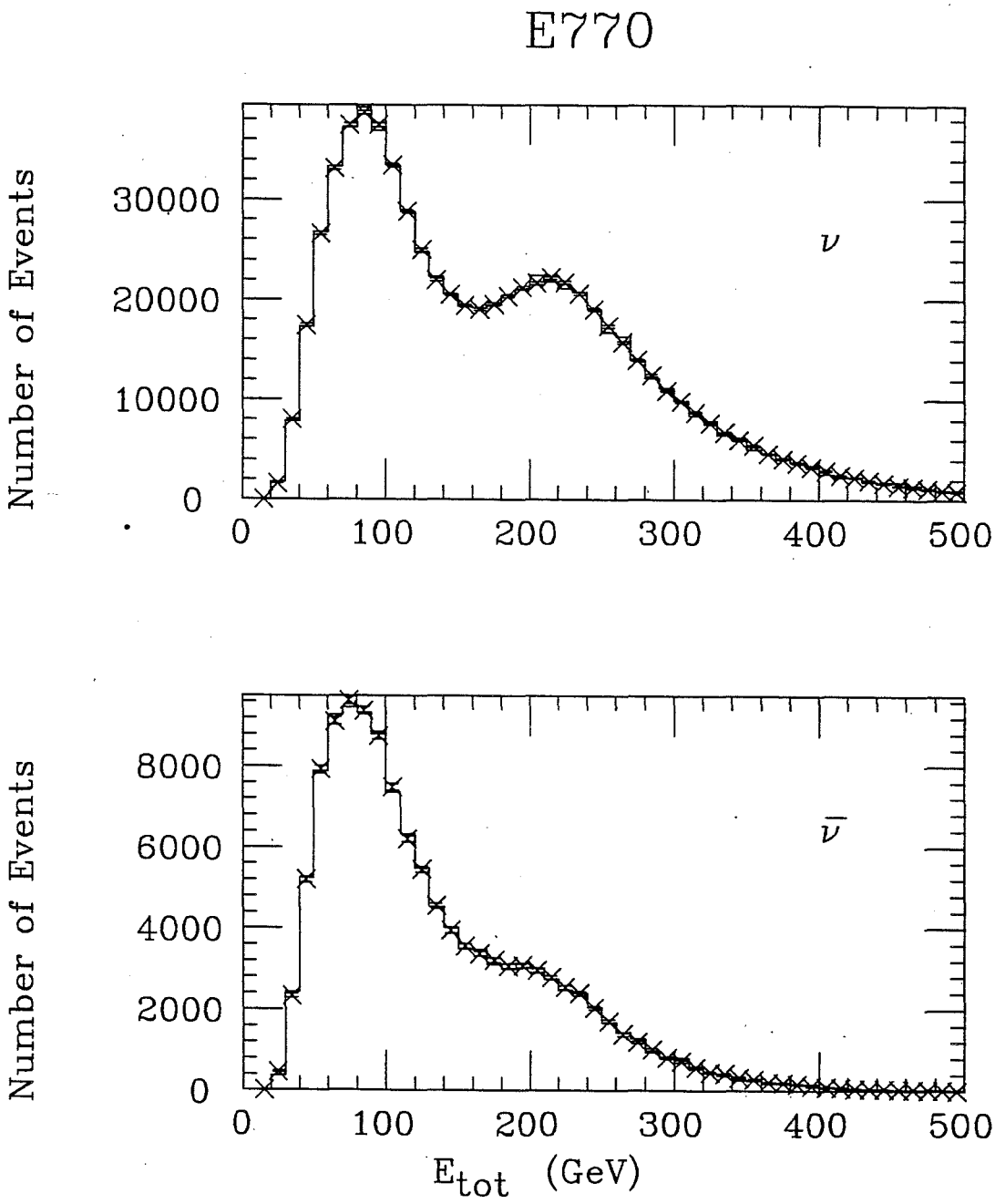

Figure 4.1b Total visible energy for the charged-current Monte Carlo (histogram) and the charged-current data (crosses) for incident neutrinos (top) and antineutrinos (bottom) in experiment E770.

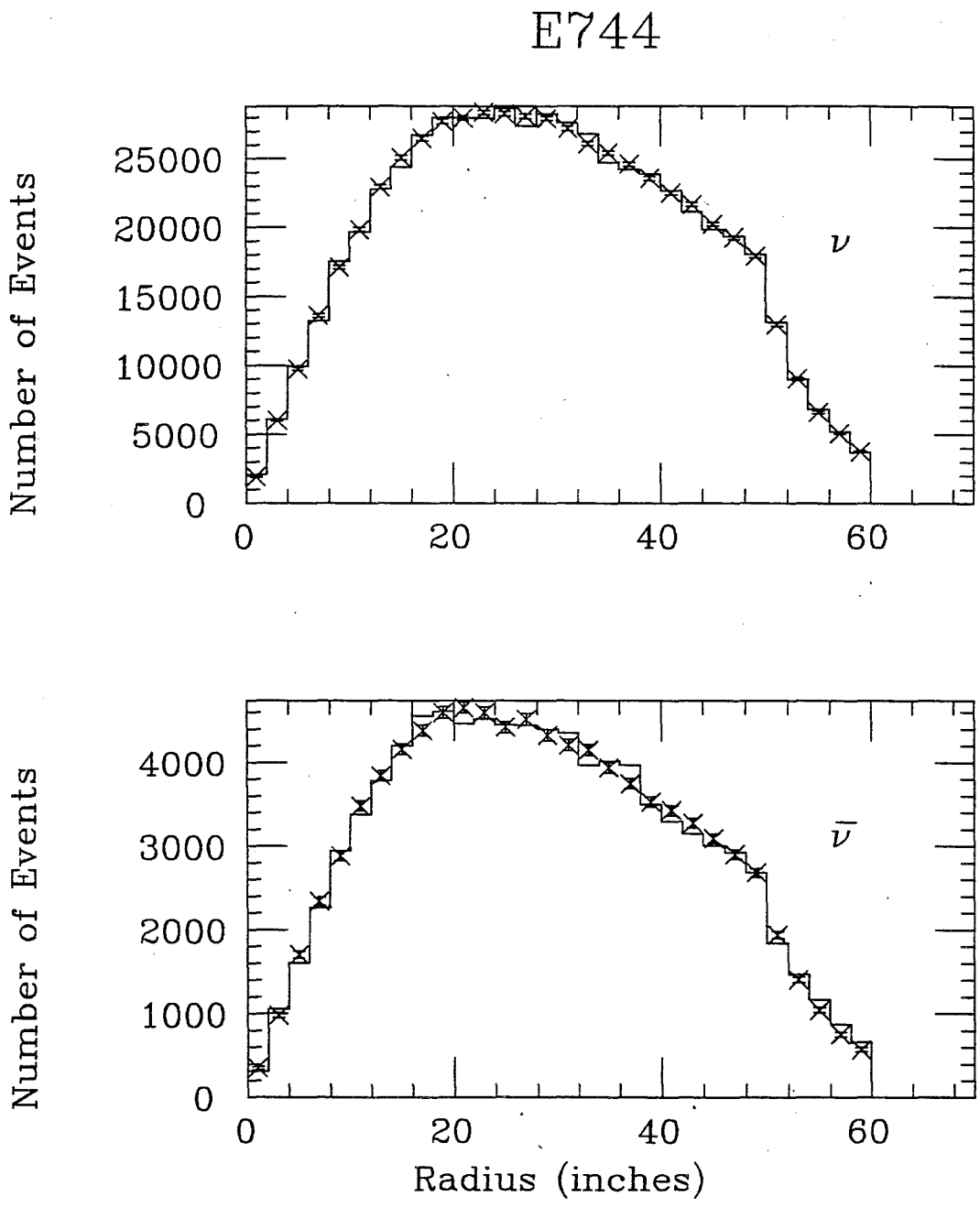

Figure 4.2a Radial position of the vertex for the charged-current Monte Carlo (histogram) and the charged-current data (crosses) for incident neutrinos (top) and antineutrinos (bottom) in experiment E744. Note events with radii greater than sixty inches are removed from the sample of charged-current events as described in Chapter 3.

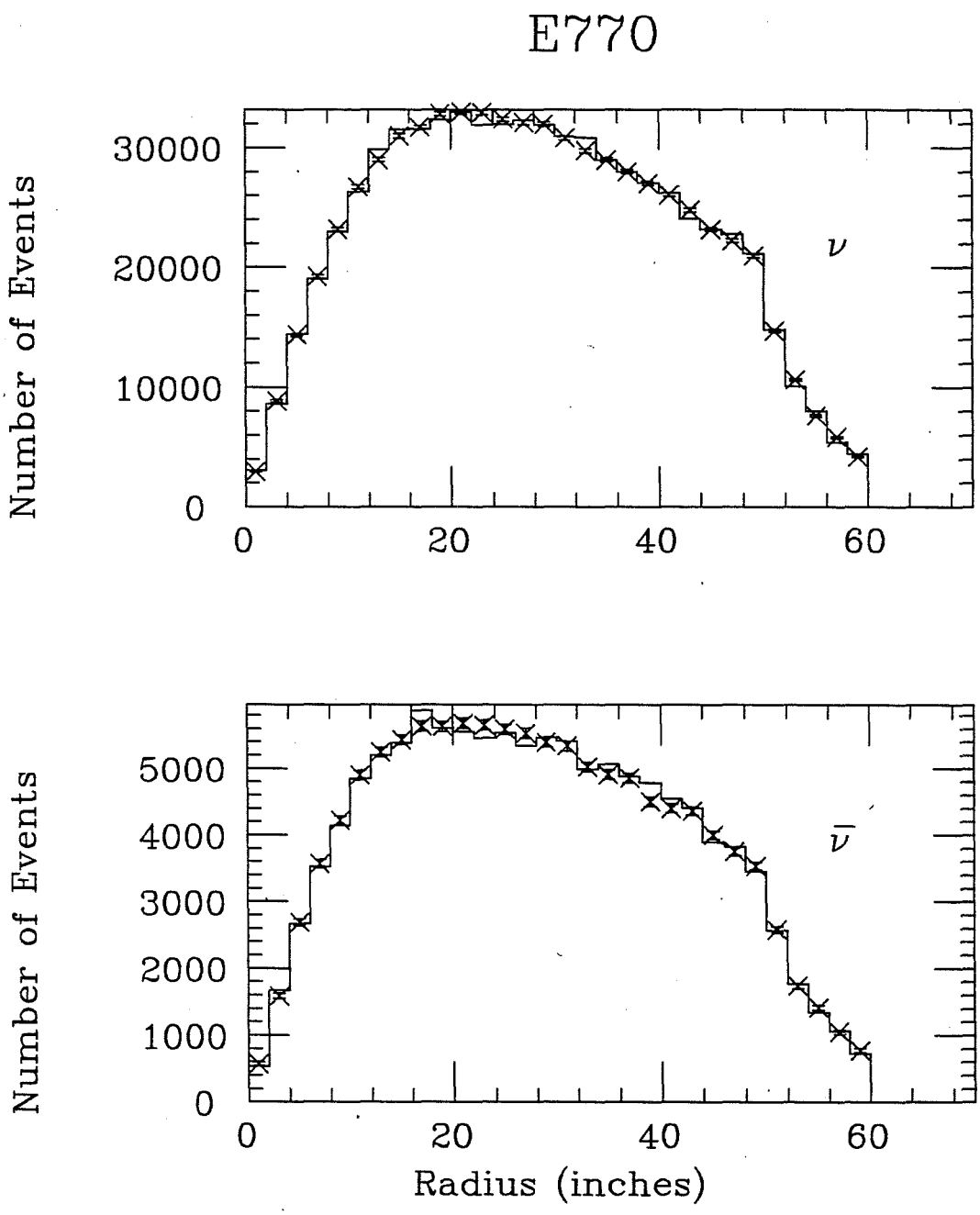

Figure 4.2b Radial position of the vertex for the charged-current Monte Carlo (histogram) and the charged-current data (crosses) for incident neutrinos (top) and antineutrinos (bottom) in experiment E770. Note events with radii greater than sixty inches are removed from the sample of charged-current events as described in Chapter 3.

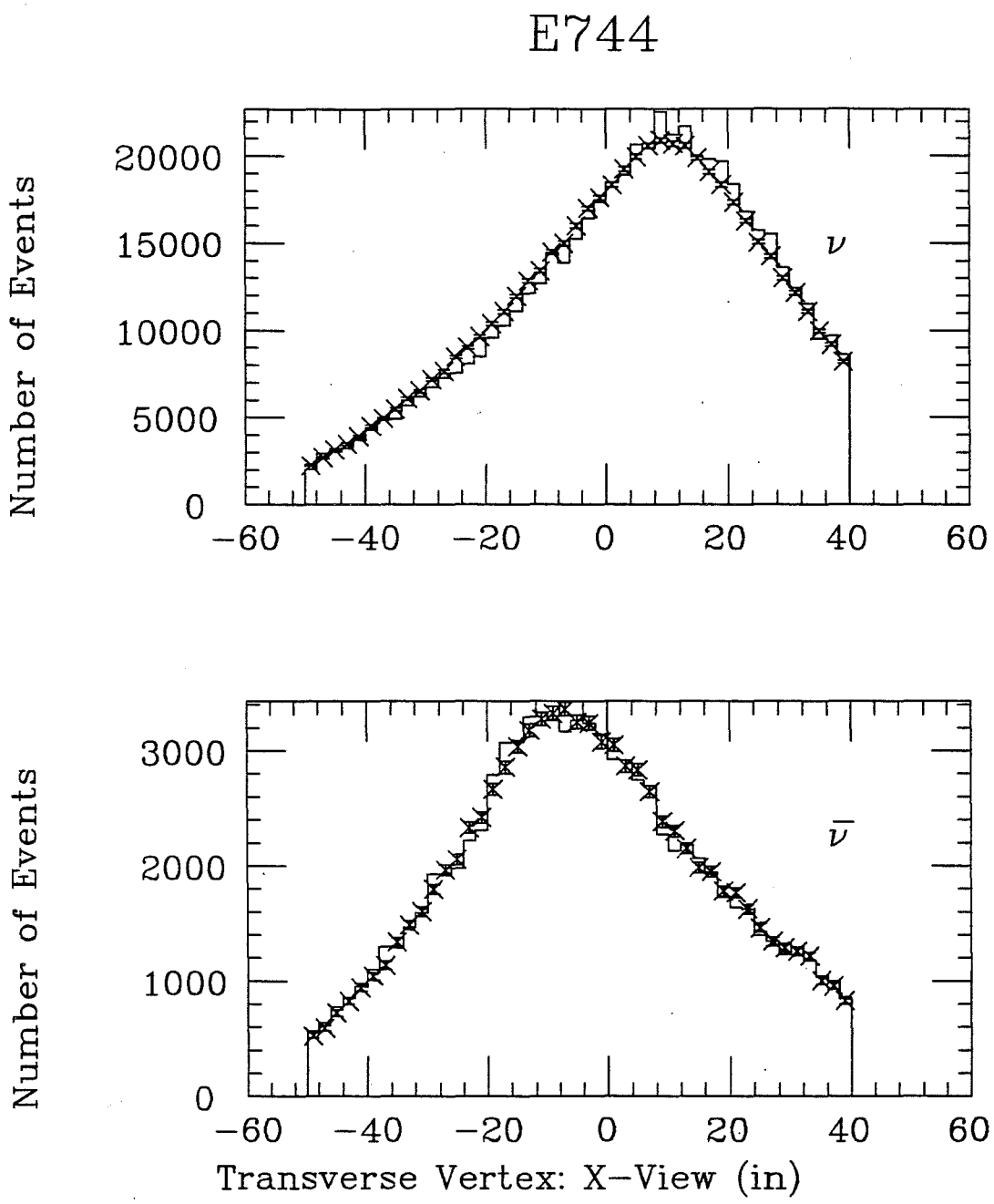

Figure 4.3a Transverse position of the vertex in the x view for the charged-current Monte Carlo (histogram) and the charged-current data (crosses) for incident neutrinos (top) and antineutrinos (bottom) in experiment E744.

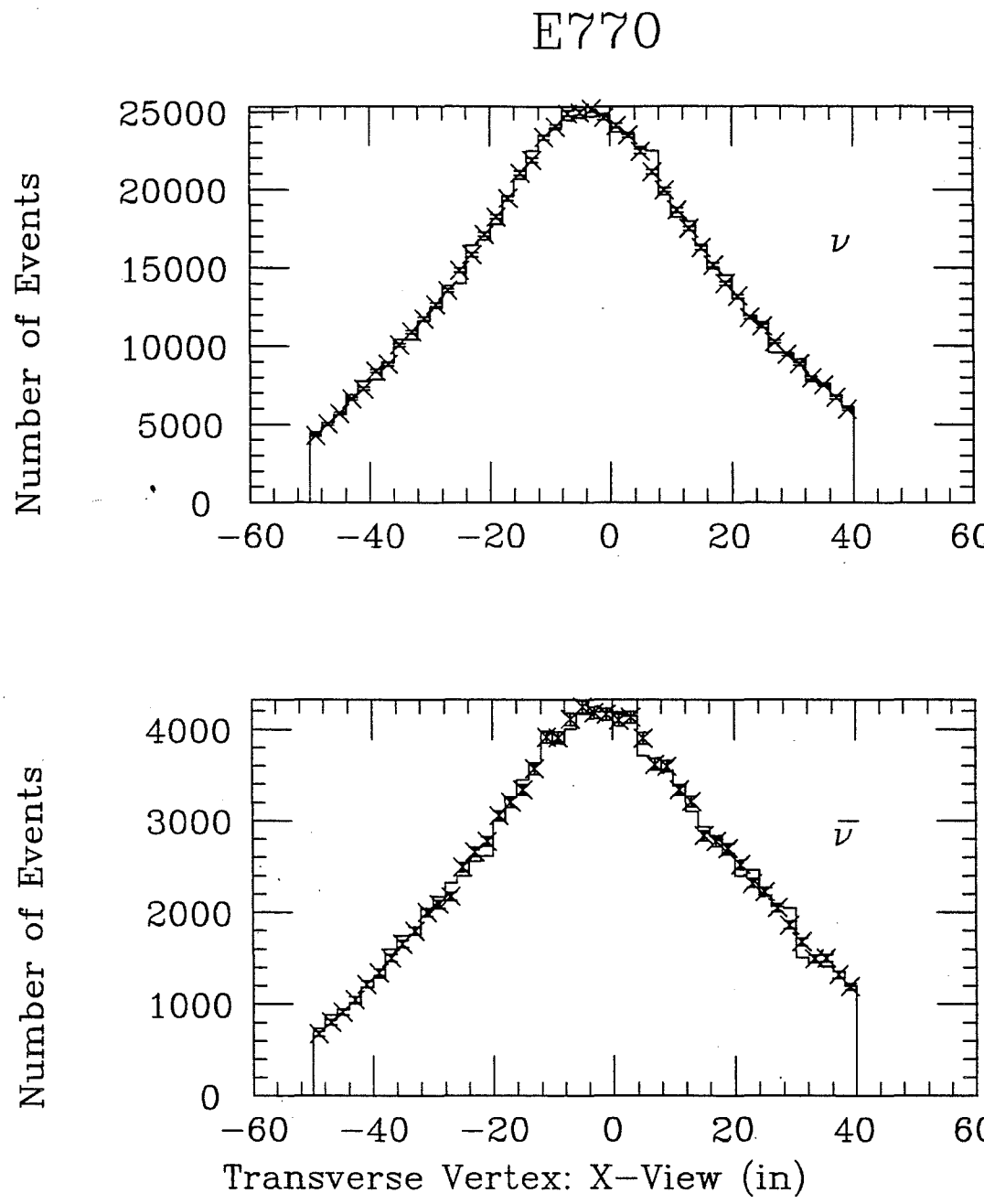

Figure 4.3b Transverse position of the vertex in the x view for the charged-current Monte Carlo (histogram) and the charged-current data (crosses) for incident neutrinos (top) and antineutrinos (bottom) in experiment E770.

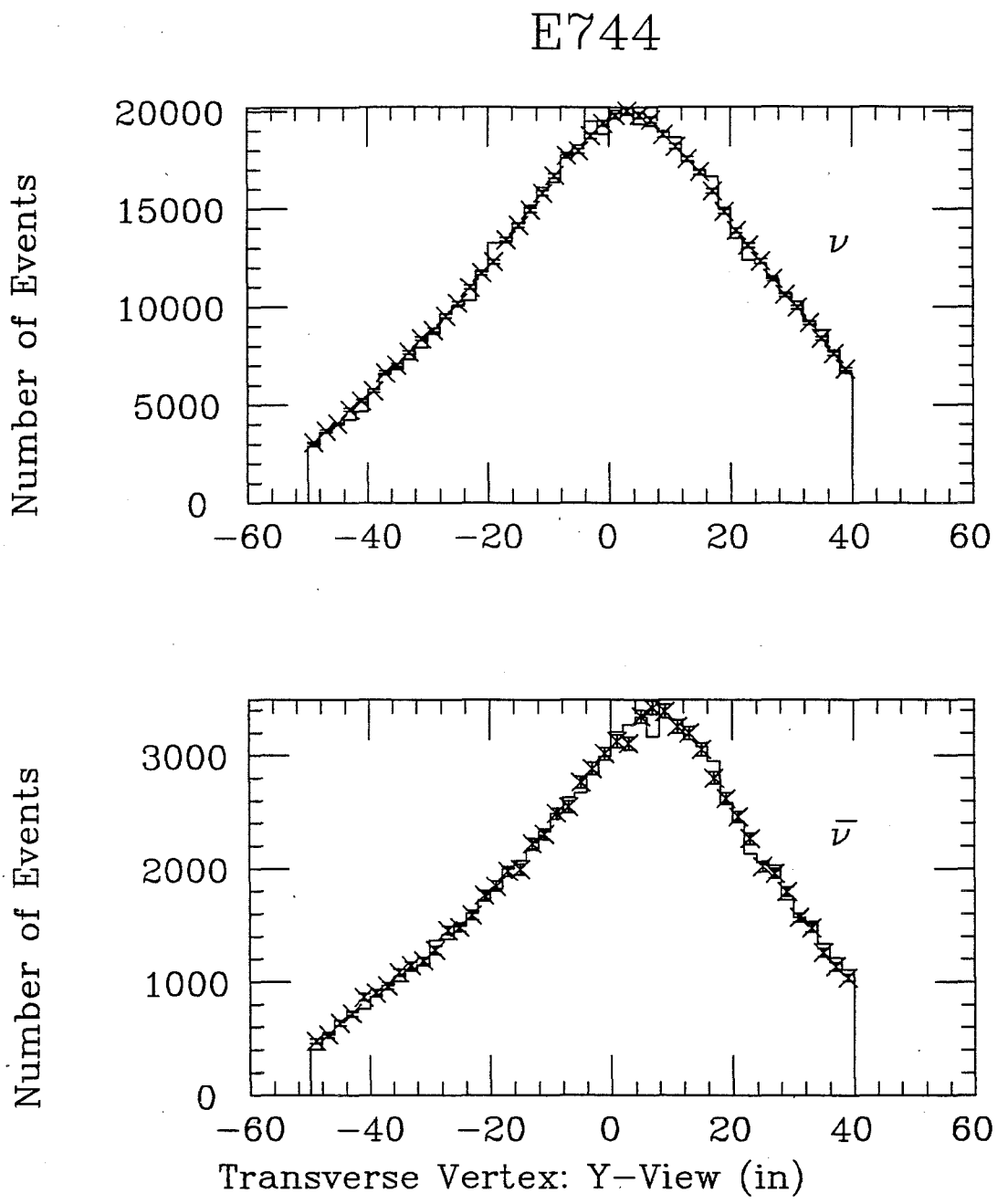

Figure 4.4a Transverse position of the vertex in the y view for the charged-current Monte Carlo (histogram) and the charged-current data (crosses) for incident neutrinos (top) and antineutrinos (bottom) in experiment E744.

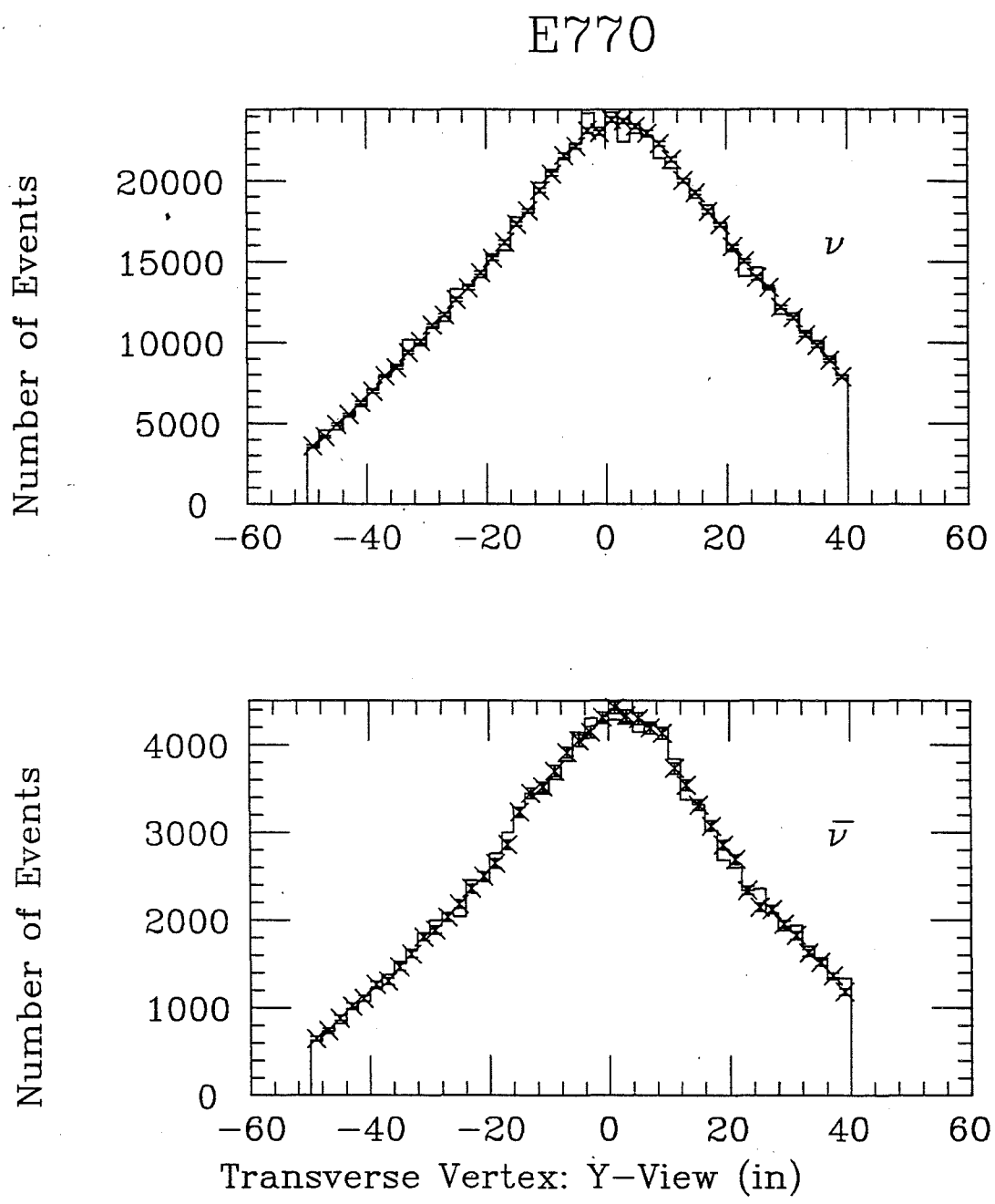

Figure 4.4b Transverse position of the vertex in the y view for the charged-current Monte Carlo (histogram) and the charged-current data (crosses) for incident neutrinos (top) and antineutrinos (bottom) in experiment E770.

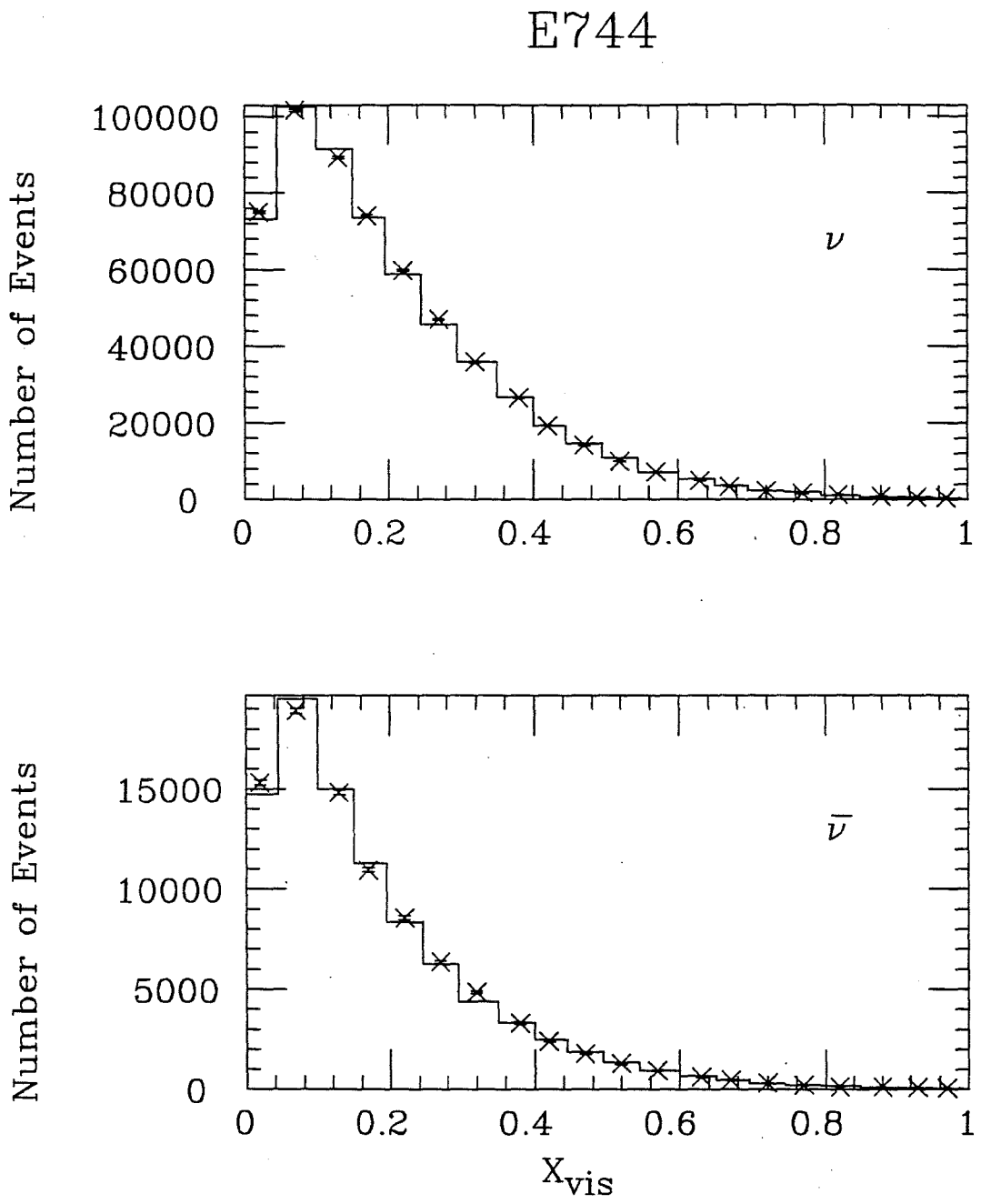

Figure 4.5a Distribution of x_{vis}, the visible Bjorken scaling variable for the charged-current Monte Carlo (histogram) and the charged-current data (crosses) for incident neutrinos (top) and antineutrinos (bottom) in experiment E744.

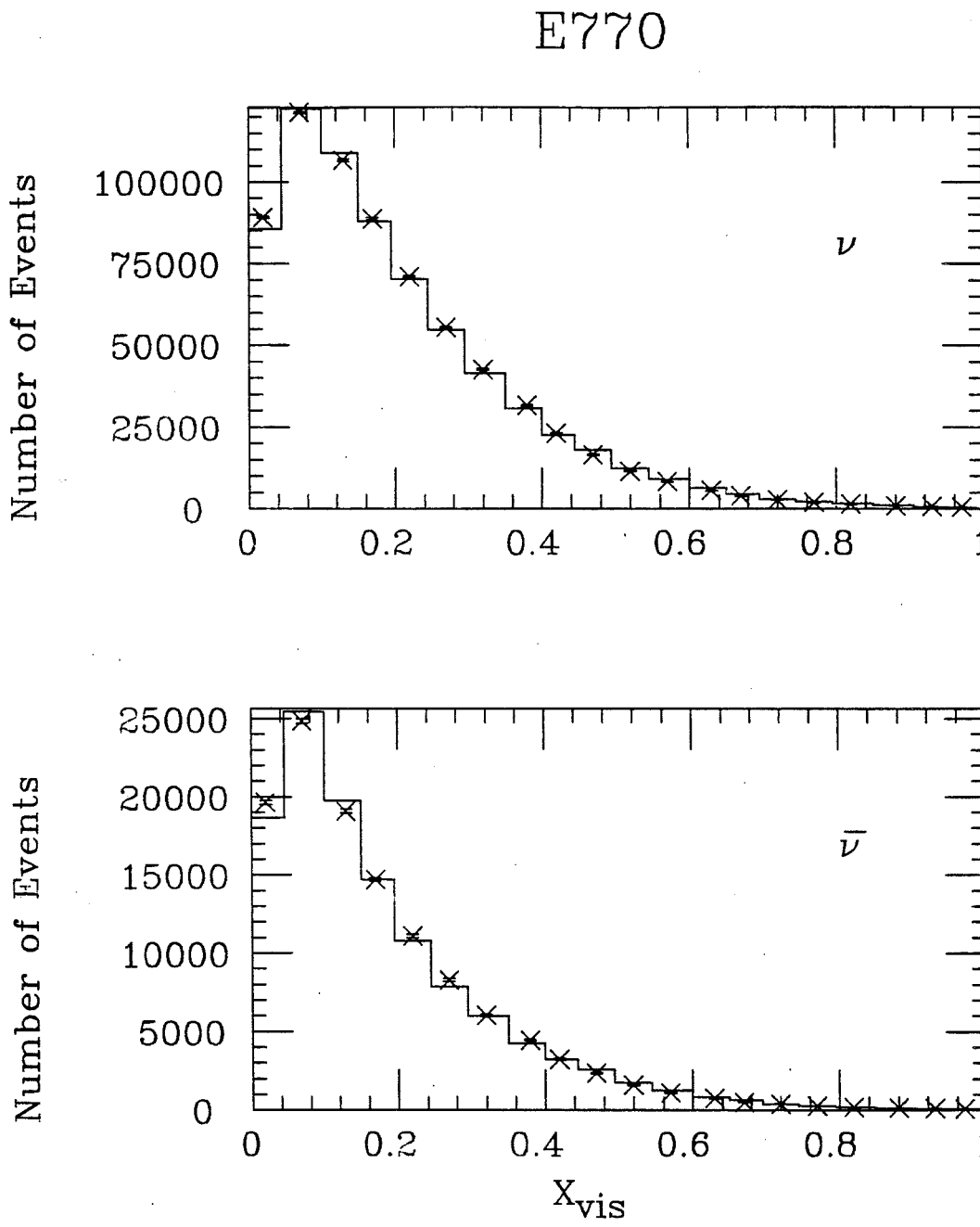

Figure 4.5b Distribution of x_{vis}, the visible Bjorken scaling variable for the charged-current Monte Carlo (histogram) and the charged-current data (crosses) for incident neutrinos (top) and antineutrinos (bottom) in experiment E770.

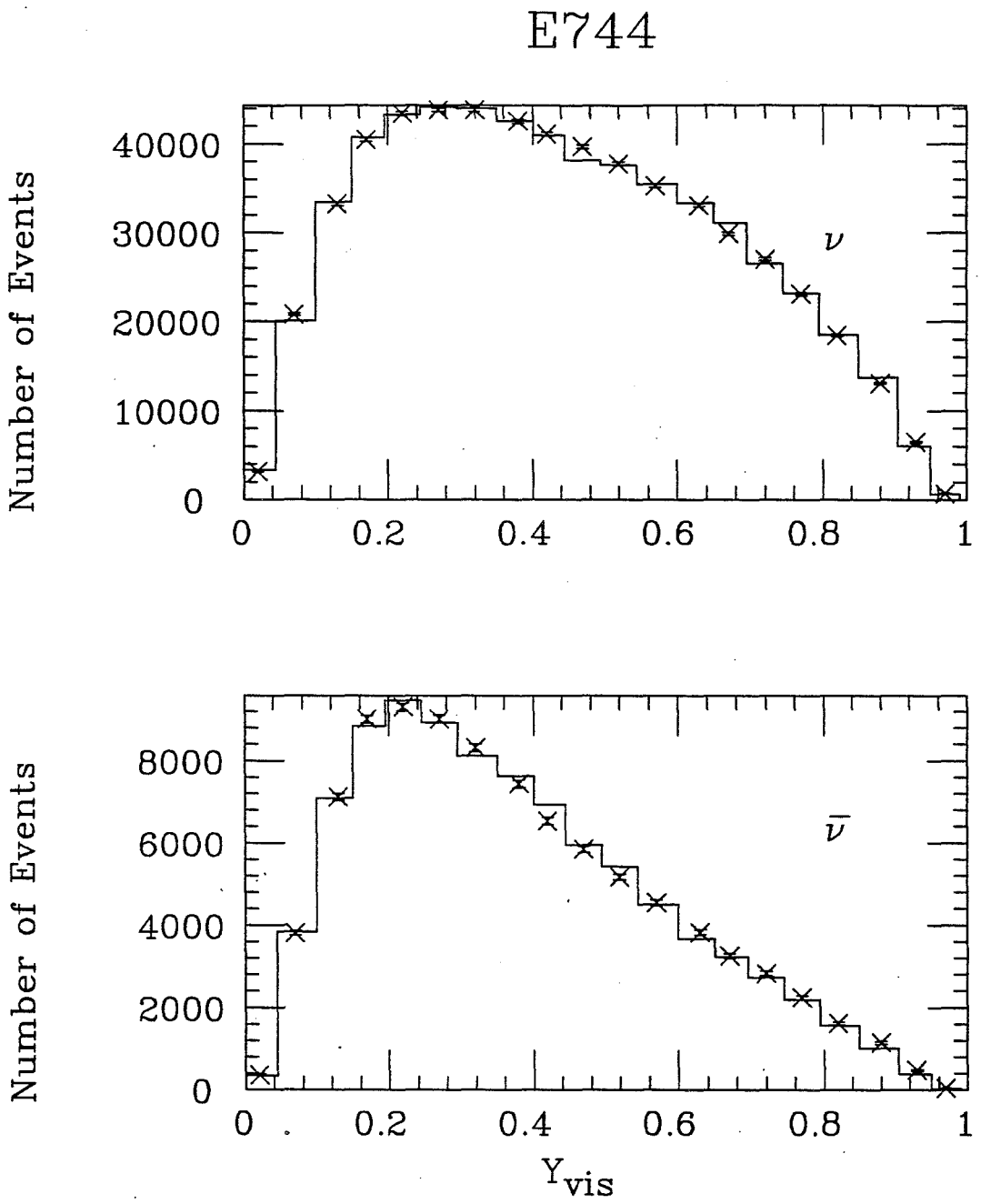

Figure 4.6a Distribution of y_{vis}, the visible Bjorken scaling variable for the charged-current Monte Carlo (histogram) and the charged-current data (crosses) for incident neutrinos (top) and antineutrinos (bottom) in experiment E744.

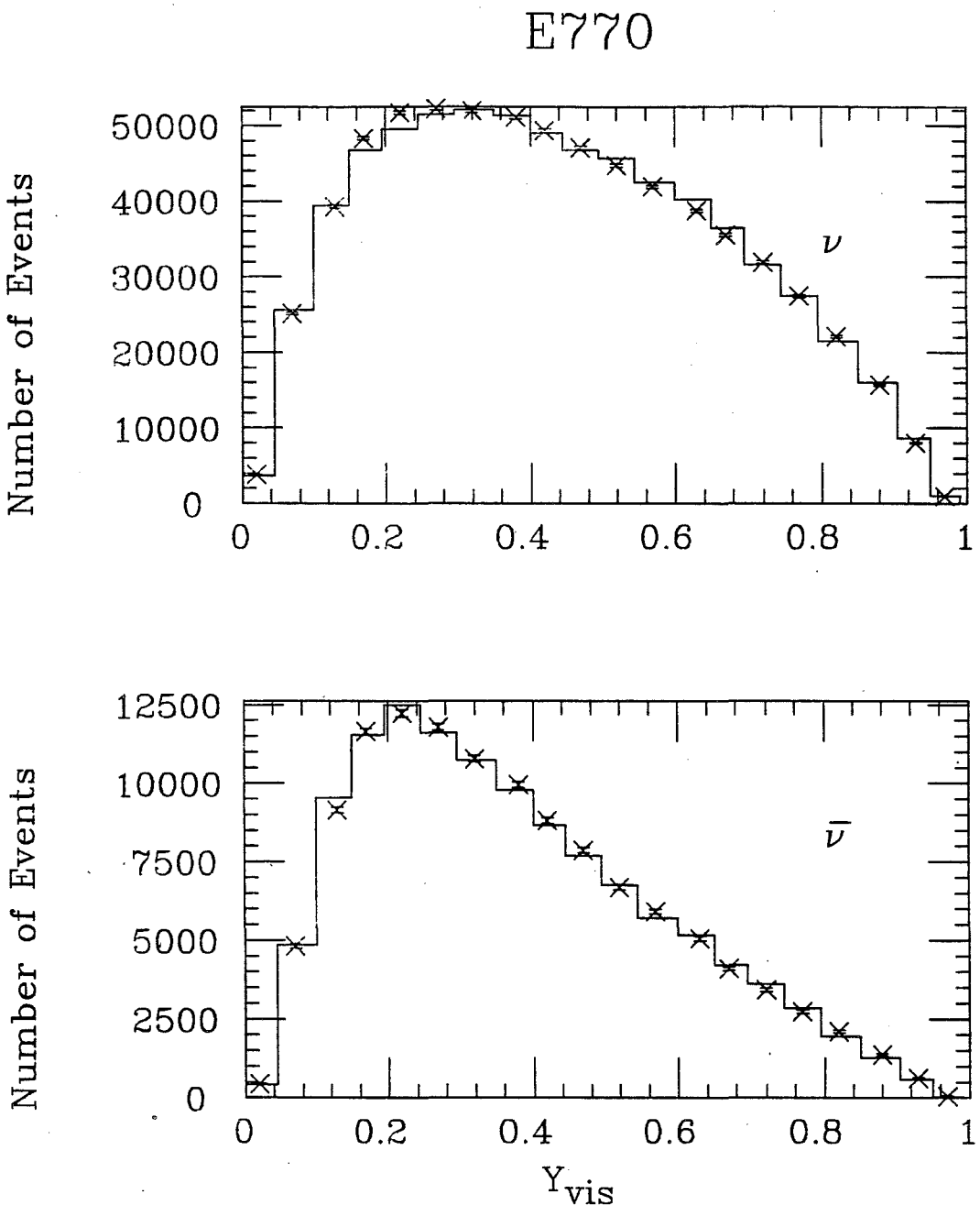

Figure 4.6b Distribution of y_{vis}, the visible Bjorken scaling variable for the charged-current Monte Carlo (histogram) and the charged-current data (crosses) for incident neutrinos (top) and antineutrinos (bottom) in experiment E770.

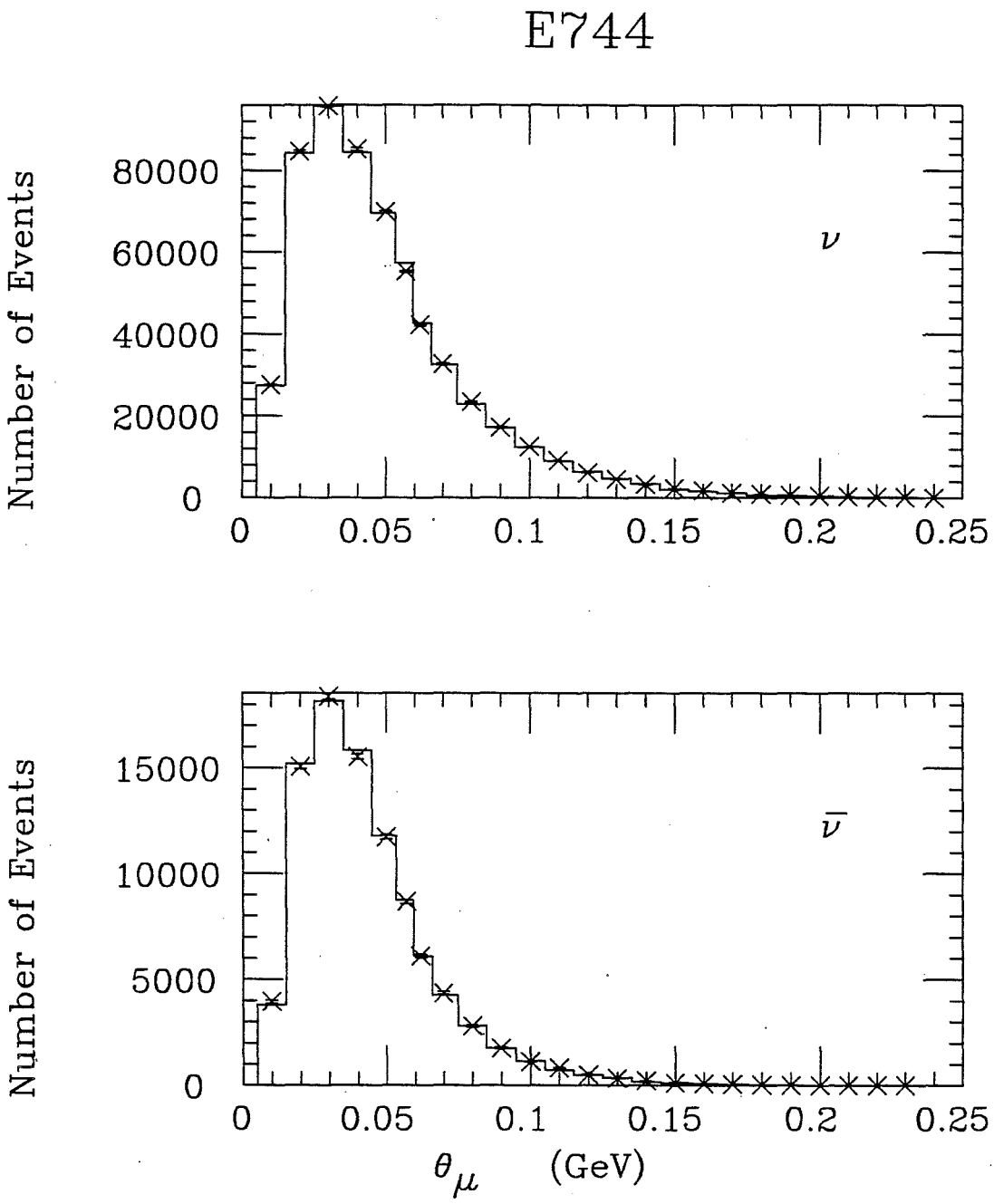

Figure 4.7a The angle of the muon at the vertex for the charged-current Monte Carlo (histogram) and the charged-current data (crosses) for incident neutrinos (top) and antineutrinos (bottom) in experiment E744.

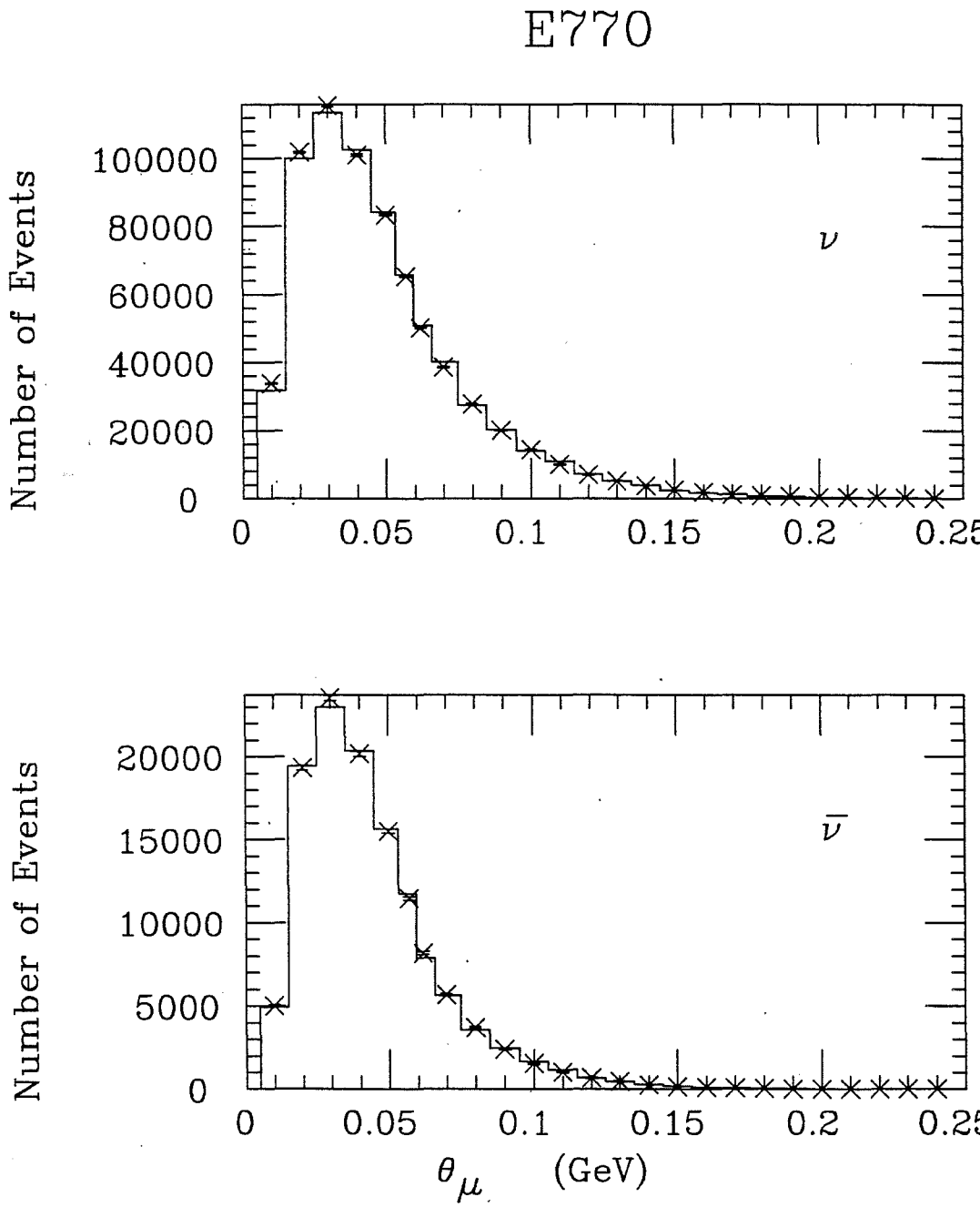

Figure 4.7b The angle of the muon at the vertex for the charged-current Monte Carlo (histogram) and the charged-current data (crosses) for incident neutrinos (top) and antineutrinos (bottom) in experiment E770.

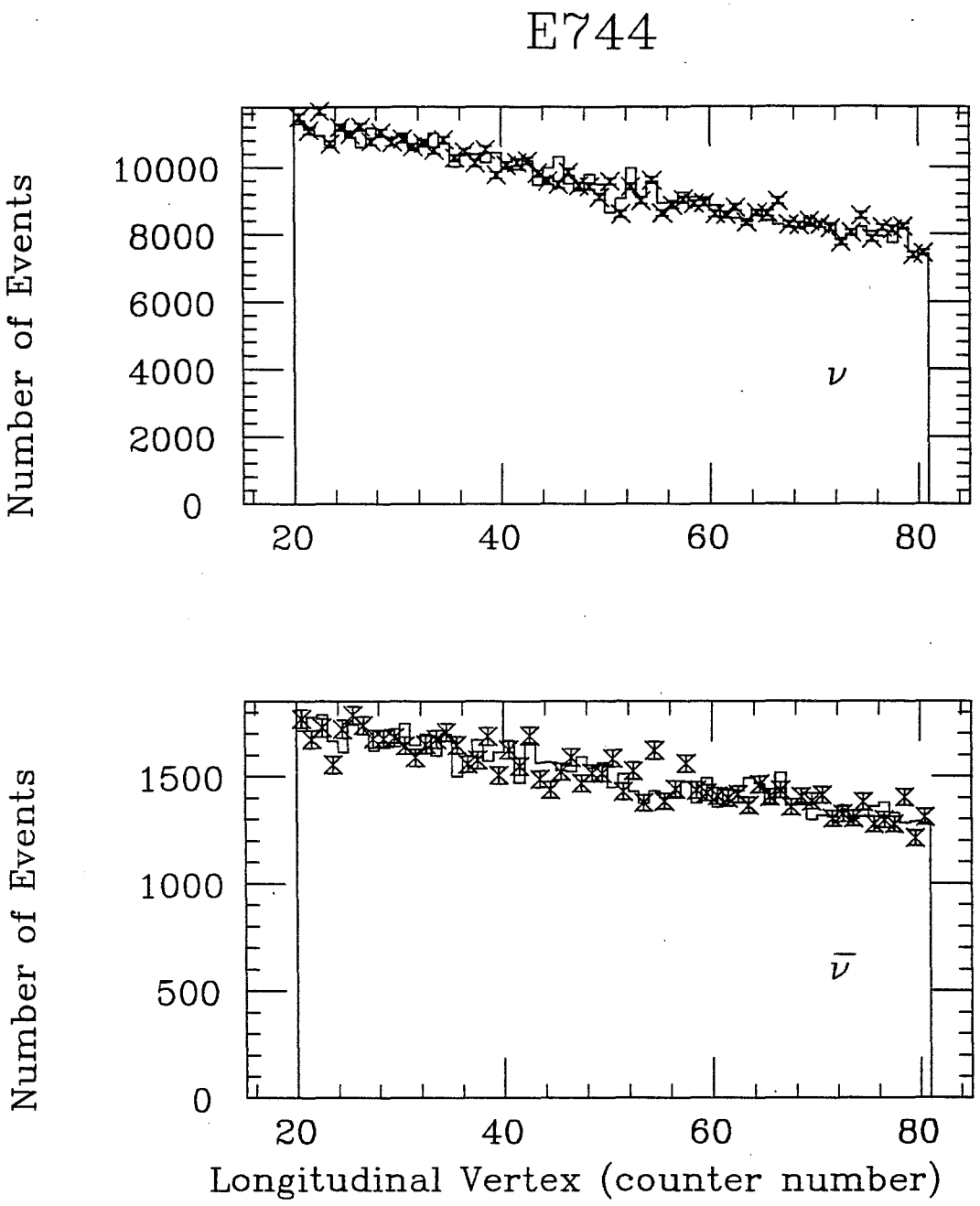

Figure 4.8a The longitudinal event vertex for the charged-current Monte Carlo (histogram) and the charged-current data (crosses) for incident neutrinos (top) and antineutrinos (bottom) in experiment E744. The calorimeter counters are numbered 1-84, where counter 1 is the most downstream counter.

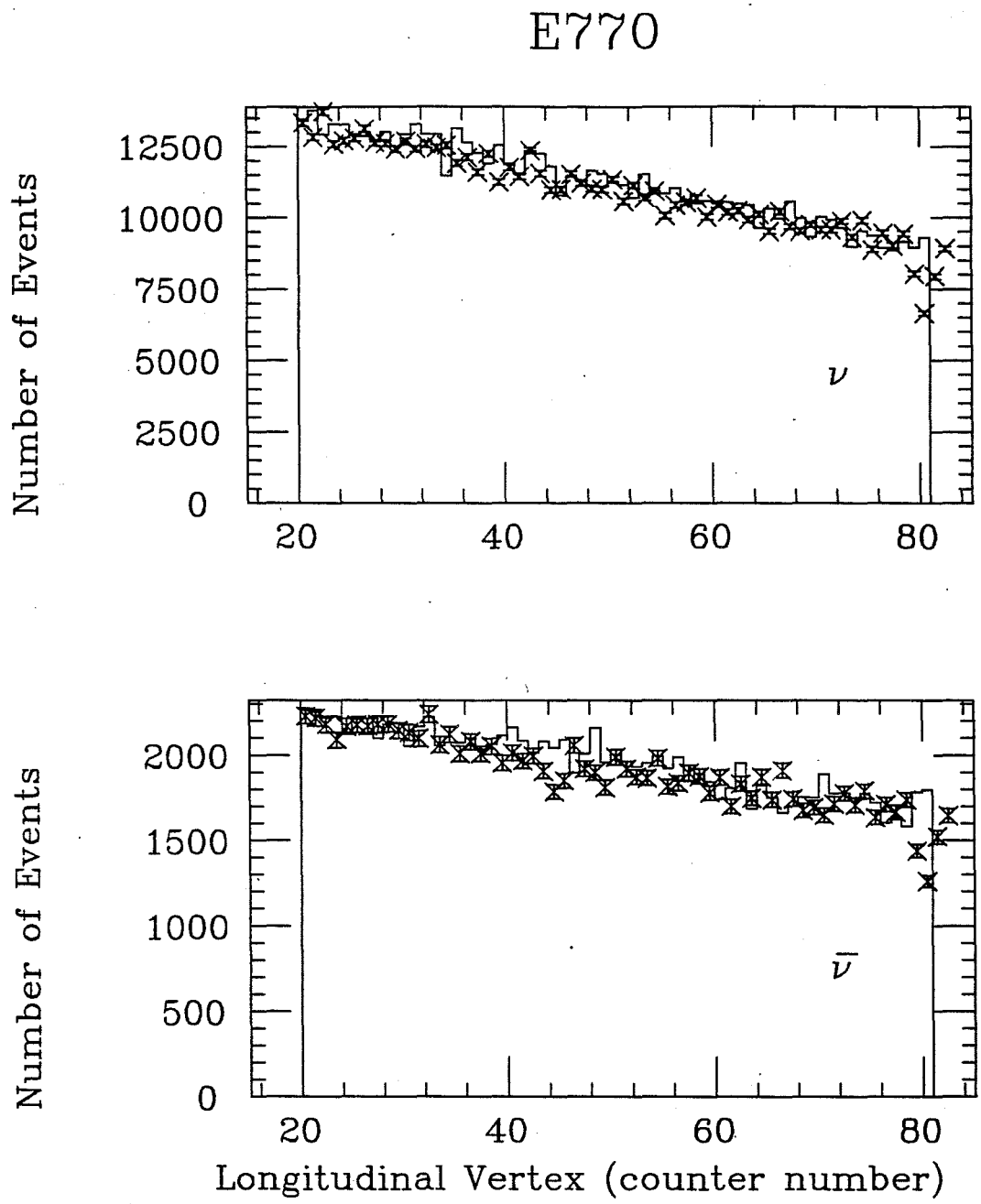

Figure 4.8b The longitudinal event vertex for the charged-current Monte Carlo (histogram) and the charged-current data (crosses) for incident neutrinos (top) and antineutrinos (bottom) in experiment E770. The calorimeter counters are numbered 1-84, where counter 1 is the most downstream counter.

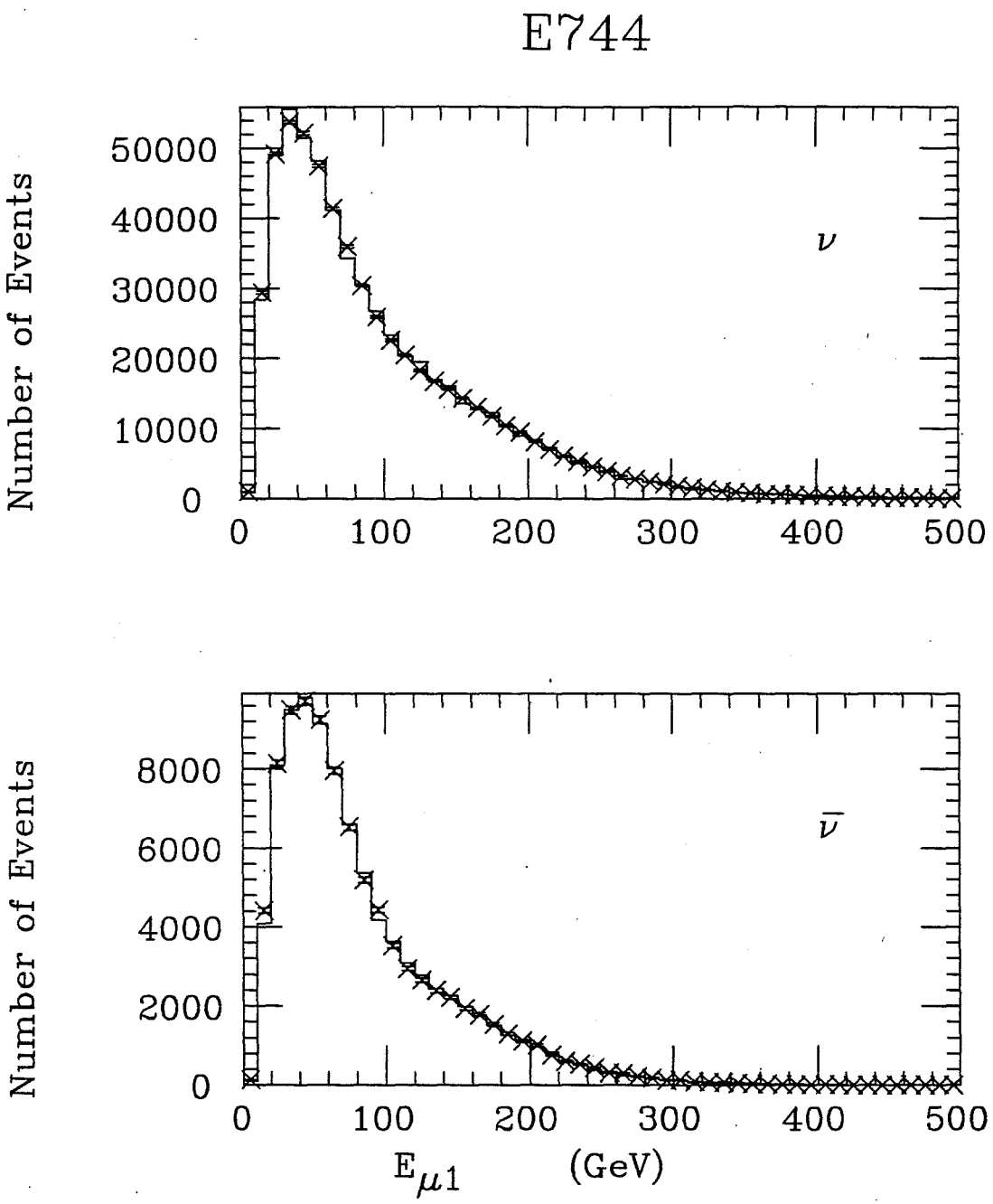

Figure 4.9a The momentum of the primary muon for the charged-current Monte Carlo (histogram) and the charged-current data (crosses) for incident neutrinos (top) and antineutrinos (bottom) in experiment E744.

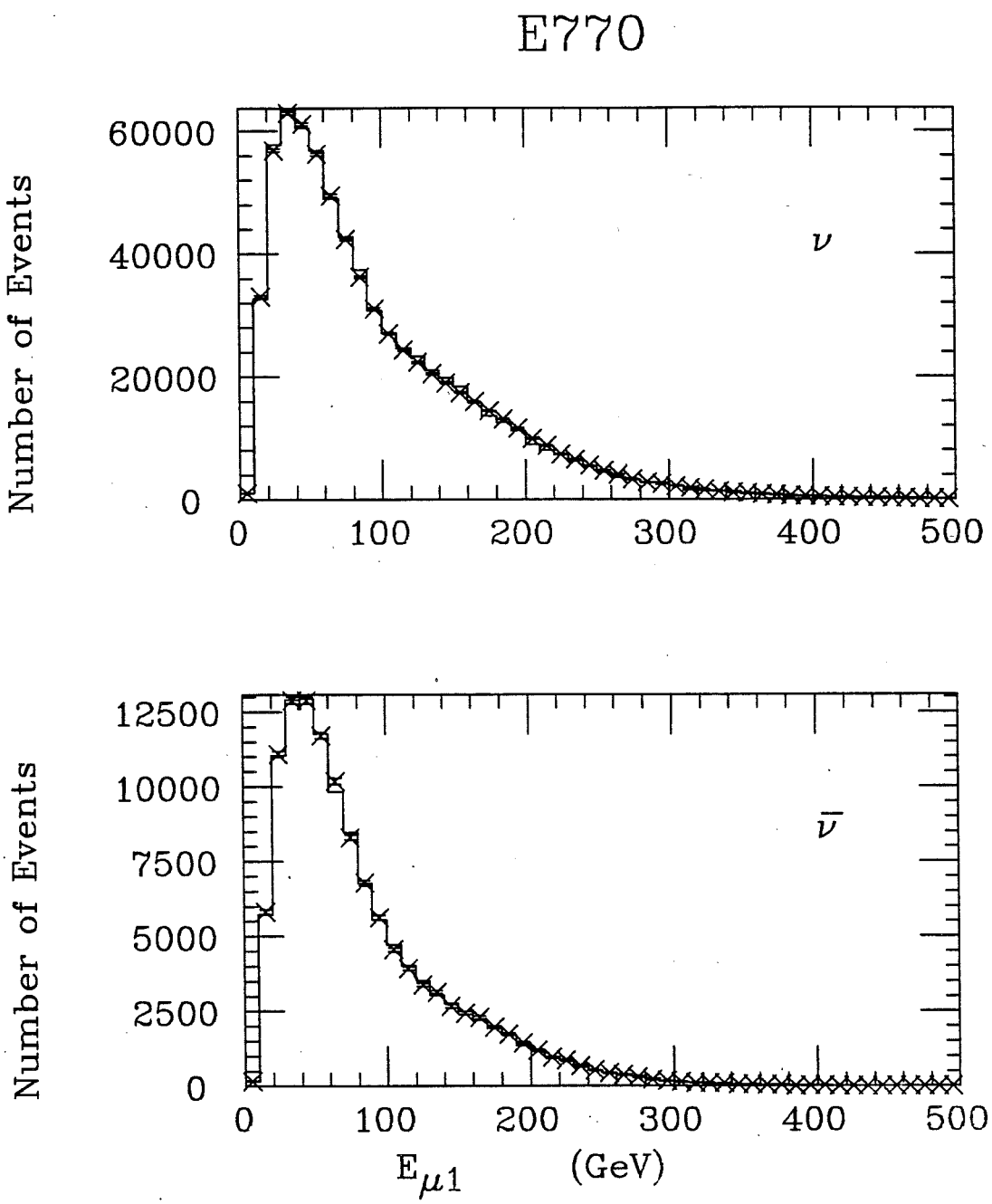

Figure 4.9b The momentum of the primary muon for the charged-current Monte Carlo (histogram) and the charged-current data (crosses) for incident neutrinos (top) and antineutrinos (bottom) in experiment E770.

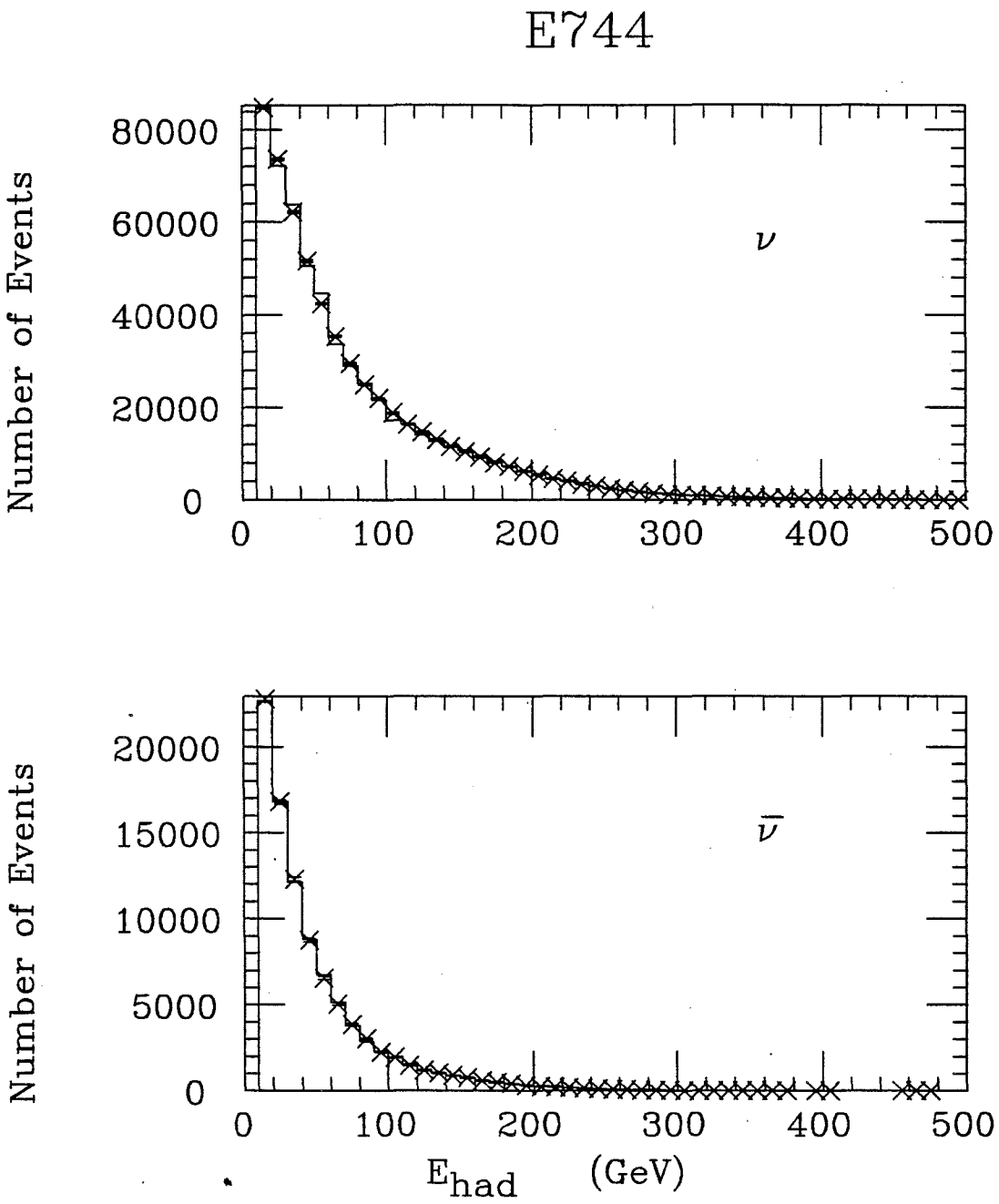

Figure 4.10a The hadron energy for the charged-current Monte Carlo (histogram) and the charged-current data (crosses) for incident neutrinos (top) and antineutrinos (bottom) in experiment E744.

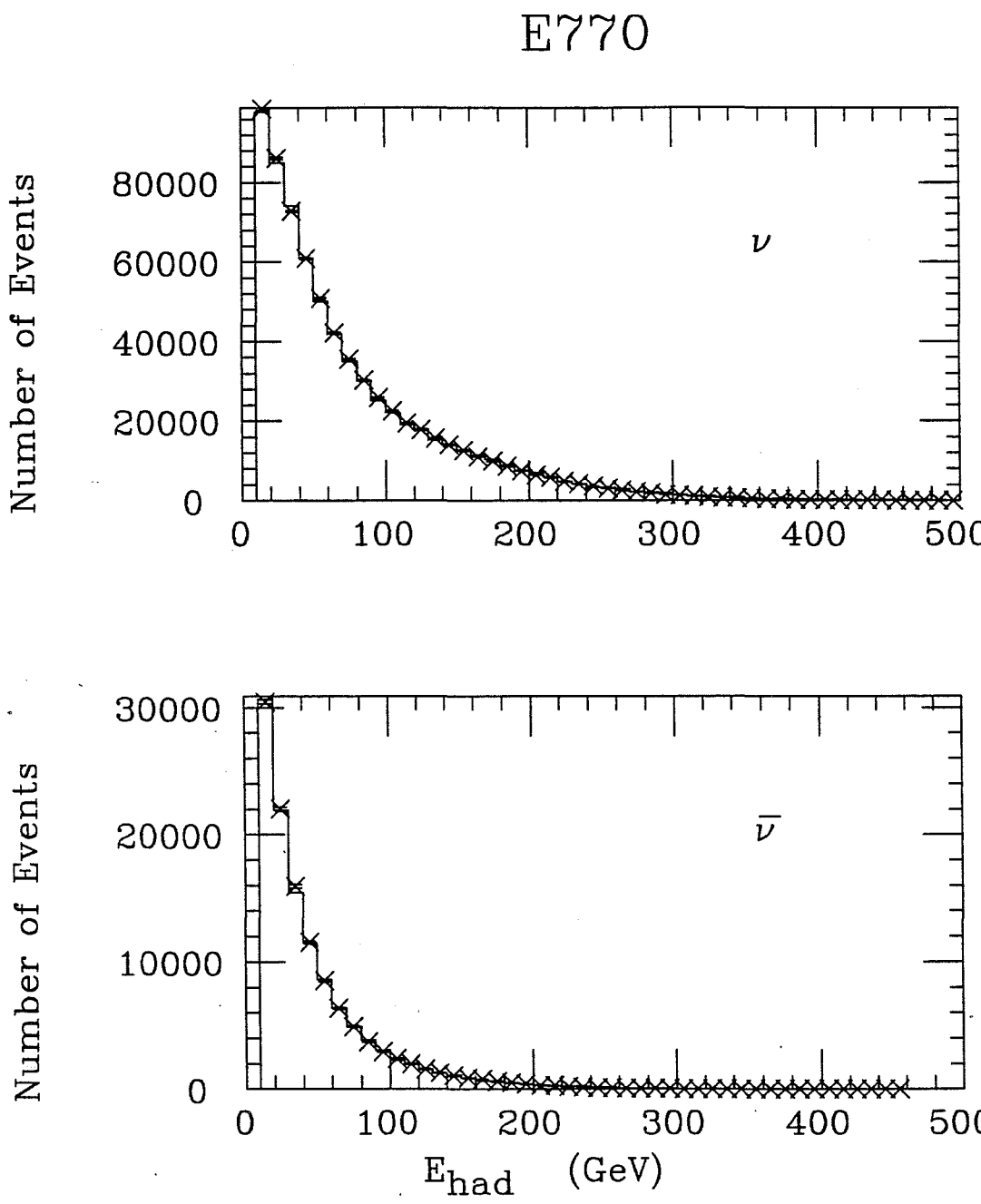

Figure 4.10b The hadron energy for the charged-current Monte Carlo (histogram) and the charged-current data (crosses) for incident neutrinos (top) and antineutrinos (bottom) in experiment E770.

Chapter 5

Measurement of the Muon Production Rate by Showering Hadrons

5.1 Introduction

Decays of pions and kaons in hadron showers of neutrino charged-current events is the largest source of background to prompt same-sign dimuon production. The rate of muon production from meson decays is about 10^{-4} per incident neutrino, whereas the expected rate of prompt same-sign dimuon production is less than 10^{-5} per incident neutrino [24]. There are two components of the meson decay background, called the vertex component and the shower component. The vertex component, shown in Figure 1.4, is from the decay of primary hadrons at the vertex. The shower component, shown in Figure 1.3, is from decays of secondary hadrons, and decays of hadrons in subsequent generations of the shower. The vertex background is described in Chapter 7. To determine the shower component contribution, we use a Monte Carlo simulation of hadronic fragmentation and hadron decay, called the shower Monte Carlo simulation, which is described in Chapter 6. The subject of this chapter is the measurement of the muon-production rate of hadronic showers in the CCFR detector that is used to set the level of muon-production in the shower Monte Carlo simulation.

Fragmentation is the process during which a struck quark and spectator quarks combine with quark-antiquark pairs to form mesons and

baryons. The fragmentation function $D_k(z)\,dz$, which depends of the target material, is the probability of finding the fragment in the range z to z + dz where z is the fraction of energy carried by the hadron of type k. Fragmentation functions are measured in bubble chamber experiments where the targets are considerably lighter than iron. However, we need to understand fragmentation in iron. Nuclear effects on fragmentation are not well understood and most models of fragmentation, for example the Lund Monte Carlo [25], deal with collisions between hadrons and free protons, ignoring nuclear effects.

To accurately model fragmentation in iron, we measured the rate of muon production in hadron-induced showers in our calorimeter and used it to set the level of muon-production in the shower Monte Carlo; which is our version of the Hadro-Lund Monte Carlo, JETSET version 6.2, modified to include nuclear effects. The use of experimental data renders the background calculation independent of the Lund model for hadronic fragmentation.

5.2 The Hadron Beam Experiment.

We measured muon-production rates of hadronic showers induced by momentum analyzed negative hadron beams of 40, 70, and 100 GeV, incident on the configuration of the CCFR calorimeter shown in Figure 5.1. At 100 GeV, the rear three target carts were positioned in the hadron beam line, which was inclined at about 68 mradians with respect to the neutrino beamline in the horizontal direction. At 40 GeV and 70 GeV two target carts were placed in the hadron beam. Rates were measured for

produced muon momenta when corrected for ionization losses back to the vertex (P_μ) greater than 4.3 GeV/c. Previous measurements were limited to P_μ greater than 11 GeV/c and hadron energies above 50 GeV [9]. At 70 GeV we used Čerenkov counters to identify the species of the incident hadron. We have eliminated the uncertainty in the level of muon-production by showering kaons with this measurement.

The hadron beam was produced by 800 GeV/c protons incident on a 38 cm thick aluminum target. Momentum-selected negative particles

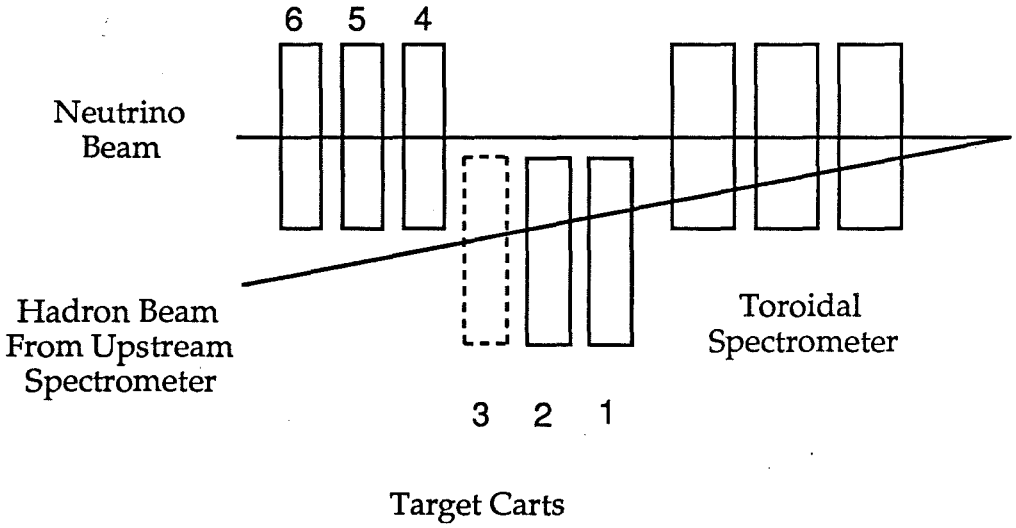

Figure 5.1 The configuration of the CCFR detector used for the hadron beam experiment. The hadron beam was inclined at about 68 mr with respect to the neutrino beam direction. Target carts 1 and 2 were moved into the path of the hadron beam for the 40 GeV and 70 GeV beams. At 100 GeV, the third target cart was also moved into the hadron beamline to provide more material.

were transported with dipole bending magnets and quadrupole focussing magnets in the NT west beamline to the detector area. The particle flux at the detector was about 1000 particles/sec and the momentum spread of the beam, $\Delta P/P$ was 1 percent at 100 GeV [8]. The momentum of each incident particle was measured using a spectrometer located upstream of the CCFR detector. The upstream spectrometer and the Čerenkov counters are described in Sections 5.3 and 5.4.

The composition of the hadron beam depended on beam energy. At 40 GeV it contained about 85 percent pions, and the fraction decreased slightly with increasing energy. The electron fraction at 40 GeV was 10 percent, and decreased with increasing energy [8]. The kaon fraction was about 5 percent as described in Section 5.4.4. The remaining beam was composed of antiprotons, and this fraction increased with increasing energy.

5.3 The upstream spectrometer

The upstream spectrometer shown in Figure 5.2, consisted of four drift chambers that give the particle position and angle before and after a pair of dipole magnets. The momentum is calculated using the bend of the particle's trajectory and the measured magnetic field of the dipoles [26].

Three of the four drift chambers in the upstream spectrometer consisted of four planes of 1 m by 1 m single-wire drift chambers. There were two planes in each of the x and y views that were offset by one quarter inch in the transverse direction to distinguish particle trajectories on the left from those on the right of the wires. The position resolution

of the chambers was about 100 μm [27]. The fourth chamber in the upstream spectrometer was the most upstream chamber of the CCFR detector. It consisted of two planes of three-wire chambers and is described in Chapter 2.

To distinguish particle tracks amid multiple hits, all possible lines were fit to the hits in the two chambers upstream of the dipole magnet and all possible lines were fit to the hits in the two downstream chambers. The two lines that were closest to each other at the bend point were chosen as the particle's trajectory.

For accurate measurement of the momentum, the path was required to pass through the dipoles in the region where the dipole field

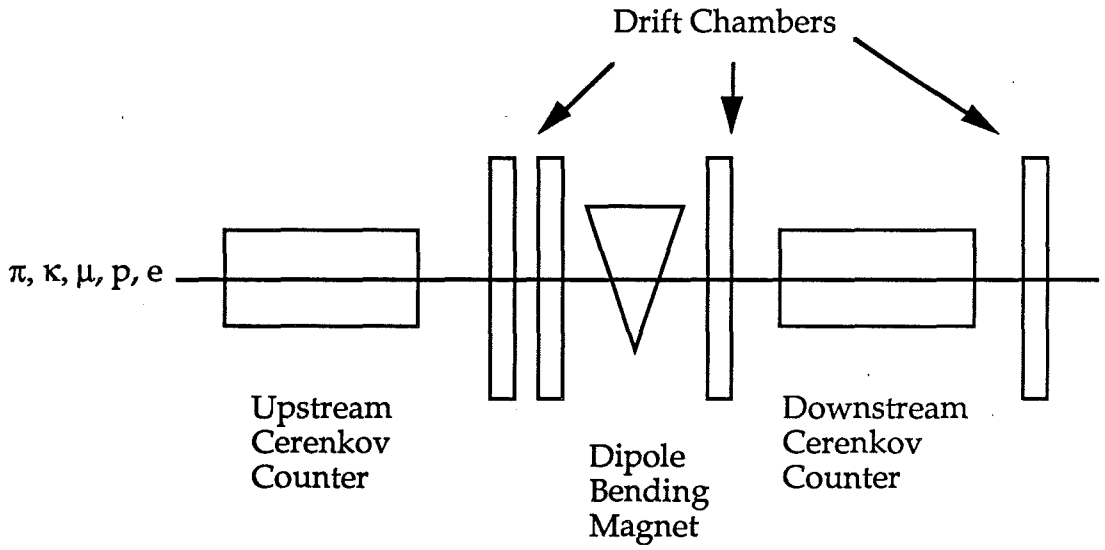

Figure 5.2 A spectrometer was located upstream of the CCFR detector, during the hadron beam experiment. The spectrometer consisted of two drift chambers just upstream of a dipole bending magnet and two drift chambers downstream. Two Čerenkov counters were used to identify pions and kaons in the 70 GeV beam.

was uniform. The dipole field was measured at the Magnet Test Facility at Fermilab using a rotating coil Gaussmeter. This tool measures the current in a 1/2" by 12 foot wire loop placed at various positions within the aperture of the dipole [28]. The dipole field was constant to 0.1 percent within ± 1 inch of the center line. At ± 1.4 inches of the center line the field was constant to 1.25 percent. This was measured at dipole currents between 250 Amps and 1200 Amps, which were used for 20 GeV to 200 GeV beam energies. A diamond-shaped cut on the position of the track at the bend point ensured that the particle stayed within the good field region. This was ±0.75" in the vertical direction and ±1.5" in the horizontal direction. The momentum resolution of the spectrometer was about 2 percent [27].

5.4 Particle Identification by Čerenkov Radiation

We used two Čerenkov counters to identify the particle species in the 70 GeV beam. Figure 5.3 shows a schematic of the Čerenkov counters used in this experiment that were designed by Stan Pruss at Fermilab [29]. Figure 5.2 shows their configuration in the test beam. This section first reviews the principles of Čerenkov radiation, then describes the Pruss counters in detail. The section concludes with a description of the off-line analysis performed on the Čerenkov data to eliminate pions that were misidentified as kaons. They were misidentified when a pion passed through the upstream counter undetected, since the upstream counter was set so that pions radiated and kaons did not. The downstream counter was set so that both pions and kaons radiated.

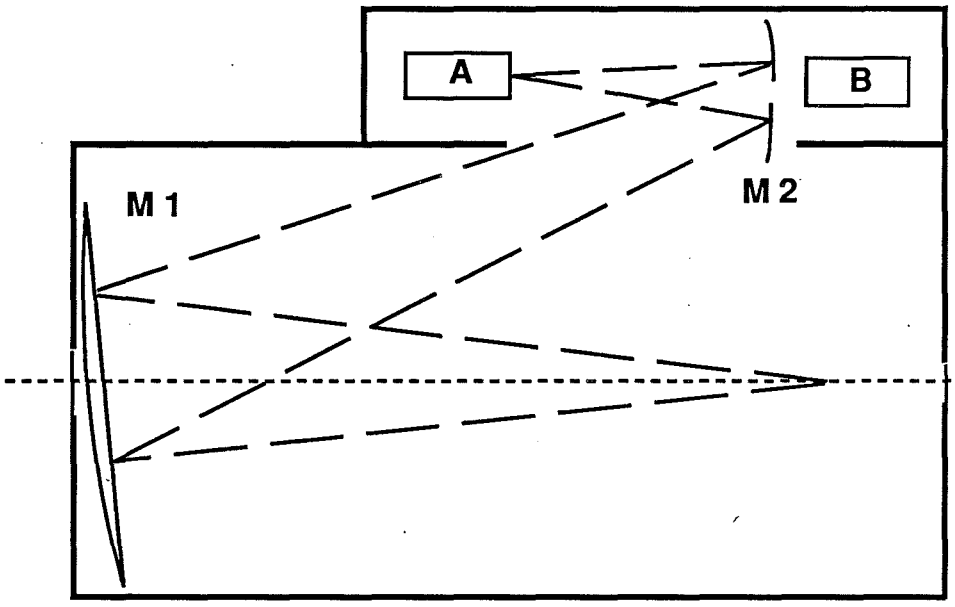

Figure 5.3 A schematic of a Pruss Čerenkov counter. If the cone of radiation is larger than 5 mr, then the light is reflected by M2 onto the photomultiplier tube A. Radiation within a cone of 5 mr passes through a hole in M2 and is measured by photomultiplier B. The path of the beam is represented by the dotted line. The path of the light is represented by the longer dashes.

5.4.1 Principles

A particle emits Čerenkov radiation in a medium when its velocity (β) exceeds the velocity of light in the medium. In other words, $\beta > 1/n$ where n is the index of refraction of the medium. This threshold can also be expressed in terms of the particle rest mass (m_0), particle energy (E), and the index of refraction (n) of the medium,

$$m_0 < E\sqrt{1 - 1/n^2}.$$

The photons are emitted in a cone at an angle θ_c where

$$\theta_c = \cos^{-1}(1/\beta n).$$

For example, 70 GeV pions with a mass of 139.6 MeV passing through helium at 4 psi emit Čerenkov light, whereas 70 GeV kaons with mass 493.7 MeV do not.

5.4.2 Pruss Type Čerenkov Counters

The Čerenkov threshold is varied by changing the index of refraction of the gas contained within the long pipe. The index of refraction is varied by changing the pressure of the gas, since

$$n = c\,P + 1,$$

where c is a constant proportional to 1/T, and T is the temperature [30]. Figure 5.4 shows the threshold angle θ_c, for various 50 GeV particles [31] as a function of pressure for a counter filled with nitrogen. Protons are below the threshold for pressures less than 8.1 psi, and kaons are below the threshold for pressures less than 2.3 psi. Electrons, muons and pions are above the threshold for pressures above 0.25 psi.

5.4.3 Operation

Radiation at angles less than 15 mr was focussed on one of two photomultiplier tubes by the spherical mirrors M1 and M2 in Figure 5.3. The upstream counter was 30.48 m long and the downstream counter was 12.19 m long. Mirror 1, which was 10″ in diameter, had a one inch hole at the center so the beam passed through it unimpeded. It focussed Čerenkov light either on mirror 2 or phototube B, depending on θ_c. If θ_c was less than 5 mrad, the light passed through a one inch circular aperture

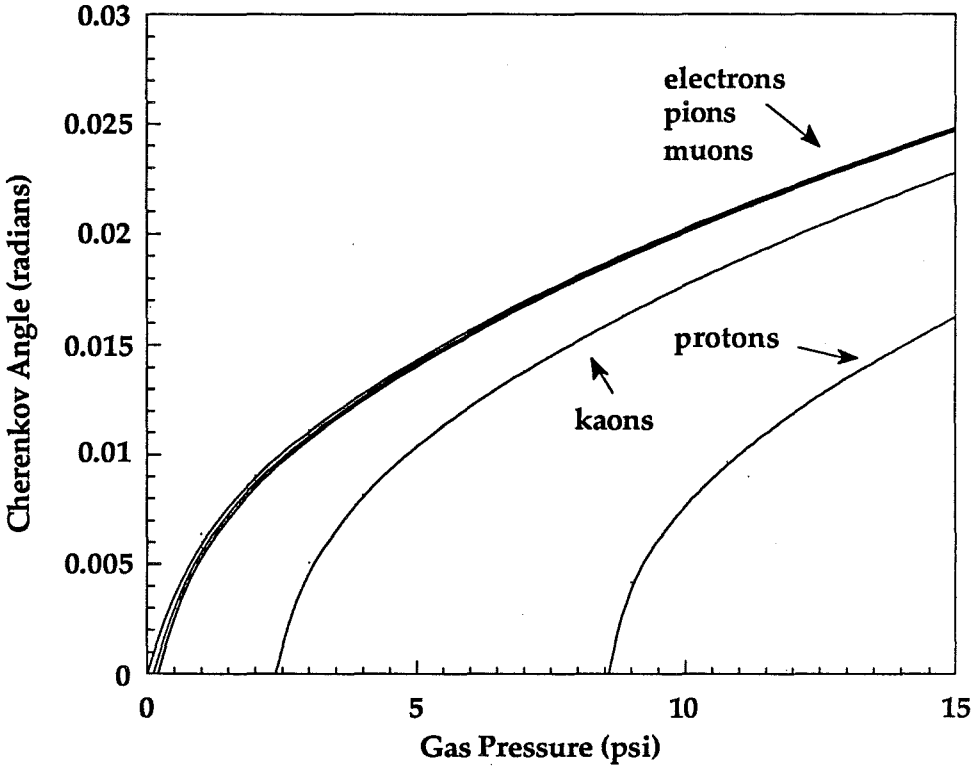

Figure 5.4 Čerenkov angle in nitrogen gas as a function of pressure for a 50 GeV hadron beam. The curves for electrons, pions and muons are barely distinguishable. Kaons radiate above 2.4 psi and protons begin to radiate at 8.5 psi.

in mirror 2 onto the photocathode of phototube B. If θ_c was greater than 5 mrad, the light was focussed by mirror 2 on phototube A.

The number of photons N, of wavelength λ, emitted by radiating particles is given by [32]

$$\frac{dN}{d\lambda} = \frac{2\pi\alpha}{\lambda^2} L \sin^2\theta_c$$

where L is the length of the radiator and α is the fine structure constant. Integrating this equation over visible wavelengths between 3900 Å and 7800 Å, we find that about 18 photons are emitted in the upstream counter for θ_c equal to 5 mr. In order to be sensitive to signals at these small angles, we used phototubes capable of resolving a single photoelectron. The RCA C31000D tube has a bi-alkali photocathode which gives a high quantum efficiency of 31 percent at 3850 Å. The tubes were operated at about 2200 volts.

The pressure in the counters was controlled by a vacuum pump and a valve to a supply of gas, either nitrogen or helium, which allowed it to range from 10^{-3} psi to 14.7 psi. During E770, the upstream counter was filled with helium at 9 psi so that pions were above the threshold for Čerenkov radiation and kaons were below at 70 GeV. The downstream counter was filled with nitrogen gas at 3 psi so that both 70-GeV pions and kaons emitted radiation.

Aligning the mirrors was a two step process. An initial coarse alignment was done before the beam pipe was evacuated. We placed a small flashlight bulb in the beam pipe about 50 feet from the mirrors, so that its light subtended about 40 mr at the counter. We adjusted the position of the mirrors so that the image of the bulb was focussed where the phototubes were located. Finer adjustment of the orientation of the large mirror was done using the beam. For this the pressure in the counter was set so that pions were well above the threshold. The large

mirror was then adjusted until the maximum intensity was measured in phototube B. Figure 5.5 gives the pressure curve for the counter filled with nitrogen for a 50 GeV beam. It shows the ratio of the number of phototube pulses in coincidence with the beam to the number of beam particles as a function of pressure. The first peak in the curve for tube B is due to electrons, pions, muons and kaons. The smaller peak at around 10 psi is due to protons. The spread of the peaks is due to the spread in θ_c which is mainly due to the momentum spread of the beam. The curve for tube A levels off at around 3 psi, where pions start radiating at 15 mrad.

The efficiency of each Čerenkov counter was greater than 98 percent, measured by setting the counters such that all beam particles were above the threshold for Čerenkov radiation. The percentage of Čerenkov signals coincident with the beam due to phototube dark noise, was measured by counting the number of Čerenkov signals in coincidence with a delayed beam gate. About 0.6 percent of the Čerenkov signals in coincidence with the beam were due to dark noise.

The Čerenkov signals were amplified by a factor of ten, digitized with LeCroy 4300 FERA ADC's and written to tape. The gain of the phototubes and ADC system was left as a parameter to be determined in the off-line analysis of the Čerenkov data, which is described below. The sensitivity of the ADC's was 0.25 pC per ADC count [8].

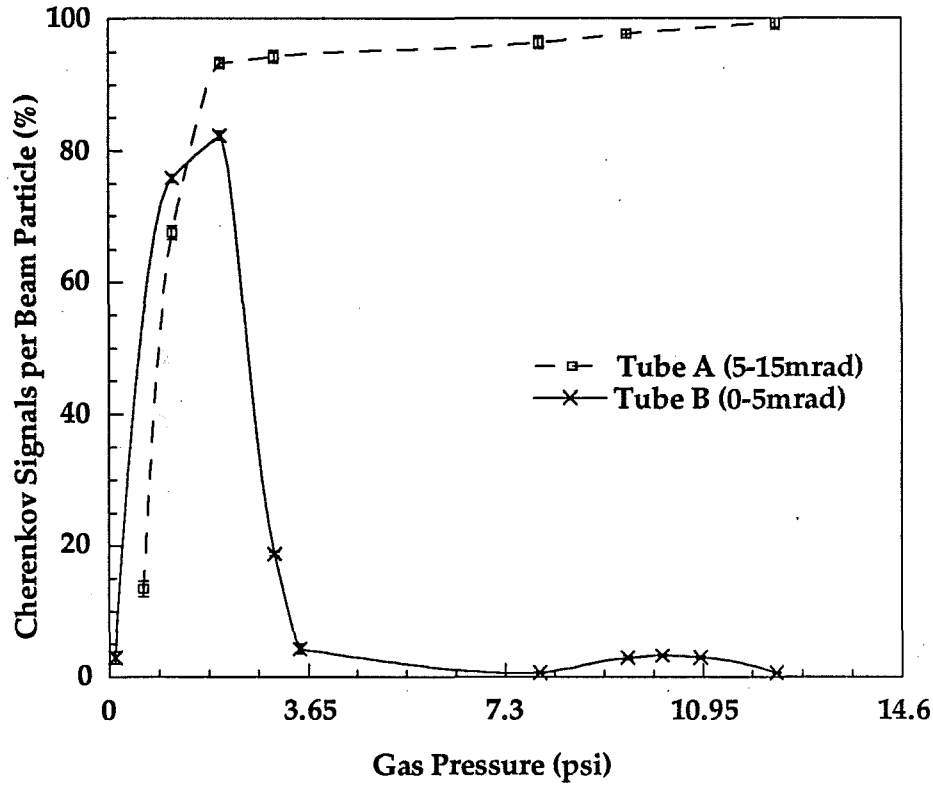

Figure 5.5 Percent of Čerenkov signals in coincidence with passage of a beam particle as a function of gas pressure for a 50 GeV beam. The counter was filled with nitrogen. Tube A measured the amount of light at angles between 5 mr and 15 mr. Tube B received light at angles between 0 mr and 5 mr. The first peak in Tube B is due to electrons, pions, muons and kaons. The small peak at higher pressure is due to protons.

5.4.4 Čerenkov Counter Data Analysis

The summed pulse heights of the two tubes in each counter are plotted against each other in Figure 5.6 to show the separation of pions and kaons for the 70 GeV hadrons. Events that passed the selection criteria described in Section 5.5 were used in this analysis. The kaon

sample is composed of events with no pulse height recorded in the upstream counter. Only events with non-zero pulse height recorded by both counters are included in the pion sample. There is some probability that a pion will not be recorded the upstream counter. This led to a 7.1% ± 6.1% contamination of pions in the kaon sample, estimated with the fits described in the remainder of this section.

The distributions of the Čerenkov counter pulse heights in each

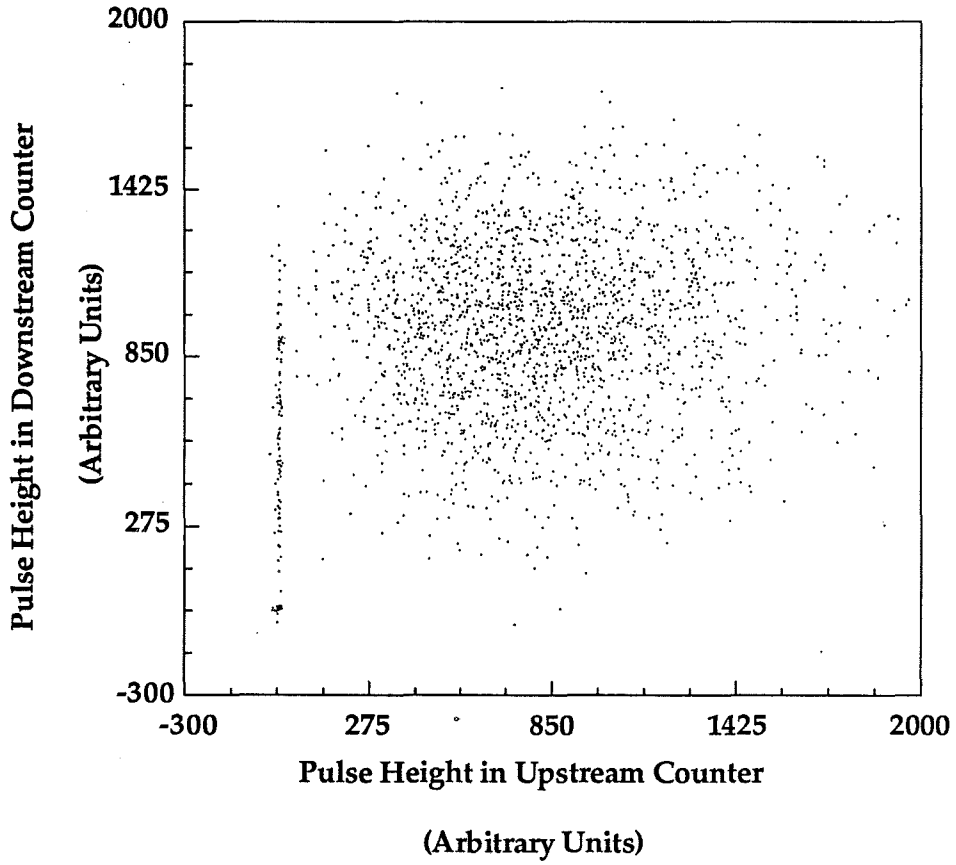

Figure 5.6 Pulse Heights in the two Čerenkov counters plotted against each other. Beam hadrons producing no pulse height in the upstream counter were identified as kaons with a 7.1% ± 6.1% contamination by pions. The remaining events were identified as pions.

counter were fit to a Poisson distribution smeared by a Gaussian representing photon statistics. One fit was made to the pion sample. Another was made to the kaon sample that included a term for the pion contamination. The function $P_\pi(n)$ gives the probability of obtaining n photoelectrons in the downstream counter for the pion sample,

$$P_\pi(n) = \frac{N}{\sqrt{2\pi}\,\sigma} \int_{n-4\sigma}^{n+4\sigma} \frac{e^{-\mu_\pi}\mu_\pi^{y}}{y!}\, e^{-(y-n)^2/2\sigma^2} dy$$

The number of photoelectrons n, is given by

$$n = \frac{\text{Number of ADC counts}}{G}$$

The mean of the Poisson distribution (μ_π), width of the Gaussian smearing (σ), normalization (N), and the number of ADC counts per photoelectron (G) were free parameters for the fit to the pion sample. For the fit to the kaon sample, the following function was used:

$$P_K(n) = \frac{N_k}{\sqrt{2\pi}\,\sigma} \int_{n-4\sigma}^{n+4\sigma} \frac{e^{-\mu_k}\mu_k^{y}}{y!}\, e^{-(y-n)^2/2\sigma^2} dy$$

$$+ \quad \frac{N_\pi}{\sqrt{2\pi}\,\sigma} \int_{n-4\sigma}^{n+4\sigma} \frac{e^{-\mu_\pi}\,\mu_\pi^{y}}{y!}\, e^{-(y-n)^2/2\sigma^2} dy$$

where the first term represents the signal due to kaons and the second term represents the pion contamination. The Poisson mean for pions (μ_π) and the Gaussian width (σ) were fixed at the values obtained in the fit to $P_\pi(n)$. The Poisson mean for the kaon distribution (μ_k) and the normalizations N_k and N_π were free parameters for the fit to $P_K(n)$. The integrals were numerically evaluated using Simpson's rule. The CERNLIB program MINUIT [33] was used to minimize the χ^2 function. The values for the fitted parameters are given in Table 5.1 along with the χ^2 of the fits.

Figure 5.7 gives the distribution of photoelectrons in the downstream counter that were selected as kaons and the result of the fit to $P_K(n)$, giving contributions from the kaons and the pion contamination separately as well as their sum. The final kaon sample was composed of events with less than 10 photoelectrons in the downstream counter insuring a contamination of less than $(1 \pm 1)\%$ from pions. Figure 5.8 shows the result of the pion-sample fit to $P_\pi(n)$, which gives the distribution of photoelectrons in the downstream counter. The ratio of kaons to pions in the 70 GeV beam was $(4.3 \pm 0.3^{o}\%$ calculated from the fits.

Fit	χ^2/dof	N	N_π	N_K	σ	G	μ_π	μ_K
$P_K(n)$	56/56	n/a	34	442	4.2	0.053	19.4	13.6
$P_\pi(n)$	114/55	10151	n/a	n/a	4.2	0.053	19.4	n/a

Table 5.1 Values of the parameters for the fit to the kaon sample and the fit to the pion sample for the 70 GeV hadron beam. The χ^2 and the number of degrees of freedom (dof) are also listed.

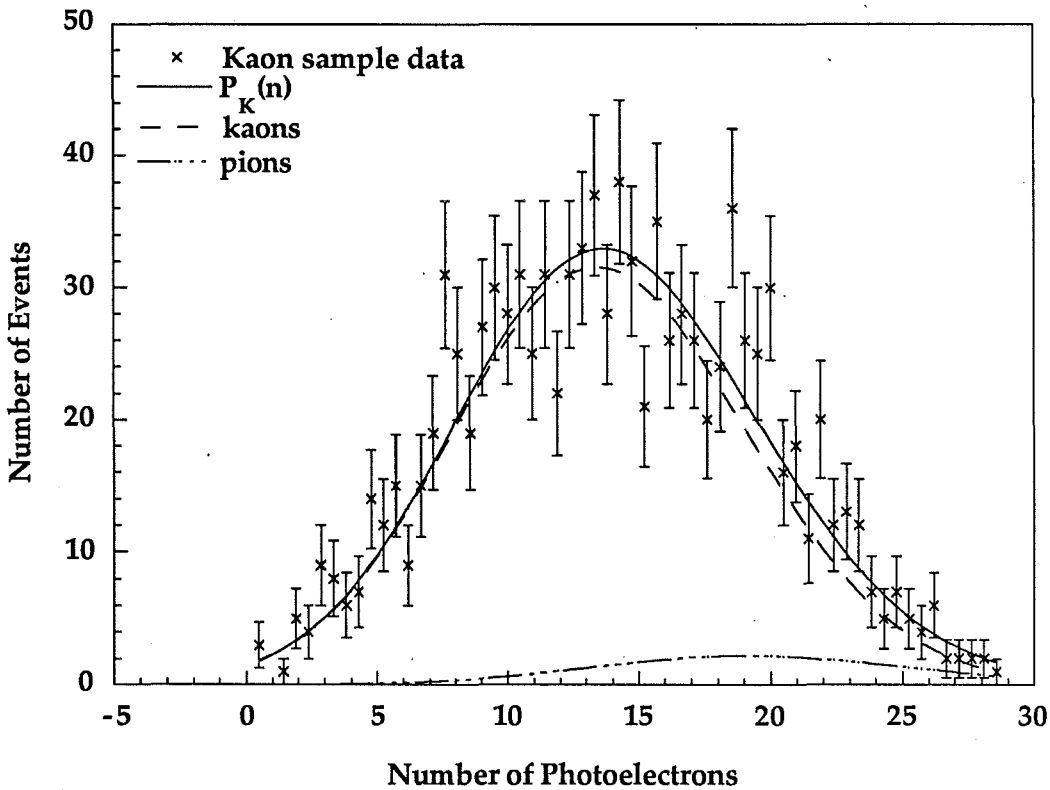

Figure 5.7 The distribution of the number of photoelectrons for the kaon sample (crosses) and the results of the fit to $P_K(n)$ (solid curves). The contribution from kaons is given by the dashed curve and the pion contamination is given by the dot-dashed curve.

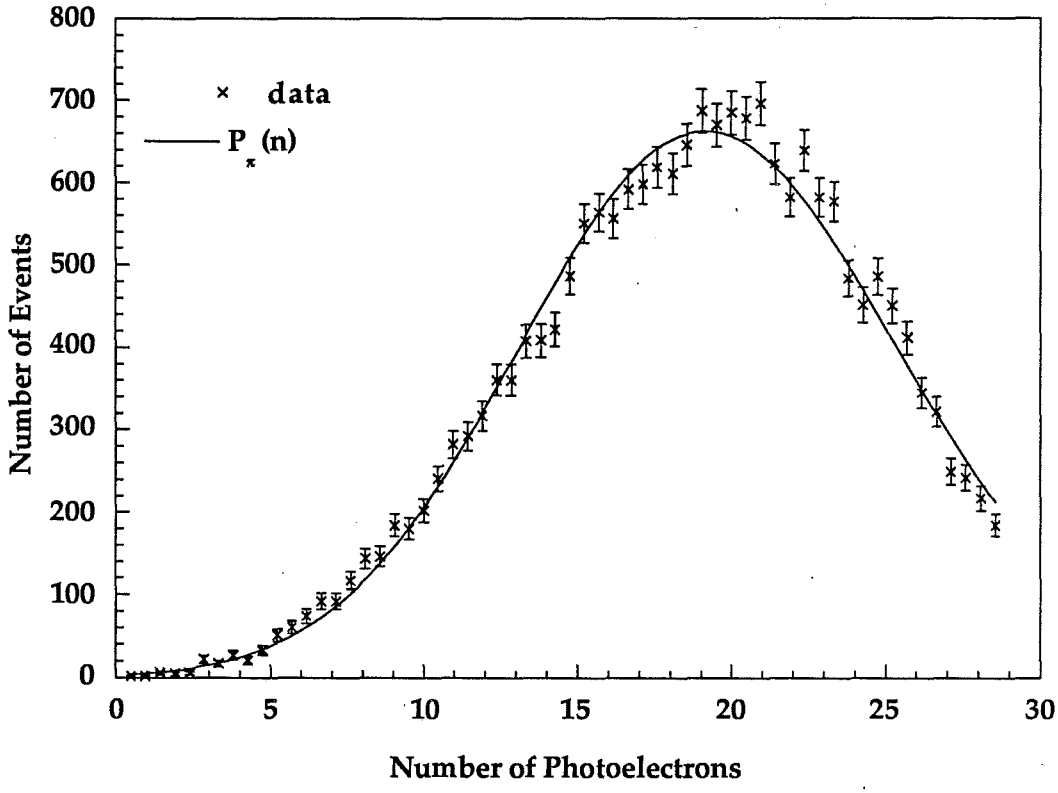

Figure 5.7 The distribution of the number of photoelectrons n, in the downstream counter for the pion sample (crosses) and the results of the fit to $P_\pi(n)$ (solid lines).

5.5 Event Selection

This section describes the criteria designed to select test beam events that were properly reconstructed in the detector and to reject electrons and beam muons.

Three types of event triggers were used in the analysis:

- Muon-production triggers: Events that deposited energy of an equivalent minimum-ionizing particle E_{mip}, in the calorimeter and in the first toroid gap over the first 23 (31) counters of the target for the two (three) cart configuration.
- Hadron-shower triggers: Events that deposited total energy in the calorimeter greater than E_{th} equal to 8.2, 13.6, and 22.7 GeV for 40, 70, and 100 GeV incident hadrons, respectively.
- Penetration triggers: Events that deposited total energy greater than E_{th} to a depth of 16 counters in the calorimeter.

The proportion of hadron-shower triggers to muon-production triggers was about 1000:1. We pre-scaled the number of hadron-shower triggers to be able to write all of the muon-production triggers to tape. The number of penetration triggers written to tape was also pre-scaled since there were around 100 for each muon-production trigger. Depending on the running conditions, we wrote between 0.1 percent and 0.8 percent of the hadron-shower triggers and penetration triggers to tape, while the total numbers of both triggers were counted. All events that produced a muon-

production trigger were written to tape. Table 5.2 gives the number of events counted and written to tape for each beam energy and each trigger type.

Beam Energy (GeV)	Muon-Production Trigger	Hadron Shower Trigger		Penetration Trigger	
	Total	Total	On Tape	Total	On Tape
40	48×10^3	38×10^6	22×10^3	1.2×10^6	17×10^3
70	39×10^3	16×10^6	36×10^3	1.8×10^6	15×10^3
100	22×10^3	13×10^6	13×10^3	2.2×10^6	18×10^3

Table 5.2 Numbers of hadron beam events incident on the calorimeter and written to tape for each beam energy and each trigger.

5.5.1 Good Hadron Events and Muon-Production Events

In order to select clean and unbiased samples of hadronically induced events the following criteria were applied to the events:

- Events were required to contain a single momentum-analyzed track in the upstream beam spectrometer and their reconstructed beam momentum was required to be within 10 percent of the nominal beam momentum.
- The transverse vertex must lie within a 60″ circular cut centered on the detector. This rejects events in the corners of

the counters where the effects of light collection efficiency were difficult to correct for.

- The track in the upstream spectrometer was extrapolated 42 m to the most upstream drift chamber of the target calorimeter, where it was required to pass within 20 cm of the position of one hit in this chamber. Events with two hits within this window were rejected. The size of the window was chosen to include errors due to the relative alignment of the spectrometer and target drift chambers in addition to drift-chamber measurement error.
- Showers initiated upstream of the target were eliminated by requiring an energy deposition in the first target calorimeter counter, which is located after 5 cm of iron, to be less than that expected from four minimum-ionizing particles.
- Since the hadron-energy resolution depends on containment of the hadron shower, events were required to have a transverse vertex within a 100"x 100" square centered on the longitudinal axis of the apparatus.
- Finally, the total reconstructed energy of the event must be within 10 percent of the nominal beam energy.

For muon-production triggers only, the muon momentum (P_μ) was required to be greater than 9 GeV/c when corrected for ionization losses back to the event vertex in the two cart configuration and 11 GeV/c in the three cart configuration. In addition, the muon must pass the single

muon cuts that are described in Section 3.2.2. These are the cuts used in the analysis of neutrino-induced charged current events that ensure the muon was properly reconstructed in the spectrometer.

The fraction of the total number of events written to tape that passed the upstream spectrometer cuts was 13 percent for muon-production triggers and 20 percent for hadron-shower triggers at 40 GeV. At 100 GeV the fraction rose to 60 percent for muon-production triggers and 95 percent for hadron-shower triggers. The fraction of events that were removed by each of these cuts, relative to the number of events passing the upstream spectrometer cuts is summarized in Table 5.3 for hadron-shower triggers and muon-production triggers. The fraction of penetration triggers remaining after each cut was the same as the fraction of hadron-shower triggers.

5.5.2 Beam muons and electrons

After these cuts, there remained some events induced by beam muons and electrons. In the muon-production measurement it is important to eliminate any beam muon contamination. We developed several cuts designed to eliminate the contamination. For example, events induced by beam electrons were eliminated with cuts on the longitudinal development of the shower, since electron-induced showers are shorter than hadron-induced showers. This is because the characteristic length for electron showers is about 2 cm, or one radiation length (X_0), whereas the characteristic length for hadron showers is about 20 cm, or one hadronic interaction length (λ_i).

Beam muons may cause a hadron-shower trigger or muon-production trigger if they produce a δ-ray. A δ-ray is an electron knocked out of an atom. Beam muons can also deposit energy by bremsstrahlung or by scattering within a target nucleon. These mechanisms all produce short showers, so most beam muons are eliminated with cuts on the shower length.

The shower length is the distance between the longitudinal event vertex V_z, and the end of the shower. As described in Section 3.1.1, V_z in neutrino interactions is given by the first of the two most upstream counters in the calorimeter recording more than $4E_{mip}$ plus the amount of energy expected from backscatter, which called albedo. For the test beam analysis only, as opposed to the neutrino analysis, the beginning of the shower was defined by taking into account the energy deposited by the incident hadron before it interacts. Therefore, the beginning of the shower is given by the first of the two most upstream counters in the calorimeter recording more than $5E_{mip}$ plus the backscattered energy. The end of the shower was defined as the first of three consecutive counters recording less than $4E_{mip}$.

The cuts on the longitudinal development of the shower are :

- Electrons and most muons in the beam were eliminated by requiring the shower length to be greater than $2\lambda_i$, or about $23\ X_0$.
- Since the depth at which the muons interact is independent of the amount of material traversed by the muon, additional

beam muons were eliminated with the requirement that the shower begin within $2\lambda_i$ of the upstream end of the calorimeter.

- The ratio R_3 is defined as $R_3 = E_3/E_{tot}$, where E_3 is the energy deposited in the three most upstream counters in the shower and E_{tot} is the total energy in the shower. It is a good indicator of the type of shower, since it is large for electromagnetic showers and small for hadronic showers. Figure 5.9 shows the distribution of R_3 for the 70 GeV hadron beam. Events with $R_3 > 0.8$ were designated electromagnetic showers and were removed from the samples. The efficiency of this cut for eliminating electrons was measured with identified electrons in the CCFR detector. For electron energies of 60 GeV, 78 GeV and 91 GeV, over 99 percent of the electrons failed the R_3 cut [34].

A summary of the fraction of events removed by these cuts is given in Table 5.3 for hadron-shower triggers muon-production triggers. The fraction of penetration triggers that were removed was about the same as the fraction of hadron-shower triggers. After these cuts were applied, any beam muons remaining in the sample of muon-production triggers were statistically subtracted from the sample as described below.

Cut type	Cumulative Fraction of Events Cut (percent)					
	40 GeV		70 GeV		100 GeV	
	T_μ	T_h	T_μ	T_h	T_μ	T_h
The transverse vertex within a 60" circular cut.	4.5	0.1	10.0	1.2	10.0	0.8
A properly reconstructed muon, muon-production triggers only.	5.7	0.1	18.0	1.2	18.1	0.8
Calorimeter hit consistent with upstream spectrometer trajectory.	9.0	8.7	20.5	18.0	20.5	18.1
One hit in first calorimeter chamber.	37.1	43.0	44.7	40.5	20.5	10.4
Vertex position in x and y less than 2.5m.	37.1	43.0	44.7	40.5	20.5	10.4
Longitudinal event vertex within $2\lambda_i$ of front face of calorimeter.	66.5	47.2	69.9	45.0	46.6	15.1
Reconstructed hadron energy within 10% of nominal beam energy.	70.9	51.6	71.3	45.7	50.1	16.6
Shower length greater than 4 counters.	75.3	51.8	78.1	46.9	60.9	19.0
R_3 less than 0.8.	75.5	51.8	78.4	46.9	61.9	19.2

Table 5.3 The cumulative fraction of events removed by the various selection criteria, starting with the number of events with a single momentum analyzed track in the upstream spectrometer that was within 10 percent of the nominal beam momentum. The column labeled T_μ gives the fractions for muon production triggers, and the column labeled T_h for hadron-shower triggers.

The probability for a muon to produce a δ-ray is independent of the distance it penetrates in the material if ionization energy loss is ignored. The number of beam muons that interact several λ_i into the detector can be used to estimate the number of beam muons expected to interact within $2\lambda_i$ by extrapolating the distribution of the longitudinal vertex at several λ_i to the beginning of the calorimeter. This was done as follows: Muon-production triggers, passing all cuts except the cut on the longitudinal vertex position, that interacted after 12 counters and before 23 (31) counters for the two (three) cart configuration comprised a sample of interacting beam muons. The latter limit is necessary since only events that interacted before 23 (31) counters could cause a trigger as described in Chapter 2. The distribution of the longitudinal interaction point of these beam muons was extrapolated back to the first $2\lambda_i$ to give the number of beam muons surviving all the selection criteria. Figure 5.10 is a plot of a hypothetical distribution of interacting beam muons to illustrate the method. Table 5.4 gives the result of this calculation and the number of muon-production triggers passing all the cuts. As expected, most of the beam muons have energies close to the beam energy. The number of beam muons was subtracted from the number of muon-production triggers that were reconstructed with negative polarity. None of the beam muons were positively charged.

P_μ	40 GeV		70 GeV		100 GeV	
(GeV/c)	N_μ	Beam μ	N_μ	Beam μ	N_μ	Beam μ
9-11	275	2	242	0	120	0
11-15	254	1	384	3	284	0
15-20	99	7	189	0	163	1
20-30	56	17	159	8	110	3
> 30	30	20	121	66	124	31

Table 5.4 Total number of muon-production trigger events passing all cuts (N_μ) and the estimated number of beam muons remaining in each momentum bin (Beam μ). This number of remaining beam muons was subtracted from the number of negative muon-production triggers.

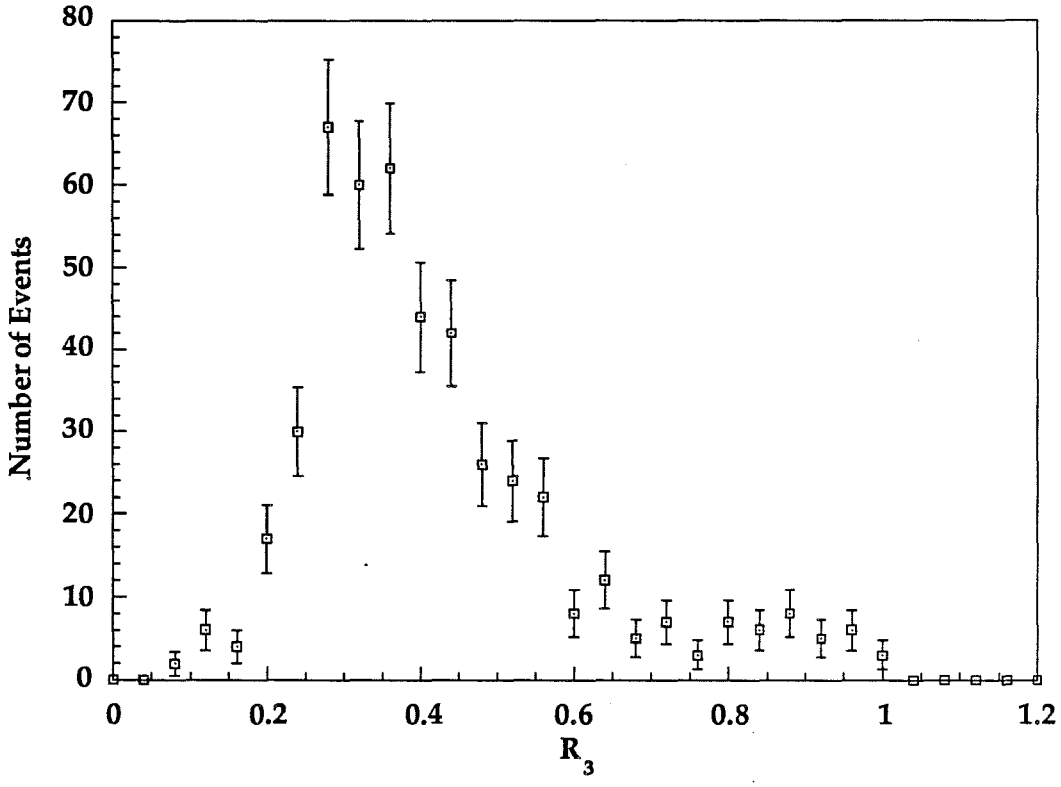

Figure 5.9 The ratio of the energy deposited in the three most upstream counters in the shower to the total energy in the shower, R_3. It is large for electromagnetic showers so events with $R_3 > 0.8$ were removed from the samples.

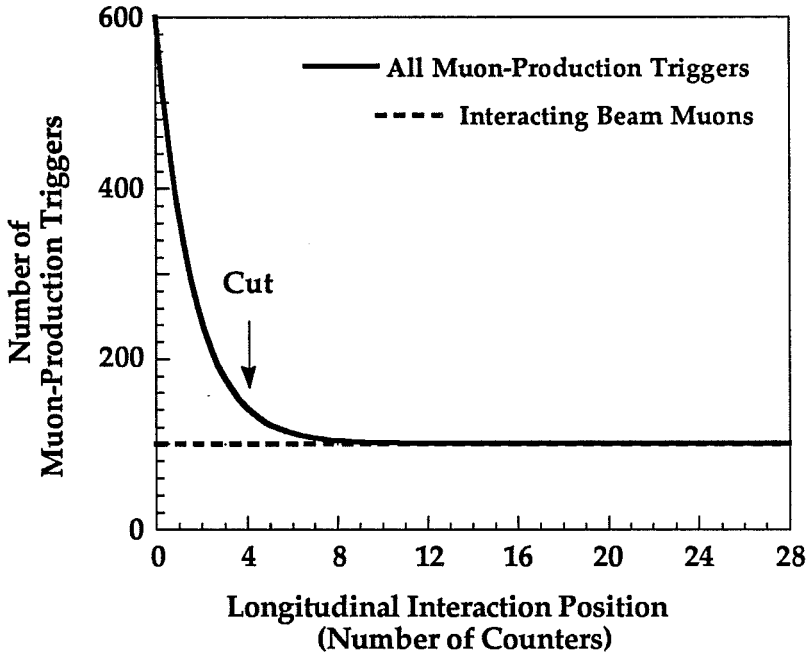

Figure 5.10 An idealized distribution of the longitudinal interaction point of muon-production triggers (solid line) showing the contribution from beam muons (dotted line). The events interacting after 12 counters and before 23 counters are all due to beam muons. Their longitudinal vertex position distribution is extrapolated back to the first two λ_i, equivalent to four counters, to obtain the number of beam muons in the sample of muon-production triggers that passed all cuts.

5.5.3 Muon Selection: $P_\mu > 4.3$ GeV/c

Muons that have less than 9 GeV/c (11 GeV/c) at the beginning of the target lose all their energy before reaching the first toroid gap for the two (three) cart configuration. These muons are called *stubs* or *range-outs*, and their energy is calculated from the range, or length of the track observed in the target calorimeter. The rate of muon-production below 9 GeV was not needed in the same-sign dimuon analysis, because the meson-decay background is too large at lower momentum cuts. However, prompt opposite-sign dimuon production rates were measured with muon momentum above 5 GeV and muon-production rates were needed below 9 GeV for that analysis [54].

Potential stubs were selected from penetration-triggers and hadron-shower triggers. These events were reconstructed as described in Chapter 3 with two exceptions. Some hadron showers contained too many particles at the shower maximum for the TDC buffers to hold, so the FADC's were used to provide the missing hit information. The TDC's and FADC's are described in Chapter 2. The second exception was in the calorimeter tracking. Stubs ranging out with very low momentum at the end of their track undergo relatively large angular deflections due to multiple Coulomb scattering. In order to measure the true length of the track, it was necessary to expand the search for hits downstream of the track found with the standard reconstruction. The end of the original track was extrapolated into the next counter and hits were added if they were within

4.5 cm of the extrapolated track. This corresponds to a two sigma deflection due to multiple Coulomb scattering for a muon momentum equal to that of a minimum ionizing particle.

The final sample of muon stubs were events that passed the above listed cuts as well as the following criteria:

- There must be at least one track in each view, x and y, of the calorimeter.
- Since very short muon tracks can be obscured by the hadron shower, we impose a momentum cut on stubs of 4.3 GeV/c for the two cart configuration or 4.7 GeV/c for the three cart configuration, which corresponds to about 18 scintillation counters or $9\lambda_i$.
- At the longitudinal vertex, the transverse distance between the track and the average beam position must be less than 20 inches. This cut eliminates overlays and cosmic ray events.

Pictures of the stubs were scanned by two physicists independently. There were a few events for which a track was not visible outside the hadron shower. These did not correspond to stubs by our definition, so we counted the number of such events and subtracted them from the stubs sample. About 10 percent were ambiguous, so a corresponding systematic error was assigned to the number of stubs. Table 5.5 gives the number of stubs that were selected and scanned and the number of events that were subtracted because they were found not to be stubs.

Energy (GeV)	P_μ (GeV/c)	Hadron-Shower Triggers			Penetration Triggers		
		total	Stubs	N-	total	Stubs	N-
70	4.3	36×10^3	20	2	15×10^3	61	3
100	4.7	13×10^3	8	0	18×10^3	78	2

Table 5.5 Number of stubs and the number of events removed from the stubs sample that were not true stubs (N-).

5.6 Final Rates

To obtain the correct normalization for $P_\mu > 9$ GeV/c and 11 GeV/c, the number of hadron-shower triggers written to tape must be scaled to give the actual number of incident hadrons interacting in the target. Similarly, to calculate the muon-production rate from the stubs data, the penetration triggers must be scaled separately and combined with the hadron-shower triggers. Finally, to compare the rates to previous measurements, they are corrected for the geometrical acceptance and energy smearing of the detector, using the shower Monte Carlo simulation described in Chapter 6, and the CCFR detector simulation described in Chapter 4.

5.6.1 Raw rates

The final rate for P_μ greater than 9 GeV/c or 11 GeV/c is given by

$$R = \frac{(N_\mu - N_B)}{N_H \, S_H}$$

where N_μ is the number of muon-production triggers passing all cuts, N_B is the number of beam muons remaining after cuts, N_H is the number hadron-shower triggers passing the selection criteria, and S_H is the scale factor given by the ratio of the number of hadron-shower triggers on tape to the total number counted by the scalers.

For P_μ greater than 4.3 GeV/c, or 4.7 GeV/c for three carts, the number of stubs that satisfied the hadron-shower trigger (N_{sH}) and penetration trigger (N_{sP}) were combined after multiplying the number of penetration triggers by the ratio of their scale factors (S_{st}),

$$S_{st} = \frac{S_H}{S_P}$$

where S_P is the scale factor for penetration triggers. The rate is given by:

$$R_{stubs} = (N_{sH} + N_{sP}\, S_{st})/N_H.$$

Tables 5.7a-5.7f give both the differential and integrated rates for positive and negative muons as a function of P_μ for P_μ greater than 9 GeV/c. Table 5.7g gives the rates for $P_\mu > 4.3$ GeV/c.

5.6.2 Acceptance corrected rates

The *acceptance* is the ratio of the number of reconstructed to generated shower Monte Carlo events. The data is divided by the acceptance to give the absolute number of events we would see with a perfectly efficient detector. Figures 5.11a-5.11d show the agreement between the momentum spectrum of the measured muon-production events and the reconstructed shower Monte Carlo events for $P_\mu > 9$ GeV/c. The agreement between the shower Monte Carlo simulation and the data is described in detail in the Chapter 7. For the purposes of the muon-production analysis, a 12 percent systematic error in the acceptance correction is given by the level of agreement between the muon-production data and the shower Monte Carlo.

In the two cart configuration, the acceptance for μ^- events when the toroids focussed μ^- was about 80 percent at 9 GeV/c and increased to about 100 percent above 15 GeV. The acceptance was about 50 percent at 9 GeV/c for μ^- when the toroids focused μ^+, and increased to about 100 percent above 15 GeV/c. Similar acceptances are found for produced μ^+ with the toriods focussing μ^+ and μ^-. All the acceptances are listed in Table 5.6. Note that the acceptance can be greater than one when events generated in one energy bin tend to be reconstructed in a lower energy bin.

Corrected muon-production rates for the toroids focussing μ^+ are consistent with the rate for toroids focussing μ^-. Therefore the rates are averaged, according to a weighted average based on statistics to give the final rate. The raw and corrected rates are given in Tables 5.7a-5.7g. They

fall steeply for beam energies below 70 GeV, and level off above 70 GeV. Calculation of the muon production rates by identified pions and kaons is treated in the same way, except for additional particle identification. Table 5.8 gives the corrected rates by pions and kaons separately. This if the first time the kaon-induced muon-production rate has been measured.

5.7 Comparison to previous measurements

Two experiments measured muon production rates by hadrons at comparable beam energies and muon momenta to those presented here. These are experiment E379 [35], a variable density target calorimeter, and experiment E744 [9]. Experiment E379 took data with negative hadron beams of 40, 75, 150, and 225 GeV. They measured integrated rates with muon momenta greater than 4.26, 8.45, 9.45, 15.45, and 20.45 GeV/c, at two target densities, 6.12 g/cm^3 and 3.06 g/cm^3. To compare our rates with the E379 rates, we interpolated their rates to the density of the CCFR detector, which is 4.18 g/cm^3, assuming that the rates scale with λ_i. We also interpolated their rates to our incident energies and muon momenta, assuming the rates depend exponentially on these variables. Experiment E744 took data with a positive hadron beam at 50 GeV, 100 GeV, and 200 GeV. To compare to these results we assume the rate for $h^- \rightarrow \mu^-$ is the same as the rate for $h^+ \rightarrow \mu^+$. The FMMF collaboration used a sand and steel shot calorimeter instrumented with flash tubes and proportional counters. Table 5.9 gives the results of the comparison, showing that we are consistent with previous measurements.

In conclusion, muon-production rates measured in E770 are consistent with measurements made in previous experiments. Our rates are based on the largest sample of muon-production data yet, which is reflected in the statistical accuracy of the measurements. We have made new measurements with 40 GeV incident hadrons. It is very important to constrain the rates at low hadron energies since the rates fall steeply below about 70 GeV. Furthermore, we have measured muon-production rates by identified pions and kaons at 70 GeV and found that the rate for incident kaons is about 20 percent higher than for pions.

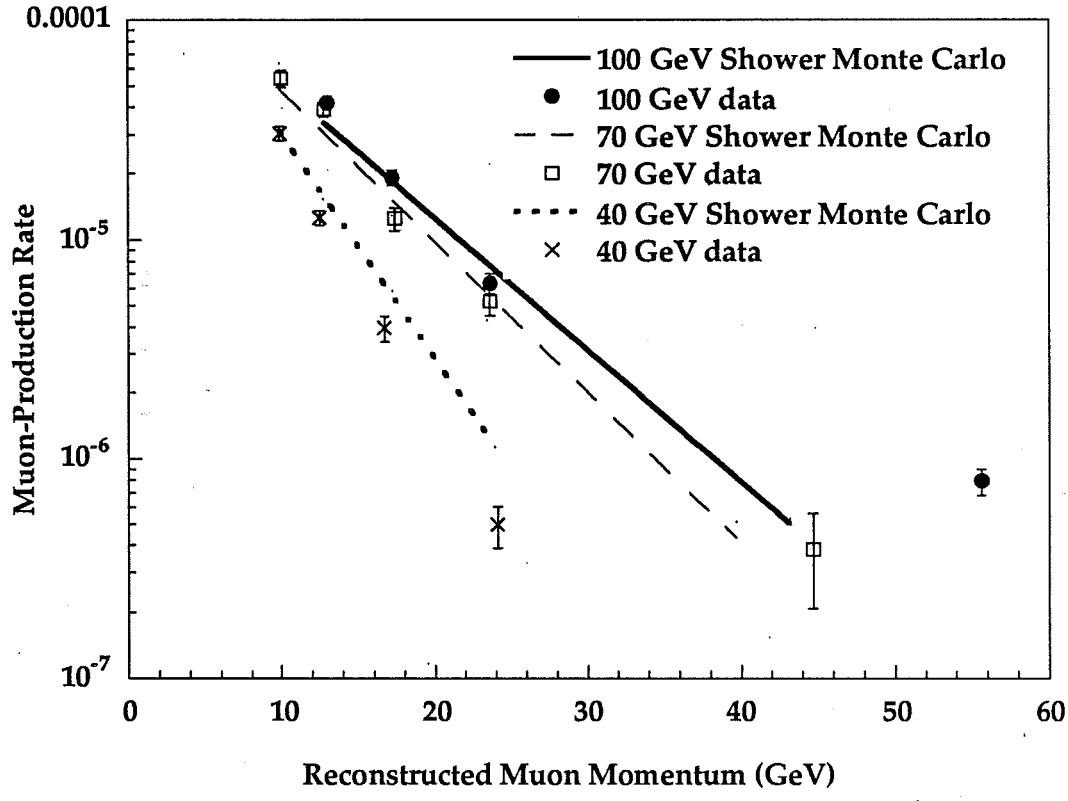

Figure 5.11a Negative muon production rates as a function of muon momentum for toroids focussing μ^-. The data rates have not been corrected for acceptance and smearing and the shower Monte Carlo rates have been propagated through the detector and reconstructed.

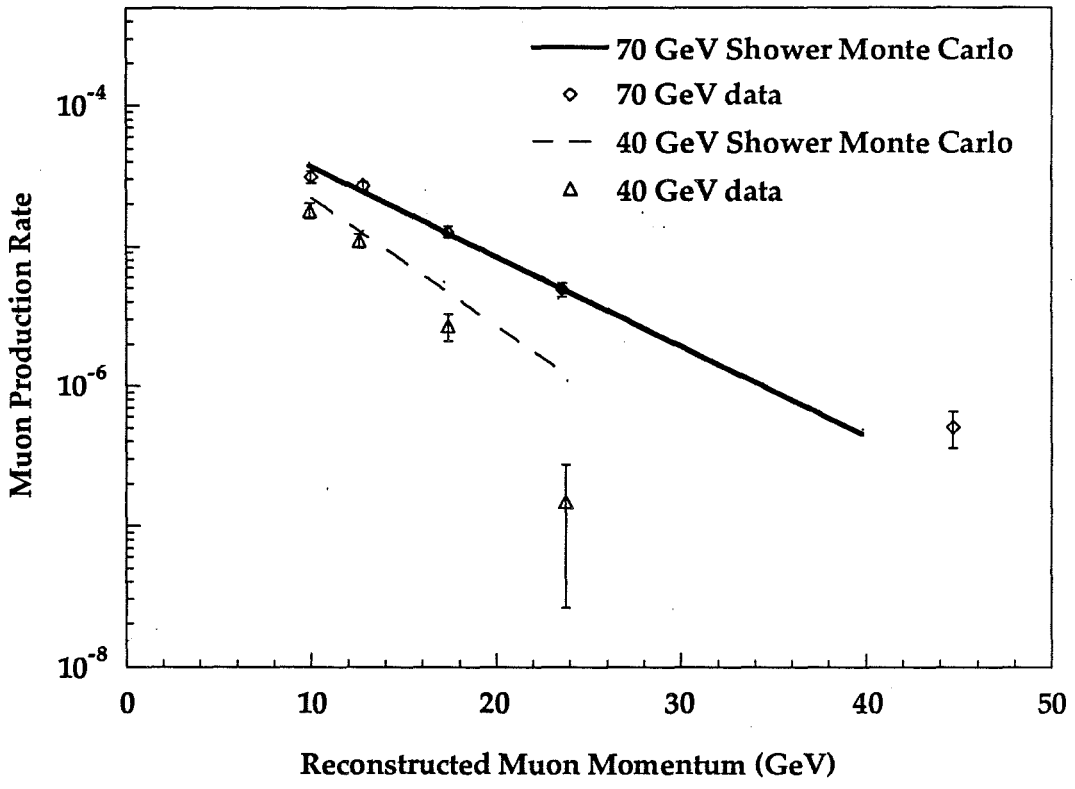

Figure 5.11b Negative muon production rates as a function of muon momentum for toroids focussing μ^+. The data rates have not been corrected for acceptance and smearing and the shower Monte Carlo rates have been propagated through the detector and reconstructed.

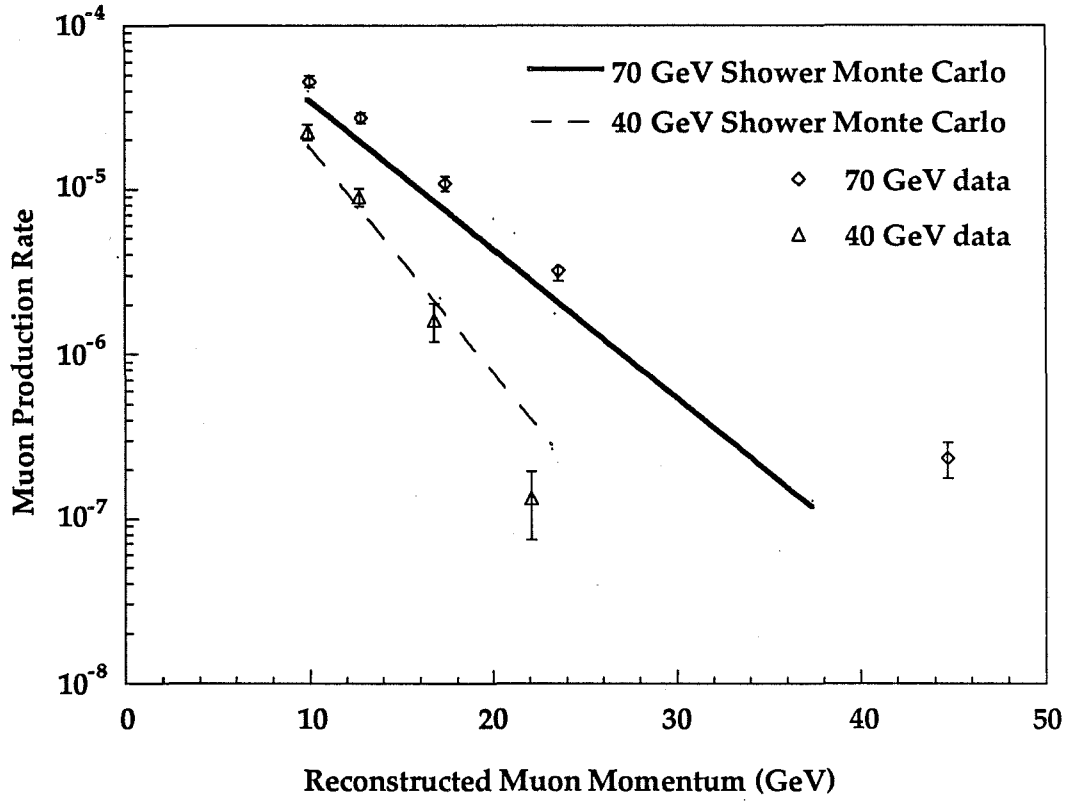

Figure 5.11c Positive muon production rates as a function of muon momentum for toroids focussing μ^+. The data rates have not been corrected for acceptance and smearing and the shower Monte Carlo rates have been propagated through the detector and reconstructed.

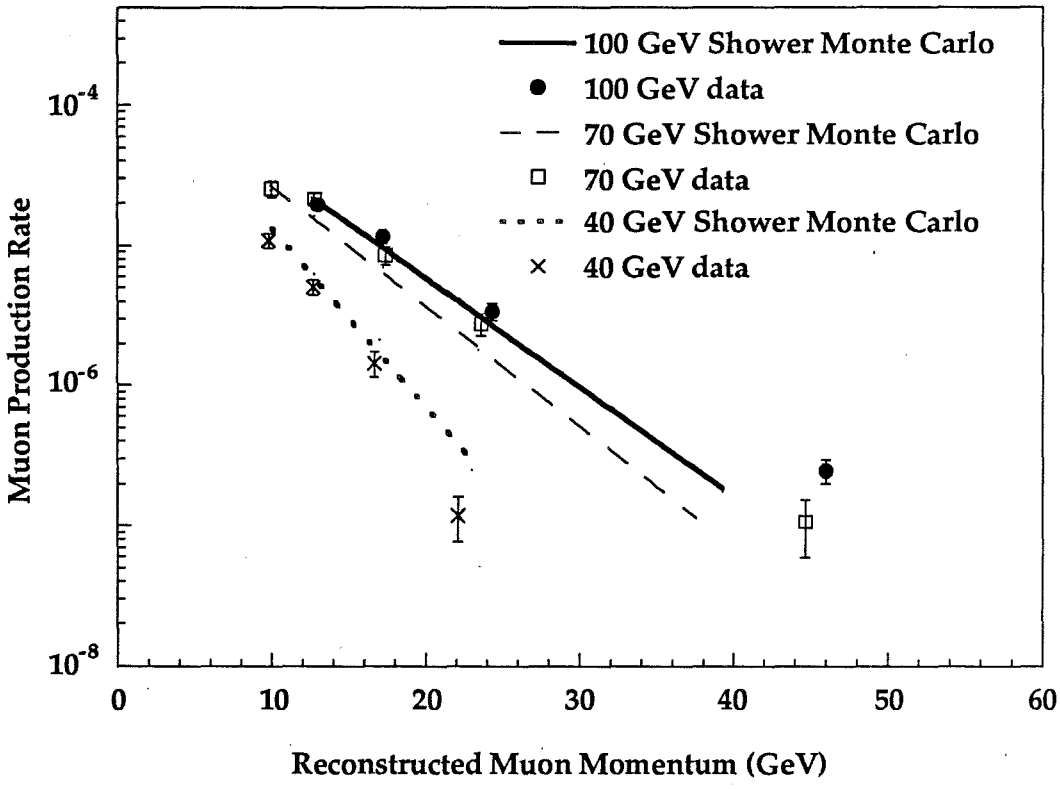

Figure 5.11d Positive muon production rates as a function of muon momentum for toroids focussing μ^-. The data rates have not been corrected for acceptance and smearing and the shower Monte Carlo rates have been propagated through the detector and reconstructed.

Acceptances

40 GeV

P_μ	Focussing $\mu+$		Focussing $\mu-$	
(GeV/c)	$\mu+$	$\mu-$	$\mu+$	$\mu-$
9-11	0.84	0.51	0.52	0.82
11-15	0.98	0.77	0.80	0.89
15-20	1.05	0.94	1.01	1.05
>20	1.11	0.99	1.10	1.03

70 GeV

P_μ	Focussing $\mu+$		Focussing $\mu-$	
(GeV/c)	$\mu+$	$\mu-$	$\mu+$	$\mu-$
9-11	0.85	0.54	0.53	0.83
11-15	0.89	0.75	0.75	0.89
15-20	0.94	0.93	0.93	0.96
20-30	5.03	0.97	0.99	1.01
>30	1.18	0.97	1.03	1.02

100 GeV

P_μ	Focussing $\mu-$	
(GeV/c)	$\mu+$	$\mu-$
9-11	0.12	0.37
11-15	0.61	0.81
15-20	0.83	0.89
20-30	0.94	0.94
>30	1.02	1.02

Table 5.6 Acceptances for the 40 GeV, 70 GeV , and 100 GeV negative beam, for focussing positive and negative muons at 40 and 70 GeV, and negative muons at 100 GeV. The acceptance calculation has a 12 percent systematic error.

Muon Production Rates

40 GeV μ+

P_μ GeV/c	Raw Focus μ+ ($x10^{-4}$)	Raw Focus μ− ($x10^{-4}$)
9-11	0.45 ± 0.05	0.22 ± 0.03
11-15	0.36 ± 0.05	0.20 ± 0.03
15-20	0.08 ± 0.02	0.07 ± 0.02
>20	0.03 ± 0.01	0.02 ± 0.01
>9	0.91 ± 0.07	0.51 ± 0.04
>11	0.47 ± 0.05	0.30 ± 0.03

P_μ GeV/c	Corrected Focus μ+ ($x10^{-4}$)	Corrected Focus μ− ($x10^{-4}$)	Corrected Rate ($x10^{-4}$)
9-11	0.53 ± 0.06	0.42 ± 0.05	0.46 ± 0.03
11-15	0.36 ± 0.04	0.28 ± 0.03	0.29 ± 0.02
15-20	0.08 ± 0.01	0.08 ± 0.01	0.07 ± 0.01
>20	0.012 ± 0.001	0.012 ± 0.001	0.02 ± 0.01
>9	0.98 ± 0.12	0.78 ± 0.09	0.85 ± 0.04
>11	0.45 ± 0.05	0.35 ± 0.04	0.39 ± 0.03

Table 5.7a Muon production rates for μ^+ produced in showers induced by 40 GeV negative hadrons. Raw rates are given for the two configurations of the toroids, focussing μ^+ and focussing μ^-. These rates are corrected for acceptance separately then averaged to give the corrected rate. The errors are statistical, there is an additional 12 percent systematic error on the corrected rates from the acceptance calculation.

Muon Production Rates

40 GeV μ−

P_μ GeV/c	Raw Focus μ− ($x10^{-4}$)	Raw Focus μ+ ($x10^{-4}$)
9-11	0.61 ± 0.04	0.36 ± 0.05
11-15	0.50 ± 0.04	0.44 ± 0.05
15-20	0.20 ± 0.03	0.14± 0.03
>20	0.14 ± 0.03	0.06± 0.03
>9	1.45 ± 0.08	1.00± 0.08
>11	0.84 ± 0.06	0.64 ± 0.03

P_μ GeV/c	Corrected Focus μ− ($x10^{-4}$)	Corrected Focus μ+ ($x10^{-4}$)	Corrected Rate ($x10^{-4}$)
9-11	0.70 ± 0.08	0.74 ± 0.09	0.73 ± 0.04
11-15	0.55 ± 0.07	0.61 ± 0.07	0.57 ± 0.03
15-20	0.14 ± 0.02	0.19 ± 0.02	0.17 ± 0.02
>20	0.010 ± 0.001	0.05 ± 0.01	0.11 ± 0.02
>9	1.39 ± 0.17	1.61 ± 0.19	1.58 ± 0.06
>11	0.70 ± 0.08	0.87 ± 0.10	0.85 ± 0.05

Table 5.7b Muon production rates for μ^- produced in showers induced by 40 GeV negative hadrons. Raw rates are given for the two configurations of the toroids, focussing μ+ and focussing μ−. These rates are corrected for acceptance separately then averaged to give the corrected rate. The errors are statistical, there is an additional 12 percent systematic error on the corrected rates from the acceptance calculation.

Muon Production Rates

70 GeV μ+

P_μ GeV/c	Raw Focus μ+ ($x10^{-4}$)	Raw Focus μ− ($x10^{-4}$)
9-11	0.87 ± 0.07	0.51 ± 0.07
11-15	1.09 ± 0.08	0.85 ± 0.09
15-20	0.54 ± 0.06	0.42 ± 0.06
>20	0.41 ± 0.05	0.33 ± 0.05
>9	2.95 ± 0.14	2.11 ± 0.14
>11	2.04 ± 0.11	1.60 ± 0.12

P_μ GeV/c	Corrected Focus μ+ ($x10^{-4}$)	Corrected Focus μ− ($x10^{-4}$)	Corrected Rate ($x10^{-4}$)
9-11	1.07 ± 0.13	0.95 ± 0.11	1.02 ± 0.06
11-15	1.22 ± 0.15	1.14 ± 0.14	1.19 ± 0.06
15-20	0.58 ± 0.07	0.46 ± 0.06	0.53 ± 0.04
>20	0.40 ± 0.05	0.34 ± 0.04	0.36 ± 0.04
>9	3.27 ± 0.39	2.89 ± 0.35	3.10 ± 0.11
>11	2.20 ± 0.26	1.94 ± 0.23	2.08 ± 0.09

Table 5.7c Muon production rates for μ^+ produced in showers induced by 70 GeV negative hadrons. Raw rates are given for the two configurations of the toroids, focussing μ+ and focussing μ−. These rates are corrected for acceptance separately then averaged to give the corrected rate. The errors are statistical, there is an additional 12 percent systematic error on the corrected rates from the acceptance calculation.

Muon Production Rates

70 GeV μ−

P_μ GeV/c	Raw Focus μ - ($x10^{-4}$)	Raw Focus μ+ ($x10^{-4}$)
9-11	1.09 ± 0.10	0.62 ± 0.06
11-15	1.57 ± 0.12	1.08 ± 0.08
15-20	0.63 ± 0.07	0.63 ± 0.06
>20	0.72 ± 0.10	0.71 ± 0.08
>9	3.99 ± 0.22	3.05 ± 0.15
>11	2.91 ± 0.18	2.42 ± 0.14

P_μ GeV/c	Corrected Focus μ - ($x10^{-4}$)	Corrected Focus μ+ ($x10^{-4}$)	Corrected Rate ($x10^{-4}$)
9-11	1.16 ± 0.14	1.31 ± 0.16	1.22 ± 0.07
11-15	1.43 ± 0.17	1.76 ± 0.21	1.56 ± 0.08
15-20	0.68 ± 0.08	0.65 ± 0.08	0.67 ± 0.05
>20	0.74 ± 0.09	0.71 ± 0.08	0.73 ± 0.07
>9	4.01 ± 0.48	4.43 ± 0.53	4.19 ± 0.14
>11	2.85 ± 0.34	3.12 ± 0.37	2.96 ± 0.12

Table 5.7d Muon production rates for μ− produced in showers induced by 70 GeV negative hadrons. Raw rates are given for the two configurations of the toroids, focussing μ+ and focussing μ−. These rates are corrected for acceptance separately then averaged to give the corrected rate. The errors are statistical, there is an additional 12 percent systematic error on the corrected rates from the acceptance calculation.

Muon Production Rates

100 GeV μ^+

P_μ (GeV/c)	Focus $\mu-$ ($\times 10^{-4}$)	Corrected Rate ($\times 10^{-4}$)
11-15	0.78 ± 0.07	1.27 ± 0.09
15-20	0.58 ± 0.07	0.69 ± 0.07
20-30	0.34 ± 0.05	0.36 ± 0.05
>30	0.17 ± 0.03	0.17 ± 0.03
>11	1.86 ± 0.11	2.49 ± 0.14

100 GeV μ^-

P_μ (GeV/c)	Focus $\mu-$ ($\times 10^{-4}$)	Corrected Rate ($\times 10^{-4}$)
11-15	1.68 ± 0.11	2.07 ± 0.12
15-20	0.96 ± 0.06	1.08 ± 0.08
20-30	0.63 ± 0.06	0.68 ± 0.07
>30	0.55 ± 0.08	0.54 ± 0.07
>11	3.83 ± 0.19	4.41 ± 0.20

Table 5.7e and 5.7f Muon production rates for μ^+ (top) and μ^- (bottom) produced in showers induced by 100 GeV negative hadrons. Raw rates are given for focussing $\mu-$. These rates are corrected for acceptance separately then averaged to give the corrected rate. The errors are statistical, there is an additional 12 percent systematic error on the corrected rates from the acceptance calculation.

Stubs Rate

E_{beam} (GeV)	P_μ (GeV/c)	Raw Rate ($x10^{-4}$)	Corrected Rate ($x10^{-4}$)
70	> 4.3	23.09 ± 2.8	24.3 ± 2.9
100	> 4.7	31.1 ± 5.4	32.1 ± 5.6

Table 5.7g Stubs muon production rates for μ^+ and μ^- together for 70 GeV and 100 GeV negative hadrons. The errors are statistical. There is a 12 percent systematic error in the corrected rates from the calculation of the acceptance.

Identified Pion and Kaon Rates

Particle Type	Acceptance Corrected rate ($x10^{-4}$)
π	$4.08 \pm 0.11 \pm 0.49$
k	$5.18 \pm 0.42 \pm 0.62$

Table 5.8 Acceptance corrected muon-production rates for 70 GeV $\pi-$ and k^- separately with P_μ>9 GeV. The first error is statistical. The second error is a systematic error that includes the error of the particle identification and the error of the acceptance correction.

Comparison to Previous Experiments

Energy (GeV)	P_μ (GeV/c)	This Experiment	Other Measurement	Source
70	4.3	$24.3 \pm 2.9 \pm 2.9$	$22.8 \pm 1.4 \pm 4.6$	E379
100	4.7	$32.1 \pm 5.6 \pm 3.9$	$35.5 \pm 1.8 \pm 7.1$	E379
40	9.0	$2.42 \pm 0.07 \pm 0.29$	$2.19 \pm 0.40 \pm 0.40$	E379
70	9.0	$7.29 \pm 0.17 \pm 0.87$	$6.39 \pm 0.40 \pm 1.28$	E744
100	11.0	$6.90 \pm 0.25 \pm 0.83$	$5.98 \pm 0.30 \pm 0.48$	E744

Table 5.9 Comparison of muon production rates measured in this experiment to results of experiments E379 and E744. The first error is statistical and the second is a systematic error associated with the acceptance correction.

Chapter 6

Simulation of the Muon Production Rate by Showering Hadrons

6.1 Introduction

The previous chapter described our measurement of the muon-production rate by showering hadrons. This chapter presents the corresponding shower Monte Carlo simulation of the incident hadron interaction, the subsequent shower, and muon production. To accurately model fragmentation in iron, we used the measured muon-production rates to set the level of muon-production in the shower simulation. In this way, the shower simulation extended the muon-production data over the full range of hadron energies. In addition, we used the shower simulation to extract the raw muon-production rates from the measurements.

The shower Monte Carlo simulation is based on the Lund Monte Carlo routine LULOPT from JETSET version 6.2 that models hadronic fragmentation [25]. Since LULOPT simulates interactions of hadrons with free protons and neutrons, rather than heavy materials like iron, we employed a two step reweighting procedure to apply the LULOPT fragmentation model to our iron target. In the first step, we reweight generated neutrino interactions with free protons to agree with fragmentation data from pion-carbon interactions. There is no applicable data on fragmentation in heavier materials than carbon so we use a parametrization of the atomic-number dependence of the total cross section

for inelastic hadron scattering to reweight events to interactions with iron. There are uncertainties in this process, but by constraining the shower Monte Carlo simulation to agree with our muon-production measurements, the predictions of the simulation are independent of the reweighting procedure and the model in LULOPT. This chapter describes our use of LULOPT, the reweighting procedure, and setting the shower Monte Carlo simulation to match our muon-production data.

6.2 Lund Fragmentation

The Lund group developed the model called *string fragmentation* in which quarks connected by color force lines behave like particles connected by a string under a constant tension of about 0.2 GeV^2 [36]. The quarks oscillate back and forth, crossing one another. A massless $q\,\bar{q}$ pair may be formed at any place along the string and heavy quark pairs may be produced at points along the string where the energy stored in the string is large enough. In either case the string splits into two independent systems oscillating back and forth, which also may create new pairs. If more than two quark pairs are formed along the string, a quark from one pair may team up with another quark pair to form a baryon.

6.3 Mechanics of the Hadron Shower Simulation

The simulation of hadron-induced showers in the detector starts by calling LULOPT to interact the incident hadron. LULOPT is again called to interact each secondary hadron produced, and again to interact each subsequent hadron. This procedure is followed for every generation of the shower until the energy of the hadron falls below 2.0 GeV. Since the hadrons

may decay before interacting, a weight is assigned to each product of the hadrons based on the probability for them to decay. When a primary hadron decays before interacting, it is called the vertex background and is treated separately in Chapter 7. The interaction and decay probabilities of each hadron species are given in appendix A.

6.4 Nuclear Reweighting

Since the Lund program LULOPT, is intended to simulate interactions with free neutrons and protons, a two step reweighting procedure was used to adapt LULOPT to an iron target. In the first step, generated events are reweighted to agree with hadron-carbon fragmentation data obtained with the Serpukov bubble chamber [37].

The Serpukov bubble chamber, filled with propane (C_3H_8), was exposed to a π^- beam at 40 GeV. The relative probabilities for $\pi^- C \rightarrow h^\pm$, $\pi^- p \rightarrow h^\pm$, and $\pi^- n \rightarrow h^\pm$ are used to reweight the free nucleon LULOPT fragmentation to carbon. The Serpukov experiment did not distinguish final state particles. However, it is necessary to understand nuclear effects on the fraction of kaons in hadron fragmentation. This is because there are two competing effects that make kaon fragmentation different than pion fragmentation. Kaons are less likely to decay to a muon than pions, but their mean lifetime is shorter. Furthermore, some of the original strangeness is passed to successive generations of the shower so that kaon-induced showers are more likely to contain secondary kaons than pion-induced showers. To eliminate the uncertainty in kaon-induced fragmentation and fragmentation into kaons, we use our kaon-induced muon-production data to set the level of kaon-

induced muon-production in the shower Monte Carlo simulation. This is described in Section 6.5.

To reweight fragmentation from carbon to iron, we use the Busza parametrization that scales cross sections for particle production as a function of both A and x_f, the atomic weight and the Feynman scaling variable [38]. The parametrization, which is a fit to the world fragmentation data, is given by

$$\left[\frac{d\sigma}{dx_f}\right]_A = A^{a(x_f)} \left[\frac{d\sigma}{dx_f}\right]_0$$

The form of the exponent is

$$a(x_f) = 0.76 - 0.55\,x_f + 0.26\,x_f^2 \qquad \text{for protons,}$$

$$a(x_f) = 0.81 - 0.55\,x_f + 0.26\,x_f^2 \qquad \text{for pions.}$$

There is about a 20 percent variation between the extremes of the world data when $a(x_f)$ is plotted as a function of x_f. Later we will see that the shower Monte Carlo rates require fine tuning as functions of the incident energy and muon momentum to match the muon-production data, which can be understood in terms of this uncertainty in $a(x_f)$.

6.5 Setting the Kaon Fraction

There are two uncertainties involving kaons. One is a 20% uncertainty in fragmentation by showering kaons [9] and the other is the level of fragmentation into kaons, since the Serpukov propane bubble chamber did not distinguish final states. These uncertainties are eliminated with our measurement of the muon production rate by showering 70 GeV kaons and pions separately in our target, described in Chapter 5. The shower Monte Carlo was adjusted to agree with these rates by varying the fraction of kaons produced in kaon-induced showers (f_K) and the fraction of kaons produced in pion-induced showers (f_π).

Figures 6.1a and 6.1b show how the rates depend on these factors. The pion rate is a slowly varying function of f_π, whereas the kaon rate is more sensitive to f_K. The final values that agree with the muon-production data are $f_K = 0.73 \pm 0.20$ and $f_\pi = 1.45 \pm 0.25$. The errors span the allowed values given by the uncertainty in the data. For comparison, the shower Monte Carlo rates with $f_K = 1$ and $f_\pi = 1$, with f_K and f_π set to the above values, and the measured muon-production rates for identified pions and kaons are given in Table 6.1. The pion rate from the shower Monte Carlo simulation did not change much. This was expected, since the data used to reweight the shower Monte Carlo was mostly from pions. The kaon rate from the unadjusted shower Monte Carlo simulation was about 15 ± 2 percent higher than the measured muon-production rate. The rate for incident kaons is larger than the rate for incident pions. There are two possible causes of this: higher multiplicities of decaying mesons in kaon-induced showers than pion-

induced showers and the shorter lifetime of kaons with respect to pions. The latter leads to a higher muon-production rate since kaons will decay before interacting more often than pions.

70 GeV Hadrons	Acceptance Corrected Data ($\times 10^{-4}$)	Shower Monte Carlo ($\times 10^{-4}$) ($f_k = 1.0, f_\pi = 1.0$)	Shower Monte Carlo ($\times 10^{-4}$) ($f_k = 0.73, f_\pi = 1.45$)
π	$4.08 \pm 0.11 \pm 0.20$	3.91 ± 0.14	3.98 ± 0.11
k	$5.18 \pm 0.42 \pm 0.38$	5.98 ± 0.31	5.09 ± 0.15
k/π	$1.26 \pm 0.11 \pm 0.11$	1.52 ± 0.09	1.27 ± 0.05

Table 6.1 Muon-production rates per incident 70 GeV π^- or K^- for produced muon momenta greater than 9 GeV/c at the vertex. The first error is statistical and the second is the systematic error from the particle identification.

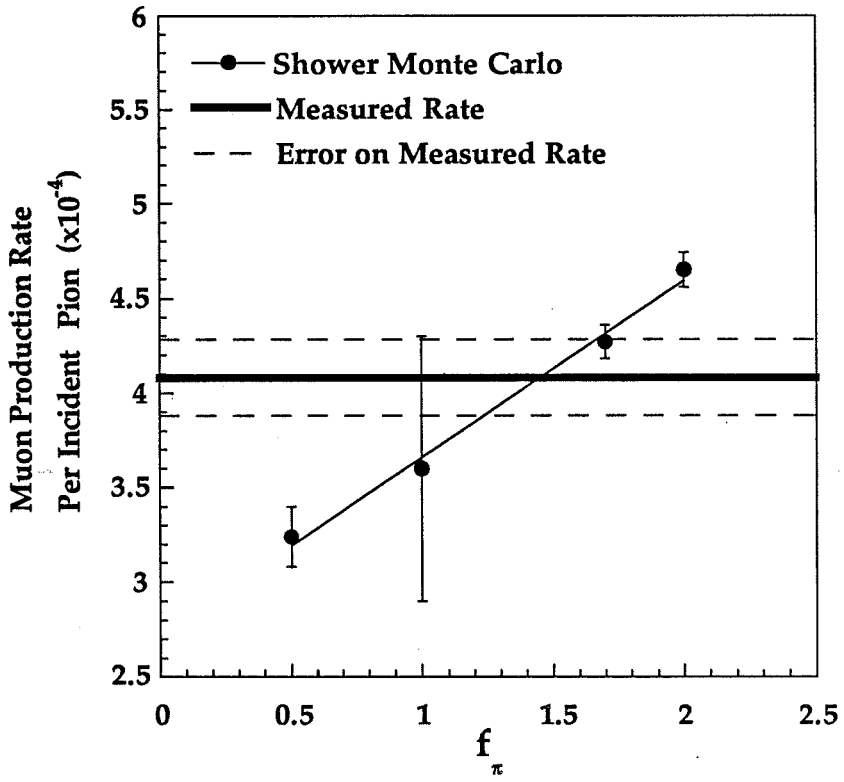

Figure 6.1a Muon production rates for incident negative pions of 70 GeV as a function of f_π, the fraction of kaons in pion-induced showers. The solid dots give the muon-production rate for pion primaries predicted by the shower Monte Carlo. The dark line gives the measured muon-production rate for pion primaries. The dashed lines give the limits of the muon-production rate allowed by the uncertainty in the measurement. The error on the points is statistical.

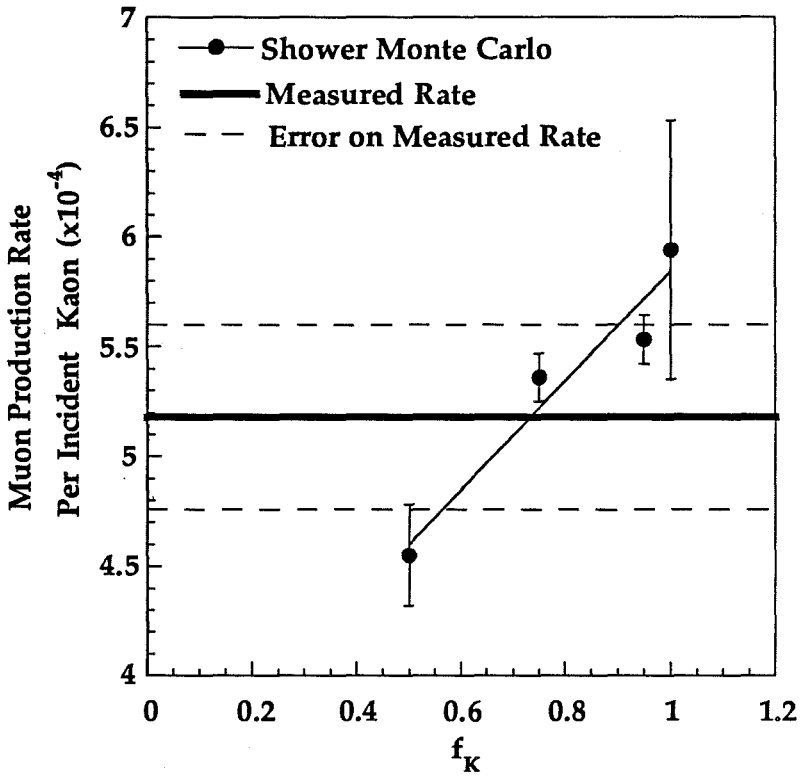

Figure 6.1b Muon production rates for incident negative kaons of 70 GeV as a function of f_K, the fraction of kaons in kaon-induced showers. The solid dots give the muon-production rate for kaon primaries predicted by the shower Monte Carlo. The dark line gives the measured muon-production rate for kaon primaries. The dashed lines give the limits of the muon-production rate allowed by the uncertainty in the measurement. The error on the points is statistical.

6.6 The Final Shower Monte Carlo Simulation

This section describes the process of matching the shower Monte Carlo rates to the measured muon-production rates that were presented in Chapter 5. By reproducing the muon-production data with the shower Monte Carlo simulation, the calculation is independent of the underlying model and we are limited only by the statistical power of the muon-production data used to determine the shower Monte Carlo simulation.

The events generated with the shower Monte Carlo were propagated through the detector, reconstructed and compared with the muon-production data. The procedure for reweighting from a free proton target to iron resulted in an overall reduction in the rates on the order of 20 percent [9]. After comparing to the measured rates, the reweighted shower Monte Carlo rates at lower hadron energy needed to be reduced further. For example, the shower Monte Carlo muon-production rates were up to $(30 \pm 6)\%$ higher than the data rates. Furthermore, the difference between the data and the shower Monte Carlo was a function of the muon momentum at the event vertex (P_μ). Figures 5.11a-5.11d gives the differential spectrum of the reconstructed muon momentum for the data and the shower Monte Carlo. At 40 GeV, the Monte Carlo rates are too high up to $(30 \pm 6)\%$, and the slope falls too slowly. At 100 GeV the opposite is true; the rates are slightly low by about $(10 \pm 5)\%$ and the slope is too high.

We fit a function, called $f(P_g, E_h)$, to the ratio of the reconstructed shower Monte Carlo rates to the measured muon-production rates $R(P_g, E_h)$,

for μ^+ and μ^- separately as a function of incident hadron energy (E_h) and average generated muon momentum in bins of reconstructed muon momentum at the vertex, P_g. The value of P_g for each reconstructed momentum bin was determined from the shower Monte Carlo simulation. The fit function, $f(P_g, E_h)$, multiplied the weights of the generated muons to match the shower Monte Carlo simulation to the measured rates. To constrain the fit at energies above 100 GeV, which is the highest energy data point, we included a point at 200 GeV from experiment E744 [9]. This data was taken directly from reference 9 in which the muon-production rates were corrected for detector acceptance. At 200 GeV, the muon-production data was compared to the generated shower Monte Carlo rates. Since both the shower Monte Carlo and data events were reconstructed in the detector in the same manner, the rates with the toroids set to focus negative muons and positive muons were averaged for the fit. The measured muon-production rates are given in Chapter 5 for focussing negative muons and positive muons separately. At 100 GeV, only data with toroids focussing negative muons was available. Since our understanding of the acceptance is good as shown in Section 5.6.2, then this does not introduce any bias.

The function $f(P_g, E_h)$ that best describes $R(P_g, E_h)$ is given by,

$$f(P_g, E_h) = A\, e^{-B z}$$

$$z = \frac{P_g}{E_h}$$

$$A = a + b \log\left(\frac{E_h}{10}\right) + c \left(\frac{E_h}{10}\right)^2$$

$$B = d + e \log\left(\frac{E_h}{10}\right) + f \frac{E_h}{10}$$

The parameters a, b, c, d, e, and f are given in Table 6.6. In regions where data was lacking, the function was set to the value at the closest measured point. For example, $f(P_g, E_h)$ for P_g greater than 40 GeV is set to $f(40\ \text{GeV}, E_h)$. The function $f(P_g, E_h)$ is plotted in Figure 6.2 as a function of the incident hadron energy for various muon momenta. Table 6.3 gives the ratio of the data to the Monte Carlo muon-production rates per incident hadron before and after the function $f(P_g, E_h)$ was applied. A point at 50 GeV from experiment E744, which was not included in the fit, is given in the table as a check of the procedure. The fit has improved the agreement between the muon-production data and the shower Monte Carlo at all hadron energies and muon momenta. Figure 6.3 shows the resulting ratios of the shower Monte Carlo simulation to the measured muon-production rates.

Polarity	a	b	c	d	e	f
μ^+	-0.3910	0.7676	-0.00268	-11.580	10.007	-0.9814
μ^-	0.5064	0.2377	0.0	-5.4049	3.5902	-0.2044

Table 6.2 Parameters used in the function $f(P_g, E_h)$ that characterizes the ratio of the Monte Carlo to the data muon-production rates per incident hadron.

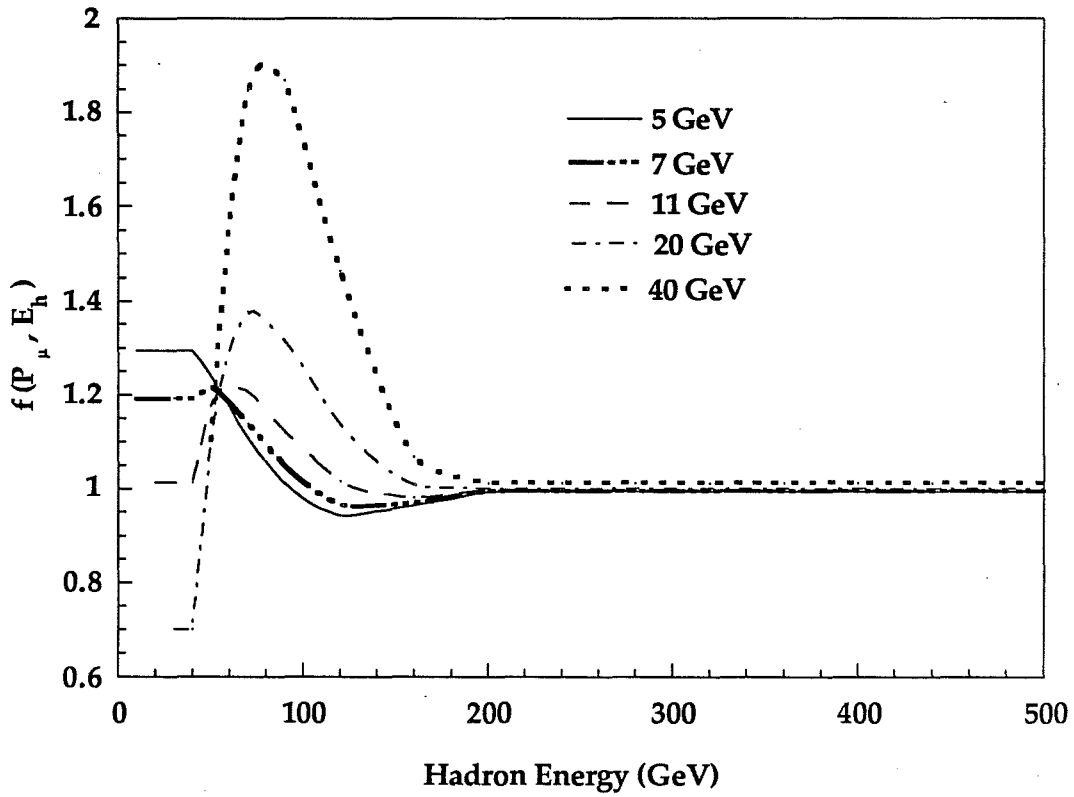

Figure 6.2a The function $f(P_g, E_h)$ that characterizes the ratio of the shower Monte Carlo to the measured muon-production rates per incident hadron as a function of incident hadron energy for μ^+-production by negative hadrons. The function is shown for various generated muon momenta.

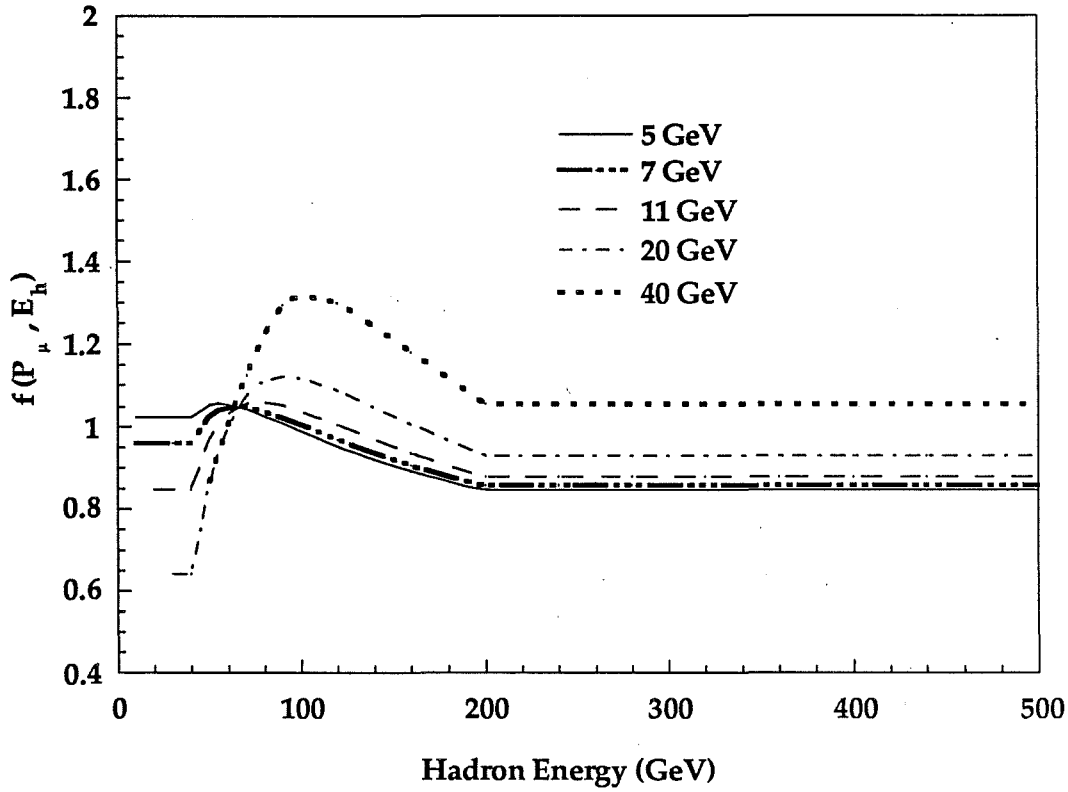

Figure 6.2b The function $f(P_g, E_h)$ that characterizes the ratio of the shower Monte Carlo to the measured muon-production rates per incident hadron as a function of incident hadron energy for μ^--production by negative hadrons. The function is shown for various generated muon momenta.

Ratio of Shower Monte Carlo to Data Rates

Beam Energy (GeV)	P_μ (GeV)	Muon Type	Included in Fit	Initial Ratio	multiplied by $f(P_g, E_h)$
- 40	>9	$+\mu$	√	1.02 ± 0.06	1.05 ± 0.07
- 40	>9	$-\mu$	√	1.31± 0.06	1.10 ± 0.06
+ 50	>11	$+\mu$		0.90 ± 0.10	1.03 ± 0.11
+ 50	>11	$-\mu$		1.17 ± 0.21	1.07 ± 0.19
- 70	5.8	$+\mu,-\mu$	√	0.88 ± 0.13	0.97±0.14
- 70	>9	$+\mu$	√	0.77 ± 0.04	0.94 ± 0.04
- 70	>9	$-\mu$	√	0.97 ± 0.05	1.05 ± 0.04
- 100	6.5	$+\mu,-\mu$	√	1.01 ± 0.21	0.98±0.21
- 100	>11	$+\mu$	√	1.08 ± 0.15	1.10 ± 0.07
- 100	>11	$-\mu$	√	0.90 ± 0.05	1.03 ± 0.06
+200	>11	$+\mu$	√	0.93 ± 0.06	0.93 ± 0.06
+ 200	>11	$-\mu$	√	1.07 ± 0.06	1.01 ± 0.06

Table 6.3 The ratio of the Monte Carlo to the data muon-production rates per incident hadron before and after applying the function $f(P_g, E_h)$ as described in the text. The errors are statistical.

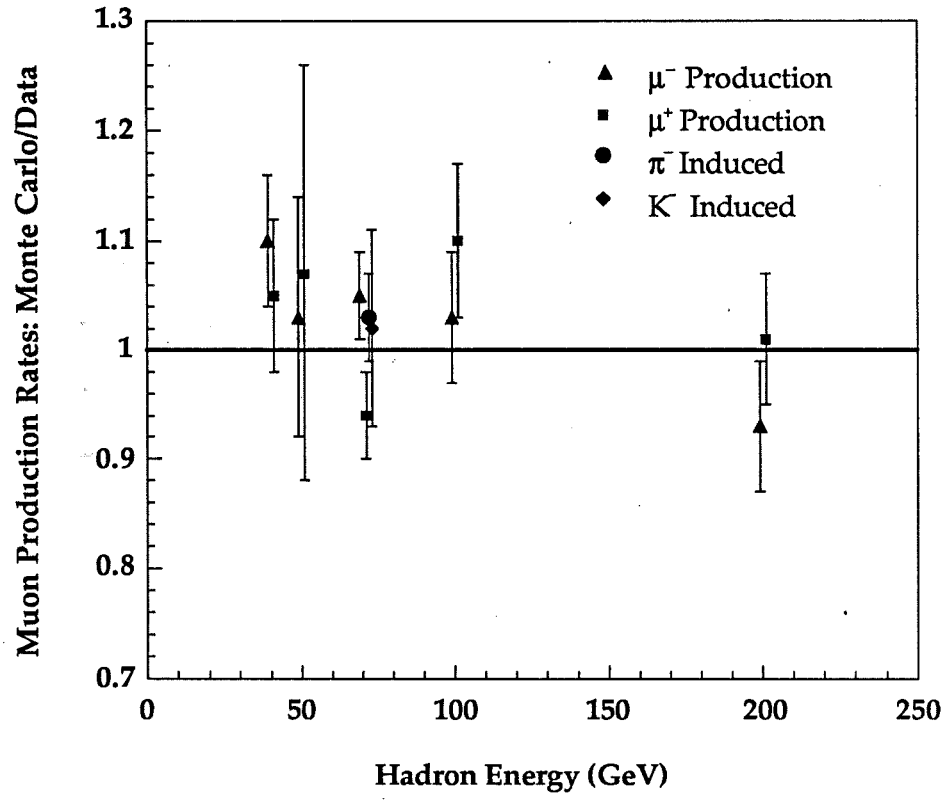

Figure 6.3 Ratio of the adjusted shower Monte Carlo to the data muon-production rates as a function of hadron energy for muon momenta greater than 9 GeV/c. At 50 GeV and 200 GeV, the beam was positive composed of positive hadrons. At all other energies the beam was negative. The results from the tagged beam at 70 GeV are also shown with μ^+ and μ^- combined.

6.7 Systematic errors

The systematic uncertainty of the shower Monte Carlo simulation is determined by the agreement with the test beam measurements used to set the simulation and the accuracy of the measurement. Overall, the final shower Monte Carlo rates agree with the measured muon-production rates within 10%. Concerning the calculation at incident hadron energies less than 40 GeV where we did not take data, we note that primary hadrons less than 40 GeV in neutrino-nucleon interactions have an average hadron energy of about 30 GeV. Therefore, the uncertainty in the extrapolation below 40 GeV was determined by the level of agreement between Monte Carlo and data at 40, 50 and 70 GeV, which is also within 10%.

The level of muon production by showering kaons was unknown in the previous experiment, E744 [9]. This source of uncertainty has been eliminated with our measurement of the rate of muon production by identified kaons in the hadron beam. Furthermore, the lowest incident hadron energy measured in that experiment was 50 GeV. This is problematic since the probability begins to drop steeply at energies below 50 GeV. This new measurement at 40 GeV renders the extrapolation to lower energies more reliable. By tuning the Monte Carlo to our comprehensive data measurements we have reduced the uncertainty in the shower component of the background from 15 percent in E744 to 10 percent in E770.

Chapter 7

Total Meson Decay Background

7.1 Introduction

Primary hadrons produced at the interaction vertex by fragmenting quarks in neutrino-deep-inelastic scattering may produce muons by decaying. This is called the *vertex background,* depicted in Figure 1.4. When the primary hadrons interact before decaying, they create secondary hadrons which may decay to muons or produce subsequent hadrons that decay to muons. This is called the *shower background* depicted in Figure 1.3. The contribution from the vertex component is more than two times larger than the shower contribution. Taken together they comprise the largest source of background and account for about 94% of the same sign dimuon signal.

The final background due to meson decays is calculated with our meson decay background Monte Carlo simulation. This is the charged-current Monte Carlo simulation described in Chapter 4, used with parametrizations of the probability to get a second muon from a vertex decay or a shower decay.

The parametrizations are obtained from a separate simulation. The Neutrino-Lund Monte Carlo is used to simulate electroweak fragmentation at the vertex of the neutrino interaction and subsequent muon production from meson decays. Neutrino-Lund is based on the

LEPTOLUND simulation developed by the Lund group [25]. Unlike hadron fragmentation simulated by the shower Monte Carlo, electroweak fragmentation is not expected to depend heavily on the nuclear composition of the target. This is because the W boson exchanged in a charged-current interaction couples weakly to matter. Neutrino-Lund generates a neutrino interaction at a specified x_{Bj}, y_{Bj} and hadron energy (E_h), forming primary hadrons and the primary muon. To simulate the vertex background, it immediately decays the primary hadrons. To simulate the shower background, the primary hadrons are interacted with the shower Monte Carlo simulation that is described in Chapter 6.

The generated dimuon events from the meson decay Monte Carlo simulation are propagated through the detector with the CCFR detector simulation and are reconstructed in the same manner as the data. The result is the total number of same-sign dimuons expected in our detector due to the meson decay background.

7.2 Electroweak Lund Fragmentation

To ensure that the Lund electroweak fragmentation model agrees specifically with neutrino scattering data, two of the Lund default parameters have been changed; the hadron energy cut-off (E_{min}) below which quark-antiquark pairs are no longer produced, and the strangeness suppression factor (λ_s) governing the relative probability for a strange quark to be pulled out of the sea. We have set λ_s at 0.2 down from the default value of 0.3. This modification puts Lund kaon fragmentation functions in better agreement with those obtained in ν-proton scattering

measured by the BEBC bubble chamber experiment [39,40]. The decrease in the background due to this modification is about 5%. The same experiment found better agreement between Lund and their data by changing E_{min} from 1.0 GeV to 0.2 GeV. However, the effect of modifying E_{min} was less than 1%. The effects of changing these parameters are included in the systematic error of the calculation.

7.3 Parametrization of the Shower Background

This section presents parametrizations of the Neutrino-Lund simulation for the shower background, which characterize the probability to produce a second muon from secondary hadrons in the hadron shower of the charged-current event. The parametrizations are extracted as a function of the hadron energy of the underlying charged-current event (E_h), the momentum of the shower muon corrected back to the vertex (P_μ), and x_{Bj} of the charged-current event.

The full shower background simulation was run at 9 incident neutrino energies: 20 GeV, 40 GeV, 80 GeV, 140 GeV, 200 GeV, 300 GeV, 400 GeV, 600 GeV, and 1000 GeV, with x_{Bj} equal to 0.2, 0.5, and 0.65, y_{Bj} set at 0.5, and P_μ greater than 4 GeV/c. Enough events were generated for better than 1% statistical accuracy on the integral probability with P_μ greater than 4 GeV/c.

The form of the fit to the shower background probability is given by,

$$\frac{dP}{dP_\mu} = \left(\frac{A_1}{P_\mu}\right)^{A_2} e^{-(A_3 z)} \{1 - z\}^2 \{A_4 + A_5 x\}^{A_6}$$

where dP is the probability to produce a muon with momentum between P_μ and $P_\mu + dP_\mu$, $z=E_\mu/E_h$ is the fraction of hadron energy carried by the second muon, and the parameters A_i are expanded in terms of E_h as follows,

$$A_i = a_{i1} + a_{i2} \log\left(\frac{E_h}{30}\right) + a_{i3} \log^2\left(\frac{E_h}{30}\right)$$

Table 7.1 gives the parameters a_{ij} for the two cases, μ^--production and μ^+-production in neutrino-induced events, which are the same-sign and opposite sign backgrounds respectively. The corresponding parameters for incident anti-neutrinos are given by reversing the muon sign. The integral over P_μ of dP/dP_μ for the same-sign background is plotted for various lower limits of P_μ in Figure 7.1, which also shows two previous background calculations. The solid curve gives the integral over P_μ of the parametrization of dP/dP_μ used in the published result of E744 [9] which is also based on the shower Monte Carlo simulation but was tuned to a limited data set as explained in Chapter 6. The dashed curve is the integral of an alternative parametrization of dP/dP_μ which was calculated by Bachmann in experiment E744 [14]. It is based on a compilation of muon-production data from various sources. The new background calculation, which was tuned to a larger sample of muon-production data measured in our detector with $P_\mu > 4$ GeV/c, lies between the two. The parametrization of reference 9 was limited to $P_\mu > 11$ GeV/c. The uncertainty in the new

parametrization of dP/dP_μ is 2 percent, due to the statistical accuracy of the shower background Monte Carlo simulation and the goodness of the fit to the shower background simulation.

Same Sign

A_i	a_{i1}	a_{i2}	a_{i3}
A_1	1.3604	-0.09049	0.0
A_2	3.7356	-0.24801	0.0
A_3	3.4547	-0.75553	0.0
A_4	5.5783	1.8321	0.3805
A_5	-0.40785	-0.10043	0.0
A_6	2.95	-0.02936	0.0

Opposite Sign

A_i	a_{i1}	a_{i2}	a_{i3}
A_1	1.3202	-0.066711	0.0
A_2	3.5760	-0.17988	0.0
A_3	2.5395	-0.73275	0.0
A_4	5.8676	1.7100	0.45437
A_5	0.25836	-0.42538	0.0
A_6	2.8424	0.00947	0.0

Tables 7.1 The top table gives the parameters used in the fit to the shower background of same-sign dimuon production and the bottom table for opposite-sign dimuon production.

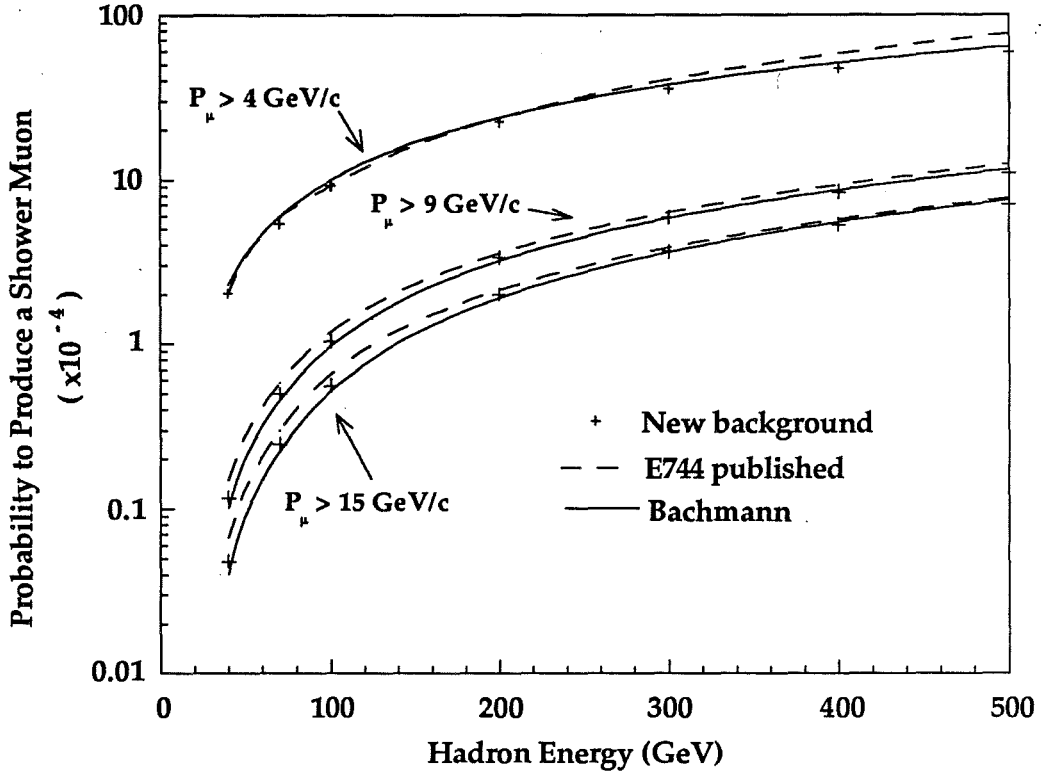

Figure 7.1 The integral over P_μ of the parametrization of dP/dP_μ, the probability to produce a shower background muon contributing to same-sign dimuon production as a function of hadron energy for momentum between P_μ and $P_\mu + dP_\mu$. The crosses give the integral of the parametrization presented in this thesis. The dashed curve gives the integral of a previous parametrization of E744 [9], and the solid curve gives the integral of the parametrization by Bachmann [14].

7.4 Vertex Decay Background

The parametrization of the probability to produce a muon from the decay of a primary hadron produced in neutrino charged-current events, called the vertex decay background, is the same as that used in experiment E744 [9] and is described in appendix B. Briefly, primary hadrons generated by Neutrino-Lund are decayed according to the decay parameters in appendix A and the probability to produce a vertex background event is parametrized as a function of E_h, x_{Bj}, and E_ν.

7.5 Full Meson Decay Background Calculation

Same-sign dimuon events are generated with the charged-current Monte Carlo simulation along with the parametrizations of the probability to produce a second muon from meson decay. The variables x_{BJ}, y_{BJ} and the total energy of the charged-current events are given by the charged-current Monte Carlo simulation. The momentum of the second muon is generated with $P_\mu > 7.5$ GeV/c using the parametrizations given above and the events are weighted by the probability to produce the decay muon. Missing energy in the hadron shower (E_{miss}) due to ν_μ production in meson decays is thrown according to distributions extracted from the Neutrino-Lund Monte Carlo simulation. Other sources of missing energy in the hadron shower, for example photons from decays into electrons, are accounted for in the hadron energy calibration of the detector. The hadron energy calibration used hadron-induced showers that have the same sources of missing energy as hadron showers in charged-current

interactions. The transverse momentum relative to the hadron shower is thrown according to a Gaussian distribution centered about zero of width σ_t given by

$$\sigma_t = \sqrt{0.7\, Z_\mu + 0.1225\, U_\mu}$$

where

$$Z_\mu = \frac{P_\mu + E_{miss}}{E_h^2 + W^2}$$

is the fractional energy carried by the decayed meson and

$$U_\mu = 1.00 + 0.0055\, W^2 \qquad \text{if} \qquad W^2 < 100\ \text{GeV}^2/c^4$$

$$U_\mu = 1.44 + 0.0011\, W^2 \qquad \text{if} \qquad W^2 > 100\ \text{GeV}^2/c^4$$

The form of the width σ_t was determined by fits to the average transverse momentum squared of charged hadrons in deep inelastic scattering of 280 GeV muons off protons, measured by the European Muon Collaboration [41].

7.6 Systematic Uncertainties in the Background Calculation

To reduce dependence on the electroweak fragmentation model in Lund, we required that the Neutrino-Lund Monte Carlo simulation agree with available measurements from neutrino deep-inelastic scattering. The uncertainty in the final meson decay background is dictated by the uncertainty in the data that is used to check the meson decay Monte Carlo simulation. For the vertex background, the dominant source of uncertainty is the uncertainty in the electroweak fragmentation functions and the uncertainty in the interaction and decay parameters of the primary hadrons. The shower component uncertainty is due to the electroweak fragmentation uncertainty and the shower Monte Carlo uncertainty. In the following sections each contribution to the uncertainty in the background is summarized, beginning with the uncertainty in the electroweak fragmentation model and ending with a discussion of the total uncertainties. A more detailed discussion of the uncertainty in the LEPTOLUND model of electroweak fragmentation is in reference 9.

7.6.1 Charged-Particle Fragmentation Measurements

The Lund fragmentation model LEPTOLUND gives good agreement with the all-charged fragmentation functions measured by the BEBC neutrino bubble chamber experiment with an average neutrino energy of 60 GeV and anti-neutrino energy of 45 GeV on protons and neutrons [42]. The net statistical uncertainty of the measured fragmentation was about 1 percent. The average W^2 of the experiment was 40 GeV^2/c^4, whereas the average W^2 in our experiment was about

80 GeV^2/c^4. Unfortunately, the data at higher W^2 than 40 GeV^2/c^4 is statistically limited. For example, the measured BEBC fragmentation data at average W^2 of 70 GeV^2/c^4 has statistical uncertainties of about 20 percent [9]. The total uncertainty of the LEPTOLUND model is 6 percent for neutrino and anti-neutrino fragmentation into charged particles, calculated from the uncertainty in the BEBC fragmentation measurements in each W^2 bin [9].

7.6.2 Extrapolation to high W^2

We must use LEPTOLUND to extrapolate the fragmentation functions above W^2 equal to 225 GeV^2/c^4 because this is the upper limit of the BEBC data on fragmentation. About half the meson decay background has W^2 greater than 225 GeV^2/c^4 where the average W^2 is 300 GeV^2/c^4. The Lund fragmentation model at higher W^2 is a linear extrapolation of the Lund fragmentation at lower W^2. Therefore, the uncertainty on the background due to this extrapolation is about 10 percent for events with W^2 greater than 225 GeV^2/c^4, based on the statistical uncertainty of the lower W^2 data. Combining this with the 6 percent uncertainty on the background at lower W^2 gives a 7.5 percent total uncertainty for neutrino fragmentation. No data on high energy antineutrino fragmentation is available so a conservative estimate of 15% in the level of anti-neutrino fragmentation is assigned to the meson decay Monte Carlo simulation, also based on extrapolations from lower W^2 BEBC data.

7.6.3 Kaon fraction

Another source of uncertainty is the relative number of different hadron species. The kaon fraction is important, because kaons decay more readily than pions. The kaon fraction is small, about 10% to 20% of all the primary hadrons. As mentioned in Section 7.2, the Lund model was finely tuned to agree with kaon fragmentation data taken with the BEBC bubble chamber experiment by setting the strangeness suppression factor, λ_s, at 0.2. An uncertainty of 5% for $\mu^-\mu^-$ and 7.5% for $\mu^+\mu^+$ due to the uncertainty in the kaon fraction was determined by varying λ_s between 0.1 and 0.3, which are the values allowed by the BEBC data [39, 40].

7.6.4 Proton fraction

The fraction of protons is very small, less than 5%. This is because it takes more energy to pull two quarks from the continuum to combine with the fragmenting quark to produce a proton. We estimate an uncertainty of 2% in the $\mu^-\mu^-$ and 4% in the $\mu^+\mu^+$ events, assuming the proton fraction in Lund is off by 50%.

7.6.5 Extrapolation to iron

The LEPTOLUND model simulates neutrino interactions with protons and the data we use to check LEPTOLUND comes from experiments using lighter nuclei as targets like neon. But we are interested fragmentation on iron, which has an atomic number A equal to 56. Measurements by the BEBC experiment at an average neutrino energy of 40 GeV showed that there is no difference between neutrino

fragmentation with a hydrogen target with A of 1, and a neon target with A of 20, within the 2 percent statistical uncertainty of the measurements [43]. A conservative uncertainty of 5 percent is associated with Lund electroweak fragmentation in iron in light of the uncertainty of the BEBC measurement.

7.6.6 Total uncertainties

The total background uncertainty of the vertex component comes from the 2 percent uncertainty in the measured particle lifetimes [44], the 2 percent uncertainty in the parametrization of the rate, and the 10.5 percent uncertainty in the LEPTOLUND fragmentation for incident neutrinos or 18.5 percent uncertainty for incident antineutrinos. This yields total uncertainties for the vertex component of 10.9 percent for neutrinos and 18.7 percent for the antineutrinos.

The shower background uncertainty has contributions from the uncertainty in the LEPTOLUND fragmentation, the uncertainty in the measured particle lifetimes and interaction lengths, and a 10 percent uncertainty in the shower Monte Carlo simulation discussed in Chapter 6. The total uncertainty in the shower background is 14.8 percent for neutrinos and 21.2 percent for anti-neutrinos. The sources and levels of uncertainties are summarized in Table 7.2.

Source	$\mu^-\mu^-$	$\mu^+\mu^+$
All-charged Fragmentation	6%	15%
Extrapolation to W^2	4.5%	4.5%
Kaon Fraction	5%	7.5%
Pion Fraction	2%	4%
Heavy Nuclear Target	5%	7.5%
Interaction and Decay lengths	2%	2%
Parametrization Error	2%	2%
Total Vertex	10.9%	18.7%
Muon-production in showers	10%	10%
Total Shower	14.8%	21.2%

Table 7.2 A breakdown of the contributions to the uncertainty in the meson decay background calculation.

7.7 Meson Decay Background Results

The generated same-sign dimuon events from the meson decay background are propagated through the detector with the CCFR detector simulation described in Chapter 4 and reconstructed in the same manner as the data. Table 7.3 gives the number of events expected in our detector due to the shower background component for experiments E744 and E770 combined in bins of total visible energy and Table 7.4 gives the expected number of events due to the vertex component. For incident neutrinos

we expect 56.32 ± 8.35 $\mu^-\mu^-$ events in experiments E744 and E770 due to the shower background and 109.45 ± 11.95 $\mu^-\mu^-$ events due to the vertex background. For incident antineutrinos, there are 3.75 ± 0.80 $\mu^+\mu^+$ events due to the shower background and 12.04 ± 2.25 $\mu^+\mu^+$ events due to the vertex background.

Shower Background

Visible Energy (GeV)	$\mu^-\mu^-$	$\mu^+\mu^+$
30 - 100	1.81 ± 0.27	0.31 ± 0.07
100 - 200	10.75 ± 1.60	1.20 ± 0.26
200 - 300	$22,39 \pm 3.33$	1.63 ± 0.35
300 - 400	13.48 ± 2.02	0.50 ± 0.11
400 - 500	6.31 ± 0.96	0.09 ± 0.02
500 - 600	1.59 ± 0.26	0.02 ± 0.01
30 - 300	34.95 ± 5.18	3.13 ± 0.67
300 - 600	21.38 ± 3.19	0.61 ± 0.13
Total	56.32 ± 8.35	3.75 ± 0.80

Table 7.3 Total number of same-sign dimuon events expected in experiments E770 and E744 due to the shower component background. The error is systematic.

Vertex Background

Visible Energy (GeV)	$\mu^-\mu^-$	$\mu^+\mu^+$
30 - 100	13.94 ± 1.53	2.77 ± 0.52
100 - 200	36.50 ± 3.99	5.09 ± 0.95
200 - 300	37.5- ± 4.11	3.31 ± 0.62
300 - 400	15.53 ± 1.71	0.74 ± 0.14
400 - 500	4.73 ± 0.53	0.11 ± 0.02
500 - 600	1.20 ± 0.15	0.02 ± 0.00
30 - 300	87.99 ± 9.61	11.17 ± 2.09
300 - 600	21.46 ± 2.36	0.87 ± 0.16
Total	109.45 ± 11.95	12.04 ± 2.25

Table 7.4 Total number of same-sign dimuon events expected in experiments E770 and E744 due to the vertex component background. The error is systematic.

Chapter 8

Trimuon and Overlay Backgrounds

This chapter presents two backgrounds to prompt same-sign dimuon production; the background due to misidentified trimuons and the background due to two overlapping charged-current events that are called overlays.

8.1 Trimuon Background

Neutrino production of trimuons becomes a background to same-sign dimuon production when the opposite sign muon is hidden in the hadron shower. The least energetic muon in a trimuon event must pass through at least twenty calorimeter counters to be identified. Twenty counters corresponds to an average energy loss of 3.1 GeV if all the energy is lost in the form of ionization. The number of trimuon events in which the opposite sign muon has momentum less than 3.1 GeV must be calculated and subtracted from the same-sign dimuon sample.

Trimuons can be produced by two mechanisms. The most copious source is *hadronic trimuon production* in which a $\mu^+\mu^-$ pair is produced in a charged-current event by the decay of a produced vector meson such as the ρ, ω, ϕ, or the J/ψ. In addition, a $\mu^+\mu^-$ pair can be produced in the continuum of the hadron shower. Hadronic trimuon production is depicted in Figures 8.1a and 8.1b. *Radiative trimuon production* is the process in which a virtual photon that is radiated by the muon, produces a

$\mu^+\mu^-$ pair as shown in Figure 8.1c. Muon pairs can also be produced by virtual photons radiated from the quark legs. However, in our treatment of trimuon production this source is included in the continuum production of a hadronic trimuons. The contribution to same-sign dimuons from radiative production of trimuons is small because the muon pairs are usually produced with masses close to the threshold of $2m_\mu$ and they rarely pass the 9 GeV momentum cut.

A Monte Carlo simulation of trimuon production is used to predict the trimuon background. Single muon events, generated with the charged-current Monte Carlo described in Chapter 4, are used as input to the trimuon generator. Two muons from one of the above mechanisms are added to the single muon event. The event is given a weight corresponding to the probability for muon-pair production. To compare the trimuon Monte Carlo to the trimuon data, generated trimuons are propagated through the detector using the CCFR detector simulation and reconstructed.

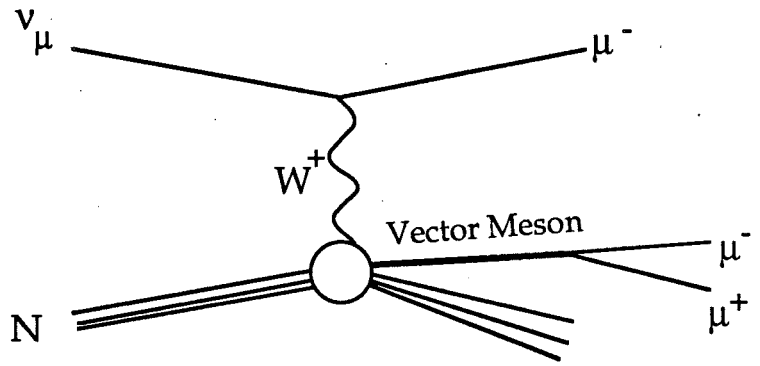

Figure 8.1a Hadronic production of a trimuon from the decay of a produced vector meson such as the ρ, ω, ϕ, or J/Ψ.

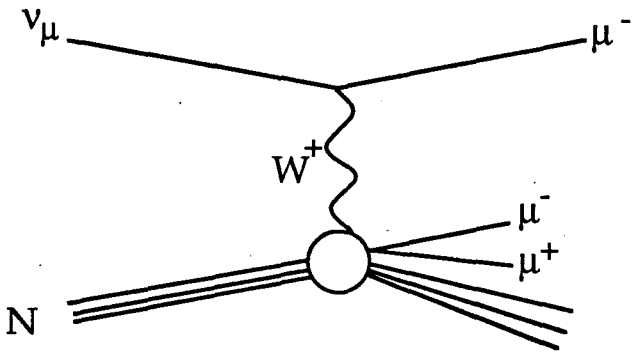

Figure 8.1b Hadronic production of a trimuon from the continuum.

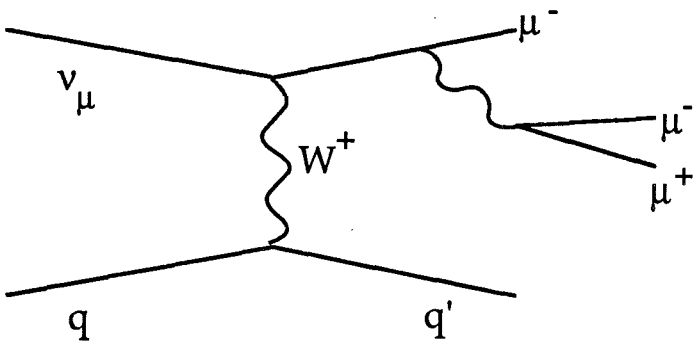

Figure 8.1c Radiative trimuon production.

8.1.1 The Trimuon Monte Carlo

A. Hadronic Production of Trimuons

The similarity between $\pi N \rightarrow \mu^+\mu^- X$ and the W boson-quark leg of the diagram in Figure 1.1a can be used to compute the cross section for hadronic production of trimuons [45], which is factorized as follows:

$$\frac{d\sigma(\nu_\mu N \rightarrow \mu^+\mu^-\mu^- X)}{dx\,dy\,d^3p\,dm_{\mu\mu}} = \frac{d\sigma(\nu_\mu N \rightarrow \mu^- X)}{dx\,dy} \frac{\lambda}{\sigma(\pi N)} \frac{d\sigma(\pi N \rightarrow \mu^+\mu^- X)}{d^3p\,dm_{\mu\mu}}$$

where the variable $m_{\mu\mu}$ is the invariant mass of the dimuon pair. The first factor is the differential charged-current cross section given by equation 4.2, which describes the lepton vertex of the trimuon event. The second piece contains the total cross section for πN interactions, which is $\sigma(\pi N)$ equal to 25 mb [44]. The parameter λ accounts for the difference between W^+N and π^+N dimuon production and is determined from the trimuon data itself to be equal to 1.3 as described below in Section 8.3. The last piece, the differential cross section for pair production in πN interactions, was measured with 150 GeV π^+ beam on beryllium at the Fermilab-Chicago cyclotron spectrometer experiment in the muon lab [46]. For this last term, we use the parametrization of the cross sections in reference 46, where the x_F distribution of hadronic trimuons is given by,

$$\frac{d\sigma}{dx_F} = A(1-x_F)^c \qquad 8.1$$

and the transverse momentum (P_T) distribution is given by

$$\frac{d\sigma}{dP_T} = B\,e^{-bP_T}$$

The parameters A, B, b, and c were determined by fitting the data for each vector meson that is produced and the continuum contribution.

B. Radiative Trimuon Production

Radiative trimuon production can be calculated accurately and is limited only by the knowledge of the parton distributions within the target nucleon. We use the parametrization given by Barger *et al* [47]

$$\frac{d\sigma(\nu_\mu N \rightarrow \mu^+\mu^-\mu^- X)}{d\sigma(\nu_\mu N \rightarrow \mu^- X)} = \alpha^2\left[0.035(\ln E_\nu)^2 - 0.19\right]$$

where α is the fine structure constant and E_ν is the energy of the incident neutrino.

8.1.2 The Trimuon Monte Carlo and the Trimuon Data

A trimuon sample was extracted from the multi-muon data to check the trimuon Monte Carlo simulation. Both the data and reconstructed Monte Carlo events were required to pass the trimuon cuts

	E744		E770		Both	
	Data	Monte Carlo	Data	Monte Carlo	Data	Monte Carlo
ν	38	20.69	23	25.15	61	45.84
$\bar{\nu}$	16	4.22	9	5.39	25	9.61
Total	54	24.91	32	30.54	86	55.45

Table 8.1 Numbers of neutrino and antineutrino trimuons in the data and trimuon Monte Carlo for $P_{min} > 4.5$ GeV. The trimuon Monte Carlo has a 40% statistical error associated with it as discussed below.

described in Chapter 3, in which two of the muons must pass the dimuon cuts and the momentum of the least energetic muon (P_{min}) was required to be greater than 4.5 GeV/c. This cut was chosen to minimize trimuons from meson decays in the shower of an opposite-sign dimuon event. The number from this source that remains in the trimuon data sample after the 4.5 GeV/c cut, is determined from the meson decay background calculation described in Chapter 7 and subtracted from the trimuon data sample. Trimuons from meson decays in the shower of opposite sign events contribute a negligible signal to the same-sign dimuon background since the opposite sign muon, which is from the charmed quark fragmentation, almost always has enough energy to be reconstructed with $P_{min} > 3.1$ GeV/c and therefore identified.

The final trimuon data sample consists of 54 neutrino and antineutrino events in E744 and 32 in E770. Of these, we expect five events in E744 and six in E770 from the meson decays in the showers of an opposite sign dimuon events. Table 8.1 gives the results from the

trimuon data and the trimuon Monte Carlo. There are about 30% ± 15% fewer trimuons per charged-current event in E770 than in E744. The difference between the number of trimuons in the two experiments is within two standard deviations. However, the level of agreement between the two experiments is included in the systematic error of the calculation, as described in Section 8.1.3.

The normalization for the trimuon Monte Carlo is given by the total number of observed trimuons, less the total number expected from meson decays, divided by the total number of reconstructed trimuon Monte Carlo events. It comes out to 1.35 ± 0.23, which sets the value of the scale factor λ described above, since the contribution from radiative trimuon production is small. The parameter λ has been estimated to be 2.1 from ρ-meson production measured in a neutrino bubble chamber experiment which is comparable to the above normalization [48].

The most important check of the trimuon Monte Carlo is how well its kinematic distributions match the trimuon data distributions. The variable ϕ_{123}, defined as the azimuthal angle between the most energetic muon and the vector sum of other two, indicates the degree of spatial correlations between the three muons. Events at high ϕ_{123} are primarily from the hadronic source because the muon pair is always associated with the hadron shower. Radiative production contributes events at lower ϕ_{123}, since the muon pair is radiated from the primary muon. Figure 8.2 shows the distribution of the variable ϕ_{123} for the trimuon data and the

normalized Monte Carlo events. Note that E744 and E770 are combined. The Monte Carlo distribution agrees well with the data.

The trimuon Monte Carlo simulation accurately reproduces the trimuon data at low m_{23}, which is the invariant mass of the muon pair produced at the hadronic vertex. This is shown in Figure 8.3 that compares the trimuon simulation to the trimuon data for $P_{min} > 3.1$ GeV/c. The agreement is expected since the pion data

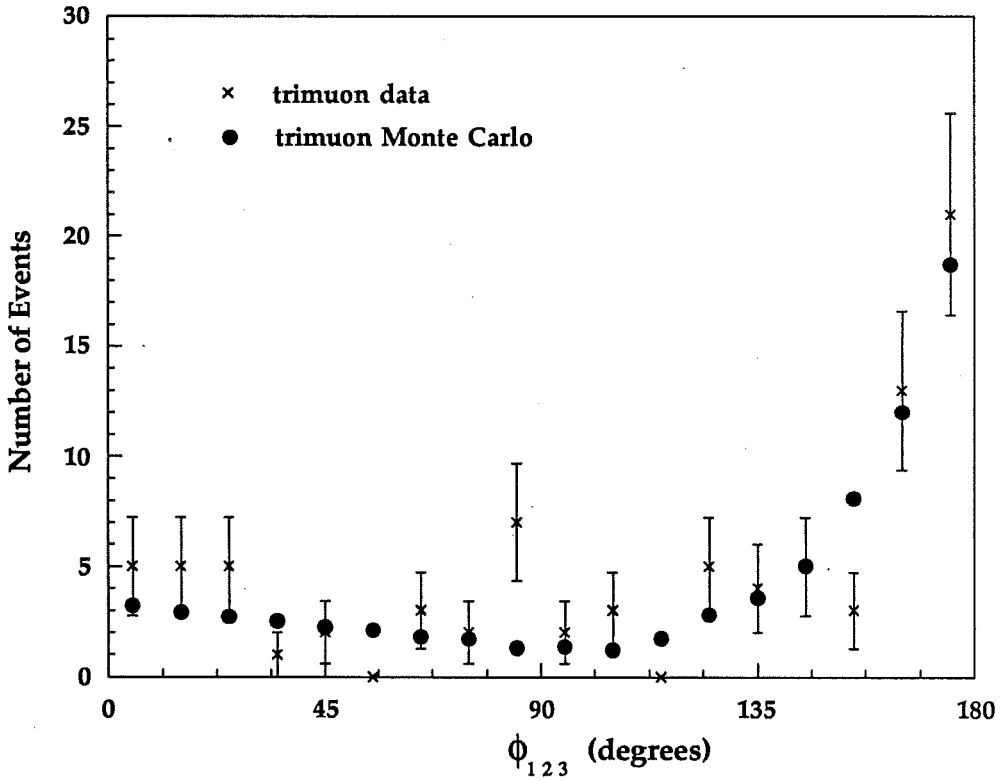

Figure 8.2 The variable ϕ_{123}, the azimuthal angle between the most energetic muon and the vector sum of the other two, for $P_{min} > 4.5$ GeV. The dots are the normalized trimuon Monte Carlo events and the data is given by the crosses. Experiments E744 and E770 are combined.

(Anderson *et al.* [46]) used to parametrize continuum production of trimuons extended down to the kinematic limit on m_{23}, which is 0.211 GeV/c^2. It is crucial that the low m_{23} region of the trimuon simulation match the trimuon data. This is because trimuon events at low m_{23} may look like dimuons since the muon pairs are produced with very small opening angles, and their tracks may not be resolved in the detector. Such events do not contaminate the same-sign dimuon data, because none of the tracks in the same-sign dimuon events had more than one hit in each view on the average. Furthermore, the pulse heights in the calorimeter downstream of the shower were consistent with just two minimum ionizing particles.

The final test of the trimuon Monte Carlo simulation is the agreement in the momentum of the unlike-sign muon (P_3), plotted in Figure 8.4, for $P_{min} > 3.1$ GeV/c. The shape of the distribution at low P_3 is dictated by the requirement that two of the muons pass the 9 GeV momentum cut. This causes a depletion of events between for P_3 between 6 GeV and 9 GeV, which is plotted in the third bin in Figure 8.4. These muons range out in between the calorimeter and the first gap of the spectrometer so they are reconstructed as if they ranged out at the front face of the spectrometer, resulting in an underestimation of their momentum.

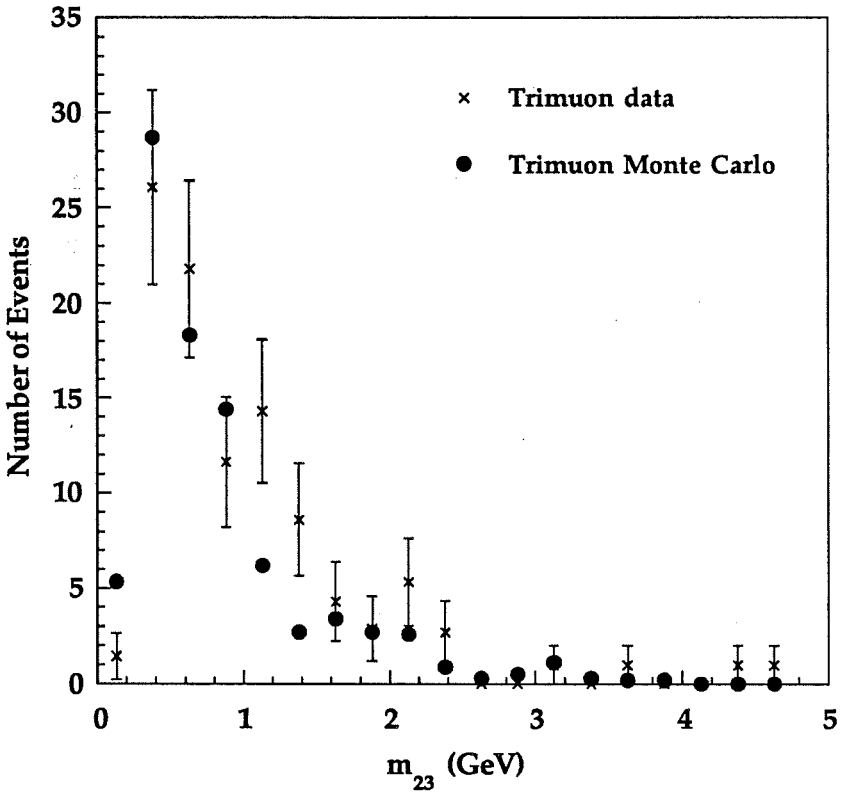

Figure 8.3 Comparison of the distribution of the mass of the μ_2-μ_3 system between the trimuon data and the trimuon Monte Carlo simulation for $P_{min} > 3.1$ GeV, where P_{min} is the momentum of the least energetic muon.

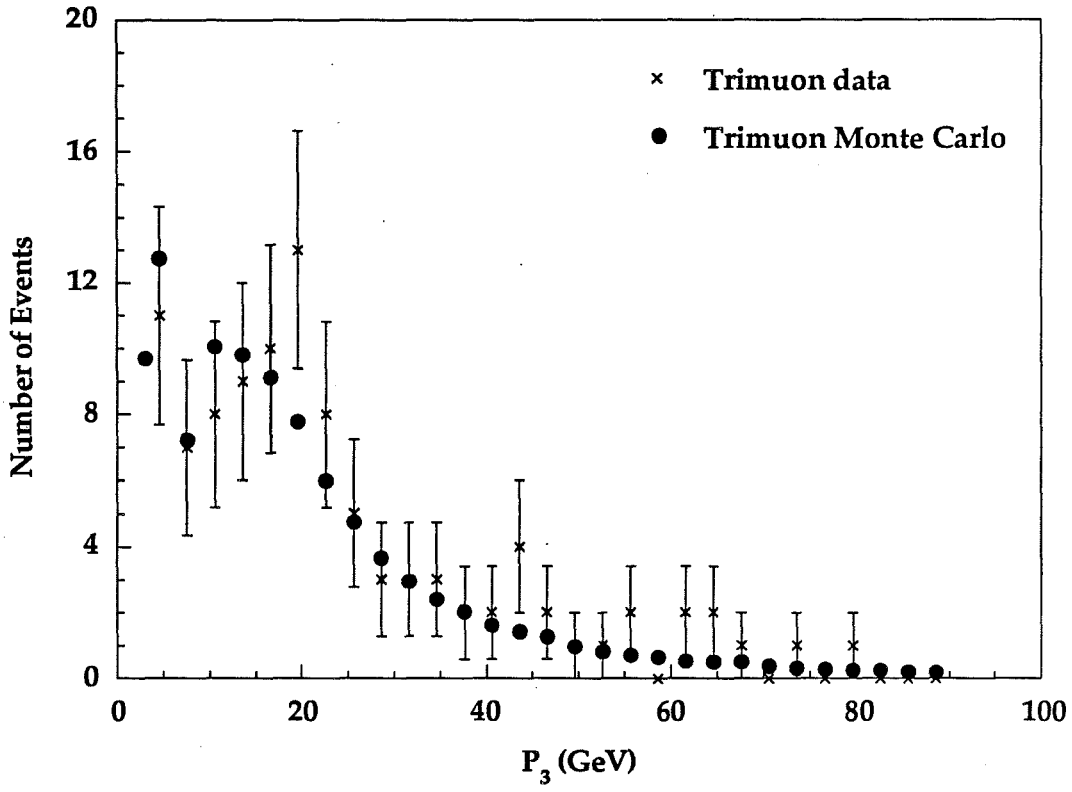

Figure 8.4 The distribution of P_3, the momentum of the unlike-sign muon for $P_{min} > 3.1$ GeV. The dots are the normalized trimuon Monte Carlo events and the crosses are the trimuon data. The lowest energy dot is the prediction of the trimuon Monte Carlo for the number of trimuons with P_3 less than 3.1 GeV, which constitute a background to same-sign dimuon production.

8.1.3 Uncertainty in the Trimuon Monte Carlo

The total uncertainty in the trimuon Monte Carlo is 50%. It comes from three sources; 1) the level of hadronic trimuons from vector meson production relative to continuum production, 2) the measurements used to extract the parametrizations for hadronic and continuum production, and 3) the level of agreement between the E744 trimuon data and the E770 trimuon data that was used to normalize the trimuon Monte Carlo. An uncertainty in radiative production is negligible since only about 0.5 radiative trimuon events are calculated to contribute to the same-sign signal [9].

1) The first contribution to the uncertainty was calculated by running the trimuon Monte Carlo assuming all hadronic trimuons are from vector meson production and then assuming they are all due to continuum production.

2) The uncertainty due to the parametrizations used to describe hadronic trimuon production, given in Section 8.1.1, was determined by varying the value c in the parametrization of the x_F-dependence in equation 8.1 between 1.0 and 4.0, which is the range of values allowed by the pion-beam measurements [46].

3) An uncertainty due to the agreement between E744 and E770 was determined from the difference between the normalization calculated with E744 and E770 separately.

The uncertainty in the trimuon Monte Carlo from items 1 and 2, was 40% [9], which was combined in quadrature with the 50% uncertainty in the normalization to give a total uncertainty of 64%.

8.1.4 The Background Due to Trimuon Production

The number of trimuon background events is plotted in the first bin of Figure 8.4. The background is small - less than 10 events - because only trimuons with very asymmetric muon pairs will be reconstructed as dimuons; one muon must have $P_\mu > 9$ GeV/c and the other $P_\mu < 3.1$ GeV/c. The trimuon background to same-sign dimuon production is listed in Table 8.2 for E744 and E770 separately and combined.

	E744	E770	E744 and E770
ν	3.74 ± 1.87	4.92 ± 2.46	8.66 ± 4.33
$\bar{\nu}$	0.43 ± 0.22	0.60 ± 0.30	1.03 ± 0.52

Table 8.2 Total numbers of same-sign background events due to trimuon production. The uncertainty is due to the systematic error in the trimuon background calculation.

8.2 The Overlay Background

Two charged-current events that arrive in the same RF bucket are called *overlays*. When they arrive at the same time in the same place, within the resolution of the detector, they form a background that must be subtracted from the sample of same-sign dimuon events. Most overlay events are eliminated with cuts on the time of passage of the tracks relative to the trigger time and on the closest transverse distance of approach between the tracks. The characteristics of identified overlay events are used to predict the number expected to fall within the timing and distance cuts. This number is small because of the precise timing and position resolutions of the detector.

8.2.1 Timing

The time that momentum analyzed tracks traverse the detector relative to the trigger time is derived from the TDC information of drift chamber hits from muon tracks in the x and y views of the first two toroid gaps. These hits give at least four independent measurements of the track time relative to the trigger time; one from each view and each gap. The resolution of the time between two tracks is about 28 ns. This is sufficient to determine if the two events occur in the same RF bucket, rather than in adjacent RF buckets. Figure 8.5 shows the time between the two tracks (Δt) for same-sign dimuon events that pass all the cuts except the timing and closest approach cuts. Most events with Δt less than 28 ns , called in-time

events, are good dimuon events. Those with Δt greater than 28 ns, called out-of-time events, comprise a sample of overlays that is used to study the overlay contamination for the events that pass all the cuts.

8.2.2 Distance of Closest Approach

As described in Chapter 3, events with a distance of closest approach (DCA) greater than 15 cm are overlays and are removed from the dimuon sample. Figure 8.6 shows the DCA distribution for same-sign dimuons passing all cuts except the timing and DCA cuts. The majority of events that fall within the cut are good same-sign dimuons.

8.2.3 Overlay Background

The distributions of the variables, Δt and DCA, are two independent means of identifying overlays. The ratio of overlays with DCA > 15 cm to the number with DCA < 15 cm is found from the distribution of the DCA for out-of-time events. This ratio is applied to the sample of in-time same-sign dimuons to give the number of overlays contaminating the final same-sign dimuon sample. The final overlay contamination, N_0 is given by

$$N_0 = \frac{N(\Delta t > 28, DCA < 15)}{N(\Delta t > 28, DCA > 15)} N(\Delta t < 28, DCA > 15)$$

where N is the number of same-sign dimuons for the different Δt and DCA requirements. For E744, N_0 is 0.5 ± 0.2 $\mu^-\mu^-$ events and 0.02 ± 0.01 $\mu^+\mu^+$ events [9].

To calculate the number of overlay background events expected in E770, we scaled the overlay background in E744 by the relative number of charged-current events in the two experiments. This method is valid provided the relative number of in-time to out-of-time overlays was the same for the two experiments. In reference 49, the ratio of the number of in-time overlays to out-of-time overlays was calculated with DCA > 20 cm, for experiments E744 and E770 separately. The ratios are 2.1 ± 1.0 in E744 and 1.3 ± 0.6 in E770, which are consistent. Therefore we can extrapolate the number of overlays in E744 to E770. The total number of overlays expected to contaminate the E770 same-sign dimuon sample is 0.6 ± 0.2 for $\mu^-\mu^-$ events and 0.04 ± 0.02 $\mu^+\mu^+$ events. The visible energy of the overlay background for both experiments was distributed according to the total visible energy distribution of the charged-current events.

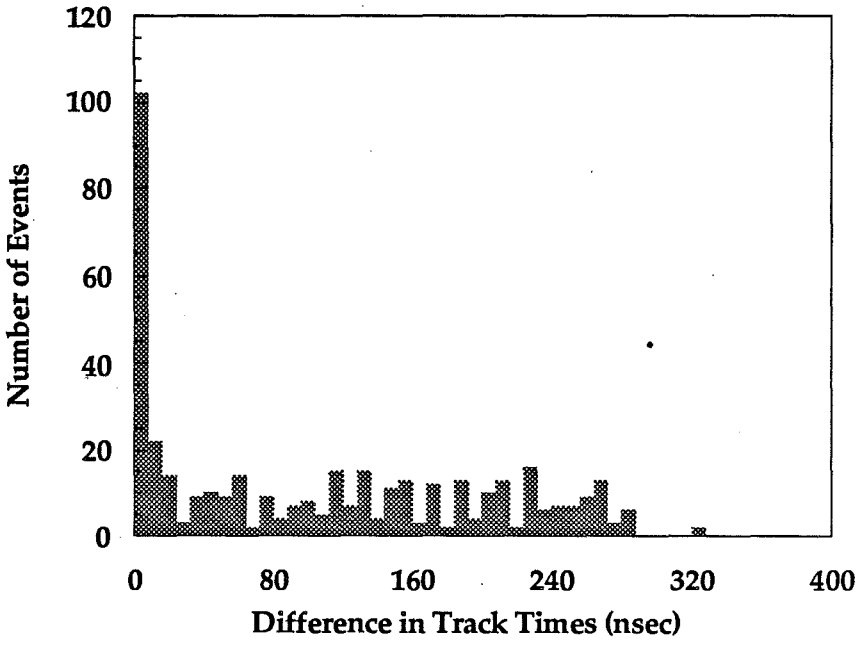

Figure 8.5 The difference in track times, Δt, for the same-sign dimuon events that pass all cuts except the DCA and timing cuts.

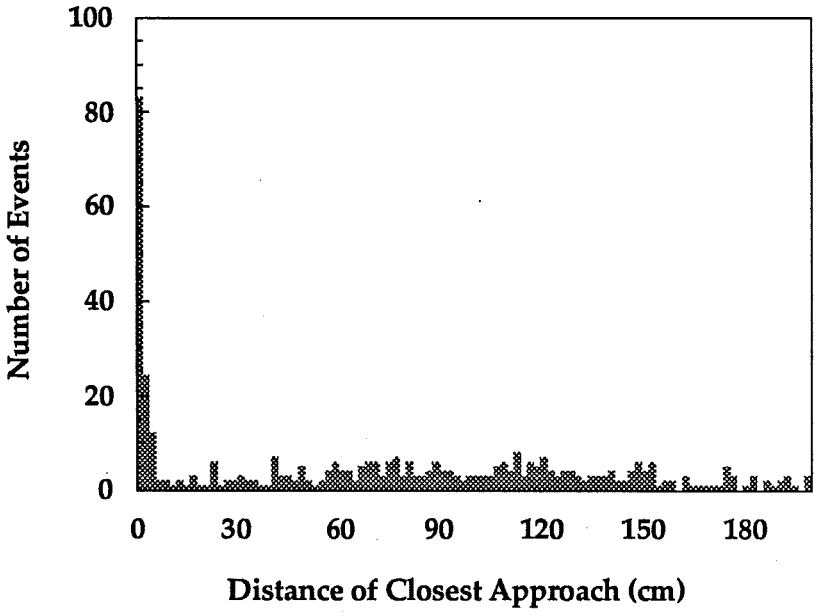

Figure 8.6 The transverse distance of closest approach (DCA) for same-sign dimuon events passing all cuts except timing and DCA cuts.

Chapter 9

Same Sign Dimuon Rates

9.1 Introduction

The final rates for neutrino same-sign dimuon production are presented in this chapter. The prompt rates are calculated from the number of acceptance-corrected same-sign dimuon events remaining after the backgrounds have been subtracted. The backgrounds consist of the meson decay background, misidentified trimuons, and overlays, which are discussed in Chapters 7 and 8. The meson decay background is the largest, contributing about 95 percent to the total background. The kinematic distributions of the meson decay background agree with those of the same-sign data and the number of meson decay events is close to the number of same-sign dimuon events. Therefore, we conclude that meson decays account for the majority of the same-sign dimuon events observed in our detector.

9.2 The Dimuon Signal, Background and Excess

The same sign dimuon sample consists of 220 $\mu^-\mu^-$ events and 25 $\mu^+\mu^+$ events from experiments E744 and E770 combined. The total calculated background is 175.54 ± 19.35 $\mu^-\mu^-$ events and 16.87 ± 3.04 $\mu^+\mu^+$ events, where the errors are systematic. This results in an excess of 44.46 ± 20.20 $\mu^-\mu^-$ events and 8.14 ± 5.17 $\mu^+\mu^+$ events over the background, where the errors are systematic and statistical combined. A breakdown of

the individual sources contributing to the background is given in Table 9.1a. Tables 9.1b and 9.1c give the individual background contributions as a function of incident neutrino energy. Figures 9.1a and 9.1b show the energy dependence of the observed same-sign dimuon events, neutrino- and antineutrino-induced, compared to that of the expected background broken down into the separate contributions. The fraction of meson decay events from the shower component increases with the total visible energy, while the overlay and trimuon contributions remain very small.

The previous same-sign dimuon background calculated in 1988 for experiment E744 [9] is compared to the present background for E744 in Table 9.2 for neutrinos and antineutrinos. The difference between the two backgrounds lies in the calculation of the shower component of the meson-decay background. As described in Section 7.3, the new shower background is based on a larger sample of muon-production data. In addition, the new shower background is based on measurements of muon production by tagged pions and kaons separately and measurements at hadron energies below 50 GeV, which were not done previously. The total backgrounds are not significantly different, but the new background has smaller uncertainties than the previous background.

To show that we can combine the data from experiments E744 and E770, the agreement between them is shown in Tables 9.3a-9.3f, which give the number of same-sign dimuon events, background, and excess in total energy bins for neutrinos and antineutrinos. The numbers for experiment E744 agree with experiment E770 across energy bins. This is expected since

the incident neutrino and antineutrino beams were similar as described in Chapter 4.

For the studies of kinematic distributions of the same-sign data, the two experiments can be combined since the kinematic distributions are consistent as shown in Figures 9.2-9.4. Figure 9.2 shows the E744 and E770 distributions of $P_{\mu 2}$, the momentum of the muon selected to have the smaller component perpendicular to the hadron shower direction. The hadron shower direction is derived from the total visible energy, the neutrino beam direction and the vector momentum of the first muon. The agreement between the two experiments in $P_{\mu 2}$ shows the effects of the reconstruction on the events are consistent. Figure 9.3 shows ϕ_{12}, the azimuthal angle between the two muons in the plane perpendicular to the beam direction. Again, the distributions are consistent, reflecting the agreement between the two experiments in the muon-angular acceptance. Figure 9.4 shows P_T, the transverse momentum of the second muon with respect to the hadron shower direction, which reflects the agreement between the two experiments in the reconstruction of the muon momentum and the angular acceptance.

Background Source	$\mu^-\mu^-$	$\mu^+\mu^+$
Vertex Contribution	109.45 ± 11.95	12.04 ± 2.25
Shower Contribution	56.32 ± 8.35	3.75 ± 0.80
Total Meson Decay	165.78 ± 18.94	15.78 ± 3.00
Misidentified Trimuon	8.66 ± 3.48	1.02 ± 0.41
Overlay Events	1.10 ± 0.44	0.06 ± 0,03
Total Background	175.54 ± 19.35	16.87 ± 3.04
Data	220	25

Table 9.1a Total background contributions from each source and the total number of events for the same-sign data. The errors are systematic.

ν Background Contributions to Same-Sign Signal

Visible Energy (GeV)	Data	Vertex (± 11%)	Shower (± 15%)	3μ (± 64%)	Overlay (± 40%)	Total Background
30-100	16	13.94	1.81	1.04	0.39	17.17 ± 1.91
100-200	45	36.50	10.75	2.73	0.35	50.33 ± 5.57
200-300	97	37.55	22.39	3.02	0.25	63.20 ± 7.00
300-400	44	15.53	13.48	1.45	0.09	30.54 ± 3.42
400-600	18	4.73	7.90	0.43	0.03	14.29 ± 1.65
30-300	158	87.99	34.95	6.78	0.99	130.71 ± 14.41
300-600	62	21.46	21.38	1.89	0.11	44.83 ± 5.00
total	220	109.45	56.32	8.66	1.10	175.54 ±19.35

Table 9.1b Background contributions of each source, the total background, and the total number of events in the same-sign data in experiments E744 and E770 combined for incident neutrinos. The uncertainties on the individual backgrounds are given at the top of the columns. The uncertainty of the total background is the systematic error of the individual contributions combined.

$\bar{\nu}$ Background Contributions to Same Sign Signal

Visible Energy (GeV)	Data	Vertex (± 19%)	Shower (± 21%)	3μ (± 64%)	Overlay (± 50%)	Total Background
30-100	2	2.77	0.31	0.20	0.03	3.31 ± 0.60
100-200	15	5.09	1.20	0.42	0.02	6.73 ± 1.21
200-300	6	3.31	1.63	0.30	0.01	5.24 ± 0.95
300-400	1	0.74	0.50	0.08	0.00	1.33 ± 0.24
400-600	1	0.13	0.11	0.02	0.00	0.26 ± 0.05
30-300	23	11.17	3.13	0.92	0.06	15.27 ± 2.75
300-600	2	0.87	0.61	0.11	0.00	1.59 ± 0.29
total	25	12.04	3.75	1.02	0.06	16.87 ± 3.04

Table 9.1c Background contributions of each source, the total background, and the total number of events in the same-sign data in experiments E744 and E770 combined for incident antineutrinos. The uncertainties on the individual backgrounds are given at the top of the columns. The uncertainty on the total background is the systematic error of the individual contributions combined.

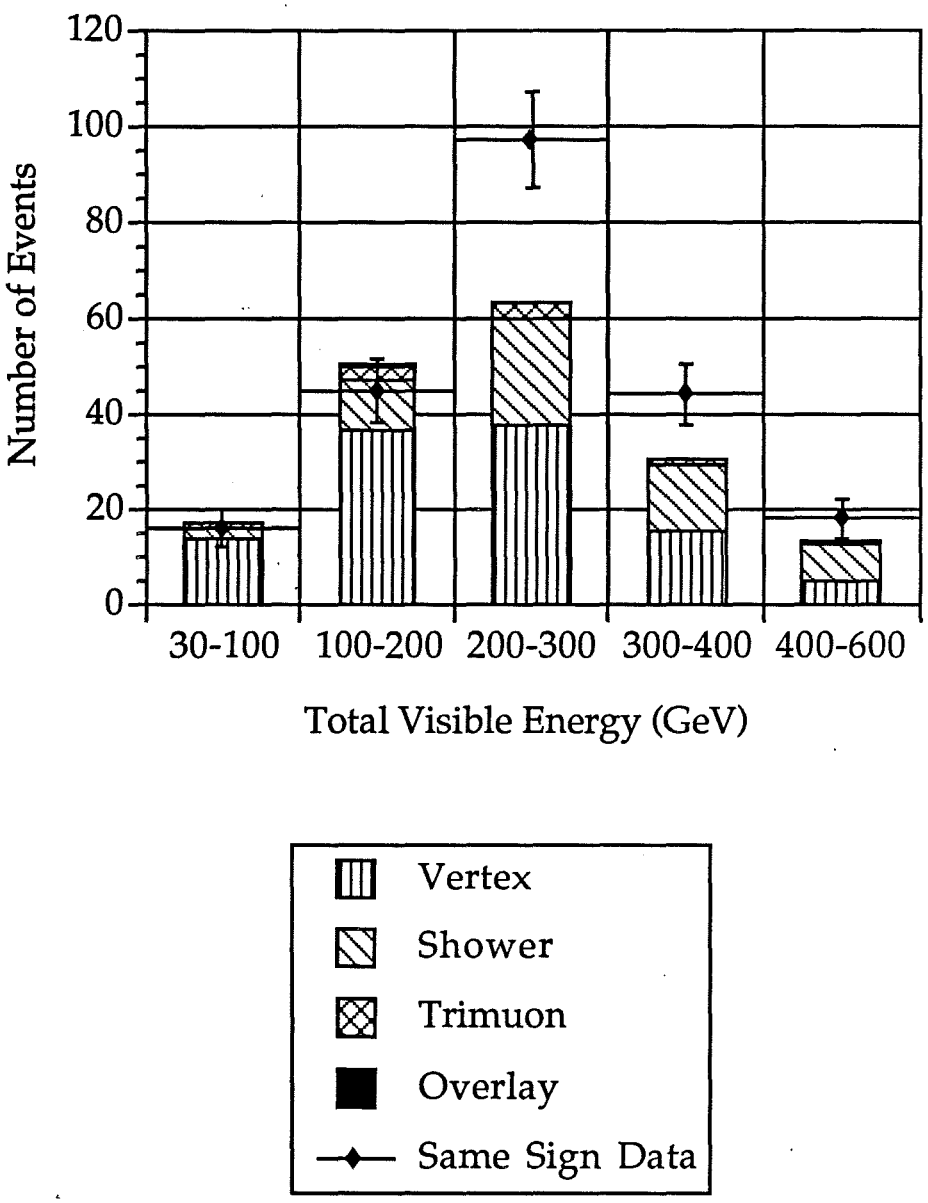

Figure 9.1a The energy dependence of the same-sign dimuon data and the individual contributions of each background for incident neutrinos in total visible energy bins. There is an 11% systematic error associated with the total background.

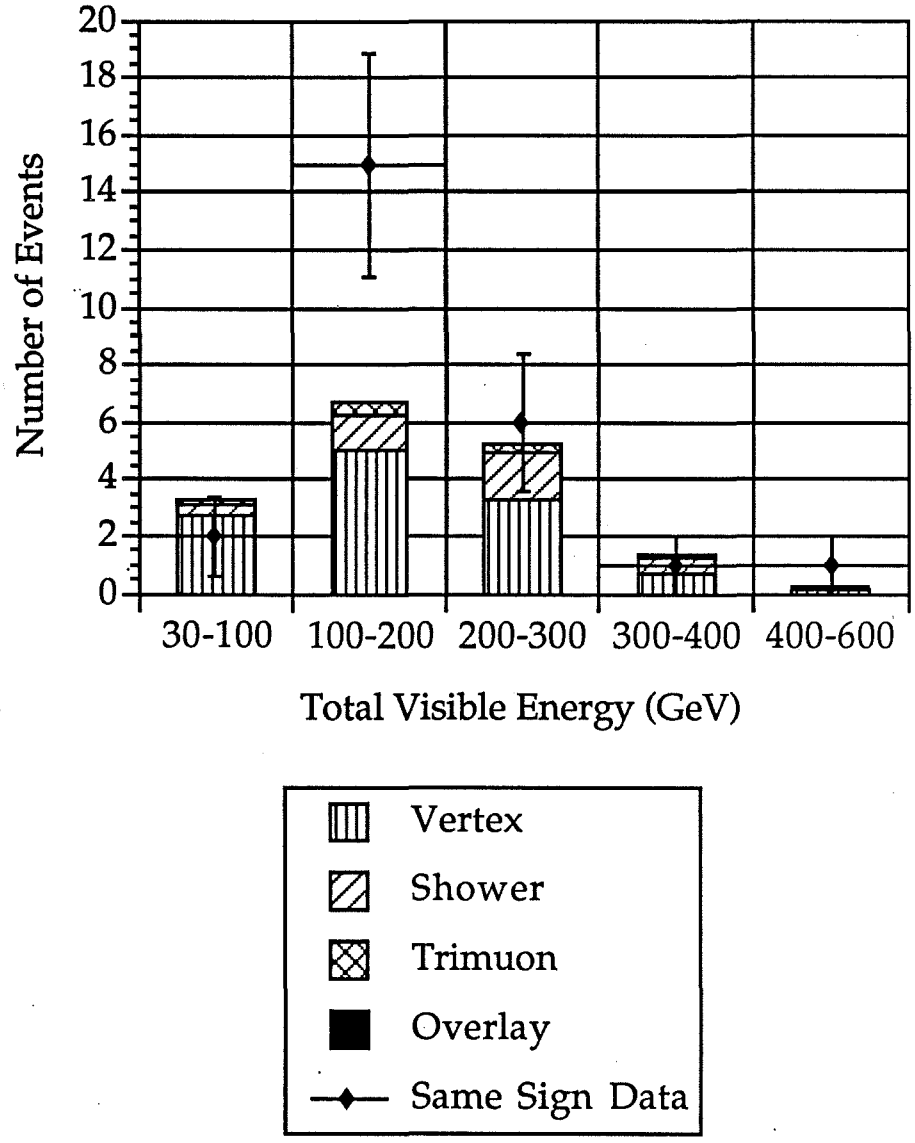

Figure 9.1b The energy dependence of the same-sign dimuon data and the individual contributions of each background for incident antineutrinos in total visible energy bins. There is an 18% uncertainty associated with the total background.

Comparison of Previous to Present E744 Backgrounds

Visible Energy (GeV)	ν Total Background (1988)	ν Total Background (1992)	$\bar{\nu}$ Total Background (1988)	$\bar{\nu}$ Total Background (1992)
30-100	6.92 ± 0.77	7.88 ± 0.89	1.47 ± 0.26	1.45 ± 0.26
100-200	23.04 ± 2.60	23.03 ± 2.56	3.31 ± 0.61	2.88 ± 0.52
200-300	31.12 ± 3.70	28.77 ± 3.20	2.92 ± 0.56	2.31 ± 0.42
300-400	14.77 ± 1.96	13.71 ± 1.56	0.83 ± 0.17	0.60 ± 0.11
400-600	6.58 ± 1.02	6.15 ± 0.75	0.08 ± 0.02	0.13 ± 0.02
30-300	61.08 ± 6.97	59.67 ± 6.60	7.70 ± 1.42	6.64 ± 1.20
300-600	21.34 ± 2.80	19.86 ± 2.24	0.91 ± 0.20	0.74 ± 0.14
total	82.46 ± 9.65	79.53 ± 8.79	8.61 ± 1.59	7.38 ± 1.33

Table 9.2 A comparison of the total background to same-sign dimuon production for experiment E744 calculated previously in 1988 [9], to the present background for experiment E744. The errors are systematic.

ν Event Excess in E744

Visible Energy (GeV)	Data Sample	Decay Background	Total Background	Event Excess
30-100	7	7.25 ± 0.85	7.88 ± 0.89	-0.88 ± 2.78
100-200	17	21.69 ± 2.50	23.03 ± 2.56	-6.03 ± 4.84
200-300	43	27.29 ± 3.15	28.77 ± 3.20	14.23 ± 7.28
300-400	25	13.02 ± 1.54	13.71 ± 1.56	11.29 ± 5.22
400-600	9	6.04 ± 0.72	6.15 ± 0.75	2.85 ± 2.34
30-300	67	56.24 ± 6.44	59.67 ± 6.60	7.33 ± 10.49
300-600	34	19.06 ± 2.23	19.86 ± 2.24	14.14 ± 6.23
total	101	75.29 ± 8.62	79.53 ± 8.79	21.47 ± 13.32

Table 9.3a Same-sign signal from neutrinos, background and excess by visible energy for E744. The background error is systematic. The errors on the excess combine statistical and systematic uncertainties.

ν Event Excess in E770

Visible Energy (GeV)	Data Sample	Decay Background	Total Background	Event Excess
30-100	9	8.49 ± 0.99	9.29 ± 1.46	-0.29 ± 3.17
100-200	28	25.56 ± 2.95	27.30 ± 4.27	0.70 ± 6.08
200-300	54	32.65 ± 3.77	34.44 ± 5.39	19.56 ± 8.27
300-400	19	16.00 ± 1.89	16.83 ± 2.67	2.17 ± 4.74
400-600	9	7.78 ± 0.98	8.14 ± 1.33	0.86 ± 3.20
30-300	91	66.70 ± 7.64	71.03 ± 11.08	19.97 ± 12.33
300-600	28	23.78 ± 2.78	24.97 ± 3.93	3.03 ± 5.96
total	119	90.48 ± 10.36	96.01 ± 14.97	22.99 ± 15.18

Table 9.3b Same-sign signal from neutrinos, background and excess by visible energy for E770. The background error is systematic. The errors on the excess combine statistical and systematic uncertainties.

ν Event Excess in E744 and E770 combined

Visible Energy (GeV)	Data Sample	Decay Background	Total Background	Event Excess
30-100	16	15.75 ± 1.82	17.17 ± 1.91	-1.17 ± 4.22
100-200	45	47.26 ± 5.42	50.33 ± 5.57	-5.33 ± 7.77
200-300	97	59.94 ± 6.87	63.20 ± 7.00	33.79 ± 12.08
300-400	44	29.01 ± 3.37	30.54 ± 3.42	13.46 ± 7.42
400-600	18	13.82 ± 1.65	14.29 ± 1.65	3.71 ± 4.55
30-300	158	122.94 ± 14.05	130.71 ± 14.41	27.29 ± 19.12
300-600	62	42.83 ± 4.95	44.83 ± 5.00	17.17 ± 9.33
total	220	165.78 ± 18.94	175.54 ±19.35	44.46 ± 24.38

Table 9.3c Same-sign signal from neutrinos, background and excess by visible energy for experiments E770 and E744. The background error is systematic. The errors on the excess combine statistical and systematic uncertainties.

$\bar{\nu}$ Event Excess in E744

Visible Energy (GeV)	Data Sample	Decay Background	Total Background	Event Excess
30-100	2	1.34 ± 0.26	1.45 ± 0.26	0.55 ± 1.42
100-200	8	2.69 ± 0.51	2.88 ± 0.52	5.12 ± 2.85
200-300	4	2.19 ± 0.42	2.31 ± 0.42	1.69 ± 2.02
300-400	1	0.58 ± 0.11	0.60 ± 0.11	0.40 ± 1.00
400-600	0	0.12 ± 0.02	0.13 ± 0.02	-0.13 ± 1.00
30-300	14	6.22 ± 1.19	6.64 ± 1.20	7.36 ± 3.81
300-600	1	0.71 ± 0.14	0.74 ± 0.14	0.26 ± 1.00
total	15	6.93 ± 1.32	7.38 ± 1.33	7.62 ± 3.96

Table 9.3d Same-sign signal from anti-neutrinos, background and excess by visible energy for E744. The background error is systematic. The errors on the excess combine statistical and systematic uncertainties.

$\bar{\nu}$ Event Excess in E770

Visible Energy (GeV)	Data Sample	Decay Background	Total Background	Event Excess
30-100	0	1.74 ± 0.33	1.86 ± 0.48	-1.86 ± 1.02
100-200	7	3.60 ± 0.69	3.84 ± 0.98	3.16 ± 2.68
200-300	2	2.74 ± 0.53	2.93 ± 0.75	-0.93 ± 1.45
300-400	0	0.66 ± 0.13	0.72 ± 0.19	-0.72 ± 1.00
400-600	1	0.12 ± 0.03	0.13 ± 0.04	0.87 ± 1.00
30-300	9	8.07 ± 1.54	8.63 ± 2.20	0.37 ± 3.15
300-600	1	0.78 ± 0.15	0.85 ± 0.22	0.15 ± 1.00
total	10	8.85 ± 1.69	9.48 ± 2.42	0.52 ± 3.33

Table 9.3e Same-sign signal from anti-neutrinos, background and excess by visible energy for E770. The background error is systematic. The errors on the excess combine statistical and systematic uncertainties.

$\bar{\nu}$ Event Excess in E744 and E770 combined

Visible Energy (GeV)	Data Sample	Decay Background	Total Background	Event Excess
30-100	2	3.08 ± 0.59	3.31 ± 0.60	-1.31 ± 1.54
100-200	15	6.29 ± 1.20	6.73 ± 1.21	8.27 ± 16.5
200-300	6	4.93 ± 0.94	5.24 ± 0.95	0.76 ± 2.63
300-400	1	1.24 ± 0.24	1.33 ± 0.24	-0.33 ± 1.02
400-600	1	0.24 ± 0.04	0.26 ± 0.05	0.74 ± 1.00
30-300	23	14.30 ± 2.72	15.27 ± 2.75	7.73 ± 5.53
300-600	2	1.48 ± 0.29	1.59 ± 0.29	0.41 ± 1.44
total	25	15.78 ± 3.00	16.87 ± 3.04	8.13 ± 5.85

Table 9.3f Same-sign signal from anti-neutrinos, background and excess by visible energy for E770 and E744. The background error is systematic. The errors on the excess combine statistical and systematic uncertainties.

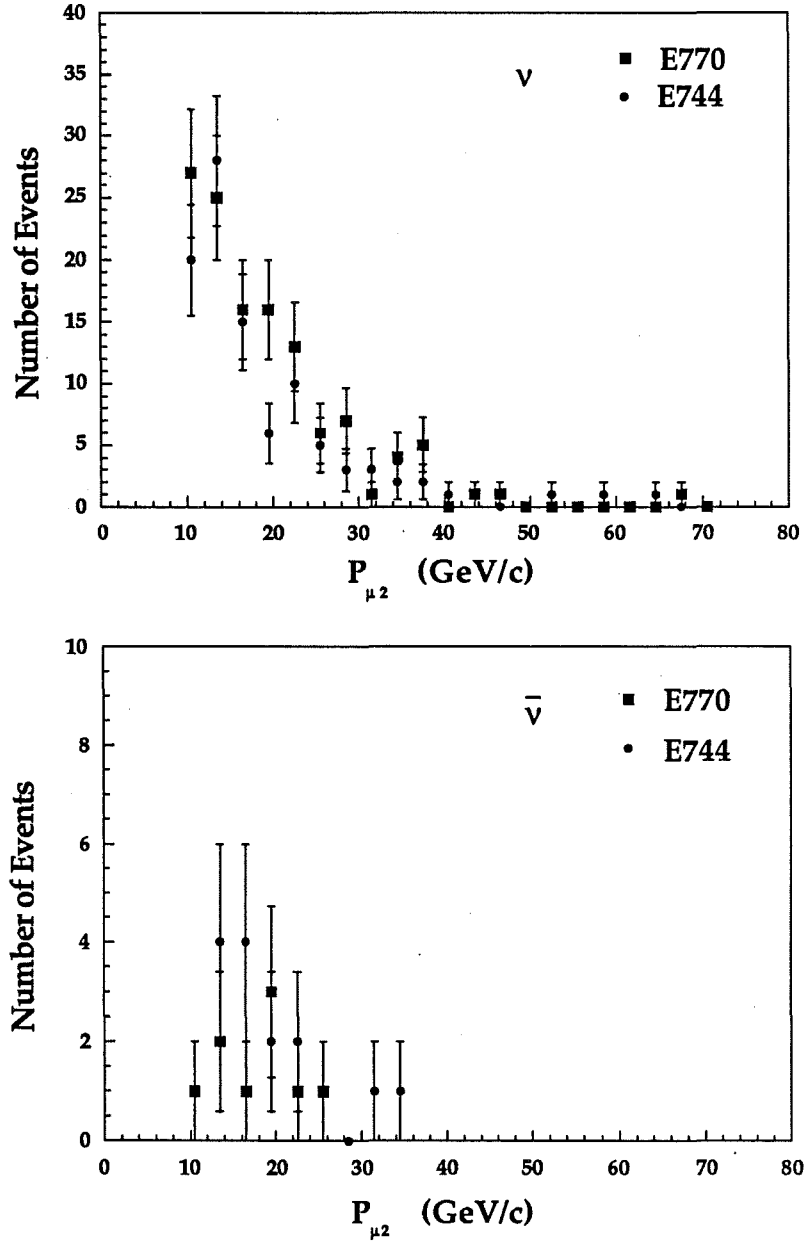

Figure 9.2 The distribution of $P_{\mu 2}$, the momentum of the second muon, selected as described in the text, for neutrino (top) and antineutrino (bottom) induced same-sign dimuons for experiment E744 (circles) and E770 (squares).

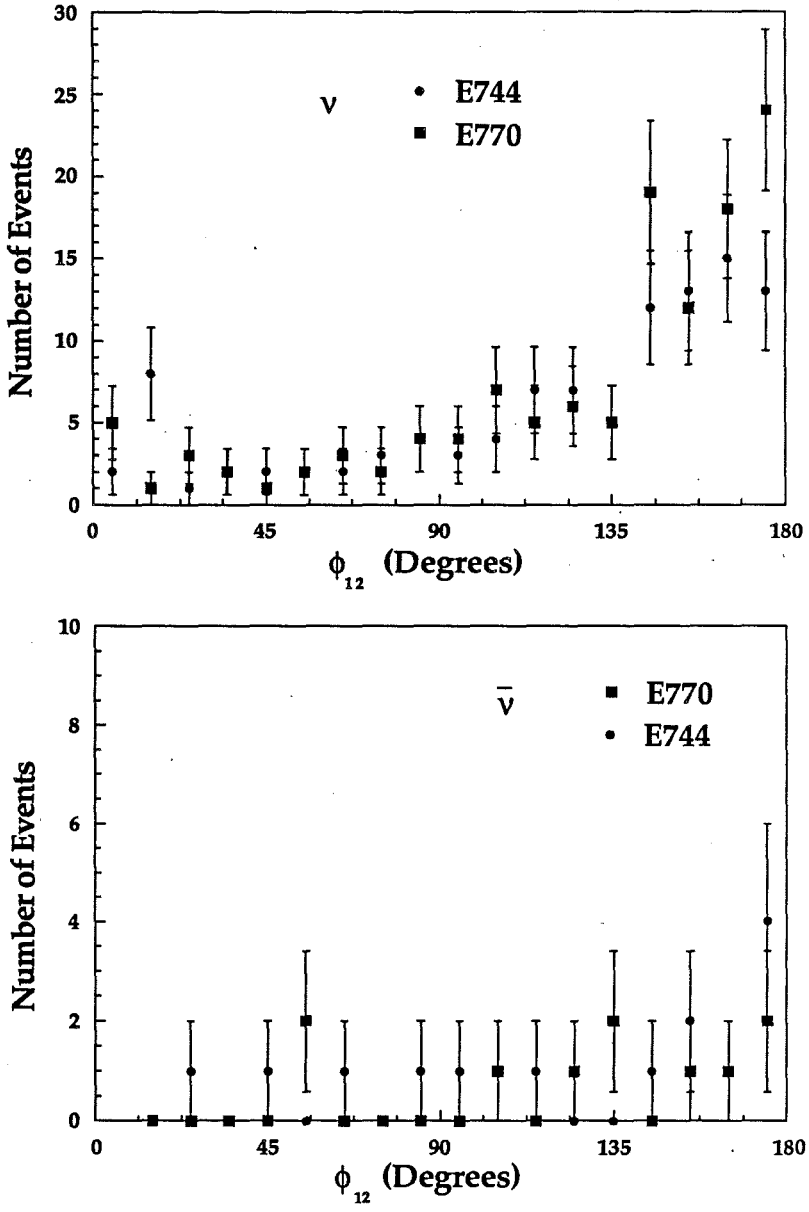

Figure 9.3 The distribution of ϕ_{12}, the azimuthal angle between the two muons in a plane perpendicular to the beam direction for neutrino (top) and antineutrino (bottom) induced same-sign dimuons for experiment E744 (circles) and E770 (squares).

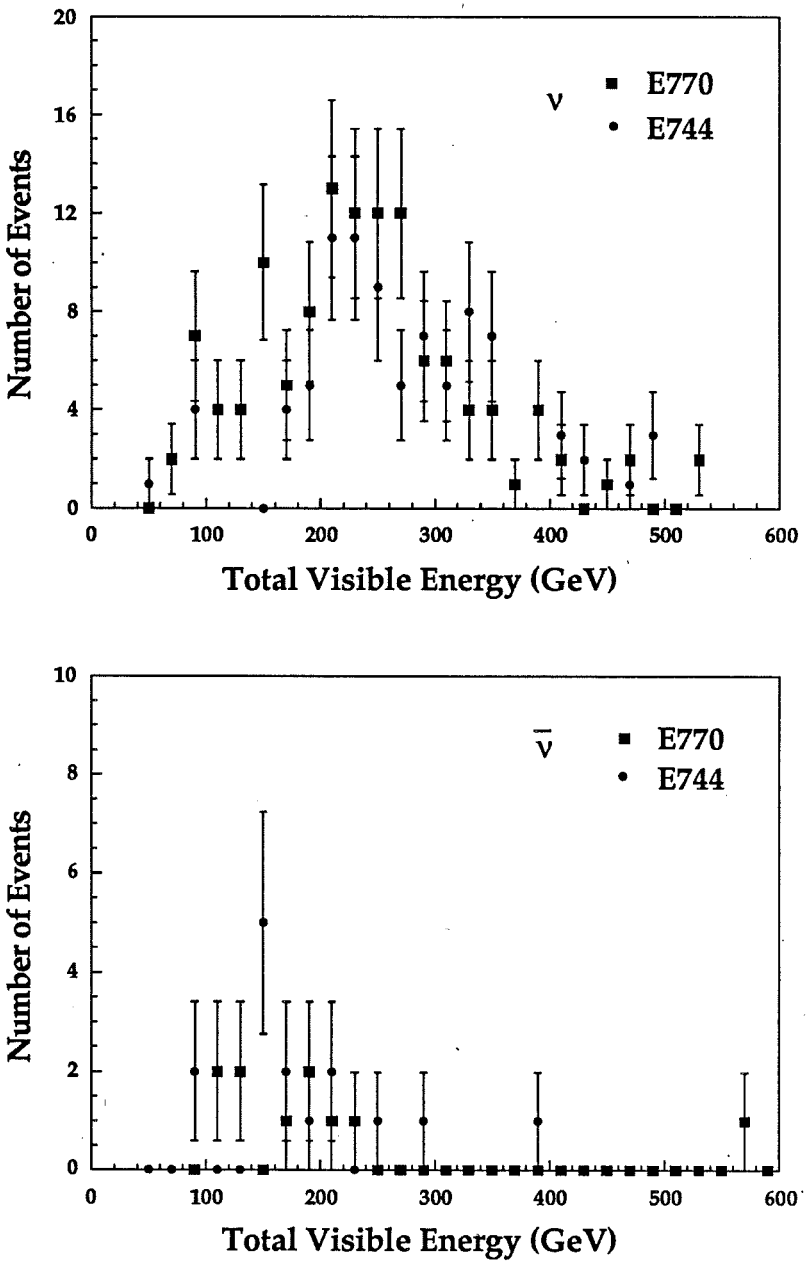

Figure 9.4 The total visible energy for E744 (circles) and E770 (squares) for neutrino (top) and antineutrino-induced events (bottom).

The remainder of this section discusses the agreement between the meson-decay background and the same-sign dimuon data to show that the non-prompt background is the source of the majority of the same-sign data. The reconstructed kinematic distributions of the meson-decay background and the combined E744 and E770 same-sign data are compared in Figures 9.5-9.9 for incident neutrinos and antineutrinos. Note that there is a small additional background from misidentified trimuons and overlays that is not plotted in these figures. Figure 9.5 shows $P_{\mu 2}$, the momentum of the muon with the smaller transverse momentum relative to the hadron shower. Since the available energy to make a second muon is determined by the fragmentation, the figure shows the agreement between fragmentation in the same-sign data and the meson decay background. In addition, the significance of the same-sign excess would not change by varying the momentum cut, except by a reduction in statistics.

Figure 9.6 shows the total visible energy and Figure 9.7 shows the hadron energy distributions. Differences in thresholds for heavy quark production at the hadronic vertex, between the same-sign data and the meson decay background, would show up in the hadron energy distribution. However, the meson decay background and the same-sign data agree in both these variables. Figure 9.8 shows ϕ_{12}, which is the azimuthal angle between the two muons projected on the plane perpendicular to the beam direction. When the second muon is associated with the hadron shower, ϕ_{12} is large. Therefore, both the same-sign data

and the meson-decay background show production at the hadron vertex, not the lepton vertex. The variable P_T, the transverse momentum of the second muon relative to the hadron shower, is given in Figure 9.9. A large P_T in the same-sign data relative to the meson decay background would indicate production of a new object. There is no significant difference between the same-sign data and the meson-decay background. The averages of several important kinematic variables are given in Table 9.4 for the same-sign data and the meson-decay background, which are all consistent.

Same Sign Data and Meson Decay Background

Average Kinematic Values

Kinematic Variable	E744 $\mu^-\mu^-$		E770 $\mu^-\mu^-$	
	Data	Monte Carlo	Data	Monte Carlo
Radius (in)	30.4 ± 3.0	28.1	27.0 ± 3.0	27.6
θ_1 (mrad)	52 ± 4	54	51 ± 5	57
θ_2 (mrad)	40 ± 3	48	45 ± 4	48
$E_{\mu 1}$ (GeV)	97.0 ± 6.8	93.3	95.9 ± 6.9	93.4
$E_{\mu 2}$ (GeV)	19.1 ± 1.8	17.3	19.1 ± 2.0	18.8
E_{vis} (GeV)	259.8 ± 10.0	258.0	248.0 ± 10.0	240.2
E_h (GeV)	141.4 ± 7.8	148.9	133.0 ± 9.3	127.8
x_{vis}	0.19 ± 0.02	0.18	0.19 ± 0.02	0.19
y_{vis}	0.64 ± 0.03	0.64	0.60 ± 0.03	0. 60
θ_{12} (mrad)	83 ± 5	89	86 ± 6	89
Q^2 (GeV^2)	33.8 ± 3.3	35.6	33.1 ± 3.6	32.0
ϕ_{12} (degrees)	123.5 ± 4.9	123.3	133.9 ± 8.0	127.7
$Z_{\mu 2}$	0.16 ± 0.01	0.15	0.17 ± 0.02	0.19
P_{t2} (GeV/c)	0.53 ± 0.05	0.56	0.57 ± 0.06	0.66
m_{12} (GeV^2/c^2)	3.16 ± 0.31	3.10	3.23 ± 0.34	3.20

Table 9.4 Average values of reconstructed kinematic variables for the same-sign data and the meson-decay background Monte Carlo. The subscripts 1 and 2 refer to the primary and secondary muons respectively. θ_1 and θ_2 are the polar angles of the muons with respect to the beam direction, E_μ is the muon energy, E_{vis} is the total visible energy, x_{vis} and y_{vis} are Bjorken scaling variables, θ_{12} is the polar angle between the two muons, ϕ_{12} is the azimuthal angle between the two muons in the plane perpendicular to the beam, $Z_{\mu 2} = E_{\mu 2}/(E_h+E_{\mu 2})$ is the fraction of the energy transfer to the nucleon that is carried by the second muon, and m_{12} is the invariant mass of the dimuon pair.

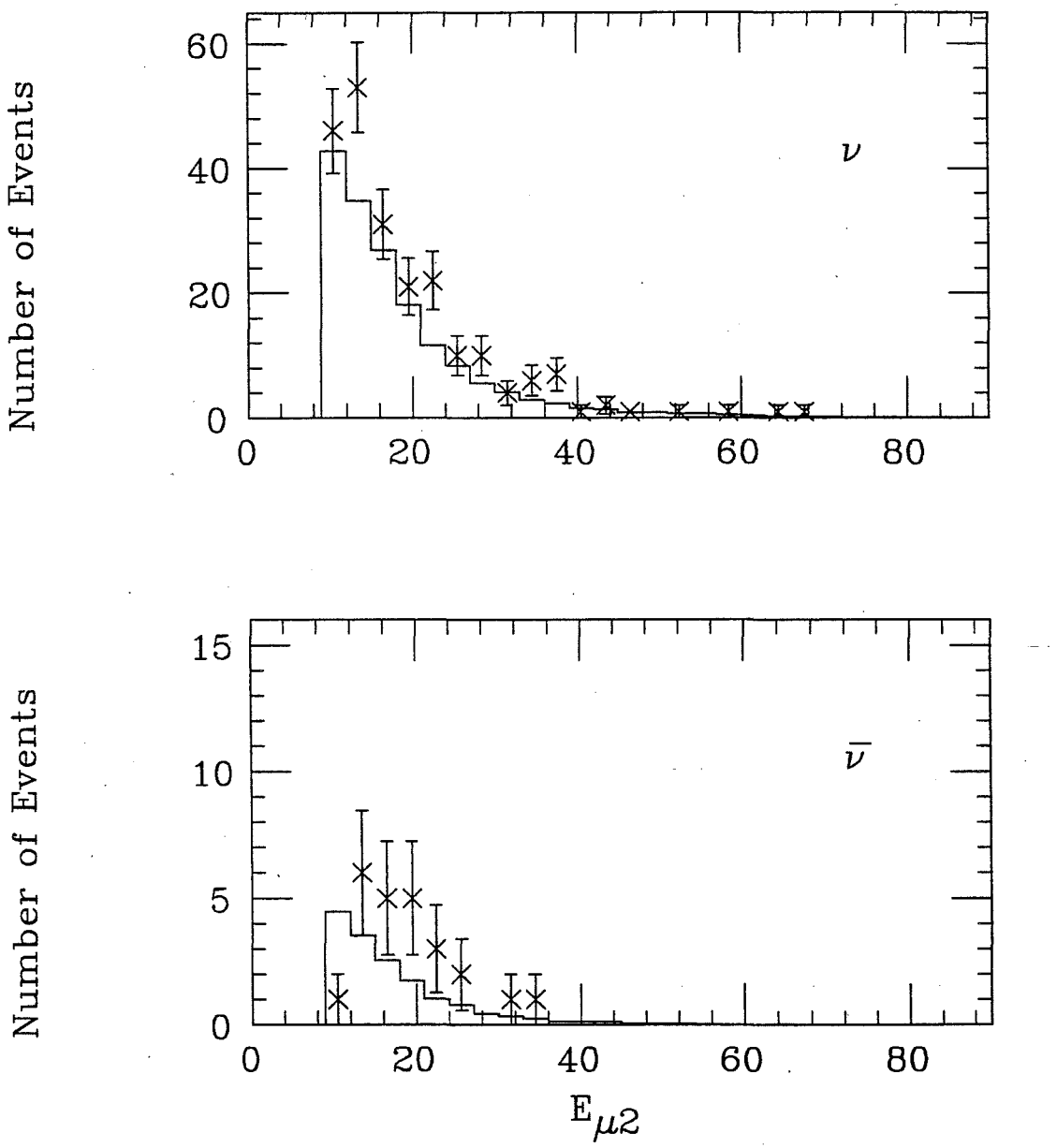

Figure 9.5 The distribution of the momentum of the second muon. The second muon is defined to be that with the smaller transverse momentum relative to the hadron shower direction. The top plot shows neutrinos and the bottom anti-neutrinos. The histogram represents the meson decay background calculation and the points are the same-sign dimuon data from experiments E744 and E770 combined.

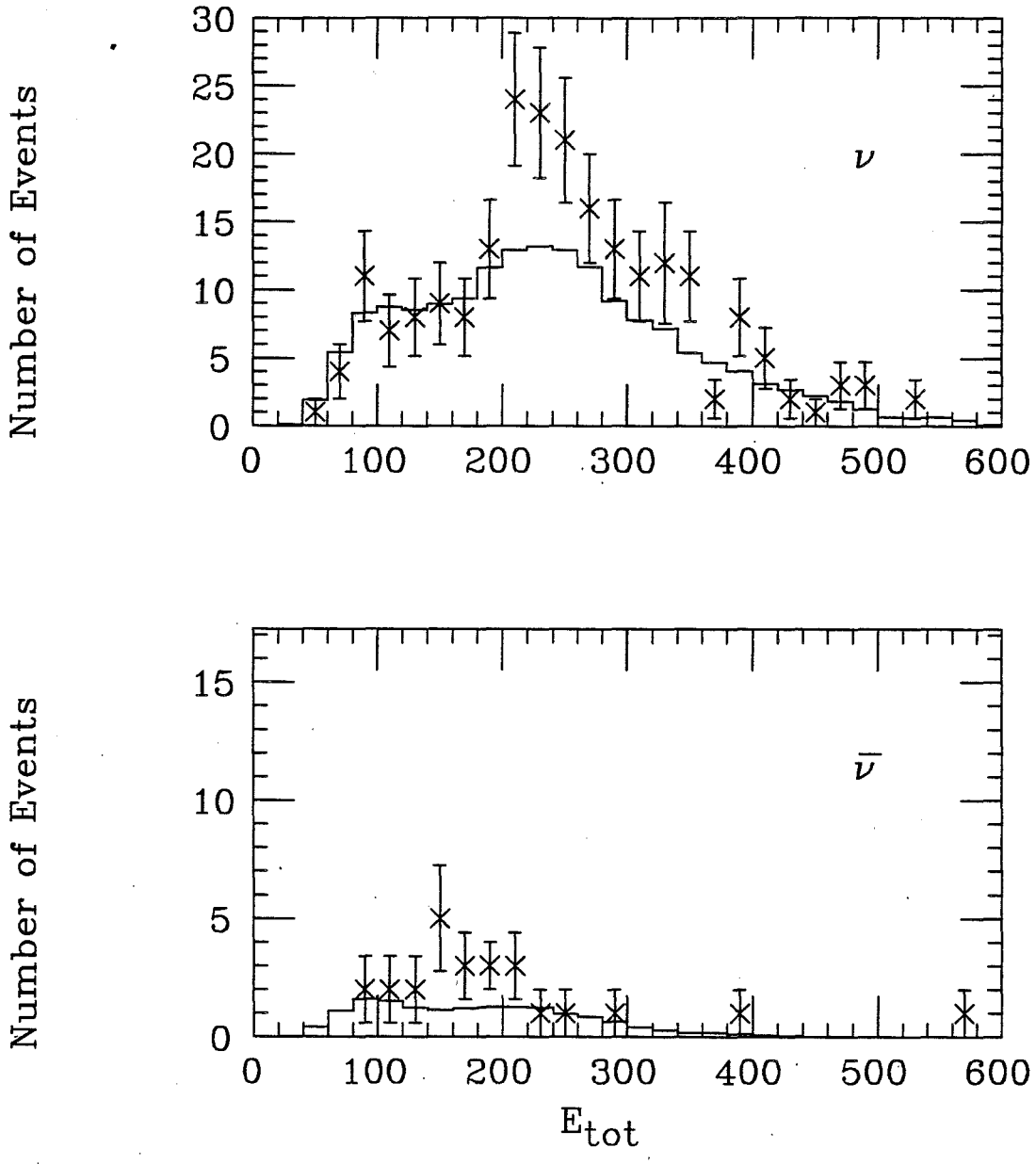

Figure 9.6 The distribution of the total visible energy. The top plot shows neutrinos and the bottom anti-neutrinos. The histogram represents the meson decay background calculation and the points are the same-sign dimuon data from E744 and E770 combined.

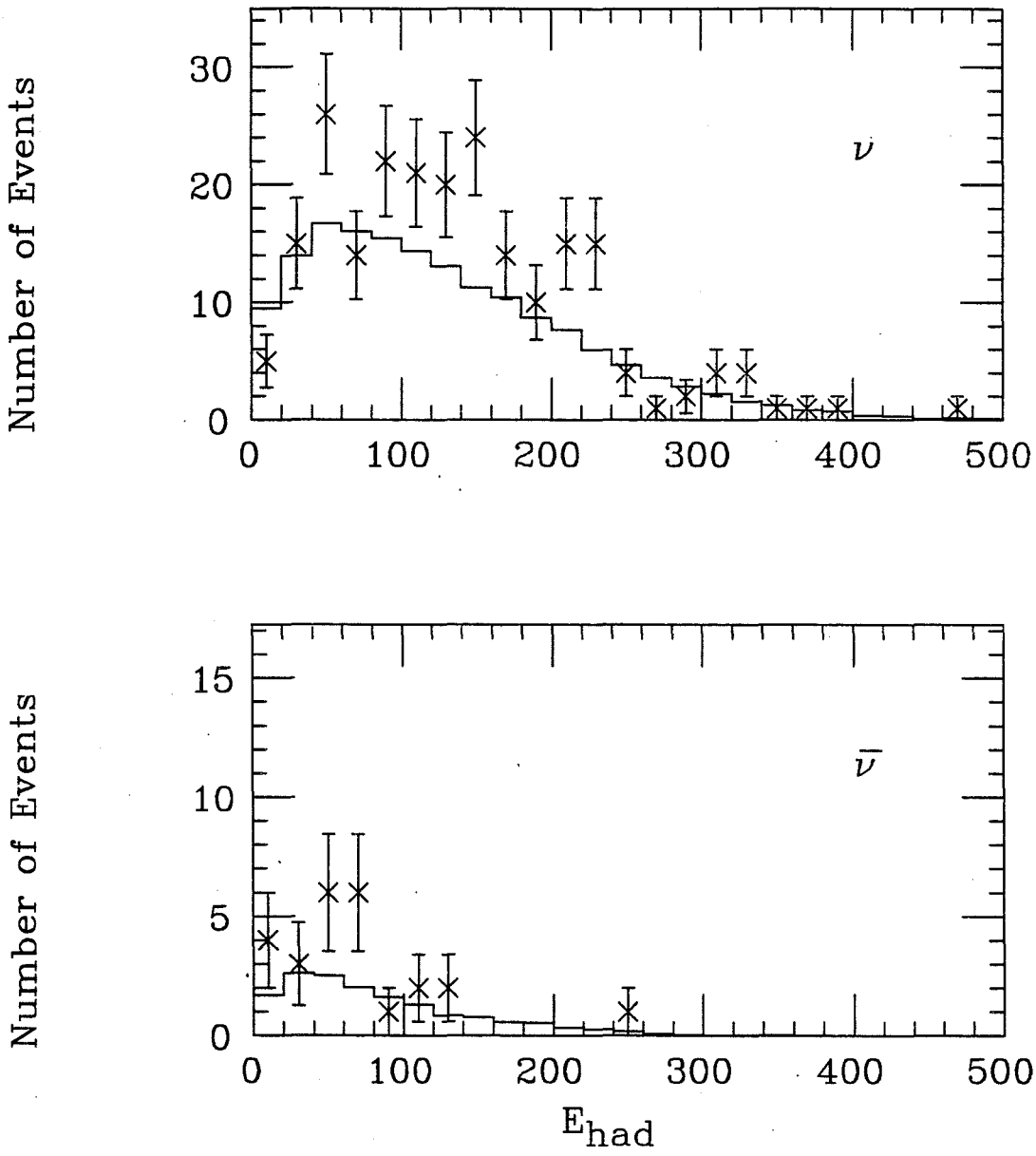

Figure 9.7 The distribution of the total hadron energy. The top plot shows neutrinos and the bottom anti-neutrinos. The histogram represents the meson decay background calculation and the points are the same-sign dimuon data from E744 and E770 combined.

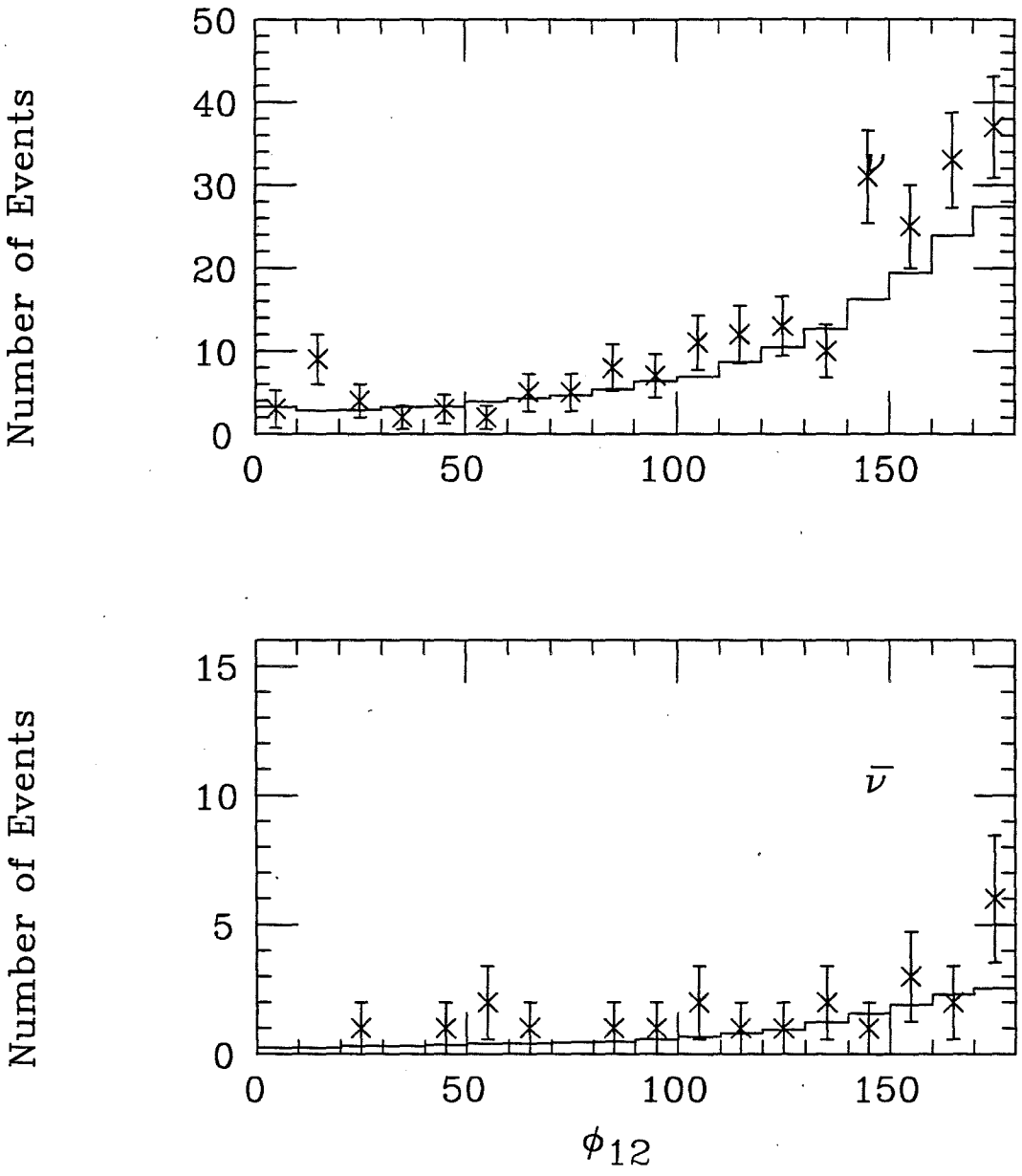

Figure 9.8 The distribution of the variable ϕ_{12}, the azimuthal angle between the two muons in a plane perpendicular to the beam. The top plot shows neutrinos and the bottom anti-neutrinos. The histogram represents the meson decay background calculation and the points are the same-sign dimuon data from E744 and E770 combined.

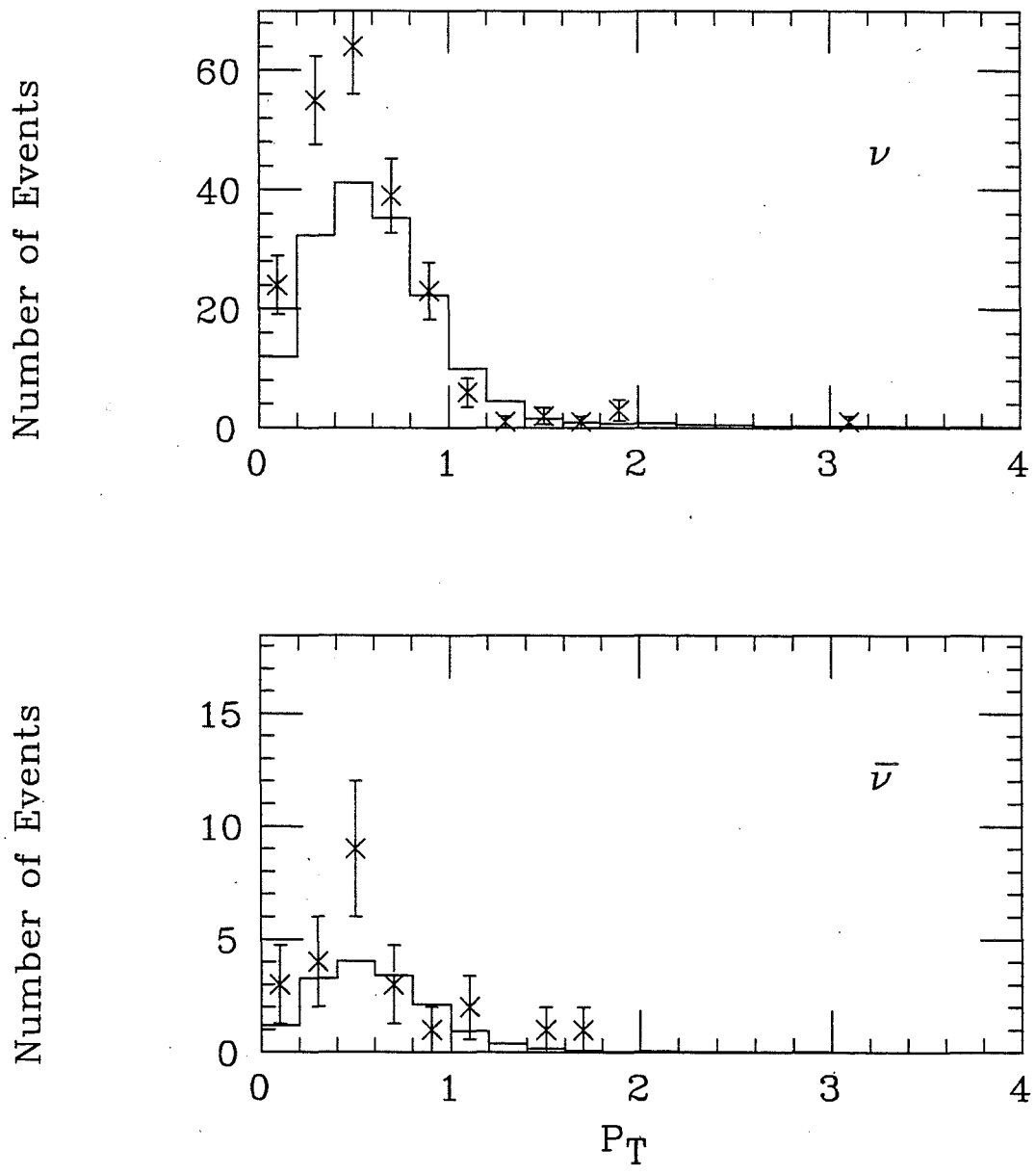

Figure 9.9 The distribution of the variable P_T, the transverse momentum of the second muon relative to the hadron shower direction. The top plot shows neutrinos and the bottom anti-neutrinos. The histogram represents the meson decay background calculation and the points are the same-sign dimuon data from E744 and E770 combined.

9.3 The Rate of Same-Sign Dimuon Production

Before calculating absolute rates of prompt same-sign dimuon production, the same-sign dimuon excess and its normalization must be corrected for the finite size and efficiency of the detector, namely the acceptance and energy smearing. For example, events where either the hadron shower or the muons exited were eliminated as described in Section 3.2 because they could not be properly reconstructed. Also, the reconstructed energy was smeared with respect to the actual energy due to the finite resolution of the detector.

The charged-current events used to normalize the rate must be corrected for acceptance. We use the CCFR charged-current Monte Carlo simulation described in Chapter 4, to provide generated events that are reconstructed in the detector. The high level of agreement between the reconstructed charged-current Monte Carlo events and the charged-current data, as shown in Sections 4.4 and 4.5, lends confidence to the calculated charged-current acceptances. The charged current acceptance is defined as:

$$\text{Acceptance } 1\mu = \frac{M_{1\,r}}{M_{1\,g}}$$

where M_{1r} is the number of reconstructed charged-current Monte Carlo events passing all the selection criteria, and M_{1g} is the number of generated charged-current events within the volume of the detector. The average acceptance for charged-current events was about 91%.

To calculate the effects of the detector acceptance and smearing on the same-sign dimuons, we used generated meson-decay events that were propagated through the detector using the CCFR detector Monte Carlo and reconstructed in the same manner as the data. The acceptance for dimuon events is given by,

$$\text{Acceptance } 2\mu = \frac{M_{2r}}{M_{2g}}$$

where M_{2g} is the number of generated meson-decay events within the volume of the detector that have generated muon momentum above 9 GeV/c and M_{2r} is the number of reconstructed Monte Carlo dimuon events passing all standard dimuon cuts, regardless of the generated momentum. The selection criteria are described in Section 3.2. Provided the kinematic features of the reconstructed meson-decay events reproduce the data, this procedure will give accurate acceptances. Comparisons of the meson-decay background with the data were presented in Section 9.2 where we showed that the kinematics of the meson-decay background match the data. The dimuon acceptances range between 20% to 45% and the average acceptance is about 35%. The acceptance for low energy

dimuons that are defocussed by the toroids is lowest because the low energy muons are bent out of the side of the spectrometer.

To calculate final same-sign dimuon rates for experiments E744 and E770 combined, the data from the two experiments are corrected for acceptance first, then summed to obtain final rates. The data from E744 and E770 must be corrected separately because there were slight differences in the steering of the neutrino beam, which translated into slightly different acceptances for the two experiments. The final rate is given by

$$R = \frac{N_2(E744) + N_2(E770)}{N_1(E744) + N_1(E770)}$$

where N_2 is the corrected excess of dimuons after background subtractions given by,

$$N_2 = \frac{[N_2(\text{raw}) - N_2(\text{background})]}{\text{acceptance } 2\mu}$$

where N_2(raw) is the raw number of same-sign dimuons passing all dimuon selection criteria and N_2(background) is the number of reconstructed background events passing all dimuon selection criteria. Similarly, N_1 is the corrected number of charged-current events given by,

$$N_1 = \frac{C \cdot N_1(\text{raw})}{\text{acceptance } 1\mu}$$

where N_1(raw) is the raw number of charged-current events passing all charged-current selection criteria, and the factor C accounts for the 2 GeV minimum hadron energy requirement imposed on all events because we did not model the detector acceptance at energies below 2 GeV. The factor C is given by,

$$C = \frac{\frac{M_{1r}}{M_1(\text{geom})}}{\frac{N_1(\text{raw})}{N_1(\text{geom})}}$$

where M_1(geom) is the number of charged-current Monte Carlo events passing all charged-current cuts except the hadron energy cut, and N_1(geom) is the number of charged-current data events passing all charged-current cuts except the hadron energy cut.

The results of the same-sign dimuon rate measurement are given in Tables 9.5a-9.5f in visible energy bins for E744, E770, and combined, and for neutrinos and antineutrinos separately. Neutrino-induced rates from E744 agree with those from E770. Antineutrino-induced rates from E744 are higher than those from E770, but the combined rate is consistent with the neutrino-induced rate. Final rates are also given in ν bins in Tables 9.5g and 9.5h for the combined E770 and E744 samples, where ν is the fraction of neutrino energy transferred to the nucleon. Threshold behavior is dependent on ν, which represents the energy available to make

the final state. Since the results from experiments E744 and E770 agree, they are combined to form the rates. The final rates for visible energy between 30 GeV and 600 GeV are

$$\frac{\sigma(\nu N \to \mu^- \mu^- X)}{\sigma(\nu N \to \mu^- X)} = (0.54 \pm 0.23) \times 10^{-4}$$

$$\frac{\sigma(\bar{\nu} N \to \mu^+ \mu^+ X)}{\sigma(\bar{\nu} N \to \mu^+ X)} = (0.52 \pm 0.33) \times 10^{-4}$$

where the errors are statistical and systematic combined. For incident neutrinos, the rate is less than 0.92×10^{-4} at the 90% C.L. For antineutrinos, the rate is less than 1.05×10^{-4} at the 90% C.L. Figure 9.10 shows these rates as a function of incident neutrino energy and Figure 9.11 shows them as a function of ν. The antineutrino- and neutrino-induced rates agree within errors. Also, there is almost no dependence of the rates on incident energy. As a function of ν, the rates begin to rise at ν of about 75 GeV, suggesting a threshold effect at the turning point. The same plot is given in Figures 9.12 and 9.13 for neutrinos, which show in addition the same-sign dimuon rate due to meson-decays. The rate due to $c\bar{c}$ gluon bremsstrahlung, described in Chapter 10, is also shown in these figures. The meson decay rate does not show as steep a rise as a function of ν that is found in the data. However, the two are consistent within the uncertainty

of the data. Furthermore, the energy dependence of the measured rates and the meson-decay rates is the same within the uncertainty of the data.

$$\nu N \rightarrow \mu^-\mu^- X : \text{E744}$$

Visible Energy (GeV)	Raw Single μ^- ($\times 10^3$)	Raw $\mu^-\mu^-$	Raw Event Excess $\mu^-\mu^-$	Accept. Corr. Rate ($\times 10^{-4}$) $\mu^-\mu^-/\mu^-$	90% C.L. Limit ($\times 10^{-4}$) $\mu^-\mu^-/\mu^-$
30-100	247.1	7	-0.88 ± 2.78	-0.06 ± 0.19	0.38
100-200	218.9	17	-6.03 ± 4.84	-0.55 ± 0.44	0.64
200-300	151.6	43	14.23 ± 7.28	1.95 ± 1.00	3.44
300-400	51.0	25	11.29 ± 5.22	4.52 ± 2.09	7.75
400-600	17.7	9	2.85 ± 2.34	3.22 ± 2.46	7.52
30-300	617.6	67	7.33 ± 10.49	0.21 ± 0.30	0.68
300-600	68.7	34	14.14 ± 6.23	4.21 ± 1.86	7.01
total	686.3	101	21.47 ± 13.32	0.55 ± 0.34	1.04

Table 9.5a Calculation of acceptance corrected same-sign rates per charged-current event for neutrino-induced same-sign dimuons in experiment E744. The errors include combined statistics and systematics.

$\nu N \rightarrow \mu^- \mu^- X$: E770

Visible Energy (GeV)	Raw Single μ^- ($\times 10^3$)	Raw $\mu^-\mu^-$	Raw Event Excess $\mu^-\mu^-$	Accept. Corr. Rate ($\times 10^{-4}$) $\mu^-\mu^-/\mu^-$	90% C.L. Limit ($\times 10^{-4}$) $\mu^-\mu^-/\mu^-$
30-100	285.9	9	-0.29±3.17	-0.02±0.19	0.40
100-200	257.0	28	0.70±6.08	0.05±0.47	0.91
200-300	187.2	54	19.56±8.27	2.57±1.08	4.16
300-400	62.4	19	2.17±4.74	0.73±1.60	3.55
400-600	22.0	9	0.86 ± 3.20	0.94 ± 3.32	6.78
30-300	730.0	91	19.97±12.33	0.49±0.30	0.94
300-600	84.3	28	3.03±5.96	0.76±1.50	3.31
total	814.4	119	22.99±15.18	0.51±0.34	0.99

Table 9.5b Calculation of acceptance corrected same-sign rates per charged-current event for neutrino-induced same-sign dimuons in experiment E770. The errors include statistics and systematics.

$\nu N \rightarrow \mu^- \mu^- X$: E744 and E770 combined

Visible Energy (GeV)	Raw Single μ^- ($\times 10^3$)	Raw $\mu^-\mu^-$	Raw Event Excess $\mu^-\mu^-$	Accept. Corr. Rate ($\times 10^{-4}$) $\mu^-\mu^-/\mu^-$	90% C.L. Limit ($\times 10^{-4}$) $\mu^-\mu^-/\mu^-$
30-100	533.0	16	-1.17 ± 4.22	-0.04±0.14	0.19
100-200	475.9	45	-5.33 ± 7.77	-0.22±0.32	0.31
200-300	338.8	97	33.79 ± 12.08	2.27±0.74	3.49
300-400	113.4	44	13.46 ± 7.42	2.48±1.29	4.60
400-500	31.4	14	2.58 ± 3.97	1.57±2.66	5.93
500-600	8.3	4	1.22 ± 2.03	0.44±0.89	1.90
30-300	1347.6	158	27.29 ± 19.12	0.36±0.21	0.72
300-600	153.0	62	17.17 ± 9.33	2.33±1.18	4.26
total	1500.7	220	44.46 ± 24.38	0.53±0.24	0.92

Table 9.5c Calculation of acceptance corrected same-sign rates per charged-current event for neutrino-induced same-sign dimuons: E770 and E744 combined. The errors include statistics and systematics.

$\bar{\nu}\,N \rightarrow \mu^+\,\mu^+\,X$: E744

Visible Energy (GeV)	Raw Single μ^+ ($\times 10^3$)	Raw $\mu^+\mu^+$	Raw Event Excess $\mu^+\mu^+$	Accept. Corr. Rate ($\times 10^{-4}$) $\mu^+\mu^+/\mu^+$	90% C.L. Limit ($\times 10^{-4}$)
30-100	66.9	2	0.55 ± 1.42	0.15 ± 0.39	1.14
100-200	40.9	8	5.12 ± 2.85	2.75 ± 1.53	5.45
200-300	16.9	4	1.69 ± 2.02	2.09 ± 2.50	7.24
30-300	124.7	14	7.36 ± 3.81	1.12 ± 0.58	2.07
300-600	3.5	1	0.26 ± 1.00	1.38 ± 5.38	18.03
total	128.2	15	7.62 ± 3.96	1.12 ± 0.58	2.06

Table 9.5d Calculation of acceptance corrected same-sign rates per charged-current event for antineutrinos and limits in experiment E744. The errors include statistics and systematics.

$\bar{\nu}\, N \rightarrow \mu^+ \mu^+ X$: E770

Visible Energy (GeV)	Raw Single μ^+ ($x10^3$)	Raw $\mu^+\mu^+$	Raw Event Excess $\mu^+\mu^+$	Accept. Corr. Rate ($x10^{-4}$) $\mu^+\mu^+/\mu^+$	90% C.L. Limit ($x10^{-4}$)
30-100	90.2	0	-1.86±1.02	-0.39±0.21	0.48
100-200	52.9	7	3.16±2.68	1.27±1.08	3.24
200-300	21.1	2	-0.93±1.45	-1.03±1.61	3.98
30-300	164.2	9	0.37±3.15	0.04±0.36	0.78
300-600	4.3	1	0.15±1.00	0.73±4.87	16.08
total	168.5	10	0.52±3.33	0.06±0.37	0.79

Table 9.5e Calculation of acceptance corrected same-sign rates per charged-current event for antineutrinos and limits in experiment E770. The errors include statistics and systematics.

$\bar{\nu}\,N \rightarrow \mu^+\mu^+X$: E744 and E770 combined

Visible Energy (GeV)	Raw μ^+ ($x10^3$)	Raw $\mu^+\mu^+$	Raw Event Excess $\mu^+\mu^+$	Accept. Corr. Rate ($x10^{-4}$) $\mu^+\mu^+/\mu^+$	90% C.L. Limit ($x10^{-4}$) $\mu^+\mu^+/\mu^+$
30-100	157.1	2	-1.31 ± 1.75	-0.16 ± 0.21	0.18
100-200	93.8	15	8.28 ± 3.91	1.92 ± 0.91	3.41
200-300	38.0	6	0.76 ± 2.49	0.43 ± 1.45	2.81
30-300	288.9	23	7.73 ± 4.94	0.51 ± 0.32	1.04
300-600	7.8	2	0.41 ± 1.39	1.04 ± 3.62	6.97
total	296.7	25	8.14 ± 5.17	0.52 ± 0.33	1.05

Table 9.5f Calculation of acceptance corrected same-sign rates per charged-current event for antineutrinos and limits, E770 and E744 combined. The errors include statistics and systematics.

$\nu N \rightarrow \mu^- \mu^- X$: ν bins

ν (GeV)	Raw μ^- ($\times 10^3$)	Raw $\mu^-\mu^-$	Raw Event Excess $\mu^-\mu^-$	Accept. Corr. Rate ($\times 10^{-4}$) $\mu^-\mu^-/\mu^-$	90% C.L. Limit ($\times 10^{-4}$) $\mu^-\mu^-/\mu^-$
20-50	817.4	13	-9.03 ± 15.98	-0.23 ± 0.10	-0.06
50-100	345.4	49	4.29 ± 7.83	0.21 ± 0.39	0.86
100-150	166.0	54	15.91 ± 7.92	1.64 ± 0.82	2.98
150-200	91.5	43	14.27 ± 6.93	2.65 ± 1.29	4.77
200-250	45.5	36	15.83 ± 6.22	5.40 ± 2.13	8.89
>250	34.7	25	3.21 ± 5.29	1.34 ± 2.22	4.98
20-150	1329.0	116	11.16 ± 13.52	0.15 ± 0.19	0.46
>150	171.7	104	33.31 ± 11.6	3.10 ± 1.09	4.88
>20	1500.7	220	44.46 ± 24.38	0.53 ± 0.24	0.92

Table 9.5g Calculation of acceptance corrected same-sign rates per charged-current event for neutrino-induced same-sign dimuons in E770 and E744 in bins of $\nu = yE_{tot}$. The errors include statistics and systematics.

$\bar{\nu} N \rightarrow \mu^+ \mu^+ X$: in ν bins

ν (GeV)	Raw μ^+ ($\times 10^3$)	Raw $\mu^+\mu^+$	Raw Event Excess $\mu^+\mu^+$	Accept. Corr. Rate ($\times 10^{-4}$) $\mu^+\mu^+/\mu^+$	90% C.L. Limit ($\times 10^{-4}$) $\mu^+\mu^+/\mu^+$
20-50	223.1	5	1.00 ± 2.26	0.10 ± 0.23	0.48
50-100	49.3	11	4.94 ± 2.41	1.87 ± 1.25	3.92
100-150	15.4	6	2.57 ± 2.44	2.87 ± 2.74	7.37
150-200	6.0	2	0.16 ± 1.45	0.43 ± 3.89	6.82
200-250	2.2	0	-1.01 ± 1.42	-6.73 ± 9.44	8.76
>250	0.9	1	0.48 ± 1.43	6.57 ± 19.43	38.44
20-150	290.8	22	8.51 ± 4.80	0.58 ± 0.33	1.11
>150	9.0	3	-0.37 ± 1.75	-0.66 ± 2.99	4.24
>20	296.7	25	8.14 ± 5.17	0.52 ± 0.33	1.05

Table 9.5h Calculation of acceptance corrected same-sign rates per charged-current event for antineutrinos and limits, E770 and E744 binned by $\nu = yE_{tot}$. The errors include statistics and systematics.

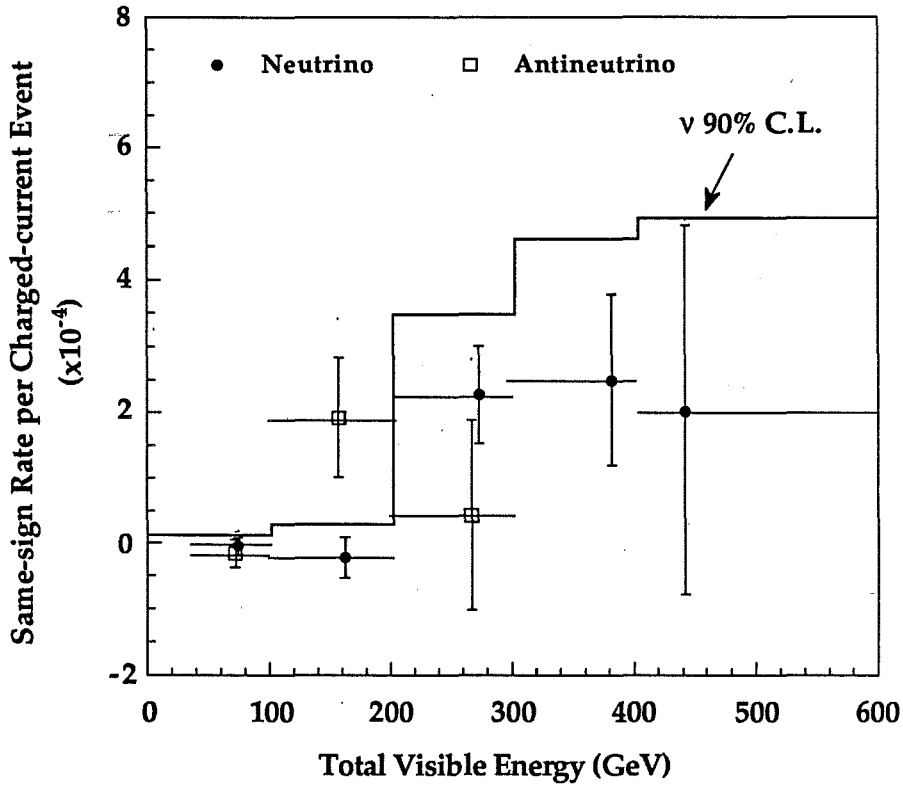

Figure 9.10 Neutrino and antineutrino prompt same-sign dimuon rates and 90% C.L. upper limit per charged-current event measured in E744 and E770, as a function of total visible energy.

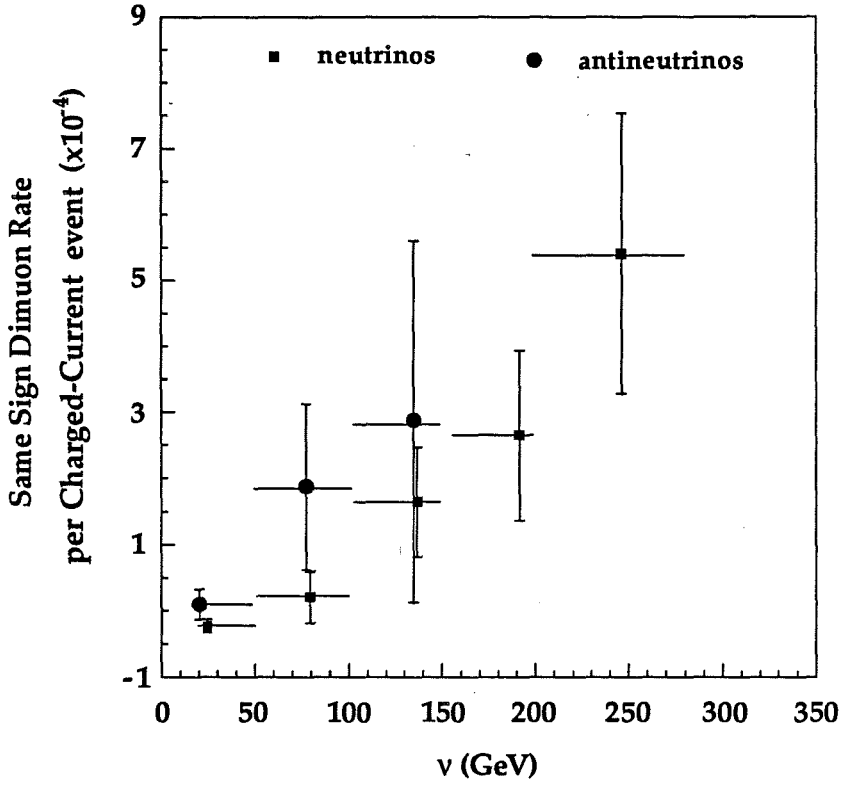

Figure 9.11 Prompt same-sign dimuon rates for neutrinos and antineutrinos per charged-current events as a function of ν, the fractional energy transfer to the nucleon.

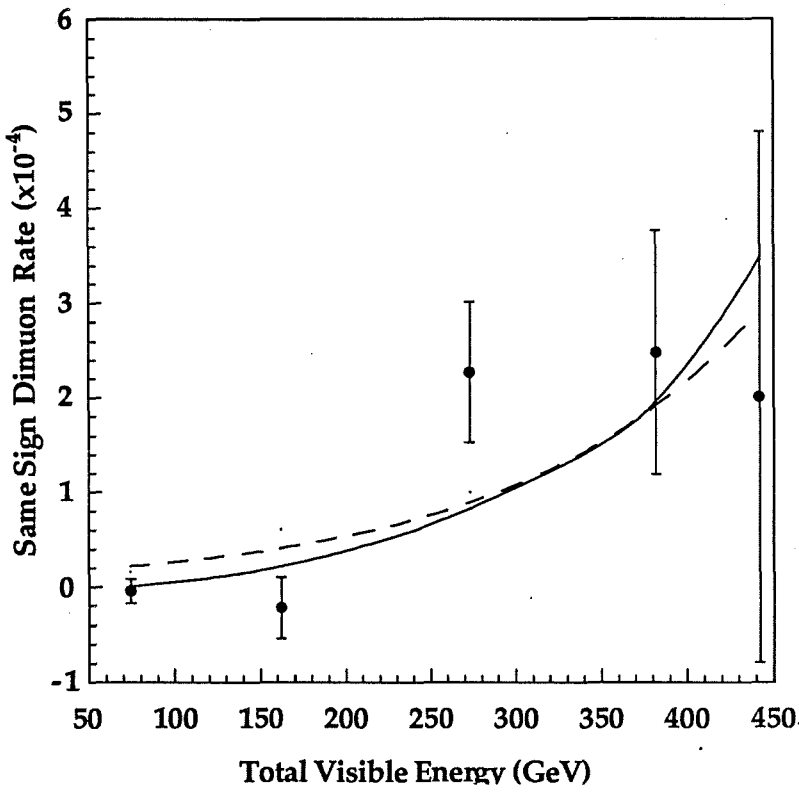

Figure 9.12 Background subtracted same-sign dimuon rates for neutrinos plotted as a function of the total visible energy. The solid curve is the result of the gluon bremsstrahlung Monte Carlo increased by a factor of 60 to the same level as the data. The gluon bremsstrahlung model has a factor of 4.2 uncertainty. The dashed curve is same-sign rate due to meson decays, scaled by 0.30 to the level of the data. It has an uncertainty of 11%.

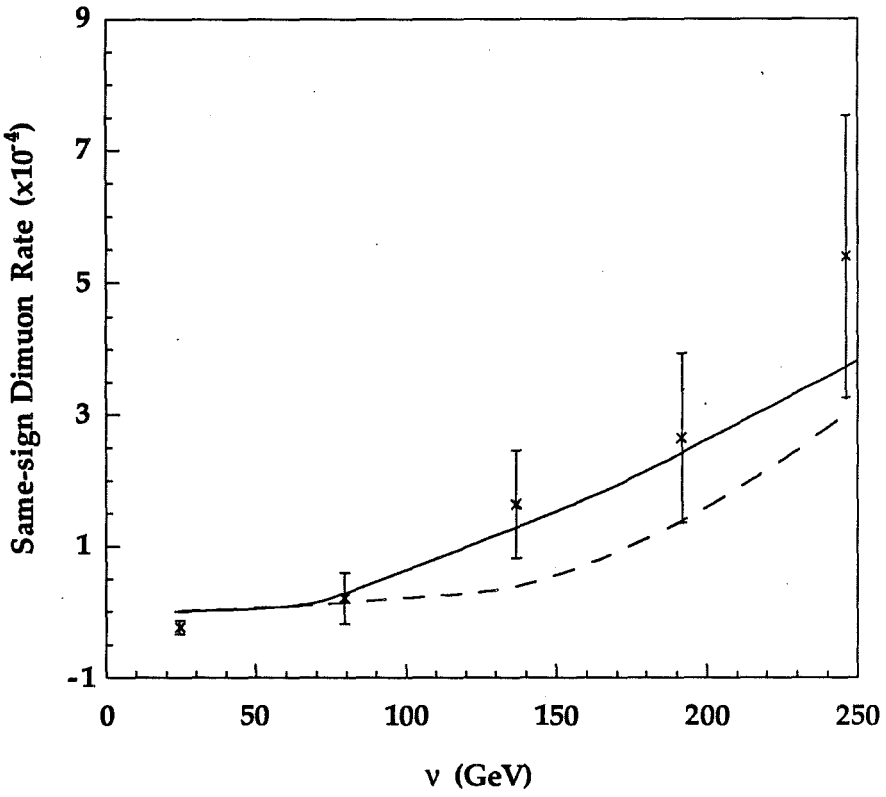

Figure 9.13 Background subtracted same-sign dimuon rates for neutrinos plotted as a function of ν, the fractional energy transfer to the nucleon. The solid curve is the result of the gluon bremsstrahlung Monte Carlo increased by a factor of 60 to the same level as the data. There is a factor of 4.2 uncertainty in the gluon bremsstrahlung rate. The dashed curve is the same-sign dimuon rate for the meson decay background, with an 11% uncertainty.

Chapter 10

The Same Sign Dimuon Excess

10.1 Introduction

Although the meson-decay background accounts sufficiently for the observed same-sign dimuons, it is interesting to explore additional sources of same-sign dimuons, in particular prompt same-sign dimuons. Processes that produce a prompt same-sign dimuon signal are all next to leading order in QCD. As such, the probability of prompt same-sign dimuon production is very small. For example, $c\bar{c}$ gluon bremsstrahlung produces same-sign dimuons in neutrino-induced interactions when the $\bar{c}$ quark semileptonically decays to a μ^-, as shown in Figure 1.3. At a rate less than 10^{-5} per charged-current interaction, this process is thought to have the highest probability to produce same-sign dimuons. Another source of same-sign dimuons is D^0-$\bar{D}^0$ mixing, shown in Figure 1.4. In this process a charmed quark, produced at the hadronic vertex of a charged-current interaction, fragments to a D^0 meson changes into a $\bar{D}^0$ meson. The $\bar{D}^0$ meson semileptonically decays, producing the second μ^-. A third mechanism that produces same-sign dimuons is bottom quark production, shown in Figure 1.5. Here, a $\bar{b}$ quark, produced at the hadronic vertex of a charged-current event, decays to a $\bar{c}$ quark that semileptonically decays. Each of these processes is discussed in detail below.

10.2 D^0-D^0 Mixing

The cross section for same-sign dimuon production through D^0-$\bar{D}^0$ mixing can be expressed as follows,

$$\frac{d\sigma^3(\nu N \rightarrow \mu^- \mu^- X)}{dx\,dy\,dz} = \frac{d\sigma^2(\nu N \rightarrow c\mu^-)}{dx\,dy} \cdot D(z) \cdot P(D^0 \rightarrow \bar{D}^0) \cdot B(\bar{D}^0 \rightarrow \mu^- \nu X)$$

where the first factor is the cross section for charm quark production at the hadronic vertex. D(z) is the probability for a charmed quark to fragment to a D^0 meson where z is the fraction of momentum carried by the D^0 meson. $B(D^0 \rightarrow \mu^- \nu X)$ is the branching fraction for semileptonic decay of the D^0 meson, and $P(D^0 \rightarrow \bar{D}^0)$ is the probability for D^0-$\bar{D}^0$ mixing to occur. Current theoretical limits on the probability of D^0-$\bar{D}^0$ mixing are less than 5×10^{-4} [50]. This is small because mixing is suppressed due to the difficulty in producing the heavy charmed quark in the final state. The semileptonic branching fraction $B(D^0 \rightarrow \mu^- \nu X)$ is about 7% and D(z) is about 60% measured in the neutrino emulsion experiment E531 at Fermilab [51]. The first factor can be approximated by the opposite-sign dimuon production rate, divided by the semileptonic branching fraction for D meson decay. Opposite sign dimuons are produced by the fragmentation and decay of a charmed quark that is produced at the vertex. The CCFR collaboration measured the rate of opposite sign dimuon production to be $(0.91 \pm 0.03) \times 10^{-2}$ over the same energies as the results in this dissertation [3]. These factors yield a rate less than about 0.02×10^{-4} per charged-current

event due to D^0-$\bar{D}^0$ mixing in neutrino-nucleon interactions averaged over the neutrino spectrum of this experiment. This is more than an order of magnitude smaller than our measured prompt rate of $(0.53\pm0.24)\times10^{-4}$. Furthermore, current experimental limits on D^0-$\bar{D}^0$ mixing by the tagged photon spectrometer collaboration at Fermilab are 0.37% at the 90% C.L. [52]. Using this limit, the upper limit on the rate of prompt same-sign dimuon production is about 0.1×10^{-4}, which is lower than our observed rate. Therefore, D^0-$\bar{D}^0$ mixing cannot contribute significantly to the observed sample of same-sign dimuons.

10.3 Bottom Production

The cross section for bottom production of same-sign dimuons is given by

$$\frac{d^3\sigma(\nu N\rightarrow\mu^-\mu^- X)}{dx\,dy\,dz_b\,dz_c} = \frac{d\sigma(\nu N\rightarrow\mu^-\bar{b}X)}{dy}\cdot D_b(z_b)\cdot B(\bar{b}\rightarrow\bar{c}Qq)\cdot D_c(z_c)\cdot B(D\rightarrow\mu^-\nu X)$$

where the first factor is the cross section for bottom production that depends on $\bar{c}$ (x), the charmed quark content of the nucleon and the effective masses of the c and b quarks. The other factors, $D_b(z_b)$ (and $D_c(z_c)$) are the fragmentation functions for producing a B (D) meson, carrying a fraction z_b (z_c) of the initial b (c) quark momentum. Finally, $B(\bar{b}\rightarrow\bar{c}Qq)$ is the branching fraction for b quark decay. Strictly speaking this should be the semileptonic decay of the B meson. But because the b quark is much

heavier than the spectator quarks in the B meson, they can be ignored. The last factor above is the branching fraction for semileptonic decay of the D meson.

Bottom production at the vertex is suppressed by phase space constraints due to the heavy mass of the b quark, which is about 5.2 GeV [44] compared to the mass of the charmed quark that is about 1.3 GeV [54]. In addition, the charmed quark content of the nucleon is small, since the c quark in the nucleon comes mainly from gluon fusion [53]. Therefore, the first term above is quite small. In addition, there are two branching fractions on the order of 10^{-2}. Barger *et al.* calculated the rate of same-sign dimuon production from bottom production to be less than 10^{-5} at 250 GeV for muon momenta greater than 9 GeV [53]. This is is over an order of magnitude smaller than our rate of $(2.27 \pm 0.74)\times10^{-4}$ at the same energies.

10.4 $c\bar{c}$ Gluon Bremsstrahlung

The cross section for $c\bar{c}$ gluon bremsstrahlung production of same-sign dimuons can be expressed as,

$$\frac{d^3\sigma(\nu N\rightarrow\mu^-\mu^- X)}{dx\,dy\,dz} = \frac{d\sigma(\nu N\rightarrow c\,\bar{c}\,\mu^- q')}{dy} \cdot D_{\bar{c}\rightarrow\bar{D}^0}(z) \cdot B(\bar{D}^0\rightarrow\mu^-\nu X) \qquad 10.1$$

where the first factor is the cross section for $c\bar{c}$ production in the neutrino interaction that depends on the effective mass of the charmed quark and

quark distributions in the nucleon. The second factor is the function describing $\bar{c}$ quark fragmentation to a $\bar{D}^0$ meson, and the third factor is the branching fraction for the semileptonic decay of the $\bar{D}^0$ meson.

This cross section is very sensitive to the effective mass of the charm quark m_c, because it controls the threshold for $c\bar{c}$ production. The gluon must have at least $2m_c$ to produce a $c\bar{c}$ pair. Furthermore, since most radiated gluons are soft, $c\bar{c}$ production is less probable for larger m_c. A mass for the charmed quark can be derived from the mass of the J/Ψ meson, which is composed of c and $\bar{c}$ valence quarks. It is about 3.10 GeV/c^2 [44] which makes m_c equal to 1.55 GeV/c^2 from half the J/Ψ mass. In perturbative QCD the mass of the charm quark is a threshold parameter, not a physical mass. More appropriate to the $c\bar{c}$ gluon bremsstrahlung environment are measurements of opposite sign dimuon production by the CCFR collaboration that yield m_c equal to 1.34 ± 0.33 GeV/c^2 [54]. For $c\bar{c}$ gluon bremsstrahlung, it is suggested that m_c should vary with the amount of momentum transfer, q^2 of the gluon according to equation 10.2 [24].

$$m_c(q^2) = m_0 \left[\frac{\ln\left(\frac{4\,m_0^2}{\Lambda_{QCD}^2}\right)}{\ln\left(\frac{q^2}{\Lambda_{QCD}^2}\right)} \right]^{\frac{12}{25}} \qquad 10.2$$

where m_0 is the charm quark mass measured in opposite sign dimuon production and Λ_{QCD} is the scale of the nucleon structure functions.

The rate of same-sign dimuon production from $c\bar{c}$ gluon bremsstrahlung has been calculated by Cudell *et al.* to be less than 0.7×10^{-4} per charged-current event at 200 GeV [24]. There were ambiguities in the choice of several parameters in their calculation, which were exploited in order to get the largest acceptable rate that agreed with available measurements prior to E744 [9]. The ambiguities were:

- the choice of the charm mass parameter, m_0 in equation 10.2,
- the choice of the structure function parametrization,
- the scale of the structure functions (Λ_{QCD}),
- the scale of the running coupling $\alpha(Q^2)$,
- the measurement error on the muon momentum cut,
- and the fragmentation function describing the charmed quark fragmentation to a D meson.

We revisit the calculation in light of the new results presented in this dissertation, the recent results on the charm mass from CCFR [54], and new results on structure functions by the CCFR experiment [18].

10.4.1 The $c\bar{c}$ Monte Carlo

Our $c\bar{c}$ Monte Carlo is based on the calculation by Cudell *et al.* [24]. It is a first order QCD calculation of the process, which uses the differential cross-section for $\nu q \rightarrow \mu^- c\bar{c}q'$ calculated by Barger *et al* [55]. The structure functions are given by Buras-Gaemers parametrizations of CCFR structure

functions [19]. The underlying charged-current event is given by the charged-current Monte Carlo simulation described in Chapter 4, so the calculated rates are over the same range of energies as our observed charged-current data.

Because the calculation is very sensitive to $m_c(q^2)$ the calculation is also sensitive to Λ_{QCD}. We use our parametrization of the structure functions measured in E744 and E770, which set Λ_{QCD} at $220 \pm 25 \pm 40$ MeV where the first error is statistical and the second systematic [22]. There is a 30% uncertainty in the calculation of the rate over the energies in this experiment due to the uncertainty in Λ_{QCD} which is determined by varying it between 180 MeV and 260 MeV. The Q^2 of our experiment ranges between 0 GeV^2/c^2 and 100 GeV^2/c^2, and averages 33 GeV^2/c^2. The calculation uses the value of m_c equal to 1.34 ± 0.33 GeV/c^2 from opposite sign dimuon production in experiment E744 [54]. An uncertainty in the calculation of a factor of four is due to the uncertainty in m_0 which was determined by calculating the rate at m_0 equal to 1.0 GeV/c^2 and m_0 equal to 1.7 GeV/c^2, also over the Q^2 range of our experiment.

There has been some question in the past about the choice of the q^2 scale for the running coupling constant, $\alpha(m_g^2)$ or $\alpha(m_g^2 - 4m_c^2)$ where m_g is the effective mass of the gluon. We use α at the scale of $m_g^2 - 4m_c^2$.

Cudell *et al.* included an uncertainty in the calculation due to muon momentum measurement error. The momentum resolution of our

detector is 11% and is understood to better than 1% as described in Section 3.1.4, so this source of uncertainty is negligible in our experiment.

Fragmentation of a c-quark to a D-meson is modeled with the Peterson fragmentation function [56] given by,

$$D(z) = \frac{1}{z\left(1 - \frac{1}{z} - \frac{\varepsilon}{1-z}\right)^2}$$

where $z = P_D/P_c$, the ratio of the D-meson momentum to the c-quark momentum. This function successfully describes charm fragmentation in e^+e^- collisions [57]. For example, the ARGUS collaboration studied the production of D^{*+} mesons in e^+e^- collisions with 10 GeV in the center of mass frame [58]. The average invariant mass $\sqrt{W^2}$, of our same-sign dimuon data is about 16 GeV. Therefore, we use ε equal to 0.19 ± 0.03 obtained with fits to ARGUS fragmentation data. The Peterson fragmentation function also provides a good model of charmed quark fragmentation in ν-N deep inelastic scattering [3]. A similar value for ε is obtained with data from the Fermilab neutrino emulsion experiment E531, at an average incident neutrino energy of 54 GeV [51]. Their data was analyzed with a cut of W^2 greater than 30 GeV^2 to render it applicable to our data with W^2 greater than 30 GeV^2. The value for ε extracted from E531 was 0.181 ± 0.060 [3] which is consistent with the ARGUS result.

The Peterson fragmentation function is applied in the gluon rest frame. This is analogous to the center of mass frame in e^+e^- collisions or

the W boson-nucleon center of mass frame in neutrino opposite-sign dimuon production. A factor of 1.2 uncertainty in the calculated rate of $c\bar{c}$ gluon bremsstrahlung due to the uncertainty in ε is determined by varying it between 0.16 and 0.21.

10.4.2 $c\bar{c}$ Monte Carlo Predictions

The rate of $c\bar{c}$ gluon bremsstrahlung with m_0 equal to 1.34 GeV/c^2 and Λ_{QCD} equal to 220 MeV is $(9 \pm 39) \times 10^{-7}$ per charged-current event for incident neutrinos integrated over the CCFR energy spectrum, or less than 0.07×10^{-4} per charged-current event at the 90% C.L. The error is composed of a factor of four error on m_0, the 30% error on Λ_{QCD}, and the factor of 1.2 error on ε. Our measured rate of prompt same-sign dimuon production, corrected for acceptance, is $(0.53 \pm 0.24) \times 10^{-4}$ per charged current event. The theoretical prediction is within 2σ of the measured same-sign dimuon rates.

To see if there is a more pronounced result in different energy bins, we give the calculated rate due to $c\bar{c}$ gluon bremsstrahlung as a function of incident neutrino energy in Figure 9.12, along with our measured rate and the calculated rate due to the meson decay background. For the comparison only, the $c\bar{c}$ and meson decay rates are normalized to the data. The energy dependence of the rates is the same for all three sources.

Figure 9.13 compares the rates as a function of ν, where ν is the fraction of incident neutrino energy transfer to the nucleon. The ν-dependence shows how the rates depend on the available energy for production of the second muon. Here the $c\bar{c}$ rates and meson decay rates

are also normalized to the data rates to compare the shape of the ν-dependences. The data rates are consistent with $c\bar{c}$. However, they are also indistinguishable from the non-prompt meson decay background. It is interesting that the meson-decay rate does not show the steep rise above 75 GeV that the $c\bar{c}$ rate does. This is probably because there is a threshold for $c\bar{c}$ production at the hadronic vertex due to the heavy charmed quark mass. The meson-decay rate does not have such a threshold, since the second muon comes from decays of hadrons in the hadron shower.

For further comparison between $c\bar{c}$ gluon bremsstrahlung and our measured rates, the generated $c\bar{c}$ events were propagated through the detector and reconstructed. The number of events due to $c\bar{c}$ gluon bremsstrahlung were subtracted off the same-sign dimuon signal along with the other backgrounds and the remaining acceptance corrected rate was calculated again. The result of this calculation is a prompt rate of

$$\frac{\sigma(\nu N \rightarrow \mu^- \mu^- X)}{\sigma(\nu N \rightarrow \mu^- X)} = (0.52 \pm 0.24) \times 10^{-4}$$

or less than 0.91×10^{-4} at the 90% C.L. There is not a significant difference between this rate and the rate measured without subtracting $c\bar{c}$ events. This is because the simulation predicted only one $c\bar{c}$ event would be observed in experiments E744 and E770. Table 10.1 gives the number of reconstructed same-sign dimuon events from $c\bar{c}$ gluon bremsstrahlung and the number of same-sign dimuon events remaining after the

ν (GeV)	Data Event Excess $\mu^-\mu^-$	$c\bar{c}$ $\mu^-\mu^-$
20-50	-9.03 ± 15.98	2.2×10^{-3}
50-100	4.29 ± 7.83	5.2×10^{-2}
100-150	15.91 ± 7.92	0.19
150-200	14.27 ± 6.93	0.18
200-250	15.83 ± 6.22	0.20
>250	3.21 ± 5.29	0.32
20-150	11.16 ± 13.52	0.24
>150	33.31 ± 11.6	0.70
total	44.46 ± 24.38	0.94

Total Energy (GeV)	Data Event Excess $\mu^-\mu^-$	$c\bar{c}$ $\mu^-\mu^-$
30-100	-1.17 ± 4.22	6.4×10^{-3}
100-200	-5.33 ± 7.77	0.15
200-300	33.79 ± 12.08	0.36
300-400	13.46 ± 7.42	0.30
400-500	2.58 ± 3.97	0.12
>500	1.22 ± 2.03	0.014
30-300	27.29 ± 19.12	0.51
>300	17.17 ± 9.33	0.43
total	44.46 ± 24.38	0.94

Table 10.1 The number of expected same-sign dimuon events from $c\bar{c}$ gluon bremsstrahlung and the number of excess same-sign dimuon events observed in the data for E770 and E744 combined in bins of ν, the fraction of energy transfer to the nucleon (left), and total energy bins (right). The errors on the data excess are systematic and statistical uncertainties combined. There is factor of 4.2 uncertainty in the $c\bar{c}$ gluon bremsstrahlung numbers.

background subtractions as a function of incident energy and ν. None of the bins show an excess of $c\bar{c}$ events over data events.

To see if there are kinematic signatures we can use to identify $c\bar{c}$ gluon bremsstrahlung, the kinematic distributions of the reconstructed $c\bar{c}$ Monte Carlo events are compared to those of the reconstructed meson decay Monte Carlo events and the background subtracted same-sign

dimuon excess in Figures 10.1-10.7. The number of $c\bar{c}$ events is normalized to the number of meson-decay events for the purpose of the comparison. The total visible energy in Figure 10.1, has a slightly higher average for $c\bar{c}$ gluon bremsstrahlung than the meson decay background. However, given the low statistics of the same-sign excess, it cannot be exploited to identify $c\bar{c}$ gluon bremsstrahlung events. Figure 10.2 shows the hadron energy. Since the data looks more like the $c\bar{c}$ gluon bremsstrahlung than meson decays in this distribution, we used the Kolmogoroff-Smirnov test [59] to obtain a quantitative measure of the agreement in shape between the hadron energy distributions. The test gives a probability that the $c\bar{c}$ distribution is the same as the data of 60%, which is inconclusive. The probability that the meson decay distribution is the same as the data is 43%, which is also inconclusive. The probability that $c\bar{c}$ and meson decay distributions are the same is 4%, which indicates that they are different as expected. Figure 10.3 shows the distribution of the momentum of the second muon which is slightly steeper for the meson decay background than for $c\bar{c}$ gluon bremsstrahlung. However, the low statistics of the data excess limit possible conclusions from these distributions. Figures 10.4 and 10.5 show x_{vis} and y_{vis}, which are the same for $c\bar{c}$ gluon bremsstrahlung and the meson decay background. Figure 10.6 shows the distribution of ϕ_{12}, the azimuthal angle between the two muons in a plane perpendicular to the beam direction and Figure 10.7 shows P_{T2}, the transverse momentum of the second muon relative to the hadron shower. These last two variables indicate if the second muon is associated with the hadron shower. In both variables, there is no difference between

the meson-decay background and $c\bar{c}$ gluon bremsstrahlung. In all cases the significance of the same-sign excess is not large enough to identify the source of the excess.

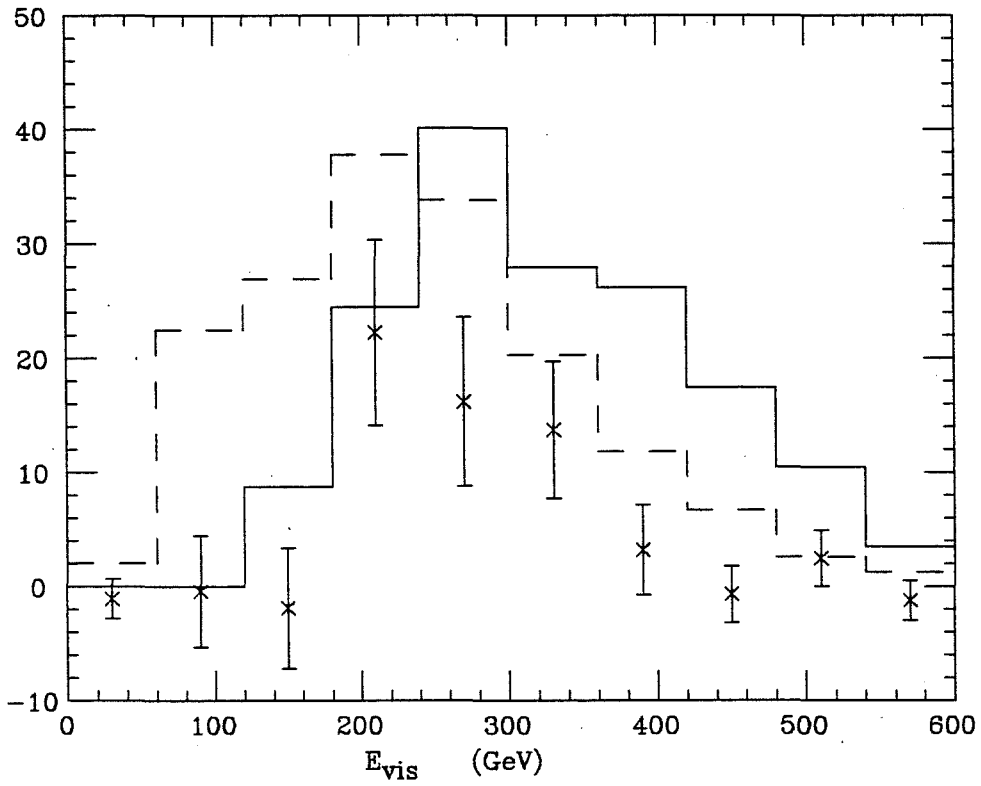

Figure 10.1 Total visible energy distributions for the meson-decay background (dashes), the $c\bar{c}$ gluon bremsstrahlung model (solid), and the measured same-sign dimuon excess (crosses). The $c\bar{c}$ gluon bremsstrahlung events are normalized to the number of meson-decay background events.

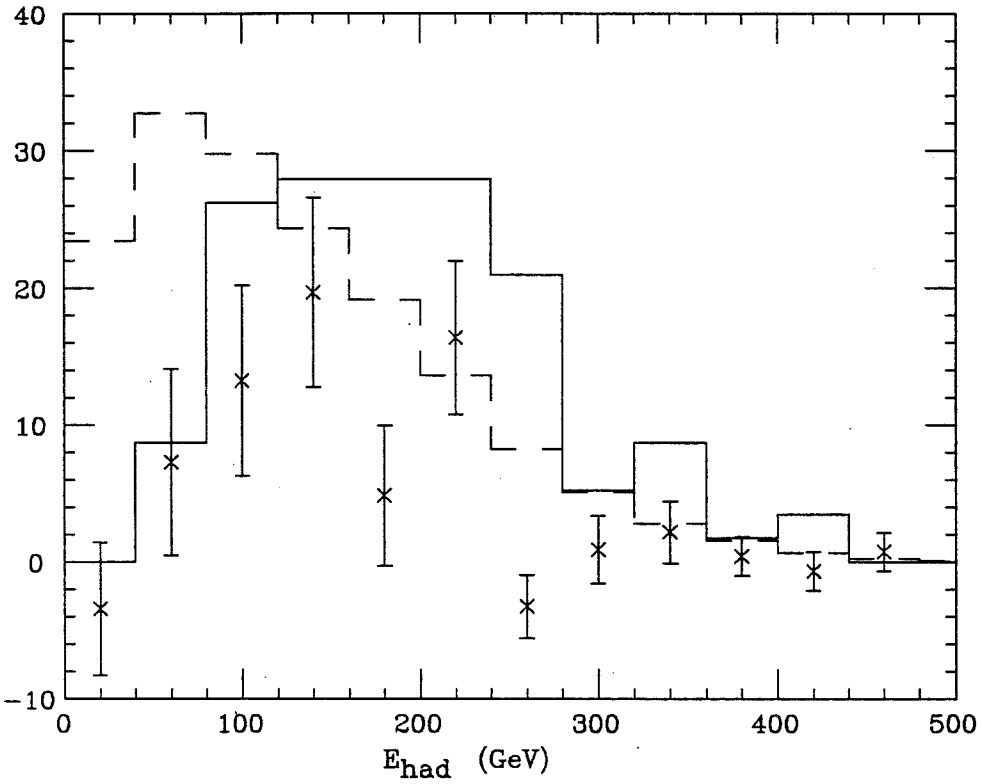

Figure 10.2 Hadron energy distributions for the meson-decay background (dashes), the $c\bar{c}$ gluon bremsstrahlung model (solid), and the measured same-sign dimuon excess (crosses).

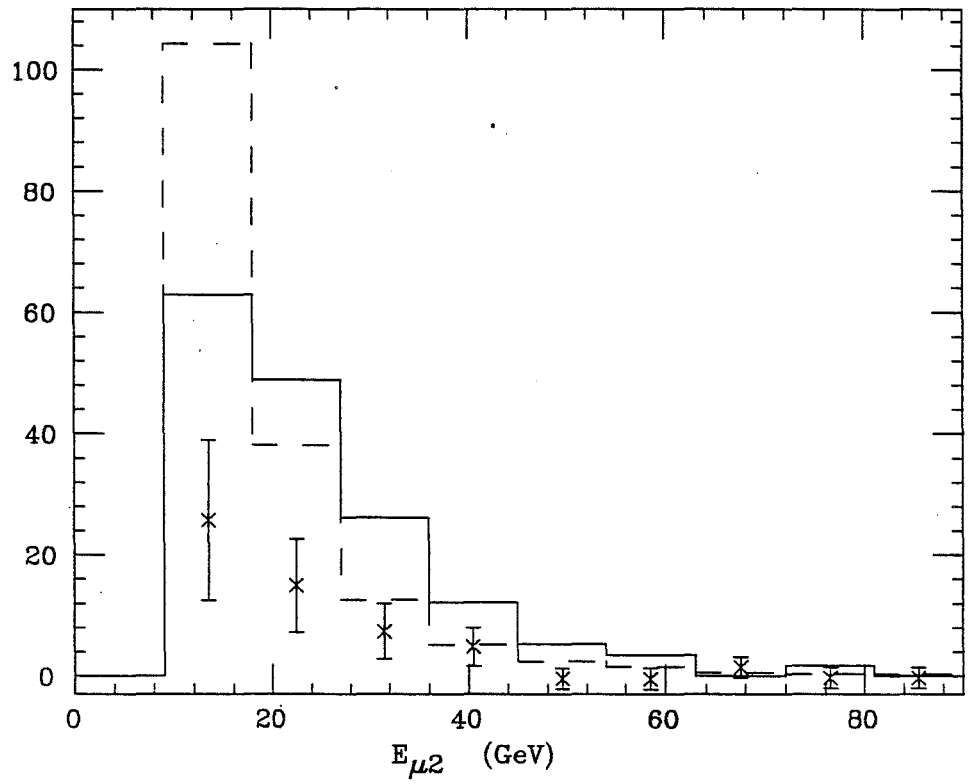

Figure 10.3 Energy of the second muon for the meson-decay background (dashes), the $c\bar{c}$ gluon bremsstrahlung model (solid),.and the measured same-sign dimuon excess (crosses).

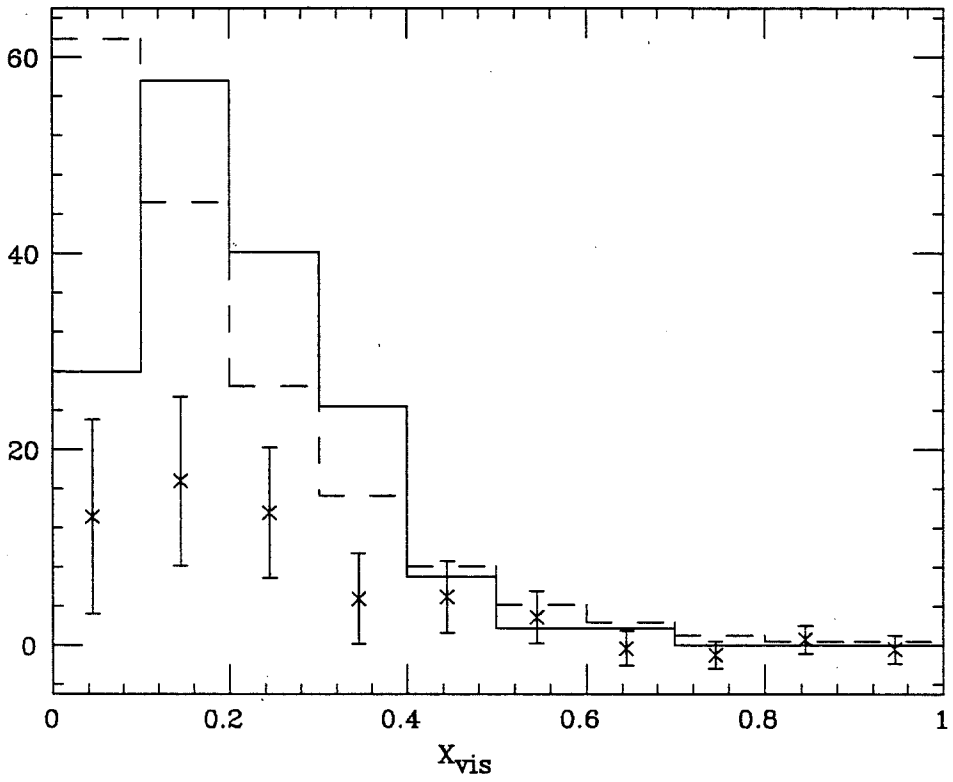

Figure 10.4 Distributions of x_{vis}, the measured Bjorken scaling variable, for the meson-decay background (dashes), the $c\bar{c}$ gluon bremsstrahlung model (solid), and the measured same-sign dimuon excess (crosses).

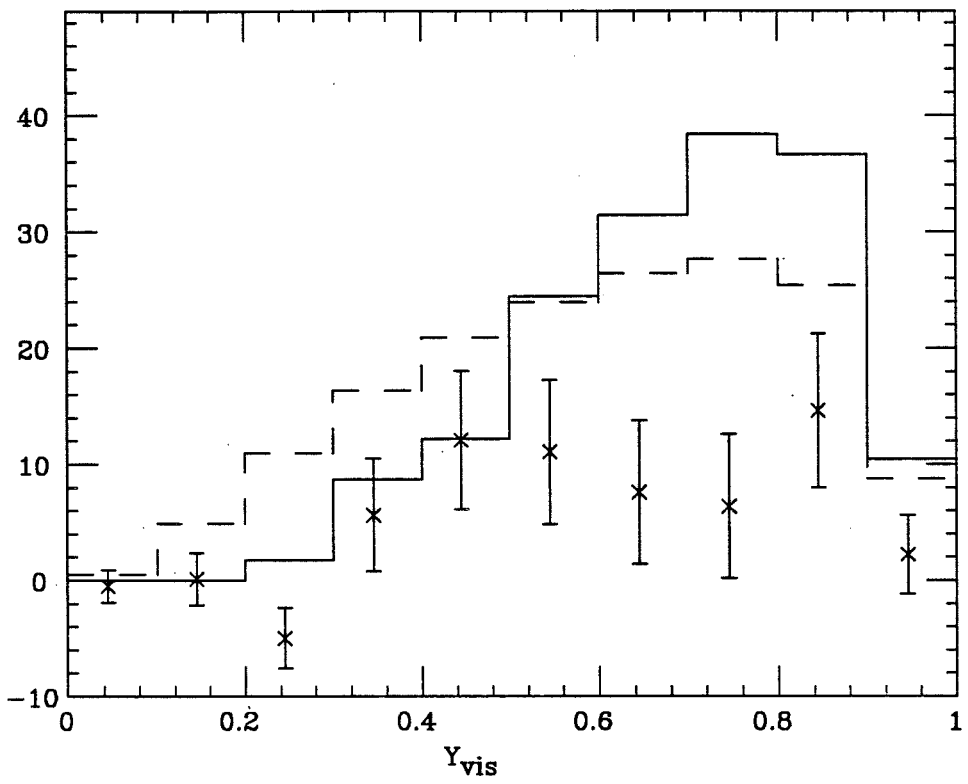

Figure 10.5 Distributions of y_{vis}, the measured Bjorken y variable, for the meson-decay background (dashes), the $c\bar{c}$ gluon bremsstrahlung model (solid), and the measured same-sign dimuon excess (crosses).

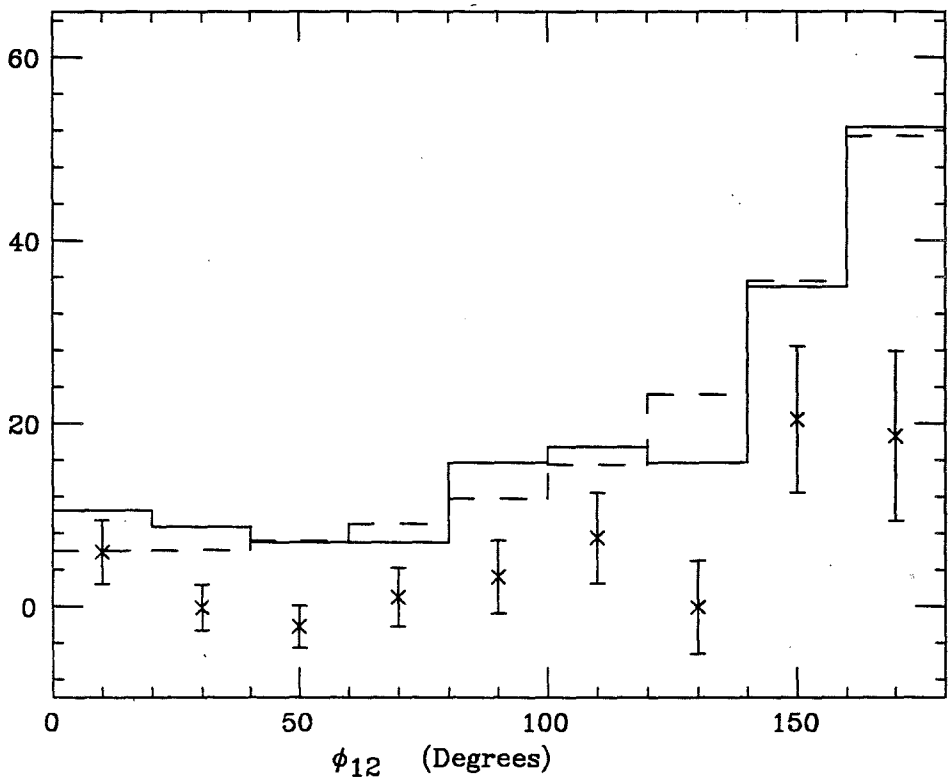

Figure 10.6 Distributions of ϕ_{12} for the meson-decay background (dashes), the $c\bar{c}$ gluon bremsstrahlung model (solid), and the measured same-sign dimuon excess (crosses).

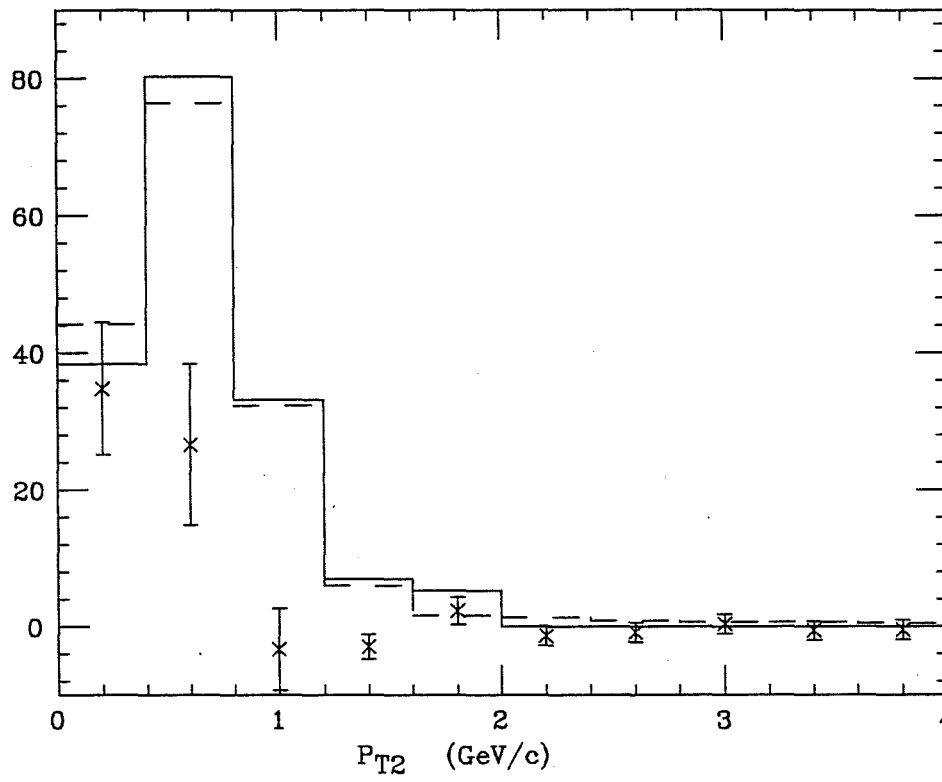

Figure 10.7 Distributions of the transverse momentum of the second muon relative to the hadron shower for the meson-decay background (dashes), the $c\bar{c}$ gluon bremsstrahlung model (solid), and the measured same-sign dimuon excess (crosses).

Chapter 11

Conclusions

We measured the prompt rate of same-sign dimuon production in neutrino-nucleon interactions for incident energies between 30 GeV and 600 GeV. The rate for incident neutrinos is $(0.53 \pm 0.24)\times10^{-4}$ per charged-current event or less than 0.92×10^{-4} at the 90% confidence level (C.L.). For incident antineutrinos, the rate is $(0.52 \pm 0.33)\times10^{-4}$ per charged-current event for 1.05×10^{-4} at the 90% C.L..

Prompt same-sign dimuon production is difficult to measure because most of the same-sign signal comes from the non-prompt meson decay background. We are the first experiment to have the advantage of precision measurements of the muon-production rate in hadron showers in our own apparatus to calculate the background due to the shower component of the meson decay background. Measurements of the muon-production rate by identified pions and kaons using a tagged hadron beam in the CCFR detector reduced the systematic error due to the shower component of the meson decay background. Other aspects of our meson-decay background simulation, particularly electro-weak fragmentation, were shown to agree with previous measurements of fragmentation in neutrino interactions as described in Chapter 7. Finally, the same-sign dimuon rates measured in this experiment and previously in experiment E744 cover the largest range of incident neutrino energies. The high energy neutrino beam and the combined data

from the two experiments E744 and E770 gave us higher numbers of same-sign dimuon events than in previous experiments.

The next section reviews each of the previous measurements and summarizes the different techniques they used to determine the non-prompt background. The following section summarizes the theoretical predictions for the prompt rate of same-sign dimuon production.

11.1 Comparison to Previous Measurements

Several experiments have measured the rate of same-sign dimuon production in ν-N interactions [5, 60, 61, 62, 63, 64], including experiment E744 in 1988 [1]. Figure 9.10 gives a comparison of the rates measured prior to E744 and the results of this experiment. Our measurements extend with significant statistics above visible energies of 200 GeV, the highest range of measurements prior to E744. Unlike some previous measurements, we do not observe a strong energy dependence of the rates. Furthermore, our rates are consistent with Standard Model calculations of $c\bar{c}$ gluon bremsstrahlung, whereas some previous measurements observed rates up to 4σ higher. The main difference between our experiment and previous experiments, other than high statistics at high energy, is the level of the subtracted meson decay background. In general the previous experiments did not have access to precision measurements of muon-production rates in hadronic showers to accurately calculate the meson-decay background.

The CHARM collaboration measured ν-induced same-sign dimuon rates at the CERN Super Proton Synchrotron (SPS) horn focused beam [62]. They observed 2.7×10^5 neutrino-induced charged-current events, with an

average energy of 60 GeV, and 74 neutrino-induced same-sign dimuon events with muon momentum at the vertex greater than 4 GeV/c. The CHARM detector consisted of a marble calorimeter instrumented with scintillation counters and drift tubes, surrounded by a magnetic frame, and followed by a muon spectrometer. Note that they did not have a background due to overlays because their detector was not as dense as ours. For total energies (E_ν) between 100 GeV and 200 GeV, they measured a prompt rate of $(7.8 \pm 1.8) \times 10^{-4}$ per charged-current event. This rate is significantly higher than our measured rate of $(-0.22 \pm 0.32)\times10^{-4}$ per charged-current event for the same incident energies but with a higher muon momentum cut of 9 GeV/c. In addition, their measurement is the most significant of previous results. This is because they calculated a lower background than would be determined by our meson decay Monte Carlo simulation.

The CHARM collaboration determined the meson decay background from the same-sign data directly from the separation (Δx) between the two muon tracks extrapolated back to the vertex. They obtained the expected Δx distribution by looking at punchthrough hadrons, which are hadrons that travel several interaction lengths before interacting. The CHARM collaboration argued that the distribution of the decay muon direction is the same as that of the parent hadrons, which can be represented by punchthrough hadrons. The Δx distribution of punchthrough hadrons was obtained from identified punchthrough tracks. However, punchthrough hadrons represent the background from decaying secondary mesons because they have a higher probability to punchthrough than primary hadrons, called

vertex hadrons [5]. Since secondary hadrons have a wider Δx distribution than the decay muons, the background calculated in this manner would tend to be underestimated. The authors later determined that the same-sign excess does not remain when the background is calculated without this bias towards the shower background [9].

The HPWFOR collaboration reported a prompt rate of $(3.0 \pm 0.8) \times 10^{-4}$ per charged-current event for energies between 40 GeV and 300 GeV and $P_\mu > 10$ GeV/c [63]. Our rate for energies between 30 GeV and 300 GeV and $P_\mu > 9$ GeV/c is $(0.36 \pm 0.21) \times 10^{-4}$, significantly lower than the HPWFOR rate. The experiment used the original Fermilab quadrupole triplet beam with an average neutrino energy of 97 GeV. They observed 1.9×10^5 neutrino-induced charged-current events and 44 neutrino-induced same-sign dimuon events with $P_\mu > 10$ GeV/c. The HPWFOR detector consisted of three sections with different densities; an iron target, a liquid scintillation calorimeter, and an iron plate calorimeter. These were followed by a muon spectrometer. They determined the background from a calculation of electroweak fragmentation and meson decay. To check their background calculation, they compared its predictions to their opposite sign dimuon data. First they extracted the prompt rate of opposite sign dimuon production from a linear fit to the rates plotted as a function of the hadronic interaction length. The rate at zero hadronic interaction length, corresponding to infinite density, is due solely to prompt production. The prompt rate of $\mu^+\mu^-$ per charged-current event was subtracted from the total rate, yielding a measurement of the meson decay

background as a function of hadronic interaction length. This agreed with their calculation of the meson decay background.

The HPWFOR collaboration did not give details in their publication about their calculation of the shower component and vertex component of the meson-decay background, which are complicated by the different densities in their detector. The relative amount of vertex decay background and shower decay background is very sensitive to the variable density of the target material through the decay probabilities. For example, the iron target, which was about 18 interaction lengths long, was followed by a liquid scintillation calorimeter that was about 1/4 the density of iron. Therefore, shower hadrons that penetrate into the scintillation counter are about four times more likely to decay than vertex and shower hadrons remaining in the iron. We found that muon-production measurements were necessary to accurately calculate the shower background in iron. Models alone were not sufficient to simulate nuclear effects on hadronic fragmentation.

The CFNRR collaboration measured a prompt rate of $(2.2 \pm 2.4)\times10^{-4}$ per charged-current event, for neutrino energies between 100 and 200 GeV and $P_\mu > 9$ GeV/c. This rate is based on 12 neutrino-induced same-sign dimuon events and 1.9×10^{4} neutrino-induced charged-current events [64]. Their result is consistent with our result of $(-0.22 \pm 0.32)\times10^{-4}$ at the same energies and muon momenta. The CFNRR detector was a dual-density steel target, instrumented with scintillation counters and followed by a muon spectrometer, also in the Fermilab Quadrupole Triplet neutrino beam. Their background was determined with a calculation of the meson-decay

background similar to our own. It simulated the vertex and shower components using measurements on muon-production in hadron showers in steel and electroweak fragmentation from bubble chamber experiments.

CDHSW measured a prompt rate of $(1.16 \pm 0.42)\times10^{-4}$ per charged-current event for neutrino energies between 100 and 300 GeV and $P_\mu > 9$ GeV/c at the CERN SPS [5]. They observed 367 neutrino-induced same-sign dimuons, only 20 of them were above 200 GeV, and 1.7 million charged-current events. Their rate is consistent with our result of $(2.05 \pm 0.80)\times10^{-4}$ also for energies between 100 and 300 GeV and $P_\mu > 9$ GeV/c. Their detector consisted of toroidally magnetized iron plates instrumented with scintillation counters and drift chambers. They were the first experiment to use a high density target. Unfortunately, overlay events turned out to be a considerable background due to the high density target combined with the high flux neutrino beam. They did not have the capacity to eliminate overlay events based on the time of passage of the muon tracks. Learning from their experience, we measured the time of passage of muon tracks and eliminated most of the overlay background. Their meson decay background, which was based on a Monte Carlo simulation, was 20% lower than ours when extrapolated to the same densities as the CCFR detector [9]. However, when CDHSW measured same-sign dimuon rates, precision measurements of the muon-production rate by hadrons were not available. We found that these measured muon-production rates were necessary to accurately calculate the shower component of the meson decay background.

Finally, the CCFRR collaboration measured a rate of $(2.4 \pm 1.7)\times10^{-4}$ per charged-current events for incident neutrino energies between 200 and 300 GeV and $P_\mu > 9$ GeV/c at the Fermilab Quadrupole Triplet Beam [60]. They observed 2×10^5 neutrino-induced charged-current events and 18 neutrino-induced same-sign dimuons. Their rate is consistent within errors with our rate of $(2.3 \pm 0.7)\times10^{-4}$ per charged-current event for the same energies and muon momenta. The CCFRR detector was the predecessor of the CCFR detector used in this experiment. Instead of drift chambers, it was instrumented with spark chambers. They calculated the meson-decay background with the same method we used. However, the muon-production data used to calculate the shower background was limited in statistics and incident energies. A comparison of our muon-production measurements to theirs in given in Section 5.7.

Tables 11.1 and 11.2 compare the prompt same-sign dimuon rates presented in this dissertation to the rates measured by experiment E744 in 1988 for incident neutrinos and antineutrinos [1]. Both the same-sign data and background of the 1988 results are consistent with measurements presented in this dissertation. For example, at neutrino energies between 100 GeV and 200 GeV, the rate published for E744 in 1988 is $(-0.67 \pm 0.55)\times10^{-4}$ compared to a rate of $(-0.22 \pm 0.32)\times10^{-4}$ for experiments E744 and E770 combined. The same-sign rate by antineutrinos measured in 1988 is twice as large as the rate presented in this dissertation, although they are consistent within uncertainties. The new measurements are based on data taken during both E744 and E770 so the statistical power is higher. Furthermore, the

calculation of the shower component of the meson decay background has been improved yielding a smaller systematic error on the background, as described in Chapter 6.

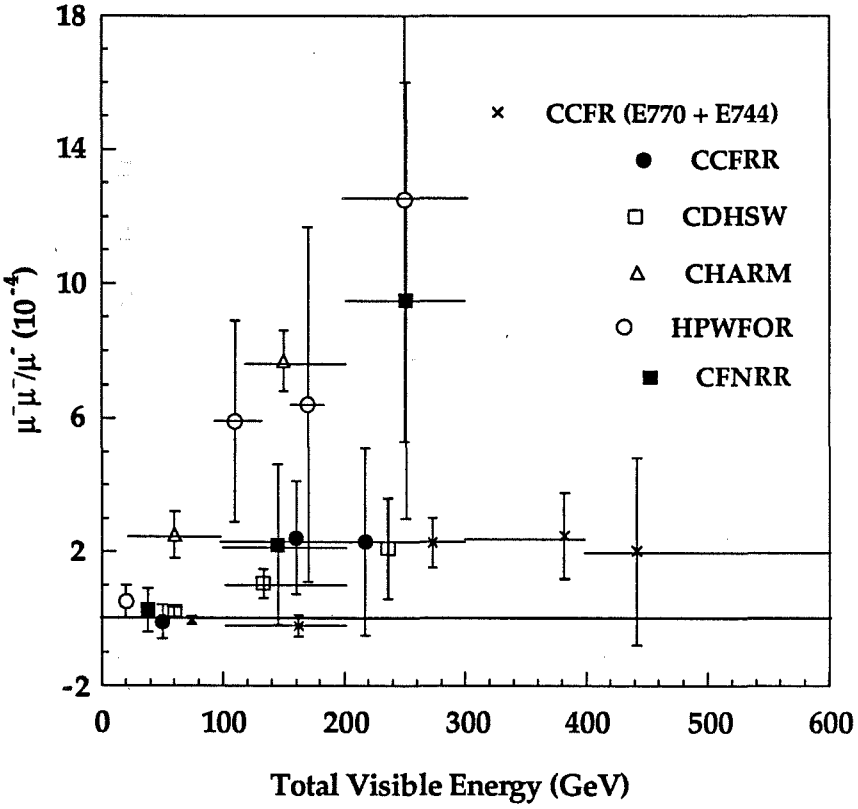

Figure 11.1 The acceptance corrected same-sign dimuon rate as a function of visible energy (crosses) compared to previous measurements.

Visible Energy (GeV)	E744 (1988) $\times 10^{-4}$	E744 and E770 (1991) $\times 10^{-4}$
30-100	0.01 ± 0.33	-0.04±0.14
100-200	-0.67 ± 0.55	-0.22±0.32
200-300	1.90 ± 1.10	2.27±0.74
300-400	3.65 ± 2.08	2.48±1.29
400-500	5.13 ± 4.45	1.57±2.66
500-600	-9.63 ± 7.41	0.44±0.89
30-300	0.24 ± 0.38	0.36±0.21
300-600	3.40 ± 1.91	2.33±1.18
total	0.55 ± 0.41	0.53±0.24

Table 11.1 Same-sign dimuon production rates by neutrinos as a function of total energy for previously published results of E744 [1, 9] and those presented in this dissertation. The errors are statistical and systematic uncertainties combined.

Visible Energy (GeV)	E744 (1988) x 10^{-4}	E744 and E770 (1991) x 10^{-4}
30-100	0.22 ± 0.61	-0.16 ± 0.21
100-200	2.79 ± 1.72	1.92 ± 0.91
200-300	1.29 ± 2.48	0.43 ± 1.45
300-400	1.05 ± 6.12	-0.85 ± 4.12
400-500	-5.40 ± 67.6	-4.60 ± 28.98
500-600	-0.90 ± 193.	6.01 ± 7.17
30-300	1.08 ± 0.69	0.51 ± 0.32
300-600	0.20 ± 5.20	1.04 ± 3.62
total	1.04 ± 0.68	0.52 ± 0.33

Table 11.2 Same-sign dimuon production rates by antineutrinos as a function of total energy for previously published results of E744 [1, 9] and those presented in this dissertation. The errors are statistical and systematic uncertainties combined.

11.2 Comparison to $c\bar{c}$ Gluon Bremsstrahlung

The measured prompt rate of same-sign dimuon production by neutrinos of $(0.53 \pm 0.24)\times10^{-4}$ per charged-current event is consistent with the calculated rate for $c\bar{c}$ gluon bremsstrahlung of $(9 \pm 39)\times10^{-7}$ and with zero. The prompt rate of same-sign dimuon production remaining after events due to $c\bar{c}$ gluon bremsstrahlung is subtracted from the signal is $(0.52 \pm 0.24)\times10^{-4}$ per charged-current event. In addition, the kinematic distributions for $c\bar{c}$ gluon

bremsstrahlung are similar to those of the measured excess and the meson decay background, so we can not distinguish events due to $c\bar{c}$ gluon bremsstrahlung based on kinematics alone as described in Section 10.2.2.

11.3 Final Conclusions

Neutrino production of same-sign dimuons was first observed in 1975 by the HPWFOR collaboration at Fermilab [65]. Since then several experiments have produced measurements of prompt same-sign dimuon production at energies up to 200 GeV, as described in Section 11.2. Before experiment E744 in 1988, there seemed to be a problem with the Standard Model predictions for the source of prompt same-signs; measured rates were several standard deviations higher than expected and theoreticians were unable to find a reasonable hypothesis for the excess.

We measured the rate of prompt same-sign dimuon production with the CCFR detector with high statistics at neutrino energies up to 600 GeV. Our measured rates are consistent with Standard Model predictions of cc gluon bremsstrahlung, which is the most likely source of prompt same-sign dimuons.

We had two advantages over previous experiments. One is the increased sample of same-sign dimuon events obtained at the Fermilab Tevatron. The second is our detailed measurement of muon-production in hadron showers that was used to calculate the shower component of the meson-decay background. We measured muon-production rates between 40 GeV and 200 GeV with high statistics. We also measured rates by identified pions and kaons, eliminating one of the largest systematic errors in

the background calculation, which was the level of muon-production by primary kaons.

More than fifteen years after the initial observation, we have enhanced our understanding of the production of same-sign dimuons. We find no evidence of anomalous same-sign dimuon production in neutrino-induced interactions. The 90% C.L. upper limit for neutrino-induced same-sign dimuon production per charged-current event is 9.2×10^{-5} and for antineutrino-induced production 10.5×10^{-5}.

Appendix A

Interaction and Decay Parameters

This appendix gives the interaction and decay parameters used in the calculation of the the meson decay background calculation.

The probability for a particle of mass m and energy E to decay is given by

$$P_d = \frac{\lambda_i}{\lambda_i + \beta\,\gamma\,c\,\tau} B_\mu$$

where τ is the proper lifetime of the particle, λ_i is the interaction length, B_μ is the muonic branching ratio, β and γ are the velocity and contraction factors of special relativity. For the CCFR detector, λ_i is calculated by extrapolating measured cross-sections on copper to iron [66]. We then scale it to the density of the CCFR calorimeter equal to $4.18\rho_{Fe}$ so that λ_i(CCFR) is equal to 1.802 λ_i. The Particle Data Group has compiled measurements of B_μ and $c\tau$ for the various particle species [44]. Table A1 gives $c\tau$, B_μ, and λ_i(CCFR) for pions and kaons in the CCFR detector.

	$c\tau$ (cm)	B_μ	λ_i (cm)
$\pi\pm$	780.4	1.000	36.36*
K^+	370.9	0.635	41.72
K^-	370.9	0.635	40.22
K^0	1554.0	0.271	41.72

Table A1. Interaction and decay parameters for the CCFR detector. *This holds for pion momenta greater than 22 GeV/c. For pion momenta less than 22 GeV/c, λ_i is given by $(2.12 \times 10^4)/(678 - 4.2\, p_\pi)$.

Appendix B

The Parametrization of Vertex Decay Muon Production

The vertex background is parametrized as a function of hadron energy (E_h), muon energy (E_μ), and x_{Bj}. The functional form is,

$$dP = \left(\frac{A}{E_\mu}\right)^B e^{-Cz}(1-z)^2 \, d E_\mu$$

where $z = E_\mu/E_h$ and the parameters A, B, and C depend on x_{Bj} as follows:

$$A = A_0 + A_1 x + A_2 x^2$$

$$B = B_0 + B_1 x + B_2 x^2$$

$$C = C_0 + C_1 x + C_2 x^2$$

where

$$x = x_{Bj} \quad \text{for} \quad 0.025 < x_{Bj} < 0.65$$

$$x = 0.025 \quad \text{for} \quad x_{Bj} < 0.025$$

$$x = 0.65 \quad \text{for} \quad x_{Bj} > 0.65.$$

The parameters A_i, B_i, and C_i are expanded in terms of $E' = \log(E_h/30.)$ as follows:

$$A_i = A_{i0} + A_{i1} E' + A_{i2} E'^2$$

$$B_i = B_{i0} + B_{i1}\,E' + B_{i2}\,E'^2$$

$$C_i = C_{i0} + C_{i1}\,E' + C_{i2}\,E'^2$$

Tables B1 and B2 lists the values of these parameters for the same sign background for neutrinos and antineutrinos.

A_i	a_{i0}	a_{i1}	a_{i2}
A_0	10.063	-1.5887	0.11658
A_1	-3.3512	1.4168	0.0
A_2	1.1309	-0.74166	0.0

B_i	b_{i0}	b_{i1}	b_{i2}
B_0	1.4709	0.11446	-0.011556
B_1	0.3	0.0	0.0
B_2	-0.3	0.0	0.0

C_i	c_{i0}	c_{i1}	c_{i2}
C_0	3.8336	0.58588	-0.17086
C_1	-1.4510	0.32336	0.0
C_2	0.0	0.0	0.0

Table B1 Parameters used in the fit to the like-sign vertex background for neutrinos.

A_i	a_{i0}	a_{i1}	a_{i2}
A_0	10.171	-1.7365	0.14772
A_1	3.4393	-0.60418	-0.19621
A_2	-0.36881	-0.43144	0.0

B_i	b_{i0}	b_{i1}	b_{i2}
B_0	1.4438	0.11772	-0.00963
B_1	0.3	0.0	0.0
B_2	0.0	0.0	0.0

C_i	c_{i0}	c_{i1}	c_{i2}
C_0	3.4293	0.60418	-0.19621
C_1	-1.3544	0.34998	0.0
C_2	0.0.	0.0	0.0

Table B2 Parameters used in the fit to the like-sign vertex background for anti-neutrinos.

Appendix C

The CCFR Collaboration

T. Kinnel, P. H. Sandler and W.H. Smith
Department of Physics, University of Wisconsin, Madison, Wisconsin 53706

C. Foudas, B. King, W.C. Lefmann, W.C. Leung, S.R. Mishra, P. Quintas,
S.A. Rabinowitz, F. Sciulli, W. Seligman, and M.H. Shaevitz
Department of Physics, Columbia University, New York, NY 10027

F.S. Merritt, M.J. Oreglia, H. Schellman, and B. Schumm
Department of Physics, University of Chicago, Chicago, IL 60637

R.H. Bernstein, F. Borcherding, M.J. Lamm, W. Marsh, and D. Yovanovitch
Fermilab, Batavia, IL 60510

A. Bodek, H.S. Budd, P. de Barbaro, and W.K. Sakumoto
Department of Physics, University of Rochester, Rochester, NY 14627

References

1. B.A. Schumm *et al.*, Phys. Rev. Lett 60 (1988) 1618.
2. D.B. MacFarlane, Z. Phys. C26, (1984)1.
3. C. Foudas, Ph.D Thesis, Columbia University, 1988.
4. V. Barger, W.Y. Keung, and R.J.N. Phillips, Phys. Rev. D24 (1981) 244.
5. H. Burkhardt *et al.*, Z. Phys. C31 (1985) 39.
6. Francis Halzen and Alan D. Martin, **Quarks and Leptons: An Introductory Course in Modern Particle Physics**, John Wiley and Sons, New York, 1984.
7. For a detailed description of the thickness and density of each calorimeter component see reference 8.
8. W. Sakumoto *et al.*, Nucl. Instr. and Methods **A294** (1990) 179.
9. B.A. Schumm, Ph.D. thesis, University of Chicago, 1988.
10. B.J. King, CCFR collaboration, Private Communication.
11. T. Ferbel **Experimental Techniques in High Energy Physics** Addison-Wesley 1987, page 274.
12. H. Budd, CCFR collaboration, private communication.
13. M. Purohit, Ph.D. Thesis, California Institute of Technology, 1983.
14. K. Bachman, Ph.D. Thesis, Columbia University, 1988.
15. A map of the magnetic field in the toroids was calculated with a numerical solution to the magnetostatic boundary value problem. The field in the gaps between the toriods was measured with a hall probe.
16. B.J. King *et al.*, Nucl. Instr. and Methods **A302** (1991) 254.
17. P.H. Sandler *et al.*, Phys. Rev. **D42** (1990) 759.
18. S.R. Mishra *et al.*, "Measurements of Nucleon Structure Functions, $F_2(x,Q^2)$ and $xF_3(x,Q^2)$, from ν-Fe Scattering at the Fermilab Tevatron, and the Mean Square Charge Test". Submitted for publication to Physical Review Letters.

19. W.C. Leung, Ph.D. Thesis, Columbia University, 1991.

20. W.C. Leung, "A Measurement of the Gross-Llewellyn Smith Sum Rule from the CCFR xF3 Structure Functions", submitted to Phys. Rev. Letters.

21. S. Dasu *et al.*, Phys. Rev. Lett, **61** (1988) 1061.

22. P. Quintas *et al.*, "A Measurement of Λ_{MS} from ν_μ-Fe Structure Functions at the Fermilab Tevatron.", Submitted for publication to Phys. Rev. Lett.

23. G. Koizumi, "Muon dE/dx and Range Tables for Tevatron Energies: Results for Some Shielding Materials" Fermilab-TM-0786, 1978.

24. J.R. Cudell, F. Halzen, K. Hikasa, Phys. Lett. **B175** (1986) 227.

25. T. Sjostrand *et al.*, The Lund Monte Carlo Programs, CERN long writeup (1986).

26. D.G. Ryan, Fermilab internal report TM-692 0621.000, 0650.000.

27 H.J. Kim, Zeus Collaboration, private communication.

28 R. Juhala, Fermilab internal report TM-434, 0621.05.

29 J. Lach and S. Pruss, "Instrumentation of the Hadron Beams in the Neutrino Area", Fermilab Publication TM-298 2254.000, April 28, 1971.

30. This equation is derived from the ideal gas law and Cauchy's dispersion formula. The former relates the pressure, P to the density of molecules, N. Cauchy's dispersion formula relates N to the index of refraction, n according to (n-1) = kN, where k is a constant.

31. During E770, data was taken with the Čerenkov counters at the 70 GeV beam energy only. The Čerenkov counters were also used with the Zeus test beam, also in lab E. The results on the efficiency of the counters is from data taken with the Zeus test beam experiment for a 50 GeV beam.

32. R.M Stermheimer in *Methods of Experimental Physics* Vol. 5A, Nuclear Physics A, eds. L.C.L. Yuan and C.S. Wu, Academic Press, New York (1961) pp. 4-55.

33. F. James and M. Roos, CERN Program Library D506, Minuit Function Minimization and Error Analysis, 1988.

34. T. Bolton, CCFR collaboration, Private Communication

35. J. Ritchie PhD. Thesis, University of Rochester, 1983.

36. V. D. Barger and R. J. Phillips: **Collider Physics**, (Addison-Wesley 1987)

37. N. Angelov et al. Yad Fiz. 25 1013(1977) [Sov. J. Nucl. Phys. 25, 539(1977)]

38. W. Busza, Nucl. Phys. **A418** (1984), 635.

39. N.J. Baker *et al.*, Physical Review **D34** (1986), 251.

40. D. Allasia *et al,*, Nucl. Phys. **B224**(1983), 1.

41. F.W. Brasse *et al.*, Proceedings of the 20th International Conference on High Energy Physics (1980) 755.

42. D. Allasia *et al.*, Z. Phys. **C24**(1984),119.

43. H.Deden *et al.*, Nucl. Phys. **B198**(1982), 365

44. Physics Letters **B239**, "Review of Particle Properties", 1990.

45. V. Barger *et al.*, Phys. Review Lett. **23** (1977) 133. T. Hansl et al, Nucl. Phys. **B142**(1978)381.

46. K.J. Anderson *et al.*, Phys. Rev. Lett **37** (1976)799.

47. V.D. Barger *et al.*, Phys. Review **D17** (1977) 2284.

48. P. Allen *et al.*, Nucl. Phys. **B194** (1982) 373.

49. P. de Barbaro Ph.D. Thesis, University of Rochester, 1990.

50. J. Donogue, Phys. Rev. D **33** (1986) 179., L. Wolfenstein,Phys. Letters **164B** (1985) 170.

51. N. Ushida *et al.* , Phys. Lett. **121B** (1983) 292.

52. J.C. Anjis *et al.*, Phys. Rev. Lett **60** (1988) 1239.

53. V. Barger, W.Y. Keung, R.J.N. Phillips, Phys. Rev. **D24** (1981)244.

54. M.H. Shaevitz, Nucl. Phys. B (Proc. Suppl.) **19** (1991) 270.

55. V. Barger, W.Y. Keung, R.J.N. Phillips, Phys. Rev. **D25** (1982) 1803.

56. C. Peterson *et al.*, Phys. Rev. **D27** (1983) 105.

57. H.D. Schulz, *et al.*, in Proceedings HEP, Bari 1985.

58. H. Albrecht *et al* Phys. Lett **105B** (1985) 235.

59. Eadie *et al.*, Statistical Methods in Experimental Physics, North-Holland (1971), pp. 269-270.

60. K. Lang *et al*, Z. Phys. **C33** (1987), 483.

61. M. Holder *et al.*, Phys. Lett. **70B** (1977), 396.

62. M. Jonker *et al.*, Phys. Lett. **107B** (1981), 241.

63. T. Trinko *et al.*, Phys. Rev. **D23** (1981), 1889.

64. K. Nishikawa *et al.*, Phys. Rev. Lett. **46** (1981) 1555.

65. A. Benvenuti *et al.*, Phys. Rev. Lett. **35** (1975), 1199.

66. S. P. Denisov *et al.*, Nucl. Phys. **B61** (1973), 61., J.C. Allaby *et al.*, Sov. J. of Nucl. Phys. **13** (1971), 295.